THE UNIVERSITY *of* EDINBURGH

Corrosion and Biofouling of Offshore Wind Monopile Foundations

Claire Canning

A thesis submitted in partial fulfilment of the requirements for the award of an Engineering Doctorate

The University of Edinburgh

2020

IDCORE

This thesis is submitted in partial fulfilment of the requirements for the award of an Engineering Doctorate, jointly awarded by The University of Edinburgh, The University of Strathclyde and The University of Exeter. The work presented has been conducted under the industrial supervision of EDF Energy R&D UK Centre, as a project within the Industrial Doctorial Centre for Offshore Renewable Energy (IDCORE).

THE UNIVERSITY *of* EDINBURGH

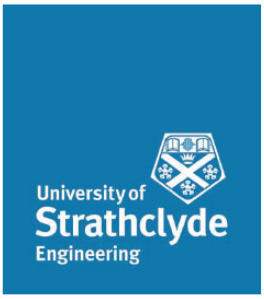

Declaration

I declare that this thesis has been composed solely by myself, that the work contained herein is my own except where explicitly stated otherwise in the text, and that this work has not been submitted for any other degree or professional qualification.

Claire Canning

January 2020

Abstract

The impact of corrosion and biofouling on offshore wind turbines is considered to be a key issue in terms of operation and maintenance (O&M) which must be better addressed. Early design assumptions for monopile foundations anticipated low, uniform corrosion rates in a sealed compartment that would be completely air- and water-tight. However, operational experience has shown that in practice it is very difficult to maintain a fully sealed compartment, with seawater and oxygen ingress frequently observed within many monopiles across the industry. A key concern is that this situation may accelerate corrosion of the internal surfaces. On the external surfaces, the accumulation of biofouling is known to impede the safe transfer of technicians from vessel to transition piece (TP) and requires frequent cleaning. It is also likely to influence the dynamic behaviour of the foundation due to the added weight and the hydrodynamic loading due to thickness and surface roughness changes. There is sufficient evidence to suggest that the current offshore wind guidelines on biofouling could be improved to optimise the design margins.

This thesis investigated the influence of internal monopile corrosion and external biofouling growth on the turbines at Teesside Offshore Wind Farm (owned and operated by EDF Energy). At Teesside, the primary drivers of internal monopile corrosion are identified as temperature, oxygen, pH and tidal variation. The influence of each of these parameters on the corrosion rate of monopile steel were investigated in a series of laboratory experiments and in-situ monopile trials. The experimental study was conducted at EDF laboratories in France using 186 corrosion coupons that were exposed to various treatments simulating internal monopile conditions. At Teesside, 49 coupons were suspended at various internal monopile locations across 5 foundations. In both cases, the weight loss measurement of coupons over time was used to determine the corrosion rates. Results suggest that tidal (wet/dry cycles) low pH and oxygen ingress have the greatest influence on the corrosion degradation of unprotected monopile steel. Internal tidal variations create a particularly aggressive corrosion environment. A decision tree matrix

has been developed to predict corrosion rate classification (high/medium/low) under a range of environmental conditions.

In parallel, a biofouling assessment was conducted at Teesside Offshore Wind Farm to determine the type and extent of marine growth on the intertidal and submerged zones of turbines. This has enabled a better understanding of the species diversity and community morphology but has also facilitated the development and testing of two sampling methodologies for the intertidal and subsea regions of offshore wind turbines; scrape sampling and remotely operated vehicle (ROV) surveying, respectively. The results of the assessment suggest a zonation pattern of marine growth with depth that is consistent with findings from other offshore wind farms and platforms. A super abundance of the non-native midge species *T. japonicas* at the intertidal zone has also been observed at other offshore wind farms in Belgium and Denmark, however, this is first evidence of its existence at a UK offshore wind farm. Removal of biofouling from the intertidal zones and jet-washing has now been optimised to coincide with peak settlement periods of mussels and barnacles. Image analysis and 3D mapping was conducted on the subsea ROV video footage to estimate thickness, roughness and added weight of biofouling.

This research provides an initial investigation into the effects of internal corrosion and external biofouling on monopile foundations at Teesside Offshore Wind Farm. The methodologies developed for this investigation and the results are critically discussed in the context of asset life assessment and improvements are suggested in further work.

Lay Summary

Early design assumptions for monopile foundations anticipated low, uniform corrosion rates in a sealed compartment. However, seawater and oxygen ingress have been detected within many monopiles across the industry, accelerating the corrosion process in particular locations. The consequences of corrosion are many and varied, and the effects of these on the safe, reliable and efficient operation of a wind turbine can often be far more serious than the simple loss of mass of a metal. Some of the harmful effects of corrosion include reduction of metal thickness leading to loss of mechanical strength and structural failure. Biofouling can potentially lead to corrosion on the external foundation surface and increase the hydrodynamic loads on the structures. EDF Energy own and operate Teesside Offshore Wind Farm and have a key interest in controlling and forecasting corrosion and biofouling through design, modelling, quality control, inspections and monitoring. This project had 3 key objectives:

1. Evaluate the current state of the monopile foundations at Teesside Offshore Wind Farm in terms of internal corrosion and external biofouling.
2. Develop a tool for predicting corrosion rate classification under a range of environmental conditions.
3. Determine good practices for assessing internal monopile corrosion and external biofouling accumulation through experimentation and field trials.

Experimental and field trials determined that that oxygen ingress, low pH and tidal action are the key environmental parameters influencing the corrosion rate of internal monopile steel at Teesside. A decision tree matrix was developed and used to predict high/medium/low corrosion rate classification under a range of environmental conditions typical of internal monopiles. The biofouling community and zonation patterns observed at Teesside are consistent with that of other UK offshore wind farms. An improved understanding of the growth cycle of mussel and barnacle species' enables the biofouling removal process at Teesside to be optimized and reduced.

Acknowledgements

I am incredibly grateful to everyone who has supported me through this extremely challenging yet rewarding journey. I would especially like to thank my supervisors; Dr. Julia Race, Prof. Elizabeth Cottier-Cook and Dr. Tariq Dawood for their support and encouragement throughout this process and for not giving up on me even despite the numerous times I gave up on myself. Special thanks to Julia for always making time for me, being an inspiration and giving me the drive to continue.

I would also like to thank the Renewables team at EDF Energy, for being an absolute pleasure to work with, and for giving the me the opportunity to learn and appreciate the real-world challenges of operating and maintaining an offshore wind farm. That experience has been invaluable and instrumental in me securing an exciting role at the Offshore Renewable Energy Catapult. I look forward to continued collaboration with the Renewables team throughout my time at ORE Catapult. Additionally, thank you to Delphine Gabriel, Emilien Burger, Yves Denos and the rest of MMC team at EDF R&D in Les Renaridères for supporting me in my laboratory work.

Of course, I would like to thank my family for encouraging and enabling me to follow my interests. Thank you for having confidence in me when I had none.

To my wonderful friends and colleagues from IDCORE, I couldn't have wished for a better group of people to share this journey with. We have been through so much together, and without your continued support and reassurance I would never have reached this stage. I cannot describe how lucky I feel to have worked alongside every one of you.

Last but not least, special thanks to Prof. David Ingram for taking a gamble on a 26-year-old Marine Biologist working in a Glasgow Call Centre, as a potential EngD candidate! Not everybody in your position would have taken a chance on me and I'm so grateful that you did.

Contents

List of Figures

List of Tables

List of Abbreviations

Ag	Silver
AgCl	Silver Chloride
AI	Artifical Intelligence
Al	Aluminium
ALWC	Accelerated Low Water Corrosion
AMSL	Above Mean Sea Level
ASTM	American Society for Testing and Materials
ATM	Atmospheric Zone
CA	Corrosion Allowance (mm)
C_d	Drag Coefficient
CL	Corrosion Loss (mm)
C_m	Inertia Coefficient
CP	Cathodic Protection
CR	Corrosion Rate (mm/y)
Cu	Copper
$CuSO_4$	Copper Sulphate
DL	Drilled Leaker
DNL	Drilled Non-Leaker

DNV GL`	Det Norske Veritas Germanischer Lloyd
DO	Dissolved Oxygen
E_a	Activation Energy
EDS	Energy Dispersive X-Ray Spectroscopy
EPS	Extracellular Polymeric Substances
Fe	Iron
FeO	Iron Oxide
FeS	Iron Sulphide
GACP	Galvanic Anode Cathodic Protection
GDP	Gross Domestic Product
GW	Gigawatt
H_2S	Hydrogen Sulphide
HAT	Highest Astronomical Tide
HISC	Hydrogen Induced Stress Cracking
ICCP	Impressed Current Cathodic Protection
IMZ	Immersion Zone
In	Indium
ISO	International Organisation for Standardization
KNIME	Konstanz Information Miner Analytics Platform
LAT	Lowest Astronomical Tide

LWP	Lower Work Platform
MDL	Minimum Description Length
MIC	Microbiologically Induced Corrosion
ML	Machine Learning
mm	Millimetres
MP	Monopile
mV	milli-volts
MW	Megawatt
NaCl	Sodium Chloride
NDL	Non-drilled Leaker
NDNL	Non-Drilled Non-Leaker
NE	Nutrient-enriched artificial seawater
NNS	Non-native species
O&M	Operations and Maintenance
OEM	Original Equipment Manufacturer
OWF	Offshore Wind Farm
PPM	Parts Per Million
ROV	Remotely Operated Vehicle
SAMS	Scottish Association for Marine Science
SBZ	Seabed Zone

SEM	Scanning Electron Microscopy
SRB	Sulphate Reducing Bacteria
SSCC	Sulphide Stress Corrosion Cracking
THW	Tidal High-Water Zone
TLW	Tidal Low-Water Zone
TP	Transition Piece
TSA	Thermally Sprayed Aluminium
WTG	Wind Turbine Generator
XRD	X-Ray Diffraction
Zn	Zinc
µm	micrometres

1 Introduction

1.1 Introduction to Offshore Wind

With a global requirement to reduce fossil fuel use and CO_2 emissions, measures are now being taken to cut energy consumption and to find sustainable alternative sources of energy [1]. Renewable energy sources have therefore received considerable attention worldwide [2]. In fact, the EU aims to obtain 20% of its energy from renewable sources, such as wind, wave, tidal, hydro-electric and solar power in addition to geothermal energy and biomass by 2020 [3]. Wind power in particular is the fastest growing renewable energy type due to the significant wind resource availability in Europe [4]. To take full advantage of this widely available resource and to extract as much energy as possible, more attention is now being focused on offshore wind [5] as public opposition to land-based renewable energy generation increases. In 2018, Europe connected 2,649 MW of new offshore wind power capacity to the electricity grid, which is equivalent to 409 new wind turbines across 18 wind farms [6]. In February 2019, Europe had a total installed capacity of 18,499MW across 11 countries and this number continues to increase. Currently, the UK is the leading the way in offshore wind development, representing 44% of all installations, and is projected to grow to a total installed capacity of 30GW by 2030 [7]. This represents the largest expansion of any type of renewable energy technology [8].

According to the most recent statistics, the average capacity of newly installed offshore wind turbines in Europe is 6.8MW, a 15% increase on 2017 [6]. The

support structure of an offshore wind turbine looks similar to that of an onshore turbine [9]. However, there are some special design considerations required offshore due to the stronger winds and wave and tidal forces [10] such as a strengthened tower to cope with wind-wave interactions and a transition piece which forms a base to support the tower. The foundation type and design is an important consideration as it accounts for 15 to 40% of the total cost of an offshore wind farm project [10]. With the majority of current wind farms constructed in shallow waters (<30m), relatively simple foundation types have been used thus far such as monopile, tripile, jacket structures and gravity based. The monopile (MP) shown in Figure 1.1A, is the most commonly used sub-structure, supporting around 81% of European offshore wind turbines [8].

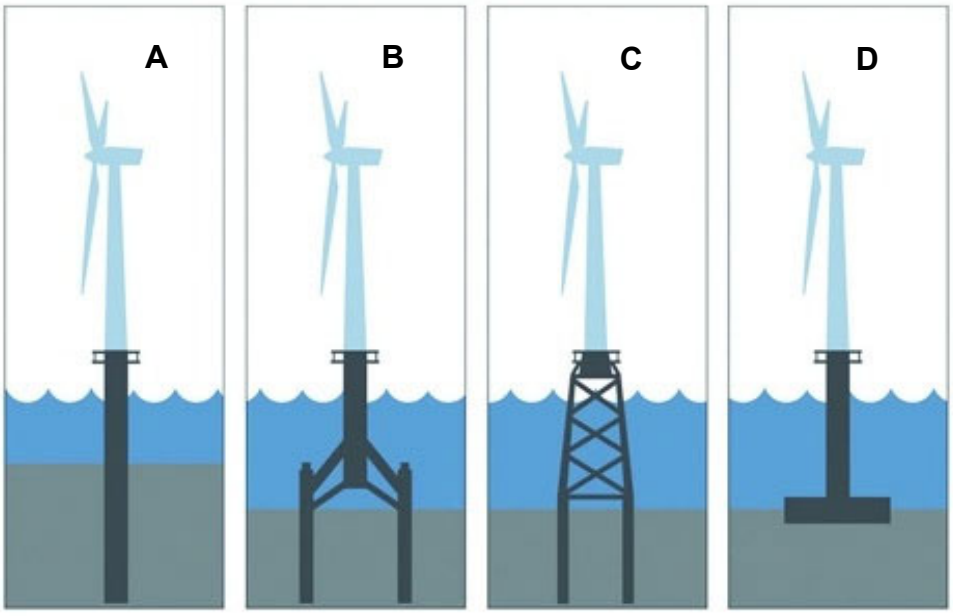

Figure 1.1: *A schematic of offshore wind turbine foundations. A) Monopile B) Tripile C) Jacket and D) Gravity based [11].*

The MP is a simple design whereby the tower is supported by one large pile, either directly or through a transition piece (TP), which is a transitional section between the tower and MP [12]. The diameter of a MP currently ranges up to 7m with the wall thickness as much as 150mm [13]. The MP is driven into the seabed where it is fully anchored. The transition piece (TP) is placed over the top of the MP with a typical overlap of 6m. The gap in-between the two structures is cemented with high-strength grout. There are typically 2 platforms found on the TP from which personnel can gain access inside the foundation: the service (lower) platform which is in close proximity to the TP/MP connection, and the airtight work platform which seals the foundation[14]. The majority of offshore wind turbines have a J-Tube to support the power cable which runs from the generator at the top of the tower down the length of the structure, either internally through the airtight platform or externally (Figure 1.2). However, more recent installations use free hanging cables from the TP rather than pulled through the foundation. This cable then transports electricity to an offshore/onshore substation where it is then sent to the grid.

The manufacturing of a MP includes hot-rolled plates to be bent via cold-rolling and longitudinally welded to form ‘cans’ of 3-7m diameter. These are subsequently joined via circumferential welding to achieve the full-length MP [15]. The double-V butt joint, in which V-shape welds are on both sides of the work piece is typically used in monopile foundations [16]. These welded joints are significantly affected by residual stresses and welding profile. The structural performance of a MP can be significantly affected by welding quality, as high

stresses local to the welded joints could results in crack initiation and catastrophic failure.

The design of monopiles is often driven by fatigue as offshore wind turbines are exposed to long-term, variable amplitude aerodynamic and hydrodynamic loading [17]. Uncertainties in environmental loading, material resistance and design models often cause the physical properties and therefore lifetimes of installed turbines to differ from design assumptions. Fatigue life calculations must therefore also consider data and measurements from on-site inspections and monitoring during the operations and maintenance phase. For MPs, the most fatigue critical location is often located near to or below the seabed where direct measurement or monitoring is particularly difficult [18].

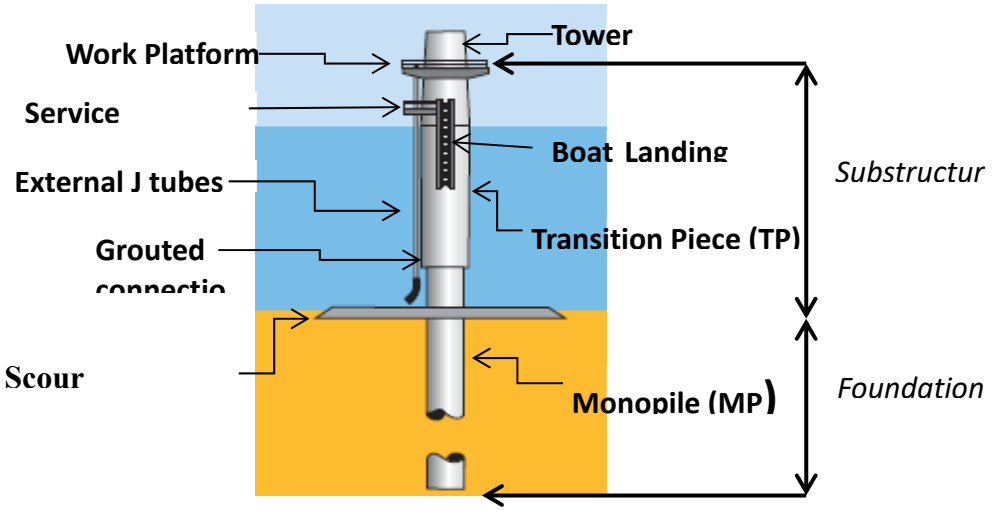

Figure 1.2: *Overview sketch of an offshore wind turbine substructure and monopile foundation. Figure adapted from* [19].

1.2 **Problem definition**

The operation of steel structures offshore is well-established in many industries such as oil and gas exploration and extraction, shipping, and power plants [20]. Often these structures are located in harsh environments, threatened by wind and wave loads. In addition, large areas can be permanently or frequently exposed to seawater, causing significant corrosive and biological stresses. The corrosive stress is not limited to seawater exposure, but can also feature wet-dry cycles, pH and temperature variations [21], and bacterial influence. Offshore structures also represent a new habitat of artificial hard substrate that will ultimately be colonised and successively develop biofouling assemblages [22].

Issues such as corrosion and biofouling in these industries have been well studied over the years, however, a full understanding of all the mechanisms involved is lacking. The impact of corrosion and accumulation of marine growth on offshore wind turbine foundations is considered to be a key issue in terms of operation and maintenance (O&M) which must better be addressed [23][24]. In the offshore wind industry, in addition to physical loading, corrosion and the accumulation of marine growth represent key additional stresses in the complex stress regime experienced by an offshore wind turbine[23]. Wind farm operators strive to avoid the deterioration of structural strength and integrity as result of these issues [25][26]. Therefore, the foundation, transition piece and turbine tower are of particular importance when considering protective measures against these stresses since they form the entire support structure of the device and are

often the most exposed areas, having to withstand extreme environmental conditions [26] i.e. atmospheric marine exposure, seawater exposure and wet-dry cycles [20].

Corrosion can contribute to fatigue cracks in offshore structures due to the synergistic interaction of cyclic loads and the influence of a corrosive environment [27]. Whilst crack growth behaviour of steels used in offshore oil and gas industries has been studied over the years [28][29], offshore wind turbines are relatively new structures and their long term corrosion fatigue performance data are scare or even non-existent [30], [31]. There are many regions of the offshore wind substructure that are uncoated or unprotected in which cracks could form and propagate leading to catastrophic failure, i.e. below the seabed.

Corrosion and biofouling could have a significant impact on the lifetime of the structures due to potentially accelerated ageing and deterioration of the materials. It is important for operators to control and forecast the development of corrosion degradation and biofouling on their assets to ensure that can fulfil their operational lifespan. In order to achieve this, corrosion protection systems, remedial works, corrosion rate prediction and an understanding of biofouling accumulation needs to be taken into consideration.

1.3 **Teesside Case Study**

Teesside Offshore Wind Farm (OWF) is located off the Northeast coast of England near Redcar and was commissioned in July 2013. The farm consists of 27 Siemens 2.3 MW turbines with a total installed capacity of 62.1 MW. These turbines have a hub height reaching 80m and have a 93m rotor diameter [32]. The monopiles are largely constructed from S355NL structural steel and range from 65mm to 85mm in thickness [32], [33]. Their average internal diameter is approximately 4m with the upper and lower limits at 4.460m and 3.775m respectively [33]. A description of Teesside OWF is given in Table 1.1 and the turbine layout is illustrated in Figure 1.3.

Table 1.1 *Teesside offshore wind farm description.*

Location	Redcar (offshore)
County	Teesside
Number of turbines	27
Turbine rating	2.3 MW
Project capacity	62.1 MW
Hub height	80 m AMSL
Rotor diameter	93 m
Manufacturer	Siemens
Commissioning date	July 2013
Number of rows	3
Number of turbines per row	9
Foundation type	Monopile with grouted TP

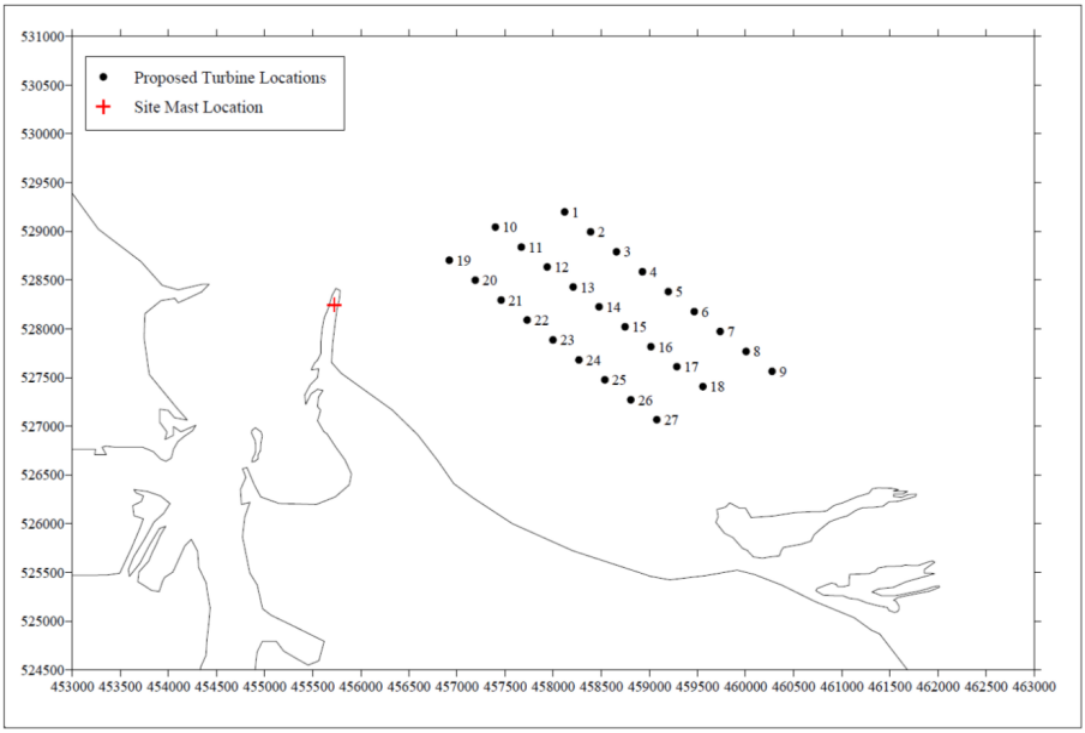

Figure 1.3: *Teesside OWF turbine layout with position of current met mast (red cross) (GB National grid coordinate system) [6]*

1.3.1 **Internal corrosion issues**

Teesside OWF turbines are supported on monopile foundations and a general schematic is provided in Figure 1.4. When considering the corrosion protection system of the internal steel, the initial design assumption envisaged the internal monopile to be completely sealed. Therefore, the corrosion process within the monopile was expected to slow and eventually cease once all residual oxygen was consumed in the air-tight compartment of the foundation.

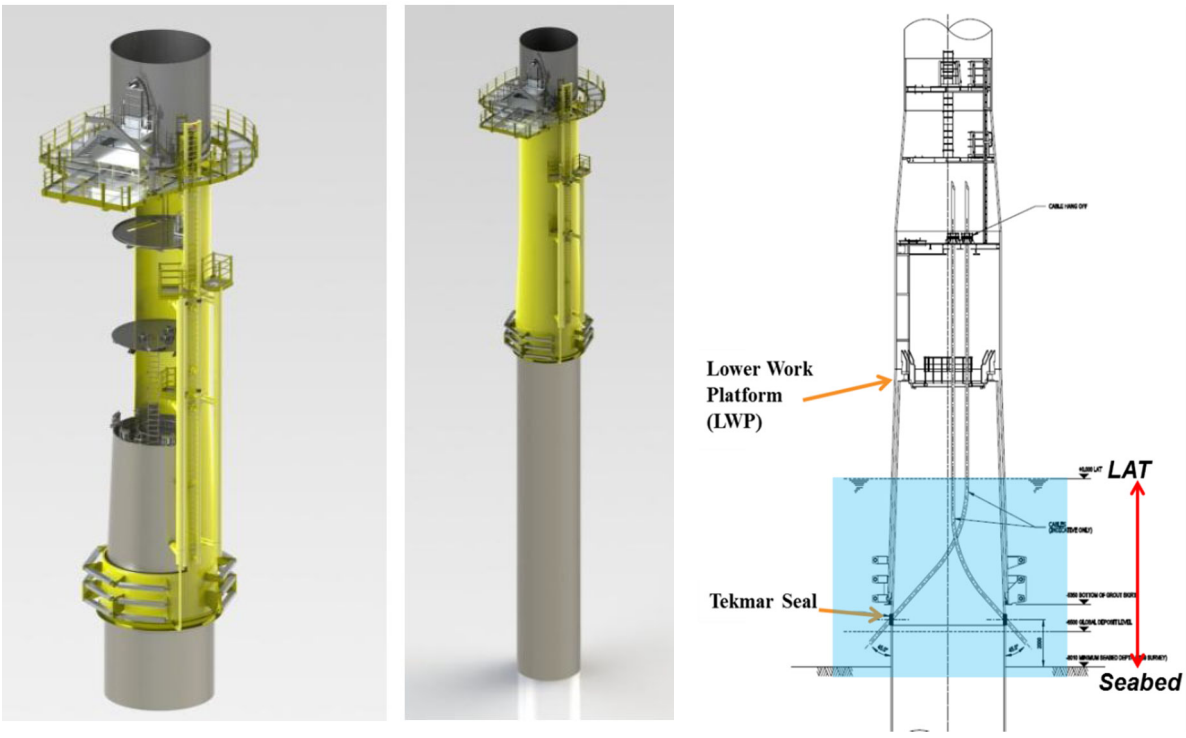

Figure 1.4: *General schematic illustrating the typical transition piece – monopile configuration at Teesside, with internal free-hanging electrical cables that exit the foundation via a Tekmar protection system.*

However, in the lower section of each monopile, there are circular ports which enable the exit of the electrical transmission cables (Figure 1.4). Each port contains a pneumatic sealing system, designed to protect the cable and prevent any ingress/egress of seawater into the foundation. This is known as the Tekmar Teklink© cable protection system (Figure 1.5).

1.3.1.1 **Leaking monopiles**

It was observed during post-construction inspections, that a number of the Teesside foundations were experiencing internal leaks, attributed to degradation of the Tekmar system. Severity of the leak differs between monopiles depending

on the number of failed Tekmar systems, however the result is an internal water level variation as the tide rises and falls. To date, 13 out of the 27 monopiles have shown signs of leakages, with the expectation the same failure will occur across the remaining foundations in the future.

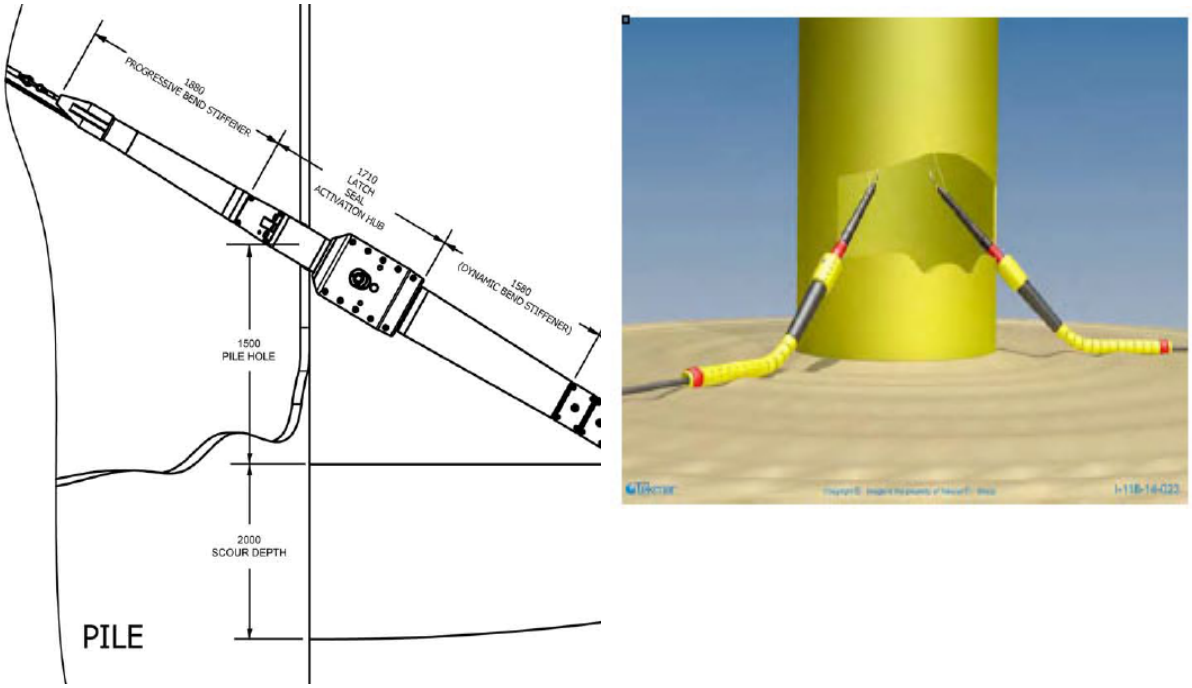

Figure 1.5: *Schematic of Tekmar Teklink© Cable Protection System installed at Teesside OWF*[34].

1.3.1.2 **Internal ventilation**

An additional issue is the periodic ventilation of the airtight platform, required for manned access to this area and the lower working platform (LWP) which can be seen in Figure 1.4. As a result, the oxygen concentration in the atmosphere above the water is increased, potentially leading to an increase in dissolved oxygen within the internal seawater. Since the internal monopile environment was

not designed to experience a tidal cycle, or oxygen ingress, it is a significant concern that the corrosion process inside the monopile will accelerate rather than cease, risking a severe reduction in the lifetime of the structure.

1.3.1.3 **Cathodic protection retrofit**

In 2011, a change in the DNV design code for offshore wind turbines [35] outlined the requirement for cathodic protection (CP) inside the monopiles of offshore wind turbines. This came as a result of industry-wide reports of leaking systems and internal water level variations. To achieve this certification, the retrofitting of two different Aluminium alloy (Al-Zn-In) galvanic anode CP systems was implemented in all 27 monopiles at Teesside; one for drilled foundations (25 year lifetime) and one for undrilled (5 year lifetime), which are shown in Figure 1.6.

Fifteen foundations were internally drilled after being pile-driven by a large hydraulic hammer. This drilling process lead to the removal of the internal soil plug and enabled the pile to reach target penetration through the mudstone. Drilled foundations were installed with a ‘’flagpole’’ type arrangement for CP consisting of between 25 to 31, 175kg anodes. The remaining 12 foundations were undrilled and maintained their internal soil plug. These foundations were installed with a smaller “anode string” CP arrangement whereby strings of anodes were attached and hung from the lower working platform. Each string supported 3 to 4 17.5kg anodes and the number of anodes required per undrilled monopile varied from 26 to 33.

a) Drilled **b) Undrilled**

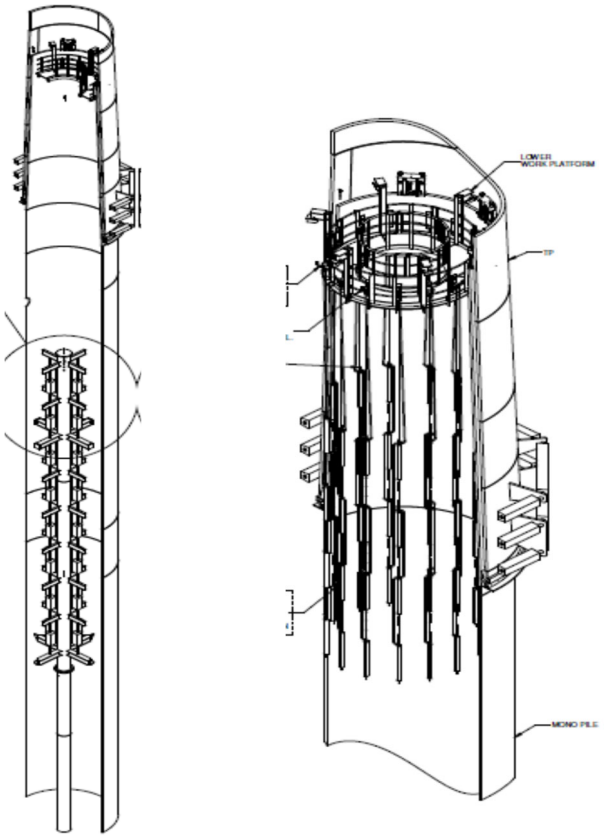

Figure 1.6: *Schematic diagrams of the flagpole anode arrangement for a) Drilled foundations and the string anode arrangement for the b) Undrilled foundations* [36]

The implementation of a retrofitted internal CP arrangement within the monopiles at Teesside has given rise to further operational issues that have been identified during routine maintenance activities and CP surveys and are defined below.

1.3.1.4 **Protection potentials below -800mV**

Section 11.4 of the DNV guidelines [35] stipulates that a CP survey must be conducted on “a few representative structures” after 365 days to confirm that the structural steel is adequately protected. A survey was conducted across 24 of

the 27 foundations to ensure that the internal anodes were performing effectively. A mix of drilled, undrilled, leaking and non-leaking structures were selected for the survey, which took place in early 2016. As outlined in the DNV recommended practice for cathodic protection design [37], recordings were taken from the anodes using a Silver/Silver chloride (Ag/AgCl) reference electrode to ascertain the protection potential (E_c^0). It is generally accepted that steel structures in seawater are protected by imposing potentials more negative than -850mV relative to a Copper/Copper Sulphate ($Cu/CuSO_4$))reference electrode or -950mV in anaerobic conditions (respectively -800mV and -900mV *vs* Ag/AgCl reference electrode) [38]–[40].. The DNV and Ramboll design code stipulates that a protective potential of -900mV should apply in anaerobic environments, including the internal mud zone where there is assumed to be high bacterial activity [41][36]. Unlike the drilled foundations, the undrilled structures contain an internal soil plug, which present favourable anaerobic conditions for corrosion-related bacteria such as Sulphate Reducing Bacteria (SRB) propagation and therefore have an increased risk of Microbiologically Induced Corrosion (MIC).

A range of potential recordings were taken from all 24 internal CP surveys and are shown in Figure 1.7. The survey highlighted specific regions of the internal steel surface that are not adequately protected by the CP system in that the protective potential is less negative than -800mV (or -900mV at the mudline). Additionally, there are some internal regions experiencing overprotection in potential, beyond the recommended DNV standard (more negative than -1000mV).

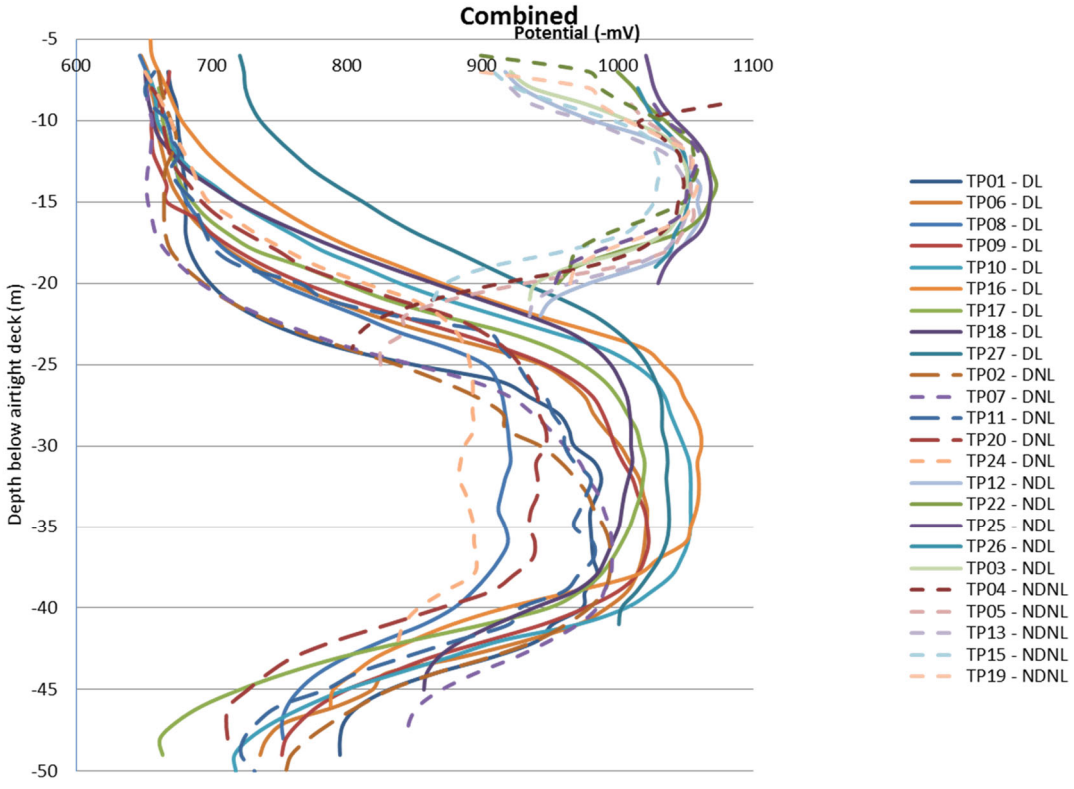

Figure 1.7: *The profile of internal protective potential with depth of foundations at Teesside OWF (All foundations have been classified as one these categories DL-Drilled Leaker, DNL-Drilled Nonleaker, NDL-Non-drilled Leaker & NDNL-Non-drilled, Non-Leaker).*

Drilled Foundations

The results of the internal CP survey indicate that in general, the drilled foundations are not achieving a minimum protection potential around the surface of the internal water level, with readings as low as -670mV at the internal water/atmosphere interface. There seems to be sufficient protection around mid-region for drilled structures, however this tends to verge into the overprotection range with many structures achieving beyond -900mV. However, towards the lower submerged zone and the seabed, the profile appears to taper off, with the majority of drilled structures not receiving adequate protective potentials. It is

possible that the performance of anodes in the leaking structures is influenced by the ingress/egress of water. The influx of fresh seawater through the failed seals replenishes dissolved oxygen concentrations to levels that would generally be considered an anaerobic environment. Dissolved oxygen is considered one of the most corrosive elements within the monopile and its continuous replenishment around this zone may impact the behaviour of the sacrificial anodes such that they are unable to achieve the minimum protection potential of -800mV.

Undrilled Foundations

Internal CP potential readings recorded within the undrilled foundations are less concerning, since all foundations are achieving and exceeding -800mV at the surface of the internal seawater and around the mid-submerged-zone. However, some structures are not achieving the Ramboll requirement of -900mV at the mud zone where there is the potential for MIC.

1.3.1.5 Protection potentials above -1050mV

According to DNV [37] , CP can cause atomic hydrogen to form at the metal surface. Within the possible range of potentials for CP by the Al-Zn-In anodes at Teesside (-800mV to -1100mV), the production of hydrogen would increase exponentially towards the negative potential limit of -1100mV. The hydrogen atoms can either combine to form hydrogen molecules or can become absorbed into the metal. Should hydrogen be absorbed, its molecules will then interact with the microstructure of steel components subject to high stresses, which may

induce cracks in the steel. This defect mechanism is known as hydrogen induced stress cracking (HISC). The grade of steel used in the construction of the MPs at Teesside (S355NL) is a ferritic-pearlitic structural steel [42]. Based on practical experience, this type of steel has proven compatibility with marine CP systems and is therefore not susceptible to HISC under normal operating conditions [41]. However, the absorption behaviour of hydrogen atoms towards the negative potential limit of the installed CP is still a risk that should be considered, given that readings are approaching the negative potential limit in some areas i.e. -1082mV at 5.1m below internal water level in WTG 05. At this level, the steel is being overprotected [41] and anodes are presumably degrading at a faster rate.

1.3.1.6 **Anode distribution**

The CP potential readings recorded within each foundation show a general trend whereby high levels of protection occur around the middle of the monopile (relative to internal seawater level). The high potential readings recorded at this region, and the insufficient readings recorded at the top and bottom levels suggest that the distribution of anodes within the monopile foundations is not optimized to achieve a uniform protection reaching from the highest internal water level down to the seabed. Instead, it appears that the protection is centred within the middle zone of the monopile foundation. Additionally, it is possible that the generated current density is insufficient to deliver the protection potential to each zone. Figure 1.6a shows the arrangement of the anode installation within drilled foundations. It can be seen that the general flagpole arrangement is installed centrally with respect to monopile height, which may support the view that the

anodes are not distributed effectively for uniform protection. However, it must be noted that the initial design for this CP system did not anticipate that the internal water level would reach the height of the lower working platform, which has unfortunately been the case in some leaking foundations. Therefore, the installed CP system was not initially designed to protect the entire steel surface, and this has since become an issue due to the unforeseen internal tidal conditions.

1.3.1.7 **Internal seawater acidification**

One of the unforeseen consequences of an aluminium anode CP system is the acidification of the seawater inside the MP. In 2014, internal pH measurements taken from all the monopiles at this site indicated that 15 foundations (more than 50%) contained seawater with a pH <6; 7 of which had a value as low as pH 4 (Figure 1.8). It is known that such low pH values can significantly reduce the current output of sacrificial anodes and prevent the CP system from working effectively [43]. A more critical issue however, is the impact on corrosion of the internal steel surfaces as a result of long-term exposure to a low pH seawater medium, pH 4 or less, as this mechanism is poorly understood and there is very literature published on this topic in the context of corrosion within offshore wind monopile foundations. The low pH conditions observed in the monopiles is attributed to the dissolution of aluminium from the anodes in a closed compartment [44]–[46] which can be seen in the following reaction:

$$Al \rightarrow Al^{3+} + 3e^{-}$$

$$\boldsymbol{Al^{3+} + 3H_2O \rightarrow Al(OH)_3 + 3H^{+}}$$

There is also believed to be a minor contribution from the formation of Hydrogen Sulphide (H_2S) from bacterial activity [45].

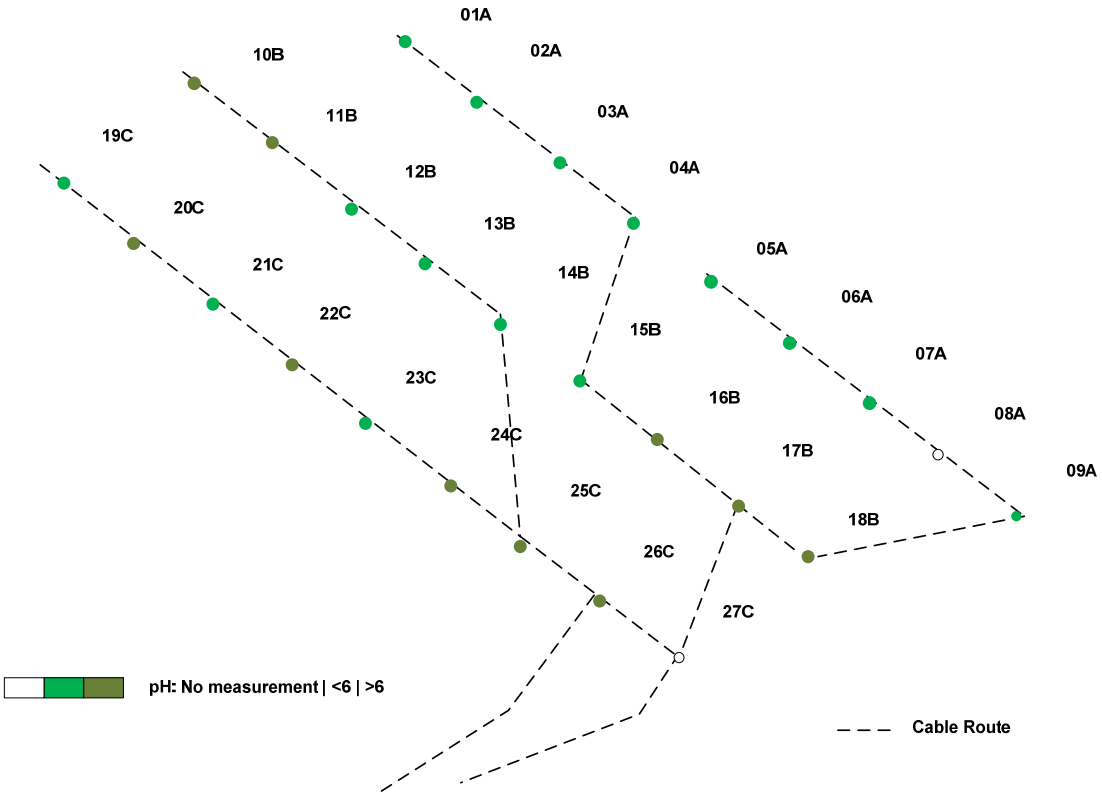

Figure 1.8: *Distribution of internal water column pH levels across all foundations at Teesside OWF.*

1.3.2 **Biofouling accumulation**

The accumulation of biofouling at the splash and intertidal zones of the turbines at Teesside has been identified as a key issue in terms of operation and maintenance, and health and safety. Technicians have reported that during the summer months and through to Autumn/Winter, these regions require intense jet-washing every 2 to 3-weeks to clear the structures of marine growth. This type of regular maintenance is particularly costly when considering the vessel,

technicians and equipment required for each trip. If the marine growth is not removed on a regular basis, the concern is that the hard-fouling species such as barnacles and mussels, will accumulate and damage or degrade the anti-corrosive coating on the TP. Furthermore, the accumulation of seaweed and kelp on the TP ladders can potentially compromise the safety of technicians transferring from the vessel to TP and vice versa, due to the slippery surface created.

1.4 **Project Objectives and Scope**

The issues described in the previous sections demonstrate how corrosion and biofouling could significantly affect the lifetime of offshore wind turbines through accelerated ageing and deterioration of materials. In light of these issues, the objectives of this project are as follows:

- To identify and evaluate the key environmental parameters influencing the internal corrosion behaviour of offshore wind monopile foundations using Teesside OWF as an experimental test case.
- To determine the individual effect of each environmental parameter on the corrosion loss of internal monopile steel through a combination of laboratory experiments and offshore trials.
- To develop a predictive tool that will estimate the corrosion rate of internal monopile steel expected under specific environmental conditions, which will then contribute to lifetime assessment of the structure.

- To develop a methodology for the assessment of biofouling on offshore wind monopile foundations and test this at Teesside OWF.
- To better understand the biofouling species composition and characteristics at Teesside OWF that will improve current maintenance practices and contribute to future work on foundation structural integrity.

1.4.1 **Thesis contribution to knowledge**

The fundamental proposition of this thesis is that:

Internal monopile corrosion and external biofouling are critical issues to consider in the design, operations and maintenance of offshore wind farms.

A better understanding of these complex issues and their individual influences on monopile structures could significantly improve the current practices and guidelines used by operators. Such improvements could lead to more cost-effective and efficient inspections and extended operational lifetimes. The novelty of the work lies in three areas:

1. The design and construction of an experimental programme, which aims to simulate specific corrosive conditions observed within the monopiles at an operational offshore wind farm and determine the effect of individual parameters on the corrosion behaviour of monopile steel.

2. The development of a predictive corrosion loss tool using a combination of laboratory data from experiments and field data from in-situ monopile trials.
3. The development and testing of two methodologies for the assessment of biofouling at the intertidal and submerged zones of offshore wind turbines.

1.5 Thesis Outline

This thesis is structured in seven chapters (Figure 1.9). Chapter 2 introduces the fundamental process of corrosion and the various mechanisms involved, particularly for offshore structures. This chapter also introduces the issue of biofouling, and reviews the literature surrounding its effect on various offshore infrastructure. The current design guidelines for biofouling on offshore wind are critically discussed.

Chapter 3 introduces the experimental programme designed to simulate real internal monopile corrosion conditions in a series of laboratory trials. The key parameters assumed to influence corrosion of the monopile are defined and the experimental design is described in detail. This chapter also presents the experimental results obtained following 15-18 months of corrosion tests.

Following on from the laboratory study described in Chapter 3, Chapter 4 presents the complementary field trials conducted within the monopiles at Teesside Offshore Wind Farm. This chapter compares the experimental results with corrosion loss data obtained from the Teesside trials and an additional

operational offshore wind farm (not owned by EDF Energy), to provide an in-depth analysis of internal monopile corrosion behaviour.

Chapter 5 is concerned with the prediction of internal monopile corrosion under a range of environmental conditions to better understand the influence of key drivers on corrosion rate. A Decision Tree predictive tool is developed from the laboratory and field data is described and presented here, illustrating how the rate of corrosion loss of internal monopile steel can be estimated at Teesside and other offshore wind farms.

Chapter 6 focuses on biofouling of offshore wind farms. In particular, this is an introduction to the comprehensive biofouling assessment at Teesside Offshore Wind Farm. The chapter describes two sampling methodologies designed for two different biofouling zones; the intertidal zone and the submerged zone. The data collected from each sampling strategy is presented and discussed in the context of generating a better understanding of species morphology and biofouling characteristics.

Chapter 7 concludes the thesis by highlighting the contribution to knowledge provided and its industrial impact. The themes and results presented earlier are drawn together to derive the final conclusions, provide recommendations for future work, and to identify the limitations.

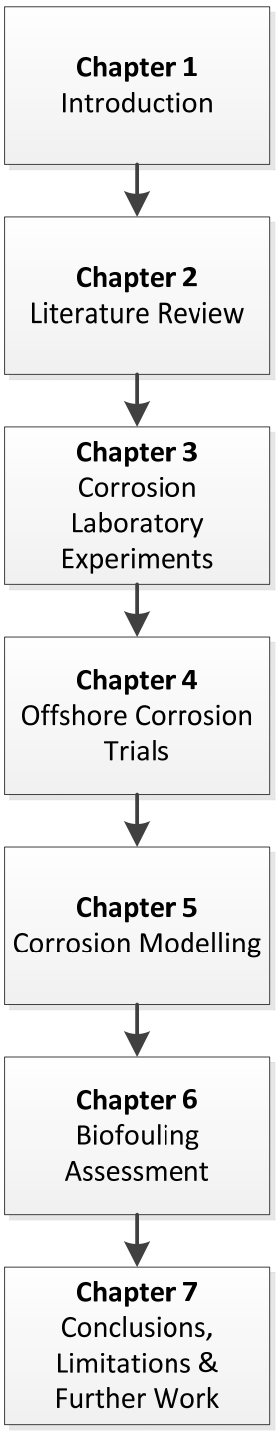

Figure 1.9: *Flowchart of thesis structure.*

2 Literature Review

2.1 Thermodynamics of corrosion

The process of extracting iron from its ore requires energy to convert iron ions from the more stable ferrous Fe^{2+} and ferric Fe^{3+} states (i.e. iron oxide) to iron atoms (metallic iron Fe)[47][48]. The ferrous and ferric configurations are naturally more abundant due to their relative thermodynamic stability compared to atomic iron. Therefore, when iron (or iron-based metals) is located in an oxidising environment (a reaction whereby a metal loses electrons), the atoms will be converted back to more stable ions. This is the basic principle of corrosion [47].

Corrosion can be defined as the destructive attack of a metal by a chemical or electrochemical reaction with its environment. The term “rusting” applies only to the corrosion of iron or iron-base alloys with the majority of corrosion products formed consisting of hydrous ferric oxide [49]. Corrosion by seawater or “aqueous corrosion” is an electrochemical reaction, which refers to the electrical potential that all metals and alloys possess when in contact with seawater at a particular pH [50]. There are four requirements for an electrochemical corrosion cell outlined below and can be seen in Figure 2.1.

1. Anode: The location where the corrosion takes place
    - Oxidation (loss of electrons)
2. Cathode: No corrosion occurs
    - Reduction (consumption of electrons)

3. Electrolyte: A conductive solution
    - Seawater, soil, moisture, etc.)
4. Electrical connection between anode and cathode

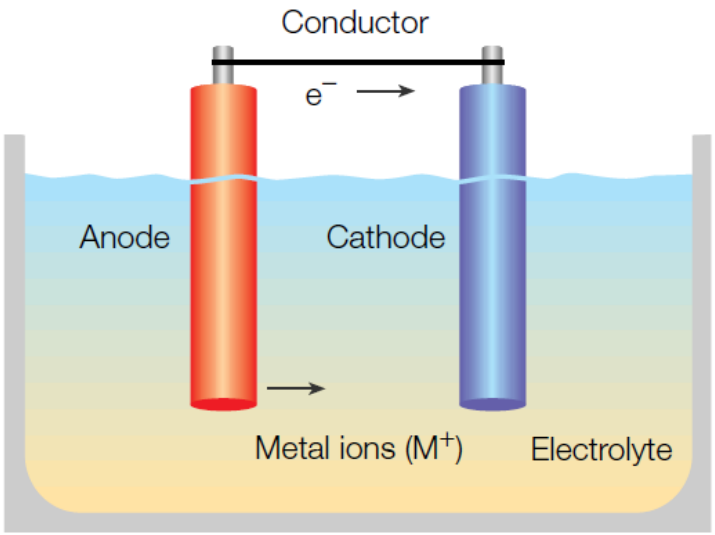

Figure 2.1: *Schematic diagram of a basic corrosion cell with an anode and a cathode connected by a conductor and immersed in an electrolyte*[48].

The anode and the cathode are connected through the electrolyte by an ionic current path and connected through the metal by an electronic path. The anode is the location on the metal surface where atoms go into the solution as metal ions and weight loss occurs. Here, the reaction is oxidation and therefore electrons are generated. The anodic reaction is as follows:

$$Fe \rightarrow Fe^{2+} + 2e^{-}$$

At the cathode there is no corrosion and no weight loss occurs. Here, a reduction reaction takes place and electrons generated at the anode are consumed. The cathodic steps can be any of the following:

$$O_2 + 2H_2O + 4e^- \rightarrow 4OH^- \quad \text{(Aerobic)}$$

$$2H_2O + 2e^- \rightarrow H_2 + 2OH^- \quad \text{(Anaerobic)}$$

$$2H^+ + 2e^- \rightarrow H_2 \quad \text{(Acidic)}$$

It is the movement of charged ions in the solution which causes a current to flow from the anode to the cathode. Corrosion of metal is one of the most significant engineering challenges that offshore industries have to contend with today, with the cost of corrosion offshore estimated to be 4% of a country's' GDP [51].

2.1.1 Forms of Corrosion

Corrosion can occur in several different forms and classification is dependent on three factors [28] :

- The nature of the corrosive material t i.e. "Wet" or "dry".
- The mechanism of corrosion, i.e. electrochemical, direct chemical reactions or microbiologically induced.
- The appearance of the corroded material i.e. uniform across the entire surface or localized to a particular area.

Offshore, 7 forms of wet "aqueous" corrosion should be considered which are defined in Table 2.1[52] and illustrated schematically in Figure 2.2[50]. Fatigue is

another important type of corrosion to be considered in the design and operation of offshore wind turbines and is included in the table and figure below.

Table 2.1: *The7 forms of wet corrosion known to occur offshore, definitions and susceptible materials. Definitions and material systems were obtained from* [50], [52][53].

Type of Corrosion	Definition	Material System
Uniform/General	A corrosive attack characterised by uniform thinning	All metals in atmospheric environment
Galvanic	Dissimilar metal corrosion where an active metal (the more noble of the two) corrodes	Galvanic coupling materials e.g. iron with copper, carbon steel with stainless steel.
Erosion-Corrosion (including Fretting)	Deterioration of a material due to the relative movement between surfaces and corrosive fluids	Stainless steel, carbon steel in flowing fluid containing abrasives. Riveted joints/structures and bolted joints/flanges. Relative motion produces deformation at the surface
Crevice	Localized corrosion on a metal surface at, or immediately adjacent to, the gap or crevice formed between two adjoining surfaces.	Associated with stagnant microenvironments which tend to occur in crevices and beneath deposits and seals e.g. at nut and rivet heads.
Pitting	Localized form of corrosion confined to small areas, by which cavities or holes are produced in the material.	Most Stainless steels and aluminium in chloride or bromide environment (water/soils).
Intergranular	The microstructure of metals and alloys is made up of grains, separated by grain boundaries. This type of corrosion is localized attack along the grain boundaries.	A particular problem in heat-treated stainless steels and high strength aluminium alloys.
Stress Corrosion Cracking (SCC)	Cracking induced by the combined influence of tensile stress and a corrosive environment. Includes hydrogen-induced SCC and sulphide SCC.	Most Stainless steels, carbon steel, nickel alloys and aluminium alloys are susceptible.
Corrosion Fatigue	Process in which a metal fractures prematurely under conditions of simultaneous corrosion and repeated cyclic loading.	Most metals and alloys.

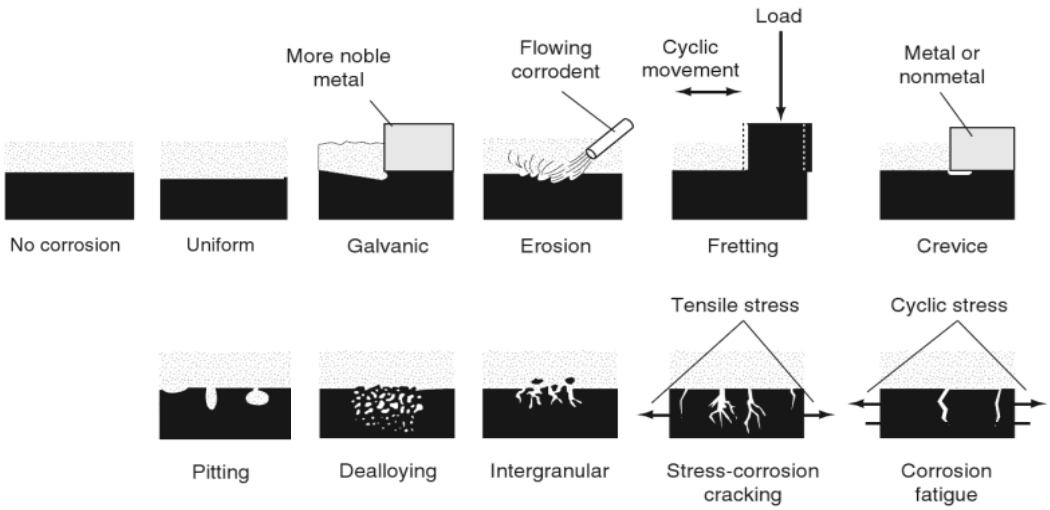

Figure 2.2: *Schematic illustrations of the common forms of corrosion* [50].

2.1.2 **Microbiologically Influenced Corrosion**

The metabolic activity of microorganisms can drastically accelerate the corrosion rate of a metal, particularly in an environment with pH level <6 and little to no oxygen [54][55]. This phenomenon is known as (anaerobic) Microbiologically Influenced Corrosion (MIC) or anaerobic biocorrosion. The presence of microorganisms have several influences on the corrosion process, however the most significant is the alteration of the metal-solution interface by the development of a biofilm [56][57]. Biofilm development on metal involves the accumulation of microbial growth on the surface over time and begins immediately after immersion [58]. The microorganisms present in biofilms do not necessarily introduce new mechanisms of corrosion but can certainly influence the occurrence and/or rate of the types of corrosion mentioned in Figure 2.2[59]. For example, the biofilm can alter the electrostatic charges of the metal surface

and, therefore significantly change the electrochemical conditions at the metal-solution interface [56]. Additionally, biofilms have been known to cause a shift in the electrical potential) of stainless steels, nickel-based alloys, or titanium alloys exposed in seawater, which may accelerate the corrosion rate [59]–[62].

The microorganisms that are of primary interest in MIC are bacteria and fungi [63]. MIC research focuses on the following types of bacteria [63], [64]:

- Sulphate-reducing bacteria (SRB)
- Sulphur/sulphide-oxidizing bacteria
- Acid-producing bacteria
- Iron-oxidising bacteria
- Manganese-fixing bacteria
- Acetate-oxidizing bacteria
- Acetate-producing bacteria

In the offshore wind industry, SRB are of particular interest as they are regarded as the key physiological group involved in MIC and are widespread in many natural and engineered aquatic environments [54]. SRB obtain energy for growth by oxidizing organic compounds to carbon dioxide (CO_2) (also known as sulphate respiration), whilst reducing sulphate (SO_4^{2-}) to Hydrogen Sulphide (H_2S). Many SRB are also able to utilize the molecular hydrogen (H_2) that is produced in the breakdown of organic compounds in anaerobic aquatic environments such as sewers, sediments and swamps [65][54]. To fully understand the SRB induced corrosion, it is necessary to understand the different mechanisms involved. Two

of the most common mechanisms are Cathodic Depolarization and Hydrogen Induced/Sulphide Stress Corrosion Cracking).

The cathodic depolarization theory illustrated in Figure 2.3 was proposed in 1934 and describes the mechanism of corrosion induced by SRB, whereby depolarization occurs through oxidation of cathodic hydrogen [66]. A metal becomes polarized when it is exposed to seawater by losing positive metal ions in an anodic reaction, and free electrons reduce water-derived protons (i.e. H^+) in a cathodic reaction. These reactions occur in an anaerobic environment and lead to the production of hydrogen gas at the metal surface, which should create a dynamic equilibrium [67]. SRB are believed to consume this hydrogen, which facilitates the oxidation of Iron (Fe) [68]. This mechanism leads to the formation of the corrosion products Iron sulphide (FeS) and Iron Hydroxide ($Fe(OH)_2$) due to an increase in the anodic reaction [67].

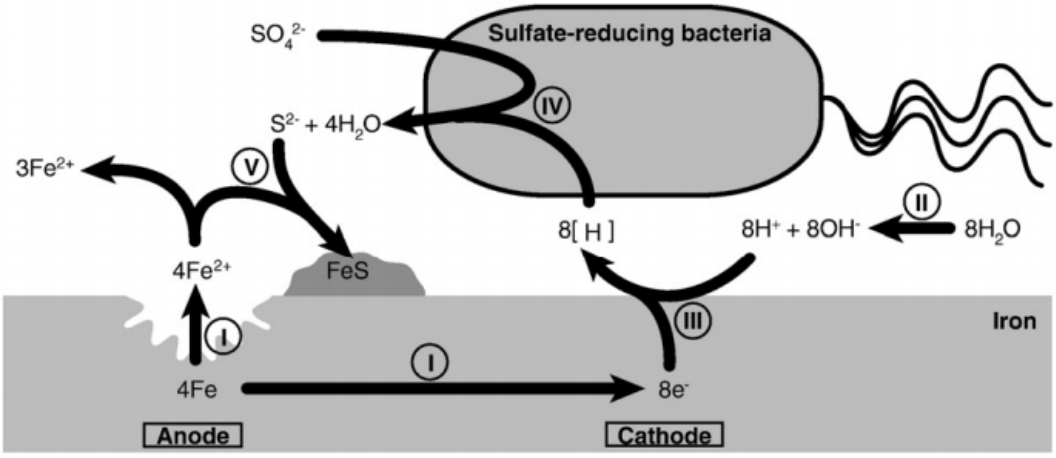

Figure 2.3: *Schematic diagram of SRB induced corrosion of iron: I. Iron dissolution, II. Water dissociation, III. Proton reduction, IV. Bacterial sulphate reduction, and V. sulphide precipitation* [67], [69].

The corrosion products can accelerate the rate of corrosion depending on the environmental and physicochemical conditions of FeS. For example, the formation of FeS on the metal surface can cause a local decrease in pH level, which breaks down the biofilm and can lead to the activation of corrosion cells between the metal surface (anode) and the FeS (cathode) [70].

2.1.3 **Hydrogen Induced/Sulphide Stress Corrosion Cracking**

Hydrogen embrittlement is the ingress of hydrogen into a component which can seriously reduce the ductility and load-bearing capacity of the material [71]. It is well-documented that hydrogen causes brittleness whenever it concentrates in microscopic regions; thus facilitating initial crack growth and potentially resulting in premature failure of the material [72][73]. In the absence of applied stress, the diffusion of hydrogen into steel can induce blistering or hydrogen induced cracking (HIC) [74]. In the presence of applied stress and residual stress, failure can occur either by hydrogen embrittlement or sulphide stress corrosion cracking (SSCC) [75]. It can be difficult to determine the source of hydrogen in metallic systems since there are so many factors which influence the absorption, adsorption and diffusion processes [76], e.g. complex processes like MIC and stress corrosion cracking (SCC). Both phenomena lead to the production of hydrogen with different levels of solubility and diffusivity which can become trapped at sites within the microstructure of a material [76] As previously mentioned, SRB are the primary bacteria in the majority of MIC cases and their release of H_2S reacts with iron to produce H_2 in the following reaction:

$$H_2S + Fe \rightarrow FeS + H_2$$

Microbiological activity is also known to enhance the entry of hydrogen produced by cathodic protection into the metal surface, especially in anaerobic environments [77].

2.2 Corrosion of Offshore Structures

There is an overwhelming amount of corrosion research dedicated to the oil and gas industries. Over 50+ years of experience in corrosion-related issues on extraction platforms, drilling equipment and pipelines etc. has documented several potential situations where corrosion may occur and cause damage. Oxygen is known to be particularly corrosive although is not generally present in producing formations. It tends to be only at the drilling stage that oxygen-contaminated fluids are first introduced. In fact, if left untreated, drilling muds will corrode well casing in addition to drilling equipment, pipelines and mud-handling equipment [48]. Crude oil and natural gas can contain a variety of high-impurity products which are essentially corrosive [78]. Highly corrosive substances in oil and gas wells and pipelines are carbon dioxide (CO_2), H_2S and free water and if continually extracted over time, they could induce corrosive effects on the internal surfaces of components [78]. Material degradation of the lines and component fittings can occur as a result of changes in fluid composition, pressure, and temperature and souring of the wells. This can seriously impact the mechanical properties of the structure such as strength and ductility.

2.2.1 **Corrosion of offshore wind turbines**

In the last 10 years, wind turbines have become more prevalent in the offshore environment. An offshore wind turbine can be divided into corrosion zones characterised by the local environment; atmospheric zone, splash zone, tidal zone, submerged zone and mud zone [79] (Figure 2.4).

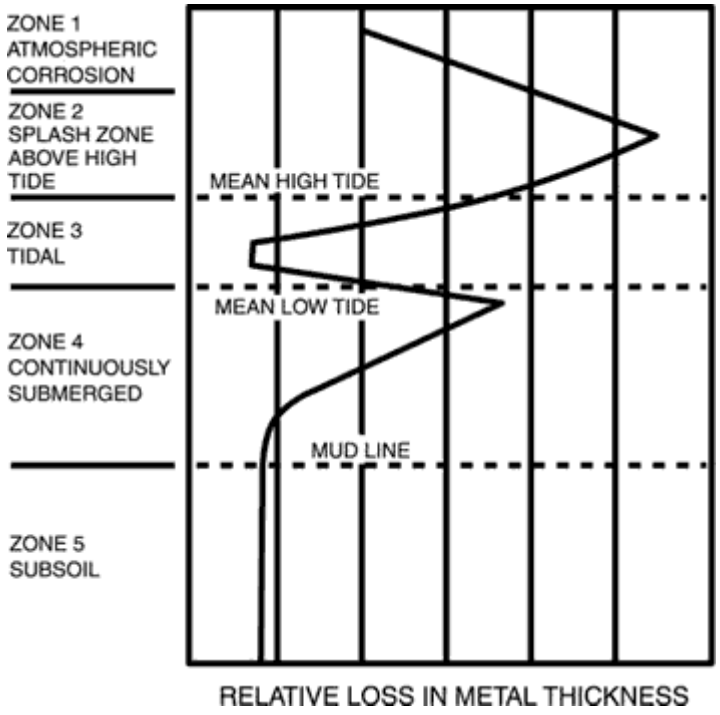

Figure 2.4: Profile of corrosion loss of unprotected steel in seawater with corresponding corrosion zones.

It is well known that corrosion rates are much faster in the splash zone (or in the submerged zone just below the water level for stagnant water)[79]. This effect occurs because the splash zone is subjected to continuous interaction with highly aerated sea water and the corrosive effects of spray, waves and tidal actions [80]. Corrosion protection of the atmospheric zone can be maintained by a range of

coatings applied to the surface, and the submerged zones can be protected using cathodic protection in the form of galvanic (sacrificial) anodes or impressed current systems (ICCP) [81]. However, achieving effective corrosion control in the splash zone is more difficult as corrosion rates are highest, particularly in structures that are fixed to the seabed and are unable to be removed from the water for routine maintenance [82].

With monopiles there is also a risk of localised corrosion in the partially buried structures, whereby differential aeration inside the structure may localise corrosion in the surface of the mud zone. The inside of the MP differs from other structures that contain stagnant water, such as ballast tanks, since there is often an issue with water ingress through malfunctioning J-tube seals [14]. The replenishment of seawater inside the monopile allows some corrosive elements, such as dissolved oxygen to freely enter the structure. Ingress of fresh sea water both increases the oxygen content in the media and affects the microbial activity. The tidal variations also increase the risk of localized attacks in connection with the tidal zone (Figure 2.5 and Figure 2.6).

Figure 2.5: *The lower part of an aluminium ladder above the lower working platform has corroded away due to tidal conditions inside an offshore wind monopile foundation* [14].

Figure 2.6: *In another monopile foundation, areas covered in corrosion tubercles are observed* [14].

Additionally, oxygen leaking into the MP can depolarize the cathodic protection [83]. This type of corrosion may not necessarily deteriorate the structural strength for thick walled steel piles, however corrosion fatigue and cracking at critically loaded points is a potential issue [84]. Furthermore, the microbiological activity e.g. that of SRB which naturally occurs in low oxygenated marine mud can produce acidic compounds, in addition to hydrogen sulphide gas (H_2S) which are known to facilitate MIC [83]. As such, the prevention of internal corrosion represents a significant challenge for offshore wind developers today.

2.3 **Biofouling of offshore structures**

The term “biofouling” refers to the growth and accumulation of unwanted biological material on offshore man-made structures such as ships, oil and gas platforms and offshore renewable energy devices. The terms “biofouling” and “marine growth” will be used interchangeably throughout this report to describe the same phenomena. These organisms tend to be intertidal and sublittoral (living near the shore) species which would commonly be observed on most rocky shorelines. Biofouling species have particular features which enable them to readily colonise artificial structures either positioned on the seabed or suspended in the water column. These features are characterised by a free-swimming larval phase; a sessile adult form which firmly attaches to the substrate and extracts nutrients from the water column [85]. Such organisms include barnacles, mussels, anemones and algae. The colonisation of sessile biofouling species

often attracts mobile species such as fish and crustaceans. The development of biofouling communities follows a pattern of colonization and succession which can be seen in Figure 2.7. The substrate becomes coated with a biofilm composed of organic material which then attracts primary and secondary colonisers onto the surface which form the microfouling community. The next stage involves the settlement of larvae and spores of tertiary colonisers such as seaweeds, mussels and barnacles which develop into the macrofouling community.

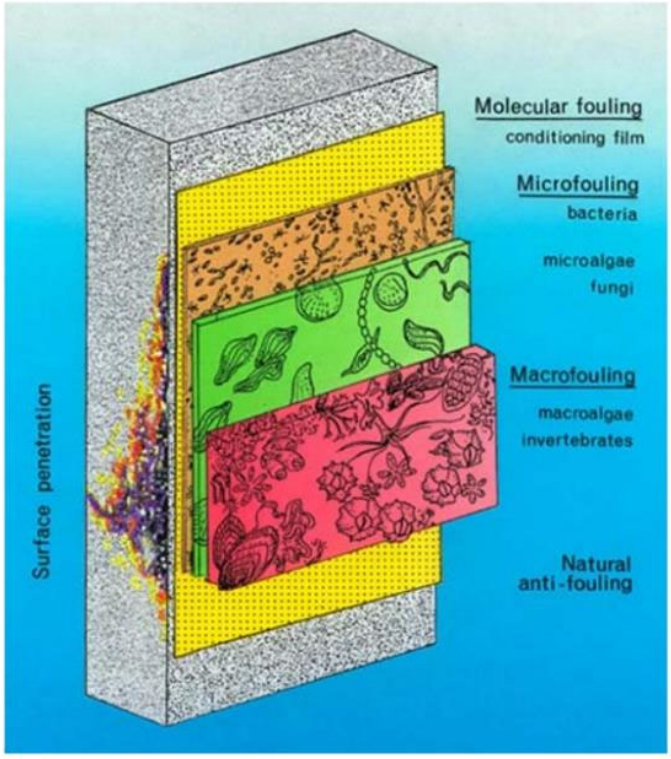

Figure 2.7: *Schematic view of the 4 primary stages of marine growth [8]*

The biofilm formation occurs within the first minutes of biological settlement (Figure 2.8). The colonization of bacteria occurs after approximately 1 to 2 hours.

This is followed by spores of macroalgae and diatoms appearing within the first week, and then the settlement of macrofouling larvae on microbial and algal films [86].

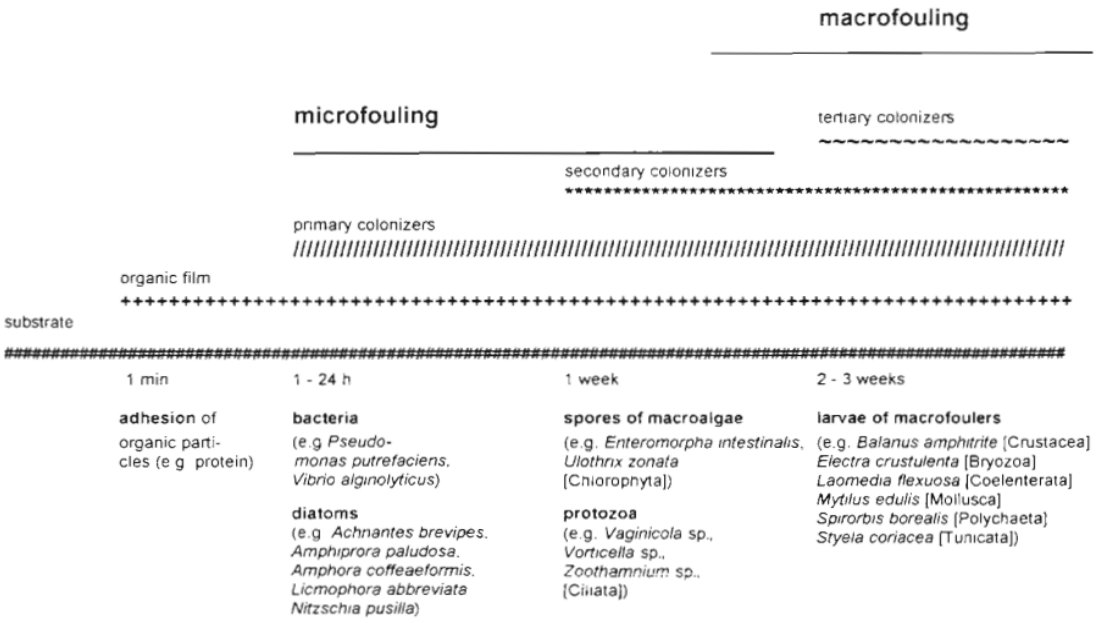

Figure 2.8: *Temporal structure of marine growth settlement on artificial offshore structures [9]*

2.3.1 **Biofouling in the oil and gas industries**

The production of gas and oil from offshore platforms in the North Sea began in the 1960's with potential biodeterioration issues initially being overlooked and/or underestimated [87]. With the development of this industry, marine fouling of offshore installations has become an increasingly interesting area of research around the world. This industry in particular has been found to have 3 main classes of offshore biodeterioration; corrosion, souring (i.e. the H_2S content of oil) and biofouling. Living organisms can affect offshore platforms either externally where the surfaces are exposed to seawater and fouling, or internally within the

plant or pipework by bacterial slimes or biofilms. Biofilms consist of microbial cells and are often surrounded by a protective matrix of extracellular polymeric substances (EPS) [88], [89] which facilitate the irreversible attachment of cells to the metal surface. EPS components can assist the transfer of electrons between the biofilm and the colonized metal leading to the deterioration of the metal through electrochemical reactions [90]. This type of interaction is of particular concern in oil pipelines whereby deterioration due to the presence of biological films can eventually facilitate structural failure and oil leakage [91]. Therefore, the presence and activity of biofilms within oil and gas pipelines is of critical importance when considering biofouling and corrosion mitigation strategies.

Biofouling on offshore platforms is not only a structural burden, but also serves to increase the surface area exposed to wave and tidal action which may threaten the safety of the platform during rough sea conditions [92]. On large oil platforms, the actual weight of the accumulated fouling may be insignificant when compared to the overall weight of the structure. Nevertheless, as previously mentioned this presence of fouling organisms on the outer surface of offshore tubular membranes increases the diameter, surface roughness and therefore the frictional drag coefficient of the member [93]. As such, the hydrodynamic loading is significantly increased. An early study calculated that a layer of fouling of 15cm thickness will increase the loading by 42.5% and the fatigue damage by 62.3%, although this is likely to depend on species [94]. Furthermore, the life expectancy of the structure decreased by 54%. Additionally, certain fouling species has been known to facilitate both corrosion (by providing a suitable environment and source of nutrients for SRB [95]) and the stress components of corrosion fatigue.

Additional damaging effects of biofouling include corrosion facilitation by the reduction of cathodic protection and the physical effects of organisms such as molluscs or sponges which bore directly into the metal surface during attachment [96], [97]. This reinforces the importance of considering the impacts of biofouling in the design specifications of offshore structures to achieve safe operation and also to improve the reliability of submerged components in terms of their expected lifetime [93].

2.3.2 **Biofouling on offshore wind turbine foundations**

It is widely known that submerged man-made structures are rapidly and extensively colonised by assemblages of marine fouling organisms [98] and this is certainly the case for offshore wind turbines [99]–[101]. Wind farms facilitate the establishment of species which would ordinarily not exist in an area dominated by soft sediment habitats in addition to the spread of non-native, potentially invasive species by means of a stepping-stone effect [101]. The vertical substrates provided by monopiles are described to support “typical pier piling communities in which mussels (*Mytilus* spp.) are the dominant fouling organism” [100], [102].

The foundations of offshore wind turbines and surrounding scour protection provide new habitats for marine organisms to colonise. This introduction of artificial hard substrata is known as the “reef effect” and is considered to be the primary modification of the marine environment following the

construction of offshore wind farms and can influence the entire food web [103]. The rapid recruitment of fouling organisms on newly installed offshore wind turbine foundations primarily occurs in two different ways; migration from the surrounding substrate or by settling of larvae [104]. The recruitment process is governed by the local hydrodynamic regime carrying the larvae to the wind farm, and then it will depend on the material and texture of the structure in respect of water depth, salinity and temperature. As previously mentioned, differences in the composition of fouling communities at particular depths are commonly observed at wind farms, and these assemblages are known to reflect zonation patterns observed in adjacent rocky shores [104].

The rapidly increasing offshore wind industry and consequent availability in hard vertical surfaces, together with the increased activities of vectors such as shipping, enables a much faster and more intense transport of certain biofouling species all over the world. Migrant species are now able to find additional and more suitable habitats to settle and to survive in regions beyond their native range [103]. These non-native species (NNS) may take advantage of new habitats through invasion or expanding their population size and strengthen their strategic position [105]. For example, the Marine Splash Midge (*Telmatogeton japonicus*) has been observed on offshore wind turbines in the southern Baltic Sea (Utgrunden 1) [106] and Danish North Sea (Horns Rev) among other locations. It is suspected to be a non-native and potentially invasive species, introduced by shipping in the eastern Atlantic Ocean. The reports of this species occurring at offshore wind farms in Europe, often in large numbers have sparked concern about its potential to extend its spatial distribution and possible undesirable

ecological impacts [106]. The introduction of invasive species can have dramatic ecological effects and threaten the local and global biodiversity [104]. For example, in the Black Sea, an invasive comb jelly *Mnemiopsis leidy,* is believed to have led to the collapse of coastal fisheries worth millions of dollars each year[107] [108]. A European species of crab (*Carcinus maenas*) is now found in Australia, Japan, South Africa and both coasts of North America, and has been blamed for the collapse of bivalve fisheries on the East coast of North America. Furthermore, there is some concern that it will out-compete migratory bird populations on the west coast of North America for favoured shellfish [109]. These dramatic changes in ecology can influence the type and propagation of marine species colonising offshore wind farm foundations.

2.3.3 **Biofouling standards and guidelines**

Marine growth is considered a significant engineering and environmental concern for both designers and operators. In response to the potential hydrodynamic, structural and operational impacts due to long-term biofouling accumulation, engineering standards and guidelines have been developed for other more established offshore industries, such as oil and gas and shipping. Many of these standards are applied within the growing offshore wind and marine renewable energy industry, to regulate how marine growth is accounted for in the engineering design and maintenance of structures. Such standards include that of Det Norske Veritas (DNV) for the design of offshore wind turbine structures

(DNV-OS-J101; Section 4) [35] which is primarily used for UK offshore wind farms. This guideline advises that marine growth should be taken into account by increasing the outer diameter of the support structure in the calculations of hydrodynamic wave and current loads. The thickness will depend on the depth below sea level and assessed based on local experience and existing measurements, although site-specific studies may be necessary [35]. Other examples include The International Organization for Standardization (ISO) ISO19901 (2005) and 19902 (2007) standards which provide some general considerations on marine growth. In ISO19902, which focuses on fixed steel offshore structures for Petroleum and natural gas industries, it is advised that the mass of marine growth expected to accumulate on the structure will be included in the dynamic model. In addition, components with circular cross-sections shall be classified as either “smooth” or “rough” depending on the amount and size of marine growth expected to have accumulated at the time of a loading event. Structural elements can be considered hydrodynamically smooth if located above highest astronomical tide (HAT) or sufficiently deep below the LAT. Site-specific data is required to reliably establish the extent of hydrodynamically rough zones [110]. Typical values for hydrodynamic coefficients for the rough and smooth cases are given (Table 2.2); C_{d} is the drag coefficient and C_{m} is the inertia coefficient.

Table 2.2: *The typical values of hydrodynamic coefficients* [110].

Surface of component	C_d	C_m
smooth	0,65	1,6
rough	1,05	1,2

Some standards advise that marine growth should be taken into account as appropriate for the location of the structure. However, detailed information on marine growth extent at specific geographic locations is poor. Guidelines tend to relate to the latitude of the installation, for example south and north of 59˚, and are often based solely on data from the North Sea. For example, the NORSOK standard prescribes values for the thickness of marine growth that may be used if no more detailed values are available for latitudes 56˚N to 59˚N (Table 2.3). The standard also states that the thickness of the marine growth is assumed to increase linearly to the given value over the first 2 years after installation. These values are reflected in the most recent version of the DNV standard [35] which also includes some recommended thickness measurements for the Norwegian Sea (Table 2.4).

Table 2.3: *Marine growth thickness recommended by NORSOK for latitudes 56˚N to 59˚N* [111]**.**

Water depth (m)	Marine growth thickness (mm)
Above +2	0
+2 to -40	100
Below -40	50

Table 2.4: *Marine growth thickness recommended by DNV* [112].

Depth below mean water level (m)	Marine growth thickness (mm)	
	Central and Northern North Sea (56° to 59° N)	Norwegian Sea (59° to 72° N)
-2 to 40	100	60
>40	50	30

In 2015, the decommissioning of two TPs at Robin Rigg Offshore Wind Farm in the Solway Firth, UK (owned and operated by E.ON), enabled photographic evidence of the marine growth that had accumulated since their installation in 2009 (Figure 2.9). Hard fouling of up to 300mm thickness was observed in the upper 2-3m of the structure. It was concluded that an expected marine growth thickness of 100mm up to 40m depth outlined in the DNV guidelines [35] is overestimated. Although some areas exceeded the 100mm thickness value, this was found to be only in the top 3m, and the remainder of the structure had minimal growth.

Figure 2.9: *Decommissioned TP from Robin Rigg Offshore Wind Farm.*

As the offshore wind industry expands and becomes more established, more biofouling information for different geographic regions has become available. In light of this, DNV are updating their standards accordingly by providing guidance notes advising developers to expect greater marine growth thickness in warmer waters and to consider this in their engineering design. Since marine growth represents an increase in the total mass, it can potentially lower the natural frequency of the structure, which should also be taken into account. Also, as marine growth has a higher specific gravity than seawater, it is expected to increase the load on offshore structures [113]. However, it has previously been suggested that in terms of the total weight, the submerged weight of the marine growth is insignificant for representative oil and gas platforms [94]. Nevertheless, the need for location-specific guidance for marine growth prediction at a higher resolution is still required and will hopefully be possible as more data becomes available from different wind farm sites.

3 Corrosion Laboratory Experiments

3.1 Introduction

In order to gain some insight as to how the internal monopile environment is affecting the corrosion behaviour of the exposed internal S355NL steel within the structures at Teesside Offshore Wind Farm, an ongoing laboratory study began in January 2016. The purpose of this study was to simulate some of the corrosive conditions observed within the monopiles at Teesside and other offshore wind farms, notably the influence of low pH seawater, the presence/absence of oxygen, temperature and the effect of internal tidal variations. It is unclear how each of these parameters individually influence corrosion of the internal steel since the rate at which they change is neither controlled nor monitored. Therefore, the experiments aim to de-couple the parameters and determine their individual effect on the corrosion rate of unprotected steel. The experimental programme was designed and set up at EDF laboratories in Les Renardières, with the help of R&D colleagues in France. In parallel to the lab work, two field monitoring campaigns were conducted at Teesside to validate these experimental results. Both laboratory and field approaches use carbon steel corrosion coupons as a proxy for the internal monopile steel and use the weight loss measurements over time to estimate the material degradation and rate of general corrosion.

The assumptions in the experimental design are that corrosion loss of carbon steel will be accelerated by exposure to the following conditions: low seawater

pH level ($4 \leq pH \leq 5.5$); wet/dry cyclic tidal variations; and oxygenated seawater. The impact of low seawater pH levels on the corrosion behaviour of carbon steel is of particular interest since many offshore wind operators have experienced the development of low internal pH within monopiles when cathodic protection (CP) using aluminium galvanic anodes is applied within a closed compartment [114]. This phenomenon has been simulated previously in experiments that demonstrated a notable reduction in pH value from 7.8 to 5 within two weeks of aluminium anode CP application [115]. This has also been observed at Teesside, particularly in the foundations that do not experience internal seawater replenishment. Table 3.1 shows the average internal seawater pH levels measured at Teesside in March 2015 and 2016 as per the guidelines detailed in Section 7 of [116]. The initial measurements indicate pH values as low as 4 in many of the monopiles. A year later, pH levels have mostly increased but generally remain less than 6. This rise in pH could be attributed to further degradation or failure of the Tekmar cable seals (the Teklink protection system), facilitating more fresh seawater ingress via the leaking seals and more mixing. Offshore wind industry and experimental experience has shown that low pH levels within internal spaces can significantly reduce the current output of galvanic anodes and prevent the CP system from working effectively [43]. Additionally, low pH conditions may prevent the beneficial calcareous deposit formation on the surface of the steel; this calcareous layer (primarily calcium carbonate) reduces the current demand for maintenance of CP [37] and is a well-known protective barrier against marine corrosion [117].

Table 3.1: *Internal monopile pH measurements from Teesside Offshore Wind Farm in March 2015 and March 2016. "Row" = Turbine Array A, B or C, "Drilled" = drilled/non-drilled monopile; D = Drilled, ND = Non-Drilled, "Leaking" = leaking/non-leaking monopile L = Leaking and NL = Non-Leaking.*

Internal pH Measurements					
Row	**Turbine**	**Drilled**	**Leaking**	**Mar-15**	**Mar-16**
A	1	D	L	4.5	5.4
A	2	D	NL	4.7	5.3
A	3	ND	NL	4	5
A	4	ND	NL	4	5.2
A	5	ND	NL	4	4.8
A	6	D	L	5.7	6.9
A	7	D	NL	4.4	5.6
A	8	D	L	-	7.4
A	9	D	L	4.3	5.4
B	10	D	L	6.4	7.8
B	11	D	NL	6.4	n/a
B	12	ND	L	4	5.7
B	13	ND	NL	4	n/a
B	14	D	NL	4.5	n/a
B	15	ND	NL	4	4.9
B	16	D	L	6.2	7.6
B	17	D	L	6.6	6.5
B	18	D	L	6.4	7.7
C	19	ND	NL	4.7	5.1
C	20	D	NL	6.5	7.7
C	21	ND	NL	4.6	4.6
C	22	ND	L	6.5	7
C	23	ND	NL	4	5.9
C	24	D	NL	6.5	n/a
C	25	ND	L	6.7	n/a
C	26	ND	L	7.1	n/a
C	27	D	L	-	n/a

With many offshore wind farm monopiles experiencing unforeseen internal tidal conditions due to seawater ingress through leaking Tekmar/internal J-tube seals, degraded grout connections or small J-tube openings/perforations, it is crucial to understand the impact this may have on the corrosion of bare monopile steel. The monopile foundation's closed compartment design was assumed to be

completely air- and watertight with low, uniform corrosion rates anticipated that would eventually cease once the residual oxygen was consumed. In this design, the dissolved oxygen in seawater would quickly be consumed by general corrosion on the steel surface and the corrosion rates would decline as the compartment became anaerobic. Nevertheless, the exposure to cyclic wet/dry tidal conditions could lead to accelerated corrosion rates of unprotected steel in the intertidal zone. It well known that the marine high tidal zone is a severe corrosion environment for unprotected steel, such as sheet piling used in seawater harbours and port structures [118]. In this zone, steel structures can be susceptible to a particularly aggressive form of localised corrosion known as Accelerated Low Water Corrosion (ALWC) that typically occurs at, or below, the low water level in tidal or brackish waters [119][120]. ALWC has been attributed to differential aeration, however is increasingly associated with Microbiological Induced Corrosion (MIC) [121]. Laboratory simulation of this exposure to wet/dry cycles will provide an approximation of how the monopile steel surface might behave under such circumstances.

In addition to being watertight, the initial design criteria for the internal closed compartment also anticipated no oxygen ingress following installation. The depletion of oxygen from this compartment was defined as an acceptable method of corrosion control in Section 11A of the DNV-OS-J101 guidelines in 2013 [81]. However, in 2014 the guidelines were amended, stating that in practice, the interiors of monopiles cannot be considered completely sealed from oxygen and water ingress and therefore alternative corrosion control methods should be adopted [35] e.g. coatings and/or cathodic protection. To comply with these

updated guidelines, a galvanic anode cathodic protection system was then installed internally within the foundations at Teesside.

One of the challenges associated with the implementation of an internal galvanic anode CP system, is the excessive formation of hydrogen (H_2) and the accumulation of hydrogen sulphide (H_2S)[122]. This scenario was observed at Teesside, with key indications including leakage of H_2 and H_2S gases above the enclosed compartment. A full report of the experience at Teesside and the solutions implemented can be found in [123]. To enable the removal of these toxic gases from the internal TP and MP, these zones require forced ventilation before every turbine visit. This ventilation process replenishes fresh oxygen in (what should be) a sealed compartment, which can facilitate further corrosion of the internal steel. This process occurs due to direct ingress of fresh air which can affect the atmospheric corrosion rate of the humid TP walls and upper work platforms, while, below the water line, corrosion is facilitated by the differential aeration between the upper water layer and the steel surface below [14]. Within the foundations at Teesside, atmospheric corrosion perpetuates due to the ingress of fresh oxygen during ventilation, while submerged corrosion is facilitated by the ingress of fresh seawater in leaking monopiles. The effect of oxygenated seawater on the corrosion rate of fully submerged carbon steel specimens is assessed in the laboratory study and results are reported in Section 3.3. The subsequent sections in this chapter describe in detail the methodology, analysis and results from the experimental study and both field campaigns at Teesside.

3.2 **Experimental Materials and Methodology**

3.2.1 **Materials**

The experimental programme consists of 150 carbon steel corrosion coupons of dimensions 50mm length x 25mm width x 3mm thickness, which were prepared with a glass bead blast finish and weighed to 0.1mg. Coupons were constructed from BS EN10025 Grade S355K2+N material, which is comparable to the monopile steel type (S355NL) in terms of chemical composition (Table 3.2).

Table 3.2: *The chemical composition of test coupons (S355K2+N)* [124] *and the monopile steel (S355NL)* [125]

Steel	Chemical Composition %											
	Al	**C**	**Cr**	**Cu**	**Mn**	**Mo**	**N**	**Nb**	**Ni**	**P**	**S**	**Si**
S355K2+N	0.038	0.18	0.05	0.24	1.18	0.01	0.005	0.02	0.24	0.011	0.002	0.34
S355NL	0.02 min	0.18 max	0.03 max	0.55 max	0.9 - 1.65	0.1 max	0.015 max	0.05 max	0.5 max	0.025 max	0.02 max	0.5 max

The compositional and microstructural properties can vary significantly between steels of the same grade from different manufacturers, and such variations can lead to substantial differences in the corrosion resistance [126]. Optical microscopic examination of the microstructure of the S355K2+N carbon steel specimens used in the experiments was conducted to ensure that it is comparable with the S355NL monopile steel. Microstructural examination of the coupons using 1% nital chemical etching [127] determined that they are ferritic-

pearlitic microstructures, with fine grains similar to that of the monopile steel (Figure 3.1). The main difference between the microstructures is that the S355NL has a banded ferritin structure whilst the S355K2+N coupon is more uniform. However, this is not expected to influence the results.

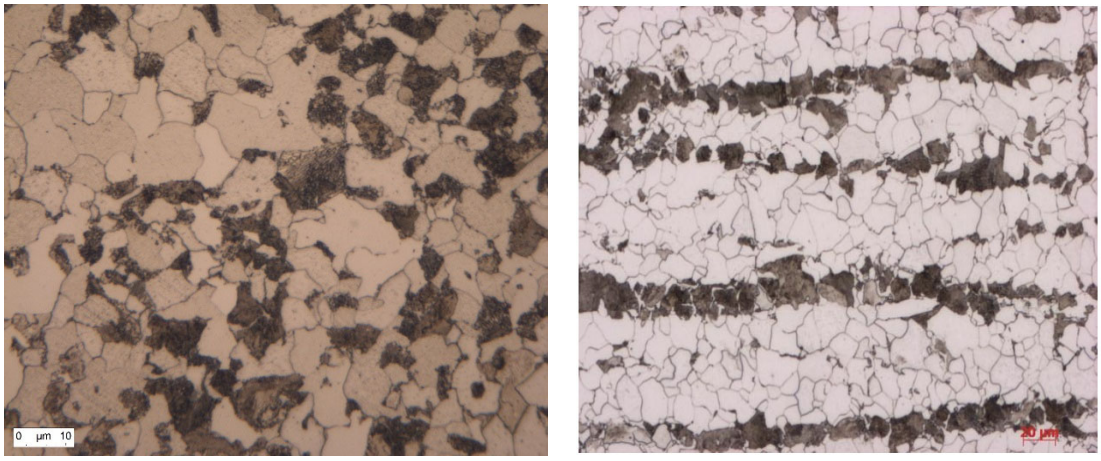

Figure 3.1: *The microstructural examination of the S355K2+N experimental coupon (Left) showing the ferritic pearlite structure (10 µm scale) similar to that observed in a microscopic micrograph of S355NL steel (20 µm scale) (Right)* [42].

3.2.2 **Coupon Setup**

Cylindrical high-density polyethylene chambers (30cm high and 10cm in diameter) were used to expose the majority of coupons to various environmental conditions. Glass chambers were used in two treatments where temperature would be manipulated. Prior to inserting the coupons into their defined test chamber, the specimens were mounted on to perforated sheets of stainless steel 316; oriented in the vertical direction and in rows of 3, using screws with rubber stoppers preventing contact between metals (Figure 3.2). Each screw could only support up to 3 coupons and still fit into the test chamber. The grills enabled the

coupons to remain in the same position throughout the entire immersion period, with all surfaces exposed to the experimental conditions within the chamber.

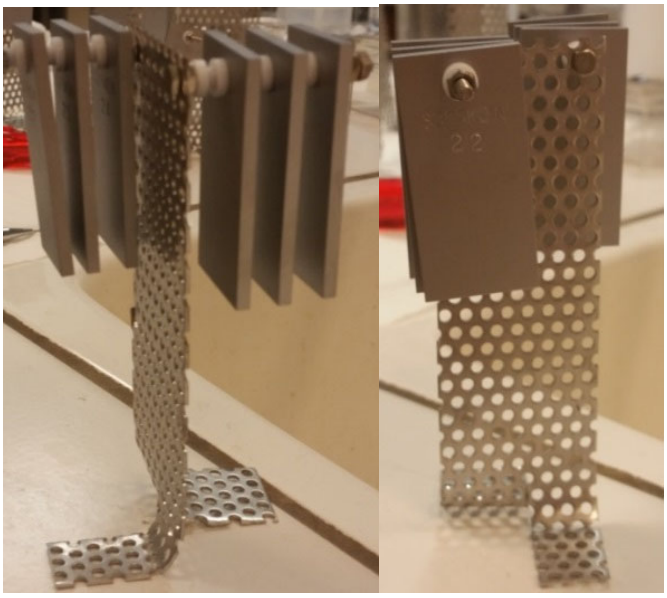

Figure 3.2: *S355K2+N coupons mounted on to a stainless-steel grill prior to immersion within a test chamber.*

Preparation of coupons involved thorough rinsing in acetone, ethanol and demineralised water followed by blast drying to remove any grease and residual surface debris before exposure to corrosion treatments.

3.2.3 **Test Conditions**

The experimental trials aim to simulate the different combinations of environmental conditions observed inside the Teesside monopiles that influence the corrosion rate of the internal steel surfaces, within a laboratory environment. In addition, the study aims to determine how each of these parameters affects

the corrosion behaviour of the internal monopile steel. The key parameters selected to replicate the internal monopile environment are as follows:

1. The influence of exposure to a semi-diurnal tidal system compared to continuous immersion. This scenario reflects the internal tidal conditions observed in leaking monopiles compared with the stagnant conditions in the fully sealed monopiles.

2. The influence of free oxygen ingress compared to a completely sealed (anaerobic) compartment. This mimics the scenario inside the monopile following long periods of ventilation of the closed compartment.

3. The influence of low seawater pH ($4 \leq pH \leq 5.5$) compared to the average seawater pH for open seawater ($7.5 \leq pH \leq 8.4$) [128]. This reflects the acidification of the internal water column due to the electrochemical reaction of aluminium alloy anodes in a closed compartment.

4. The influence of nutrient-enriched seawater containing live bacteria* compared to 35g/L sodium chloride (NaCl) artificial seawater solution. With no real seawater available for laboratory trials, a nutrient-enriched solution was considered a suitable substitute and method for testing the influence of marine bacteria on the degradation of samples.

**The nutrient-enriched seawater used in these experiments is Nutri-Seawater® Aquarium Saltwater (U.S. Patent #6,376,229) containing over 11 million natural live marine bacteria per gallon* [129].

Bulk solutions of both NaCl and nutrient-enriched artificial seawaters were produced and decanted into chambers, with each chamber containing up to 2 litres of solution. In order to achieve pH 4, an acetate buffering solution was added to 50% of each bulk solution until the pH level stabilized at 4 to 4.5. Chambers were monitored 2 to 3 times a week to ensure the pH level remained below 5.5 and additional buffering solution was added if required. Similarly, in the "regular pH" test conditions, a pH level of 8 to 8.2 was maintained by adding tris(hydroxymethyl)aminomethane hydrochloride to chambers in which the pH levels drop to below 8. All pH levels were monitored regularly to prevent the range from drifting. This was particularly important in the "open-air" trials with free access to oxygen, as evaporation of the seawater solutions could lead to a pH increase in the acidic chambers and pH decrease in the non-acidic chambers.

The experimental conditions for each chamber were determined to ensure that every possible combination of parameters 1 to 4 was tested. Table 3.3 and Table 3.4 outline the test conditions in each chamber at both pH 8 and pH 4, respectively. In order to better assess the effects of long-term corrosion on the steel, a subset of coupons to be immersed in nutrient-enriched seawater were pre-corroded before the experiments began. The fifth column in both Table 3.3 and Table 3.4 detail the chambers selected for pre-corroded specimens. Pre-corrosion was achieved by exposure of coupons to 48 hours of salt spray (fog)

treatment. This approach followed the standard practice ASTM B117 – 16 guidance document [130]. This accelerated corrosion technique was used specifically for the longer-term (12 and 15 month) bacteria-infused seawater trials as there is considerable evidence to support the assumption that the long-term corrosion phases of mild steel are governed by bacterial activity in the rust layers that have accumulated over years of exposure [131]. Several coupons from the same trials were omitted from pre-corrosion to enable a comparison between the accelerated and non-accelerated corrosion rates.

Ideally each chamber would contain the same number of test coupons, however a limited number of coupons were available for the total number test conditions detailed in the laboratory trials. As such, the number of coupons in each chamber ranges from 1 to 15 (Table 3.3 and Table 3.4).

Table 3.3: *The test matrix for each chamber investigating the effects of type of seawater and oxygen at pH 8. *Chamber 9 is the tidal simulation and is not replicated at low pH. "NE' = Nutrient-enriched artificial seawater.*

pH 8 Test Chambers					
Chamber	**Oxygen**	**Seawater**	**No. of Coupons**	**Pre-Corrosion**	**Temp (°C)**
1	Y	NaCl	6	N	23
3	N	NaCl	6	N	23
5	Y	NE	6	Y	23
7	N	NE	6	Y	23
9*	Y	NaCl	15	N	23
10	Y	NaCl	4	N	10
11	Y	NaCl	4	N	30
12	Y	NE	2	N	23
14	N	NE	2	N	23
16	Y	NaCl	9	N	23
18	N	NaCl	9	N	23
20	Y	NE	9	N	23
22	N	NE	9	N	23

Table 3.4: *The test matrix for each chamber investigating the effects of type of seawater and oxygen at low pH. There is no tidal simulation replicated at low pH. "NE" = Nutrient-enriched artificial seawater.*

pH 4 Test Chambers					
Chamber	**Oxygen**	**Seawater**	**No. of Coupons**	**Pre-Corrosion**	**Temp (°C)**
2	Y	NaCl	6	N	23
4	N	NaCl	6	N	23
6	Y	NE	6	Y	23
8	N	NE	6	Y	23
13	Y	NE	2	N	23
15	N	NE	1	N	23
17	Y	NaCl	9	N	23
19	N	NaCl	9	N	23
21	Y	NE	9	N	23
23	N	NE	9	N	23

The test chambers requiring exposure to oxygen were unsealed, allowing oxygen to readily diffuse into the seawater medium. The counterpart chambers that required completely anaerobic conditions were housed in an anaerobic glove box; a completely sealed container which allows objects to be manipulated using in-built gloves. The glove box remained free of oxygen by pumping inert nitrogen gas into the container to maintain 0 ppm of oxygen.

One of the key parameters to be investigated was the influence of tidal conditions. This experiment was designed with the assumption that a leaking

monopile will enable fresh oxygenated seawater ingress to the internal structure, which will facilitate mixing and maintain a pH level comparable to that of the ambient seawater. As such, this trial was only conducted at pH 8 and not replicated in acidic conditions. The set up involved the construction of a tidal simulator consisting of two large plastic containers, two Eheim Universal 300 water pumps (similar to that found in a small aquarium), with two timers attached. A plastic beam was placed across the top of one container, from which coupons were suspended from individual insulated wires and fully submerged in the NaCl solution. The timers were set to pump water from one container to another twice a day, every 6 hours. This treatment simulates the semi-diurnal tidal cycle at Teesside, which experiences two high and two low tides each day. Due to the timed water pump, the coupons experience alternating immersion and aeration periods of 6 hours. The tidal simulation assumes that the rate of change from wet to dry and vice-versa is constant. In reality, the rise and fall of the tide occurs gradually in the field, however it was not possible to replicate this gradual change in the laboratory since the pump would immediately begin to shift water between chambers when triggered by the timer.

The initial set up of the tidal chamber is shown in Figure 3.3 where coupons are being exposed to a 6-hour dry cycle. The tidal chamber required frequent replenishment every 1 to 2 weeks as the NaCl solution was quick to evaporate. This regular replenishment ensured that the coupons were fully submerged during the wet cycles.

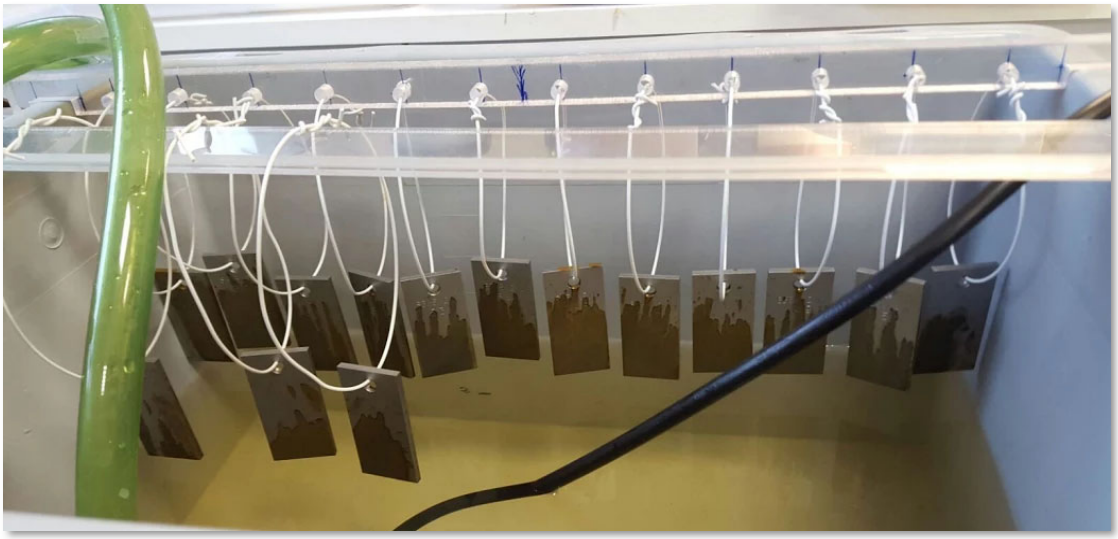

Figure 3.3: *The initial set up of the tidal chamber with coupons exposed to a period of aeration.*

Experiments were conducted at a fixed temperature of 23˚C, however, to determine the corrosion rates at 10˚C (average seawater temperature at Teesside), two additional chambers containing the control treatment of NaCl at pH 8 and free oxygen ingress were set up; one at 10˚C and the other at 30˚C. The corrosion rates from these coupons after 15 months of exposure were used to determine the activation energy (E_a); the minimum energy required in a chemical system to result in a reaction. This can be calculated directly given at least two known temperatures and a rate constant at each temperature using Arrhenius Equation [132]. It is a well-known and useful tool for determining the effect of temperature on the corrosion rate.

3.2.4 **Coupon Analyses**

Coupons were removed from test chambers at 3-month intervals, for 15 months, for weight loss analyses. Coupons were removed from the anaerobic glove box

using the attached gloves, enabling the test chambers to be manipulated and coupons to be removed from the system without introducing any oxygen. Upon removal, coupons are cleaned and descaled of the remaining corrosion product and weighed to establish the corrosion loss and corresponding rate of corrosion using the procedure outlined in the ASTM Standard Practice D2688 – 15 [133]. If the build-up of corrosion product on a coupon is substantial and cannot be removed after one cleaning regime, the process is repeated until the entire product is removed and only the steel is visible. The removal of corrosion product was conducted in accordance with the ASTM Standard Practice G1-03 [134]. The removal schedule for each set of coupons over the 15-month period is indicated in Table 3.5.

Table 3.5: *The removal period for each coupon in the laboratory trials.*

			Removal time (months)				
chamber	N° of Coupons	Coupon ID	3	6	9	12	15
1	6	1-2-3-4-5-6				1, 2, 4	3, 5, 6
16	9	74-75-76-77-78-79-80-81-82	74-76	77-79	80-82		
2	6	7-8-9-10-11-12				7,8,10	9,11,12
17	9	83-84-85-86-87-88-89-90-91	83-85	86-88	89-91		
3	6	13-14-15-16-17-18				13,14,16	15,17,18
18	9	92-93-94-95-96-97-98-99-100	92-94	95-97	98-100		
4	6	19-20-21-22-23-24				19,20,22	21,23,24
19	9	101-102-103-104-105-106-107-108-109	101-103	104-106	107-109		
5	6	25-26-27-28-29-30				25,26,28	27,29,30
20	9	110-111-112-113-114-115-116-117-118	110-112	113-115	116-118		
6	6	31-32-33-34-35-36				31,32,34	33,35,36
21	9	119-120-121-122-123-124-125-126-127	119-121	122-124	125-127		
7	6	37-38-39-40-41-42				37,38,40	39,41,42
22	9	128-129-130-131-132-133-134-135-136	128-130	131-133	134-136		
8	6	43-44-45-46-47-48				43,44,46	45,47,48
23	9	137-138-139-140-141-142-143-144-145	137-139	140-142	143-145		
12	2	63-64				63	64
13	2	65-66				65	66
14	2	67-68				67	68
15	1	69					69
9	15	49-50-51-52-53-54-146-147-148-149-150-151-152-153-154	49-51	52-54	146-148	149-151	152-154
10	4	55-56-57-58				55,57	56,58
11	4	59-60-61-62				59,61	60,62
TOTAL	150		27	27	27	34	35

3.3 **Experimental Results**

The weight loss was measured on 150 coupons removed from chambers at 3-month intervals for a total of 15 months exposure (18 months for the tidal scenario) to various combinations of environmental conditions outlined in the beginning of the previous subsection, 3.2.2. The weight loss over time was used to estimate the corrosion rate of each specimen using the standard test method specified in [133]:

$$\boldsymbol{Corrosion\ rate\ (mm\ per\ year)} = \frac{\boldsymbol{K * W}}{\boldsymbol{a * t * d}} \qquad \textit{Eq. 3.1}$$

$K = a\ constant\ with\ the\ value\ 8.76 * 10^4\ (for\ the\ units\ mm/\text{y})$

$W = weight\ loss\ (g)$

$d = the\ density\ of\ the\ metal\ (7.85 g/cm^3)$

$a = exposed\ area\ of\ the\ coupon\ (29.5 cm^2)$

$t = exposure\ time\ (hours)$

3.3.1 **The Tidal Chamber**

The simulation of a semi-diurnal tidal system was set up to determine the influence of wet/dry cycles on the corrosion rate of monopile grade steel. The coupons in this chamber were exposed to particularly aggressive corrosion

conditions and exhibited significant degradation. Table 3.6 details the corrosion data obtained from coupons that were exposed to wet/dry cycles in the experimental tidal chamber over a period of 18 months. Figure 3.4 displays the appearance of the coupons at each 3-month removal period up to 12 months. The visual appearance of the coupons prior to cleaning shows a considerable accumulation of a hard, red corrosion product that increases with time. The appearance of Coupons 152, 153 and 154 following 18 months of wet/dry cycles can be seen in Figure 3.5. The coupons had undergone such corrosive conditions that they began to split and break during the cleaning process. The corrosion data obtained from Coupon 152 was discounted as the corrosion product could not be completely removed and the sample had degraded too much for analysis.

Table 3.6: The corrosion data obtained from coupons exposed to the wet/dry cycles in the tidal chamber

Chamber	Coupon	Time (months)	Corrosion Rate (mm/y)	Mean CR (mm/y)	Corrosion Loss (mm)	Mean CL (mm)	Standard error
9	49	3	1.0336	1.1652	0.2852	0.3216	0.0315
9	50		1.2353		0.3409		
9	51		1.2268		0.3385		
9	52	6	0.7686	0.8059	0.3906	0.4095	0.0167
9	53		0.8183		0.4159		
9	54		0.8308		0.4222		
9	146	9	0.6493	0.6395	0.5162	0.5084	0.0218
9	147		0.6085		0.4838		
9	148		0.6606		0.5252		
9	149	12	0.5948	0.5569	0.6143	0.5752	0.0339
9	150		0.5393		0.5570		
9	151		0.5367		0.5543		
9	152	18	~~0.130~~	0.5225	~~0.1908~~	0.7695	0.1319
9	153		0.586		0.8626		
9	154		0.459		0.6762		

Figure 3.4: *The accumulation of corrosion product on coupons extracted from the tidal chamber. From top left to bottom right the coupon exposure time was 3; 6; 9 and 12 months.*

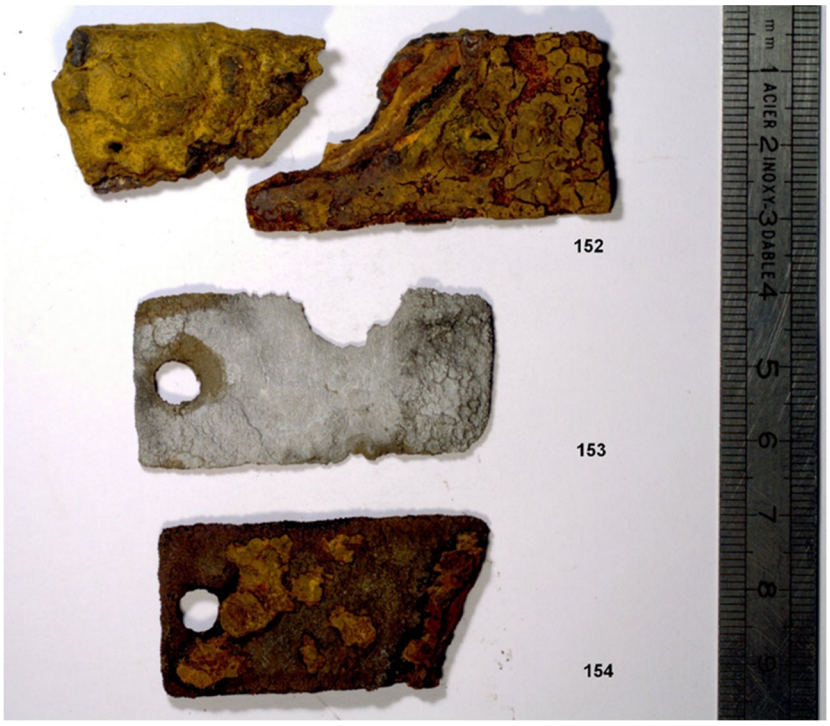

Figure 3.5: *Appearance of corrosion coupons following 18 months of experimental tidal conditions*

Table 3.6 indicates that the average corrosion loss increases slightly over time by approximately 0.1mm/y. However, despite the increasing metal loss, the average rate of corrosion over time has slowly decreased with the least amount of degradation occurring from 9 to 12 months. The greatest material loss was observed after 18 months.

Figure 3.6 compares the corrosion loss of coupons exposed to tidal conditions with those in the equivalent non-tidal (stagnant) fully submerged conditions (Table 3.7). After 3 months the average corrosion loss for the tidal coupons is approximately 43 times greater than those in fully submerged chambers. However, after 12 months, this acceleration factor has reduced to 16 (0.5752mm compared to 0.036mm).

A non-linear regression analysis was conducted with the SOLVER function in Microsoft Excel 2016, on both data sets using the iterative non-linear least squares fitting method. The function assumes corrosion loss to be a function of a time using the power law $CL = Kt^n$ where CL is corrosion loss (mm), t is time (months), K and n are regression parameters determined by the solver. The tidal model assumes the function . The non-tidal comparison data follows an almost linear pattern and assumes the function $C = 0.003t^{1.03}$.

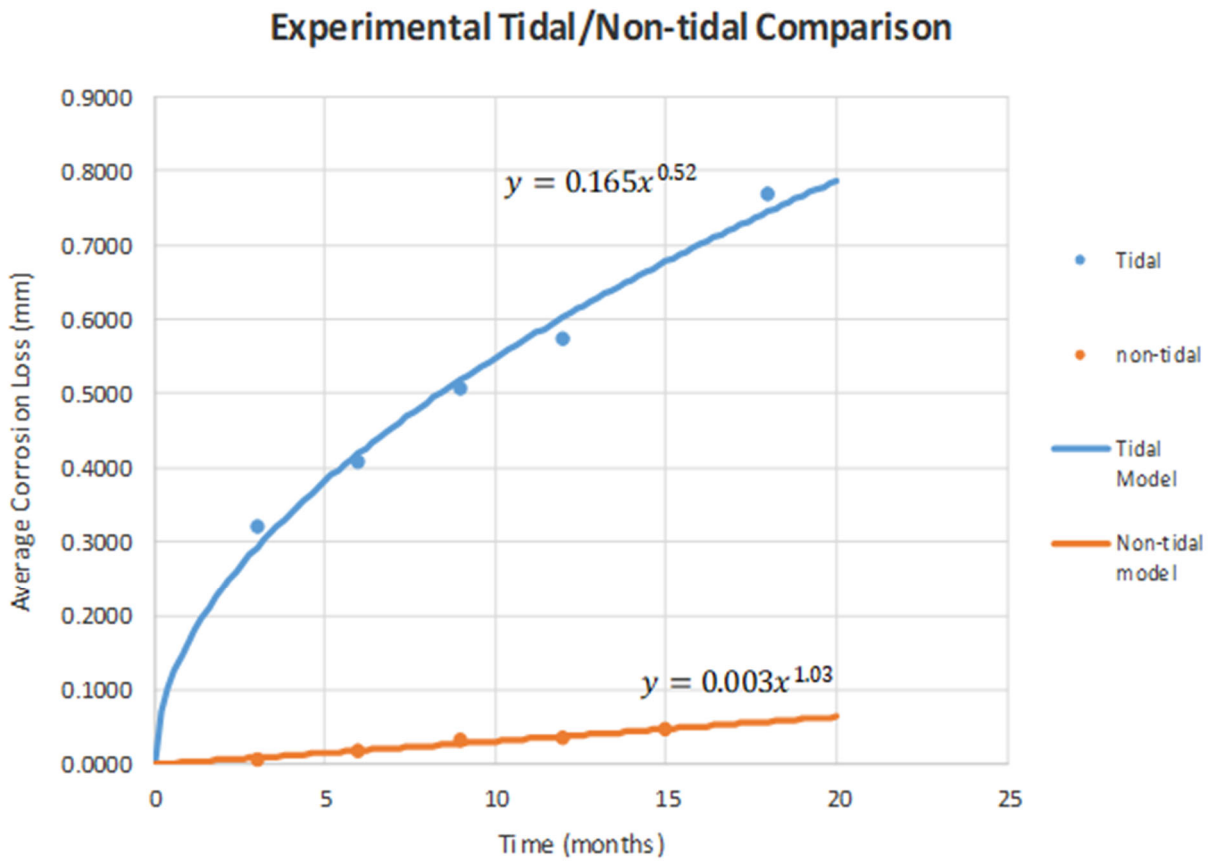

Figure 3.6: *The corrosion loss of carbon steel coupons exposed to wet/dry (tidal) cycles compared with those exposed to stagnant (non-tidal) conditions at pH 8.*

3.3.2 **Non-Tidal Chambers**

3.3.2.1 **Influence of oxygen**

To determine the potential influence that oxygen ingress has on the corrosion rate of the internal monopile steel surfaces, the experimental trials compared the corrosion behaviour of coupons in aerobic and anaerobic conditions. The aerobic conditions assume a constant diffusion of oxygen at the waterline until it is saturated (6 -8 ppm)[135]. Table 3.7 shows the results obtained at pH 8 in the oxygenated NaCl solution. Conditions were replicated in an anaerobic

environment and the results are shown in Table 3.8. A mechanical fault with the anaerobic glove box prevented any access to the chambers for a 6-month period following the first coupon removal at 3 months. As a result, all coupons due for removal from the anaerobic chambers at 6 and 9-month intervals were not removed until 12 months when the fault was rectified. It can be seen from Table 3.8 that corrosion data is only available a 3, 12- and 15-month intervals. A comparison of the aerobic/anaerobic data in NaCl solution at pH 8 is presented in Figure 3.7.

Table 3.7: *The corrosion data obtained from the coupons immersed in aerobic conditions, NaCl solution at pH 8.*

Chamber	Coupon	Time (months)	Corrosion Rate (mm/y)	Mean CR (mm/y)	Corrosion Loss (mm)	Mean CL (mm)	Standard error
16	74	3	0.0289	0.0270	0.0080	0.0075	0.0005
16	75		0.0253		0.0070		
16	76		0.0269		0.0074		
16	77	6	0.0330	0.0341	0.0168	0.0173	0.0005
16	78		0.0340		0.0173		
16	79		0.0351		0.0178		
16	80	9	0.0397	0.0402	0.0315	0.0319	0.0010
16	81		0.0393		0.0312		
16	82		0.0415		0.0330		
1	1	12	0.0375	0.0351	0.0384	0.0360	0.0021
1	2		0.0344		0.0352		
1	3		0.0335		0.0343		
1	4	15	0.0359	0.0367	0.0463	0.0473	0.0011
1	5		0.0367		0.0473		
1	6		0.0376		0.0485		

Table 3.8: *The corrosion data obtained from the coupons immersed in anaerobic conditions, NaCl solution at pH 8.*

Chamber	Coupon	Time (months)	Corrosion Rate (mm/y)	Mean CR (mm/y)	Corrosion Loss (mm)	Mean CL (mm)	Standard error
18	92	3	0.006	0.006	0.001780	0.0017	0.0001
18	93		0.006		0.001776		
18	94		0.006		0.001665		
18	95	12	0.002	0.002	0.001842	0.0017	0.0001
18	96		0.002		0.001615		
18	97		0.002		0.001586		
18	98		0.002		0.002017		
18	99		0.002		0.001663		
18	100		0.002		0.001651		
3	13		0.002		0.001685		
3	14		0.002		0.001557		
3	15		0.002		0.001631		
3	16	15	0.001	0.001	0.001657	0.0016	0.0002
3	17		0.001		0.001421		
3	18		0.001		0.001715		

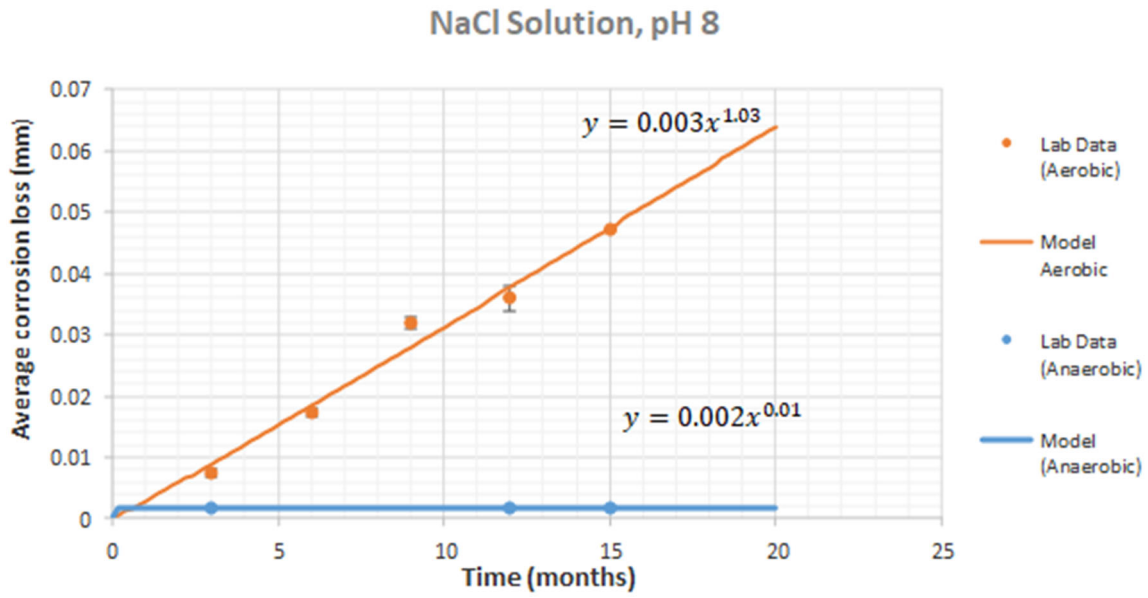

Figure 3.7: *The average corrosion loss of carbon steel coupons immersed in NaCl solution at pH 8 in aerobic conditions (red markers) and anaerobic conditions (blue markers).*

A non-linear regression analysis was conducted on both datasets again using the power function. For both aerobic and anaerobic conditions the function follows an almost linear trend; $CL = 0.003t^{1.03}$ and $CL = 0.002t^{0.01}$.

The same analysis was performed on coupons extracted from the pH 4 NaCl solutions. The aerobic and anaerobic datasets are presented in Table 3.9 and Table 3.10, respectively. In Table 3.9, the 12-month corrosion loss for coupon 7 was removed from the analysis as the result was unusually high compared to the other two coupons and was deemed to be an outlier. Figure 3.8 displays the results at pH 4 that follow a similar trend to those at pH 8 with a greater corrosion loss observed in aerobic conditions. After 9 months the average corrosion loss in aerobic conditions appears to stabilize at around 0.05mm. In the non-linear regression analysis, the functions applied to the data was $CL = 0.006t^{0.81}$ for the aerobic coupons and $CL = 0.003t^{0.15}$ for the anaerobic coupons.

Table 3.9: *The corrosion data obtained from the coupons immersed in aerobic conditions, NaCl solution at pH 4.*

Chamber	Coupon	Time (months)	Corrosion Rate (mm/y)	Mean CR (mm/y)	Corrosion Loss (mm)	Mean CL (mm)	Standard error
17	83	3	0.029	0.031	0.0080	0.0086	0.0005
17	84		0.033		0.0090		
17	85		0.032		0.0088		
17	86	6	0.070	0.045	0.0354	0.0229	0.0109
17	87		0.033		0.0167		
17	88		0.032		0.0164		
17	89	9	0.065	0.065	0.0521	0.0513	0.0008
17	90		0.063		0.0504		
17	91		0.065		0.0515		
2	7	12	0.118	0.073	~~0.1206~~	0.0518	0.0008
2	8		0.051		0.0524		
2	9		0.050		0.0512		
2	10	15	0.050	0.050	0.0501	0.0502	0.0004
2	11		0.050		0.0499		
2	12		0.050		0.0504		

Table 3.10: *The corrosion data obtained from the coupons immersed in anaerobic conditions, NaCl solution at pH 4.*

Chamber	Coupon	Time (months)	Corrosion Rate (mm/y)	Mean CR (mm/y)	Corrosion Loss (mm)	Mean CL (mm)	Standard error
19	101	3	0.014	0.014	0.0039	0.0038	0.0003
19	102		0.014		0.0039		
19	103		0.012		0.0034		
19	104	12	0.005	0.004	0.0046	0.0046	0.0015
19	105		0.004		0.0045		
19	106		0.004		0.0044		
19	107		0.005		0.0051		
19	108		0.007		0.0069		
19	109		0.007		0.0067		
4	19		0.003		0.0031		
4	20		0.003		0.0031		
4	21		0.003		0.0030		
4	22	15	0.002	0.002	0.0030	0.0030	0.0001
4	23		0.002		0.0029		
4	24		0.002		0.0031		

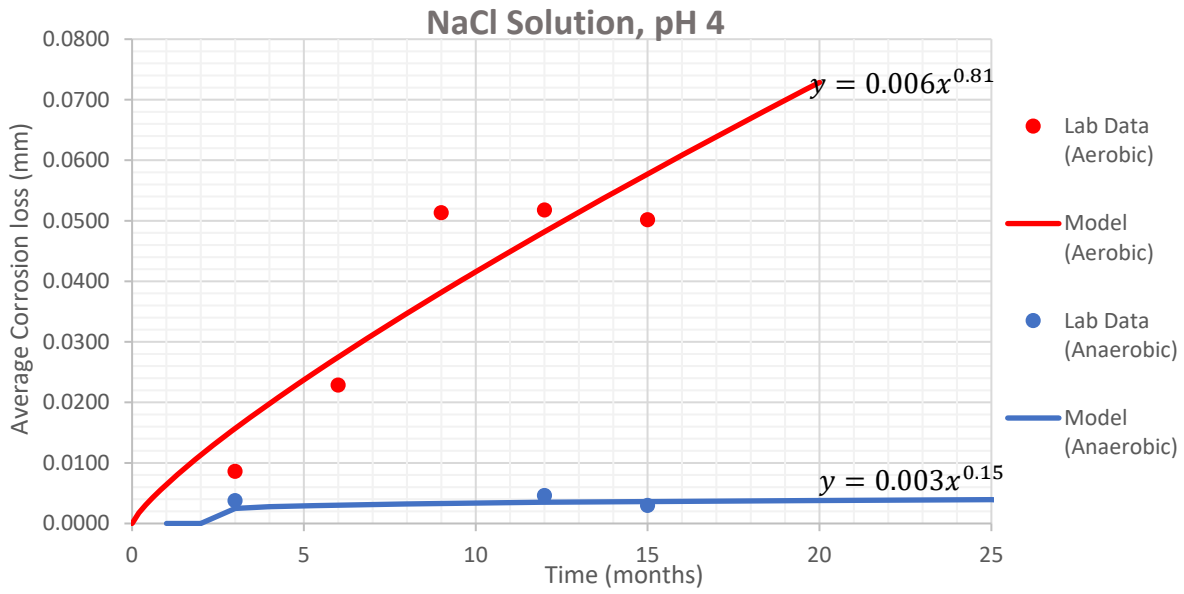

Figure 3.8: *The average corrosion loss of carbon steel coupons immersed in NaCl solution at pH 4 in aerobic conditions (red markers) and anaerobic conditions (blue markers).*

In addition to the NaCl solution, coupons immersed in artificial seawater solution enriched with nutrients were analysed in the same way to determine the influence of oxygen on corrosion rate. The results from the chambers at pH 8 are shown in Table 3.11 for the aerobic conditions and Table 3.12 for the anaerobic conditions. Figure 3.9 compares both aerobic and anaerobic datasets in pH 8 solution. As with the NaCl solution, the corrosion loss continues to increase over time in the presence of oxygen, and at 15 months, the average loss is around 30x greater than that of the equivalent anaerobic conditions. A non-linear regression analysis on both datasets using the power function determined that $CL = 0.0016t^{1.43}$ for aerobic conditions and $CL = 0.008t^{0.5}$.

Table 3.11: *Corrosion data obtained from coupons immersed in aerobic nutrient-enriched artificial seawater solution at pH 8.*

Chamber	Coupon	Time (months)	Corrosion Rate (mm/y)	Mean CR (mm/y)	Corrosion Loss (mm)	Mean CL (mm)	Standard error
20	110	3	0.036	0.035	0.0098	0.0096	0.0002
20	111		0.034		0.0094		
20	112		0.035		0.0097		
20	113	6	0.038	0.039	0.0194	0.0198	0.0004
20	114		0.040		0.0202		
20	115		0.039		0.0199		
20	116	9	0.043	0.043	0.0344	0.0340	0.0004
20	117		0.042		0.0338		
20	118		0.042		0.0337		
12	63	12	0.061	0.061	0.0621	0.0621	0
12	64	15	0.059	0.059	0.0756	0.0756	0

Table 3.12: *Corrosion data obtained from coupons immersed in anaerobic nutrient-enriched artificial seawater solution at pH 8.*

Chamber	Coupon	Time (months)	Corrosion Rate (mm/y)	Mean CR (mm/y)	Corrosion Loss (mm)	Mean CL (mm)	Standard error
22	128	3	0.006	0.007	0.0017	0.0019	0.0001
22	129		0.007		0.0020		
22	130		0.007		0.0019		
22	131	12	0.004	0.004	0.0045	0.0039	0.0005
22	132		0.004		0.0045		
22	133		0.004		0.0040		
22	134		0.003		0.0036		
22	135		0.004		0.0038		
22	136		0.003		0.0035		
14	67		0.003		0.0036		
14	68	15	0.002	0.002	0.0023	0.0023	0

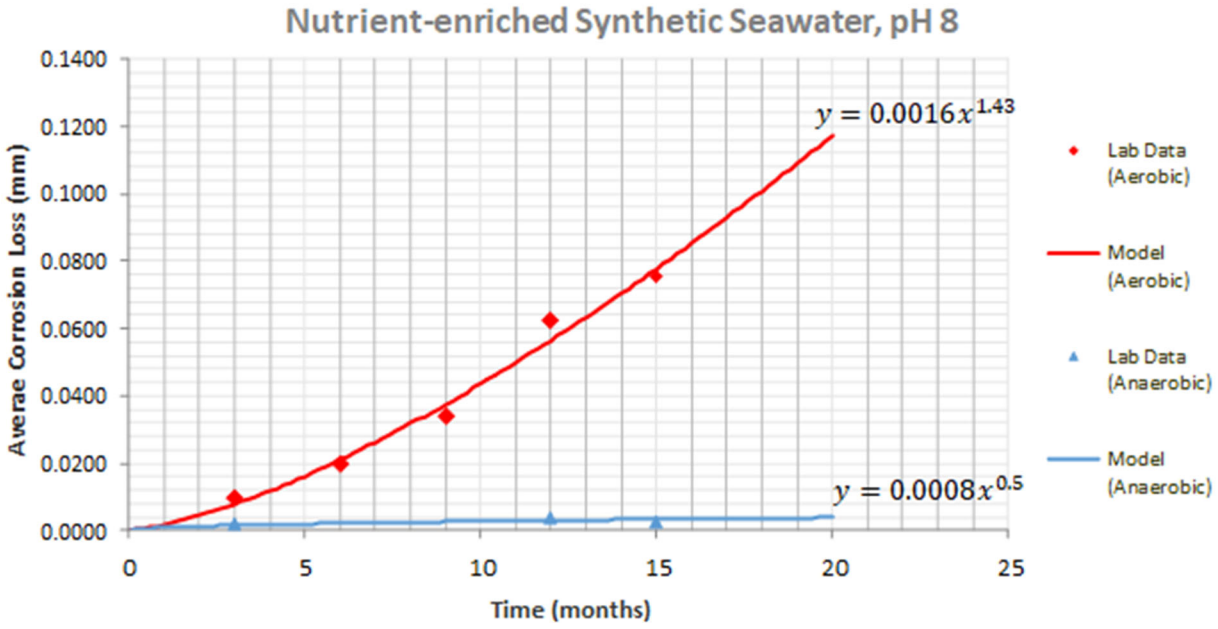

Figure 3.9: *The average corrosion loss of carbon steel coupons immersed in nutrient-enriched artificial seawater at pH 8 in aerobic conditions (red markers) and anaerobic conditions (blue markers).*

The corrosion loss results obtained in the pH 4 chambers for aerobic and anaerobic artificial seawater conditions are presented in Table 3.13 and

Table 3.14 respectively, and graphically represented in Figure 3.10. In Table 3.13, coupon 125 was removed from the analysis since the average corrosion loss was 3 times higher than the other two coupons removed at 9 months and was believed to be an outlier. A similar trend in the average corrosion loss in aerobic conditions is observed at pH 4 when compared with pH 8 with significantly greater losses observed over 12 to 15 months (coupons 65 and 66). Again, the acceleration factor at 15 months is around 30x in the presence of oxygen compared to when oxygen is removed from the test chambers. It can be concluded that the presence of oxygen accelerates the corrosion loss of carbon steel by a factor of 30 in both NaCl and artificial seawater solutions.

Table 3.13: *Corrosion data obtained from coupons immersed in aerobic nutrient-enriched artificial seawater solution at pH 4.*

Chamber	Coupon	Time (months)	Corrosion Rate (mm/y)	Mean CR (mm/y)	Corrosion Loss (mm)	Mean CL (mm)	Standard error
21	119	3	0.033	0.025	0.0091	0.0069	0.0019
21	120		0.022		0.0061		
21	121		0.020		0.0055		
21	122	6	0.027	0.026	0.0136	0.0130	0.0005
21	123		0.025		0.0128		
21	124		0.025		0.0127		
21	125	9	0.143	0.073	~~0.1138~~	0.0306	0.0010
21	126		0.039		0.0313		
21	127		0.038		0.0298		
13	65	12	0.154	0.154	0.1579	0.1579	0
13	66	15	0.176	0.176	0.2266	0.2266	0

Table 3.14: *Corrosion data obtained from coupons immersed in anaerobic nutrient-enriched artificial seawater solution at pH 4.*

Chamber	Coupon	Time (months)	Corrosion Rate (mm/y)	Mean CR (mm/y)	Corrosion Loss (mm)	Mean CL (mm)	Standard error
23	137	3	0.018	0.018	0.0049	0.0048	0.0001
23	138		0.018		0.0049		
23	139		0.017		0.0048		
23	140	12	0.006	0.007	0.0064	0.0070	0.0008
23	141		0.006		0.0063		
23	142		0.006		0.0064		
23	143		0.008		0.0081		
23	144		0.007		0.0076		
23	145		0.007		0.0075		
15	69	15	0.005	0.005	0.0069	0.0069	0

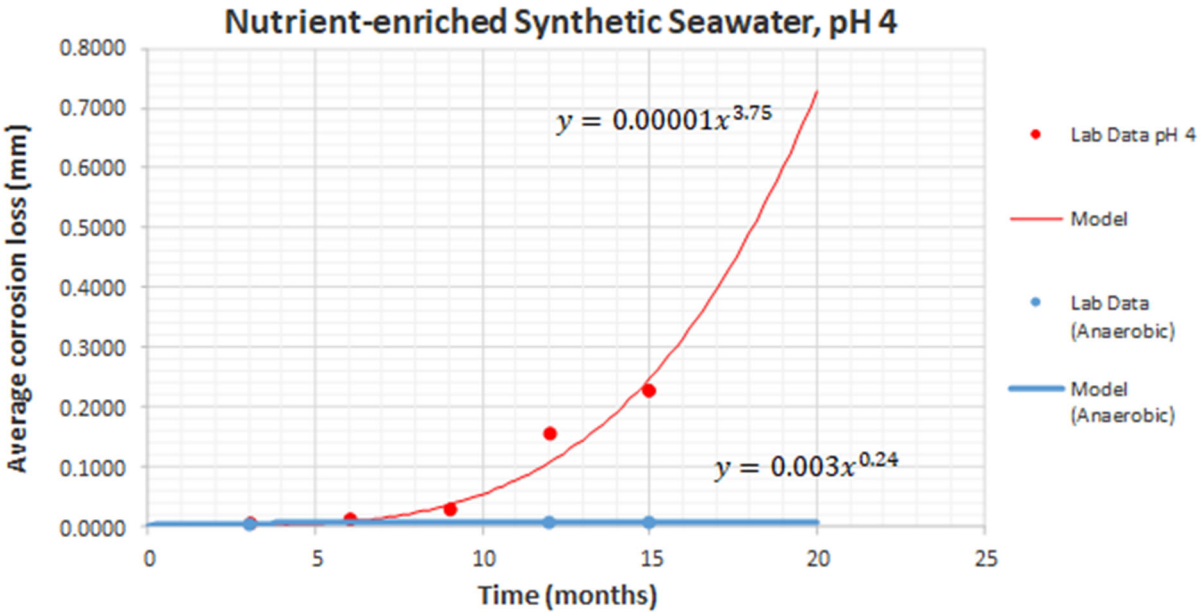

Figure 3.10: *The average corrosion loss of carbon steel coupons immersed in nutrient-enriched artificial seawater at pH 4 in aerobic conditions (red markers) and anaerobic conditions (blue markers).*

3.3.2.2 **Influence of pH**

To determine the influence of pH, results presented in the above tables were plotted to compare the average corrosion loss in solutions at pH 4 and pH 8. Figure 3.11 displays the trends across the different combinations of parameters. Generally, the average loss at pH 4 is consistently higher than that at pH 8. With the exception of the aerobic NaCl chamber, coupons in pH 4 solutions had an average corrosion loss 2-3 times higher than coupons in the pH 8 chambers at the end of the trial. Therefore, corrosion loss of carbon steel is potentially 3 times greater in low pH environments compared to a normal seawater pH.

In Figure 3.11A, the average corrosion loss is continuing to increase with time at

pH 8, whereas at pH 4 the corrosion loss begins to stabilize at around 9 months. The contrary result would be expected at low pH since this would potentially prevent the formation of a protective surface layer and facilitate further corrosion.

A)

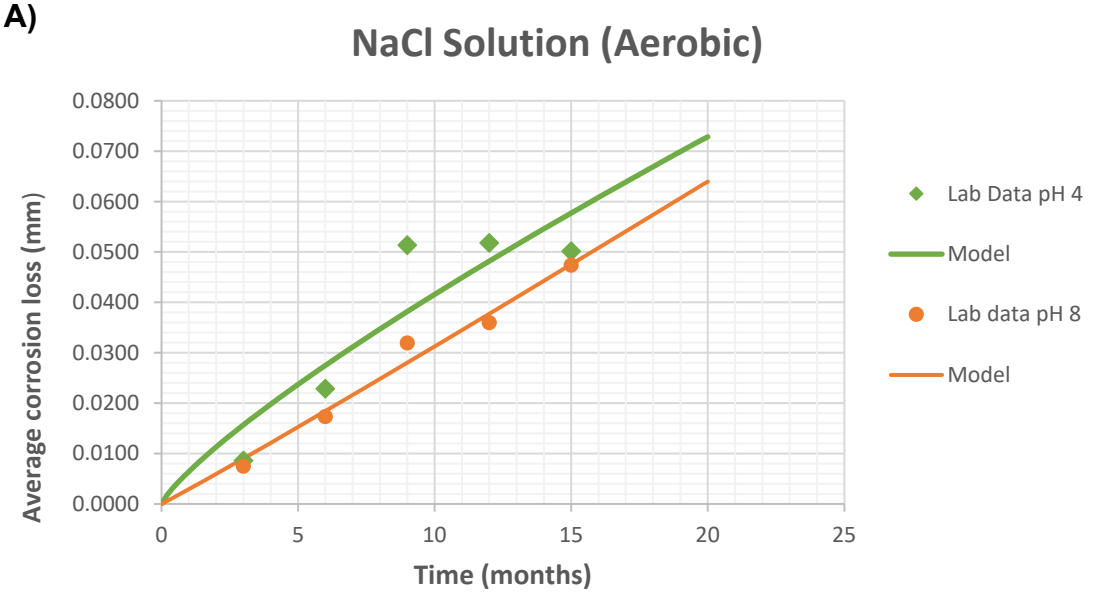

B)

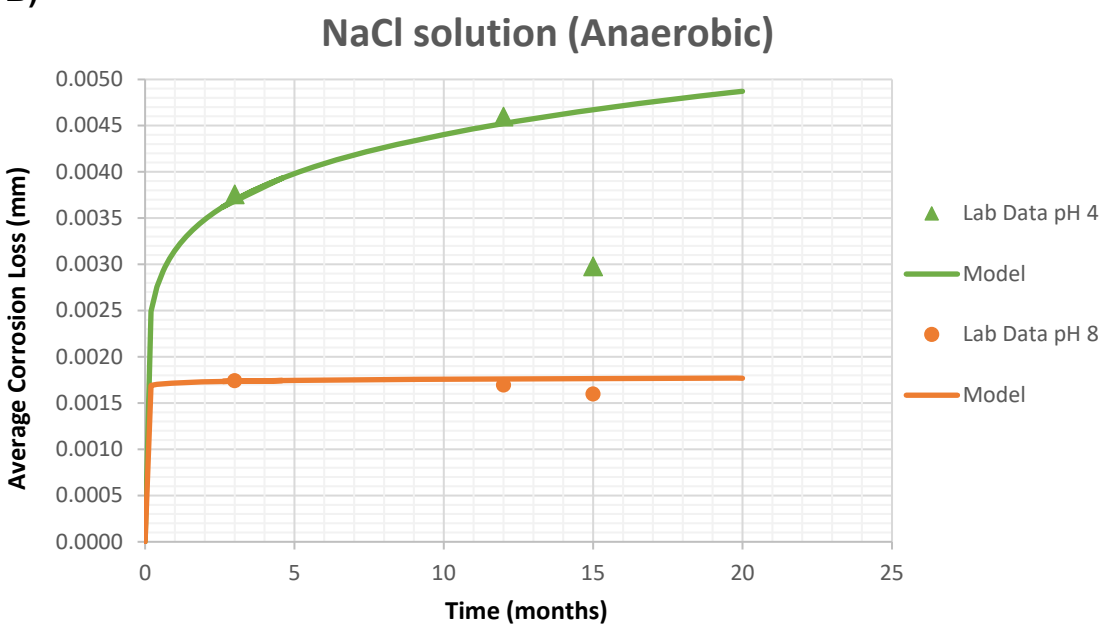

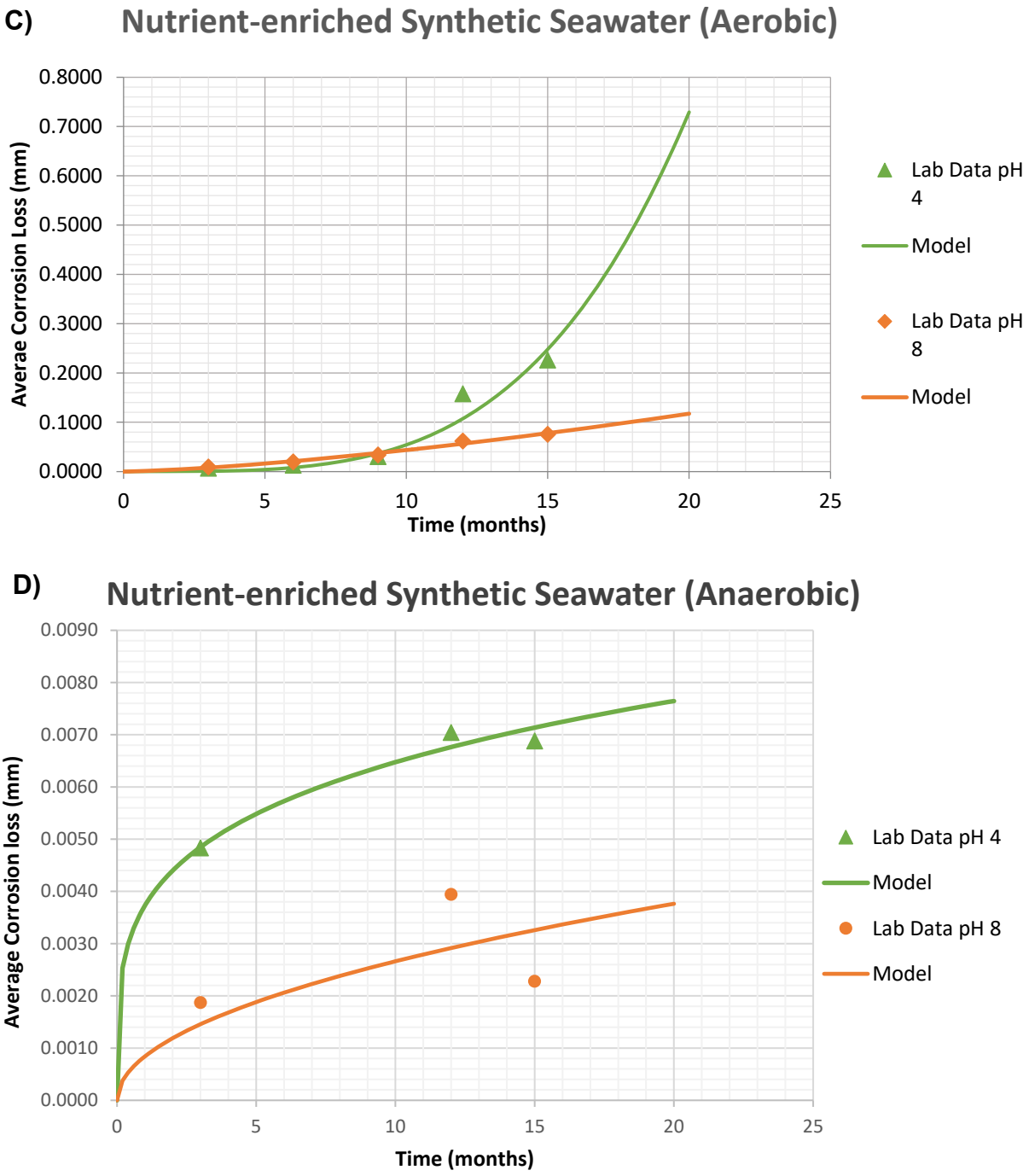

Figure 3.11: *A comparison of the pH 4 and pH 8 corrosion loss results in A) NaCl solution (aerobic), B) NaCl solution (anaerobic), C) nutrient-enriched artificial seawater (aerobic) and D) nutrient-enriched artificial seawater (anaerobic). The pH 4 results are indicated in green and pH 8 results in orange.*

3.3.2.3 **Influence of pre-corrosion**

Twenty-four coupons (25 to 46) to be immersed in the nutrient-enriched synthetic seawater trials underwent 48 hours of salt-spray testing to pre-corrode the specimens and determine the effect on overall material loss after 12 and 15 months of laboratory trials.

Figure 3.12: *Coupons 25 to 46 immediately following 48 hours of salt spray treatment.*

This accelerated corrosion technique was conducted on the majority of coupons immersed in artificial seawater since long-term corrosion phases of mild steel in seawater are governed by anaerobic bacterial activity in the rust layers that have accumulated over many years of exposure [131]. Figure 3.12 displays the pre-corrosion conditions that coupons were exposed to in the salt spray chamber. Seven coupons (63-69) did not undergo pre-corrosion to enable a comparison between accelerated and non-accelerated test corrosion rates. Figure 3.13 indicates that at pH 8, pre-corrosion does not increase the average corrosion loss, and in fact, at 12 months the average loss is 0.06mm for specimens with or

without pre-corrosion. At 15 months, the coupons that were not exposed to salt spraying actually had a greater average corrosion loss than those that were pre-corrosion; 0.076mm compared to 0.061mm. A similar trend was observed at pH 4 when oxygen was present (Figure 3.14). At 12 months, the pre-corroded specimens had an average corrosion loss of 0.049mm, however, those were not pre-corroded had an average loss that was 3 times greater, 0.158mm. At 15 months, there remains a factor of three difference: 0.227mm (without pre-corrosion) and 0.075mm (with pre-corrosion).

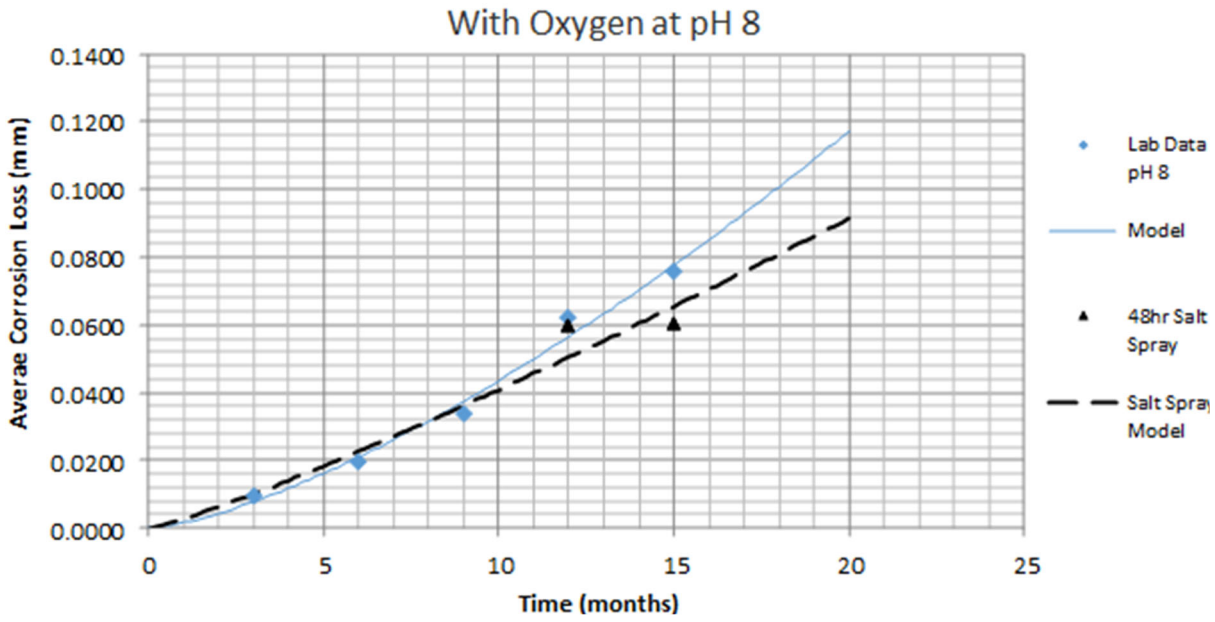

Figure 3.13: *The average corrosion loss of coupons pre-exposed to 48 hours of salt spray testing before immersion in nutrient-enriched synthetic seawater (black markers), compared to the non-pre-corroded equivalent specimens at pH 8 and aerobic conditions (blue markers).*

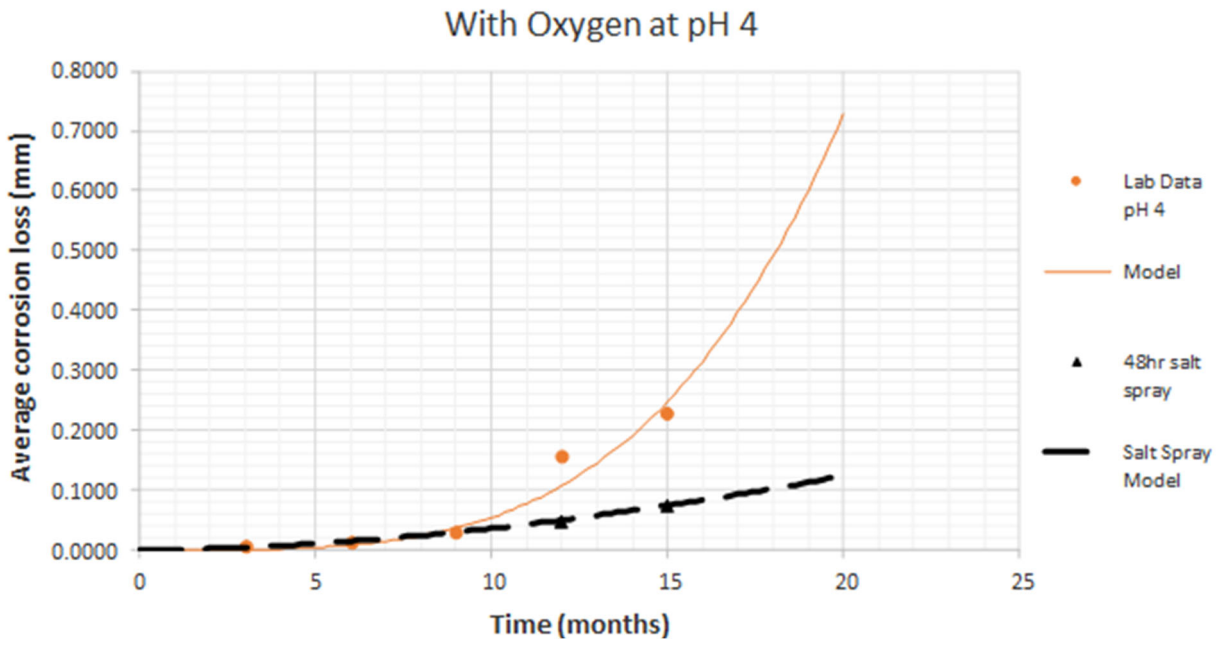

Figure 3.14: *The average corrosion loss of coupons pre-exposed to 48 hours of salt spray testing before immersion in nutrient-enriched synthetic seawater (black markers), compared o the non-pre-corroded equivalent specimens at pH 4 and aerobic conditions (orange markers)*

In anaerobic conditions, the observation is reversed - pre-corroded coupons have a considerably higher corrosion loss than those without pre-corrosion (Figure 3.15 and Figure 3.16). At pH 8, the average corrosion loss at 12 and 15 months is a factor of 10 higher for pre-corroded specimens compared to those without pre-corrosion. At pH 4, this acceleration factor reduces to 4 (Figure 3.16). Salt-spray testing is a well-known method of accelerating the corrosion process so these results would be expected. However, in anaerobic conditions, the pH level does not seem to influence the average corrosion loss since this value remains at approximately 0.03mm at both 12 and 15 months. Given the results in Figure 3.10, it would be expected that the pre-corroded specimens exposed to a lower pH would experience greater corrosion loss over time than those at normal seawater pH.

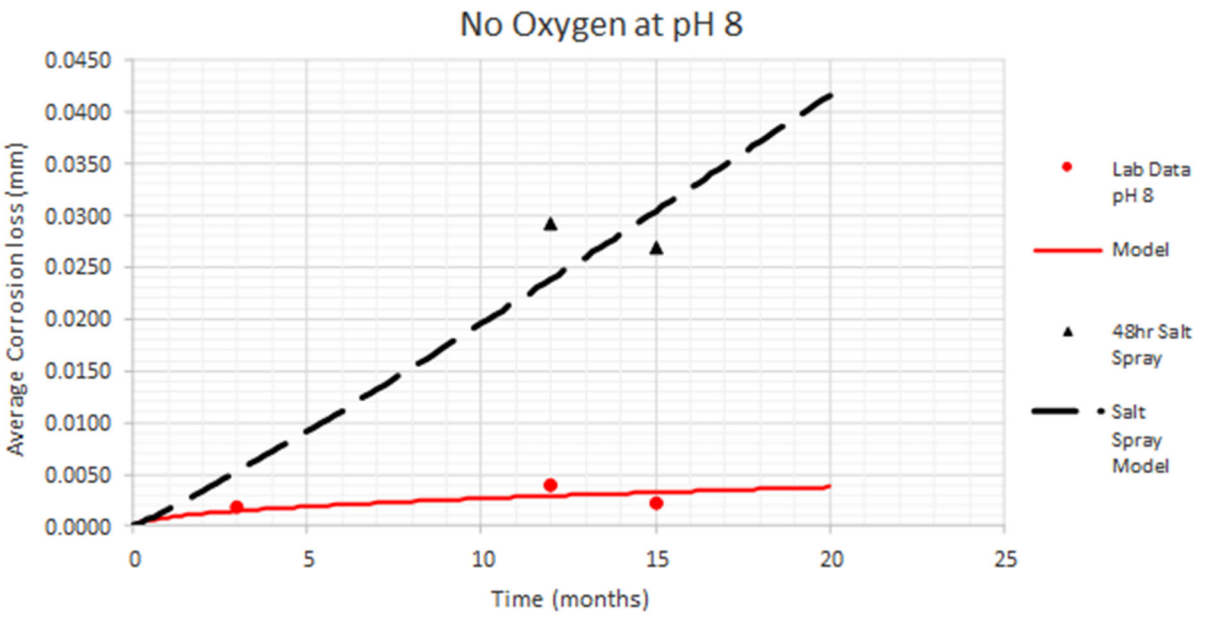

Figure 3.15: *The average corrosion loss of coupons pre-exposed to 48 hours of salt spray testing before immersion in nutrient-enriched synthetic seawater (black markers), compared to the non-pre-corroded equivalent specimens at pH 8 and anaerobic conditions (red markers).*

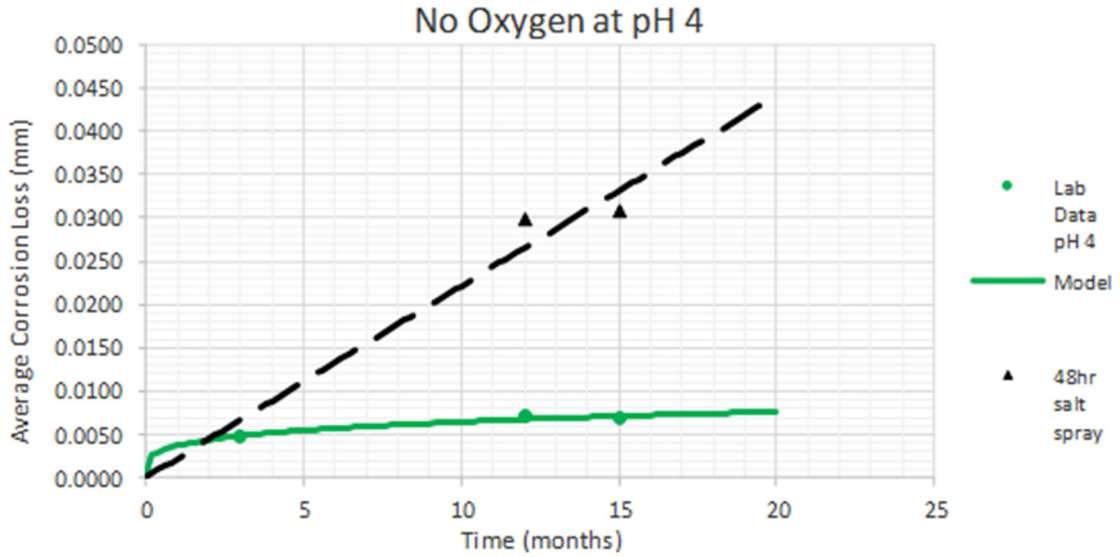

Figure 3.16: *The average corrosion loss of coupons pre-exposed to 48 hours of salt spray testing before immersion in nutrient-enriched synthetic seawater (black markers), compared to the non-pre-corroded equivalent specimens at pH 4 and anaerobic conditions (green markers).*

3.3.2.4 **Influence of temperature**

The effect of temperature on the corrosion rate of coupons immersed in NaCl solution at pH 8 and exposure to oxygen was determined by measuring the Activation Energy (Ea) using Arrhenius Equation. The Arrhenius equation defines an exponential relationship the rate constant of a chemical reaction (corrosion in this instance) and the temperature [132]:

$$K = A^{(-\frac{Ea}{RT})} \qquad \textit{Eq. 3.2}$$

Where:

K = Rate Constant (Corrosion Rate in mm/y)

R = Gas Constant (8.314 J/mol K)

T = Temperature (Kelvin)

Ea = Activation Energy (kJ/mol)

A = The Arrhenius pre-exponential (frequency) factor

The activation energy was calculated for the corrosion of carbon steel coupons at different temperatures; 10°C, 23°C and 30°C with constant pH level and NaCl solution. The input values and results are presented in Table 3.15. The Arrhenius plot is shown in Figure 3.17. The Ea calculated for the rate of corrosion at the different temperatures was 14.6 kJ/mol. This is the minimum energy requirement that must be met for corrosion to take place.

Table 3.15: *The input values for the Arrhenius Equation and the calculated activation energy* (Ea).

Temp (°C)	Temp (K)	R (J/Mol K)	1/T	K	Ln K	slope	Ln A	A	Ea (kj/mol)
10	283.5	8.314	0.0035	0.034	-3.3814	-1755	2.7636	15.8570	14.5917
23	296.2	8.314	0.0034	0.037	-3.2968				
30	303.2	8.314	0.0033	0.053	-2.9375				

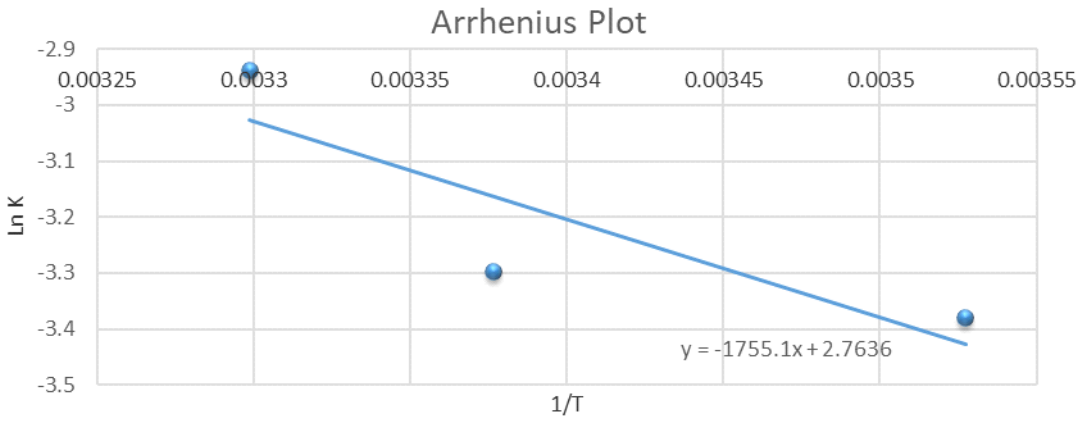

Figure 3.17: *The Arrhenius plot showing the natural logarithm of the corrosion rate constant (K) plotted against the inverse of the absolute temperature (T).*

3.4 **Discussion**

The experimental trials were conducted under the following assumptions about the corrosion rate of monopile steel given the internal environmental conditions at Teesside Offshore Wind Farm:

1. Samples exposed to tidal conditions will exhibit faster corrosion rates than those that are fully immersed.
2. Samples exposed to aerobic environments will exhibit faster corrosion rates than those in the anaerobic chamber.

3. Samples exposed to acidic conditions will exhibit faster corrosion rates than those exposed to representative seawater pH levels.
4. Samples exposed to seawater with live marine bacteria will exhibit faster corrosion rates than those in NaCl solutions without bacteria.

The results indicate that wet/dry cyclic tidal variations did influence the corrosion rate of coupons quite considerably compared to those in fully submerged conditions. After 3 months, the corrosion rate of samples in the tidal chamber were 43 times greater than those fully submerged. This factor of corrosion reduced steadily throughout the duration of experiments, however after 12 months, the rates obtained from samples in the tidal chamber will still 12x greater than those that were fully immersed. The average corrosion rate of tidal samples reaches approximately 0.5mm/y after 18 months of testing which corresponds to approximately 12.5mm over a 25-year period (the design life for turbines at Teesside). This is 5x greater than the DNV design guidance of 0.1mm/y for the internal tidal zone [35] and is more consistent with the 0.4mm/y rate posed by Momber for the splash zone of steel offshore structures [21]. The experimental results suggest that the tidal simulation is aggressively corrosive and perhaps not entirely representative of the internal monopile conditions. The corrosion allowance (CA) applied to the internal splash/tidal zones for the Teesside monopiles was 4mm (Extreme) and 2mm (Fatigue) [36]. Therefore, if the internal steel was corroding at a rate of 0.5mm/y it is highly likely that a catastrophic failure would have already occurred, given that the wind farm has been operational since 2013. Nevertheless, the CA assumes that corrosion of the internal splash/tidal zone is governed by the action of tide only [36]. In practice, there are likely to be

various corrosion mechanisms at play, governed by not just tidal action, but microbiological activity, dissolved oxygen, temperature and pH fluctuations.

The conditions within the tidal simulation were different to that of the chambers, not only because of the wet/dry cycles, but because this large container was completely open to the surrounding atmosphere and would evaporate quickly. Therefore, regular replenishment of artificial seawater was required to ensure that samples were consistently immersed and aerated. The regular infills of fresh artificial seawater to the top of the chamber does not realistically represent the internal monopile environment, whereby fresh seawater would enter the foundation from the bottom of the monopile via the cable seals located close to the seabed. Even if the leak rate is high, the mixing between the seawater at the tidal zone (near the lower working platform) and the seawater by the seabed is expected to be minimal, and not representative of the top-ups given to the experimental tidal chamber. With more time and resource, a mock monopile would have been developed for this experiment with different leak scenarios, that could more realistically reflect the extent of the tidal conditions within each monopile.

Ideally the tidal simulation experiment would have taken place over many years to understand if the corrosion rate will continue to decrease and stabilize over time as corrosion product accumulates. However, given the time constraints of the research project, the maximum allowable trial was 18 months. Nevertheless, useful data was obtained which could be extrapolated and allowed assumption 1 to be accepted.

As expected, the presence of oxygen accelerates the corrosion process by facilitating the oxidation process. In anaerobic conditions, the corrosion loss remains stable and negligible. By 12 to 15 months immersion, the corrosion rates in the aerobic conditions have stabilized at 0.035-0.036mm/y. However, between these periods, the acceleration factor of oxygen raises from 20 to 30; i.e. after 15 months the corrosion loss is 30x greater in the presence of oxygen than without. This poses a concern for the Teesside monopiles which require 24 hours of ventilation prior to any internal inspection and/or maintenance. By opening the air-tight hatch and allowing fresh air to flow in to the monopile, this replenishes the dissolved oxygen in the internal seawater which will perpetuate the corrosion process.

Dissolved Oxygen (DO) levels are a good indicator of how much oxygen is in the water to allow corrosion to occur. However, throughout the duration of the experimental trials it was not possible to monitor DO content across each chamber. This is a key element which should be incorporated into any future experiments to measure the influence of DO content on corrosion rate. During a corrosion monitoring campaign at another UK offshore wind farm, it was assumed that a high monopile leak rate would correspond to a high DO content and high corrosion rate, and this is somewhat reflected in the results (Figure 3.18). The identity of the wind farm and the Turbine ID have been blacked out for confidentiality reasons, however there are variations across the results, with DO readings missing from 3 turbines. The highest corrosion rate observed in this study does not reflect the highest DO reading, however across all samples taken there does appear to be a relationship between corrosion rate and DO.

Nevertheless, the results will depend on the internal location where samples were taken and if the graph reflects the average of multiple samples.

The corrosion rates obtained from samples within the anaerobic chambers were deemed to be negligible across all treatments. Elevated corrosion levels were observed in the anaerobic chambers containing the nutrient-enriched artificial seawater compared to those that had marine bacteria following 3 months of immersion. It is expected that the live bacteria at the start of the trial may have contributed to the corrosion of samples early on but are likely to have died off throughout the remainder of the trial. In the later extractions after 12 months immersion, the anaerobic corrosion rates are consistent between the artificial seawater samples and those immersed in the nutrient-enriched solution.

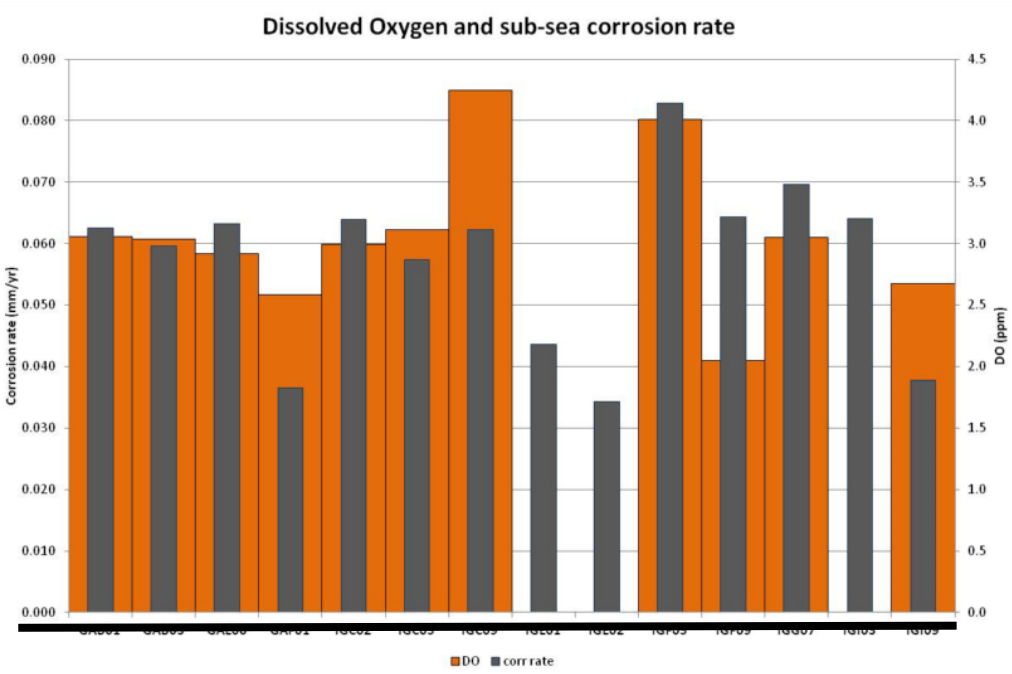

Figure 3.18: *Dissolved Oxygen (ppm) and corrosion rate (mm/y) within monopile foundations at a UK offshore wind farm* [136]*).*

The results of the experimental trial reflect assumption 2, in that across all samples, the corrosion coupons exposed to aerobic conditions exhibited a greater corrosion rate than those under anaerobic conditions.

One of the most interesting elements of the laboratory trials, was investigating the influence of low pH on the corrosion rate of monopile steel. Where the influence of tidal action and oxygenation is generally well-understood for offshore structures, the creation of acidic conditions due to the cathodic protection process in a closed monopile environment and its general effect on corrosion, is a phenomenon that is not well-understood, particularly within the offshore wind industry. In addition, other than the experience at Teesside and discussions with other wind farm operators, there are very little published examples in literature. In general, the average corrosion rates of coupons immersed in low pH conditions (between 4 to 5.5.) were 2-3 times higher than those samples in equivalent conditions but at higher pH (between 7.8 to 8.2), except for the aerobic NaCl chamber. The highest corrosion rates observed during the pH trials were from samples immersed in the nutrient-enriched artificial seawater after 12- and 15-months immersion. This could suggest that the influence of marine bacteria on corrosion rate is evident after 12 months exposure to aerobic, low pH conditions. Alternatively, the high corrosion rates observed on these samples may also suggest evidence of aggressive localized corrosion, facilitated by bacteria.

Further investigation on the effects of low pH on monopile steel is urgently required to better understand the impacts of long-term exposure to a low-pH seawater medium, particularly if the cathodic protection system is to be

replaced every 5-years as per the design criteria [36]. One of the suggested solutions to the internal acidification problem experienced by several wind farm owner/operators, is to drill holes in all sealed foundations and introduce a controlled leak of surrounding seawater. This has been discussed at industry conferences and O&M forums, and in fact has been implemented by at least one operator. The issue with forcing leaks into the system, is not only the issue of internal tidal activity, but the structural implications of drilling into foundations and controlling the flow.

During the trials it was necessary to monitor the pH levels regularly (every couple of days) to ensure they did not drift beyond the boundary conditions. With additional time and resource, experiments would have been conducted under more controlled environments, with consistent and exact pH levels across all samples. This would enable the investigator to draw conclusions on the specific impact of controlled pH variations on the corrosion rate of monopile steel. Nevertheless, operational experience and environmental monitoring indicates that the internal monopile environment is continuously fluctuating and therefore pH level will never remain constant. These results support assumption 3, given the elevated corrosion levels at lower pH are typically higher than those at ambient seawater pH.

Due to laboratory constraints, it was not possible to use real, live, seawater or source different types of bacteria associated with bacterial corrosion such as SRB. To counter this issue, nutrient-enriched (NE) seawater with natural live marine bacteria and live ocean saltwater, was purchased in bulk and topped up

as necessary during experiments. Without using real seawater from the internal monopile to conduct experiments, it is difficult to replicate the exact composition artificially in a laboratory environment. Further testing is required using real seawater with representative bacteria to determine the influence on corrosion rate.

4 Offshore Corrosion Trials

4.1 Introduction

To complement the corrosion laboratory study, internal corrosion monitoring at Teesside was undertaken in parallel with the experiments. Observations from the corrosion monitoring campaign provide validation to the experimental results and further help to develop an empirical model for the long-term internal corrosion assessment of monopiles. The corrosion monitoring conducted at Teesside consists of two corrosion coupon campaigns and the installation of live monitoring equipment within two turbines. Separate to this project and as part of EDF's O&M strategy, live condition monitoring sensors were installed within turbines 03A and 13B and provide continuous data on pH levels, cathodic protection potential, hydrogen and hydrogen sulphide gas levels.

The first internal corrosion coupon campaign was conducted in September 2014, which provided corrosion loss data for 12 coupons across 5 foundations over a period of 120 to 157 days. Following this study, significant improvements were made to the experimental design, selection of coupons and the allocation of coupons within the monopile, which prompted a second monitoring campaign to begin in August 2016 with 49 coupons installed across 5 foundations. This campaign will run for 24 months, however, a subset of 15 specimens will be removed in September 2017 for analyses and comparison with the 12-month experimental results. The removal of some coupons after 12 months whilst

keeping the remainder in for a further 3 months, allows any change in corrosion rates over this time to be evaluated.

4.2 Offshore Monitoring Methodology

4.2.1 2014 Corrosion Coupon Campaign

Twelve 76mm x 13mm x 1.5mm mild steel coupons were installed within 5 foundations at Teesside Offshore Wind Farm at various locations where cathodic protection readings were deemed to be insufficient (Table 4.1). Coupons were tied at one end to a nylon wire, which was weighted at the bottom, and hung from the internal lower working platform to various depths. Removal of coupons took place after 97 to 156 days of immersion, followed by weight loss (see [133] for procedure).

Table 4.1: *The locations of 12 corrosion coupons installed within monopile foundations at Teesside in 2014.*

Turbine	No. of Coupons	Coupon ID	Location
1A	2	915	1.2m below waterline
		916	1m above seabed
3A	2	908	1m below waterline
		909	Seabed
5A	3	849	1m below waterline
		850	Central
		917	0.5m above seabed
9A	2	910	1m below waterline
		911	1m above seabed
10B	3	912	Central
		913	Lower work platform
		914	0.1m above seabed

Coupons were taken to EDF R&D labs in Les Renardières for non-destructive and destructive testing. Coupon 911 was left untreated following removal so that the corrosion product remained intact. This coupon was used for the majority of non-destructive material tests. Coupon 911 was located just 1m above the seabed within the monopile of WTG 9A (a drilled foundation) as shown in Figure 4.1. Therefore, an in-depth analysis of this coupon would give a good indication of how the internal steel surface towards the seabed is affected by corrosion.

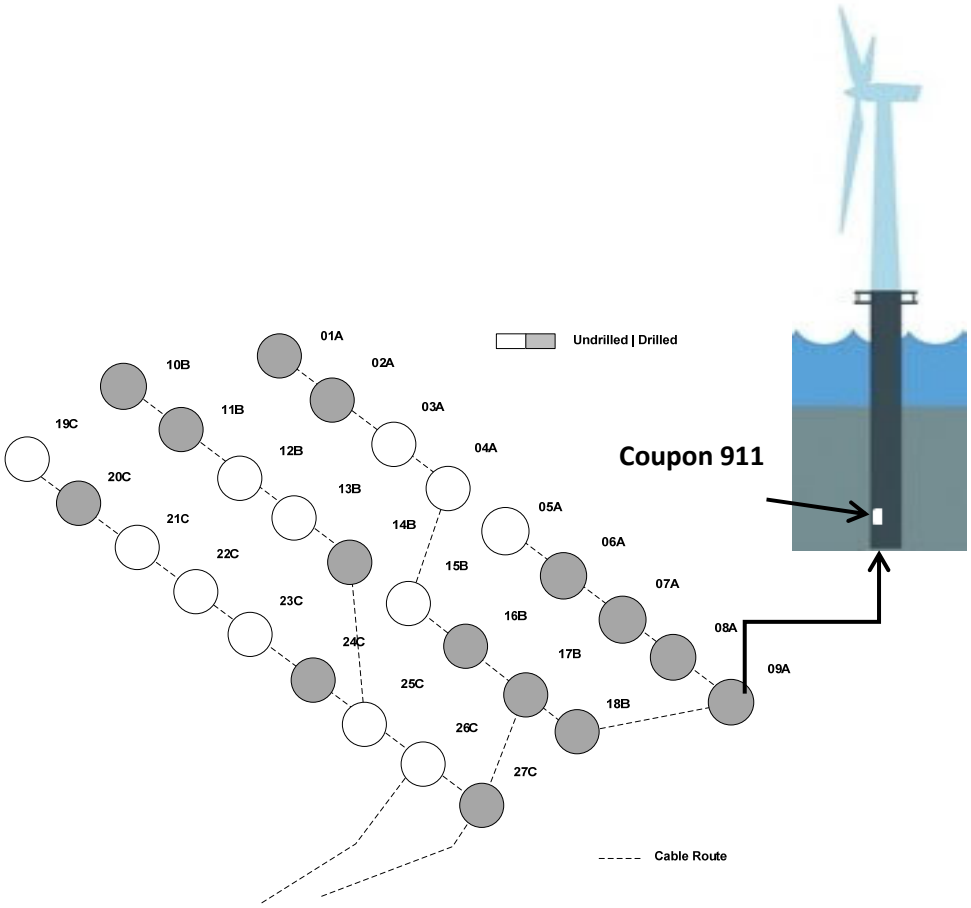

Figure 4.1: *The WTG array layout and the location of Coupon 911 within the MP of WTG 9A.*

4.2.2 **Summary of Non-Destructive Tests**

4.2.2.1 **Scanning Electron Microscopy (SEM)**

A scanning electron microscope (SEM) produces images of a sample by scanning it with a focussed beam of electrons (Figure 4.2). This was used to investigate the morphology of the corrosion product (oxide film) that was preserved on coupon 911 using an approach based on Zeiss SIGMA field emission SEM.

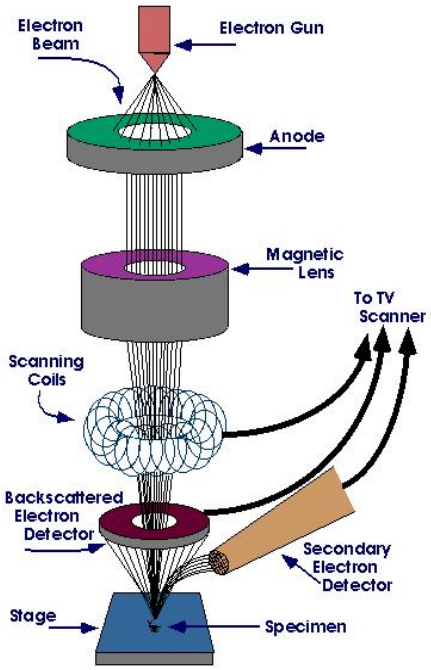

Figure 4.2: *Diagram of a Scanning Electron Microscope* [137].

4.2.2.2 **Energy Dispersive X-ray Spectroscopy (EDS)**

EDS examines the interaction between an incident primary electron beam and atoms on the coupon surface. This results in the emission of X-rays which

contains the energy characteristics of the detected elements. As each element has a unique atomic structure, it produces a unique set of peaks in the resulting X-ray emission spectrum measured. EDS enabled the identification of specific elements present on the coupon and their relative spectra were used to evaluate the chemical composition of the corrosion products on the surface of coupon 911.

4.2.2.3 **Binocular Microscopy**

The monochrome SEM images of coupon 911 were compared with that of high-resolution colour pictures using an Olympus DP 2-Twain binocular microscope. Using Perfect Image© software, the colour images could be viewed and edited on a computer screen simultaneously.

4.2.2.4 **X-ray Diffraction (XRD)**

X-ray diffraction is a tool used for identifying the atomic and molecular structure of a crystal, in which the crystalline atoms cause a beam of incident x-rays to diffract into many specific directions. The identification and characterization of compounds is possible based on their diffraction pattern. The diffraction data is presented in a diffractogram in which the diffracted intensity is shown as a function of 2θ (the scattering angle between the x-ray beam axis and the diffraction ring). XRD patterns from coupon 911 were recorded using a Rigaku Geigerflex powder diffractometer (equipped with a detector from Siemens). The data were collected in the range 10˚ to 110˚ in 2θ with a 0.05˚ 2θ step and an integration time of 5 s per step. The phases were analysed using EVA software

(BRUKER) 2002 edition and the database PDF2 version 2002 (volumes 1 to 52, 65, 70-89).

4.2.2.5 **3D Optical Profilometry**

3D optical profilometry is a non-destructive technique that analyses the surface topography of a specimen and generates a 3D profile. It is a useful technique for accurately measuring corrosion pit depth on steel samples. 3D optical profilometry was performed on all coupons tested at Teesside apart from 850 and 917 that were misplaced during retrieval and 911, which was the focus of all other non-destructive analyses. The BRUKER profiling machine was programmed to take a series of images within a pre-defined area of the coupon made up of 36 segments in a 6 x 6 square which was approximately 67.5mm^2 (Figure 4.3). The optical profiler then produced a surface map of this area for each coupon that was used to characterize the topography.

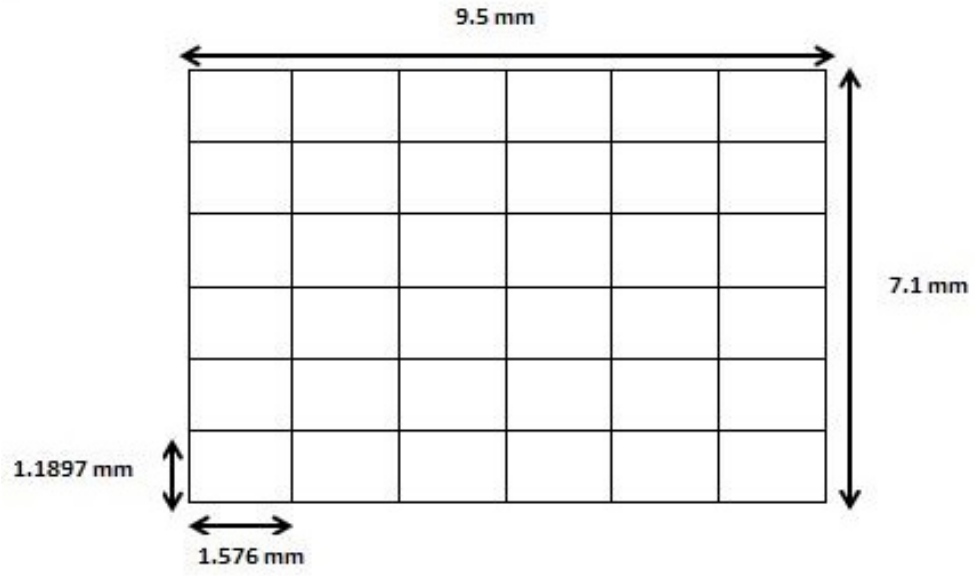

Figure 4.3: *The programmed test area on each coupon where a series of images were taken for 3D optical profiling*

4.2.3 **Summary of destructive tests**

4.2.3.1 **Polishing and Nital Chemical Etching – Microstructural Examination**

As previously mentioned, the monopiles at Teesside are constructed of S355NL structural steel, which has a ferritic-pearlitic microstructure. A microstructural examination of the Teesside coupons by polishing and chemical etching was conducted to ensure that they are comparable to the monopile steel in terms of corrosion resistance.

Etching of carbon steel enhances the microstructural features such as grain size and phase features. Chemical etching selectively attacks specific microstructural features and consists of a mixture of acids with oxidising or reducing agents. The steps involved in the polishing and preparation process for the chemical etching are outlined in Table 4.2. The images of each step can be found in Appendix A.

Table 4.2: *The polishing and preparation process for coupons prior to Nital chemical etching.*

Step	Process	Figure
1	Machine slicing into 2 segments of approximately 1.5cm (one containing the holes and the other without a hole)	Figure 7.1 and Figure 7.2
2	Embedding the 2 segments in an epoxy resin with the sliced area exposed	Figure 7.2
3 **a)** **b)** **c)** **d)**	Polishing the sliced area of both specimens using various emery papers and lubricants in the following order: • MD-Piano 220 for 50 seconds (using water as a lubricant) • MD-Largo for 8 minutes, using 9μm diamond particle solution • MD/DP-DAC for 3 minutes using 3μm diamond particle solution • MD/DP-NAP for 3 minutes using 1μm diamond particle solution	Figure 7.3 and Figure 7.4
4	Specimens are placed in an ultra-sonic cleaner to agitate the surface and remove any excess diamond product	Figure 7.5
5	Repeat step 3d)	Figure 7.6

After the slicing, embedding in resin and polishing process, the samples underwent chemical etching. Nital; a dilute mixture of ethanol and concentrated nitric acid, is the most common etchant for plain-carbon and low alloy steels and was used to expose the microstructural grains. The polished samples were immersed in 5% nital solution for 30 seconds until the etching effect was achieved and then examined under an optical microscope. Following this process, the steel samples were analysed under a microscope to observe the enhanced microstructure and compared to the S355NL micrograph in Figure 3.1.

4.2.4 **2016 Corrosion Coupon Campaign**

A second monitoring campaign commenced in August 2016 with coupons installed across 5 foundations. Following on from the 2014 campaign, improvements were made to the design of the trials and the deployment procedure, including a change in coupon steel type, number of units per string and the coupon spacing within each monopile. This latest campaign ran for 24 months but a subset of 10 coupons were removed after 12 months for analysis. These results provide valuable in-situ corrosion loss data at the atmospheric, intertidal, submerged, and mud zones for each monopile, in addition to providing validation for the results from the experimental programme.

49 coupons of the same size and material and same surface preparation as the experimental specimens [124] were deployed in 5 monopile foundations; 1A, 5A, 10B, 13B, and 22C. Within each foundation, two coupons were attached to the ladder leading to the lower working platform in the atmospheric zone (apart from 1A where only one coupon was attached to this zone). The remaining 40 coupons were attached to 10 nylon wires (4 coupons per wire). Each coupon was attached at a pre-determined location on the wire which corresponded to the depth in the monopile relative to the lower working platform (Figure 4.4). Two wires (each with 4 coupons) were attached from the lower working platform of each monopile.

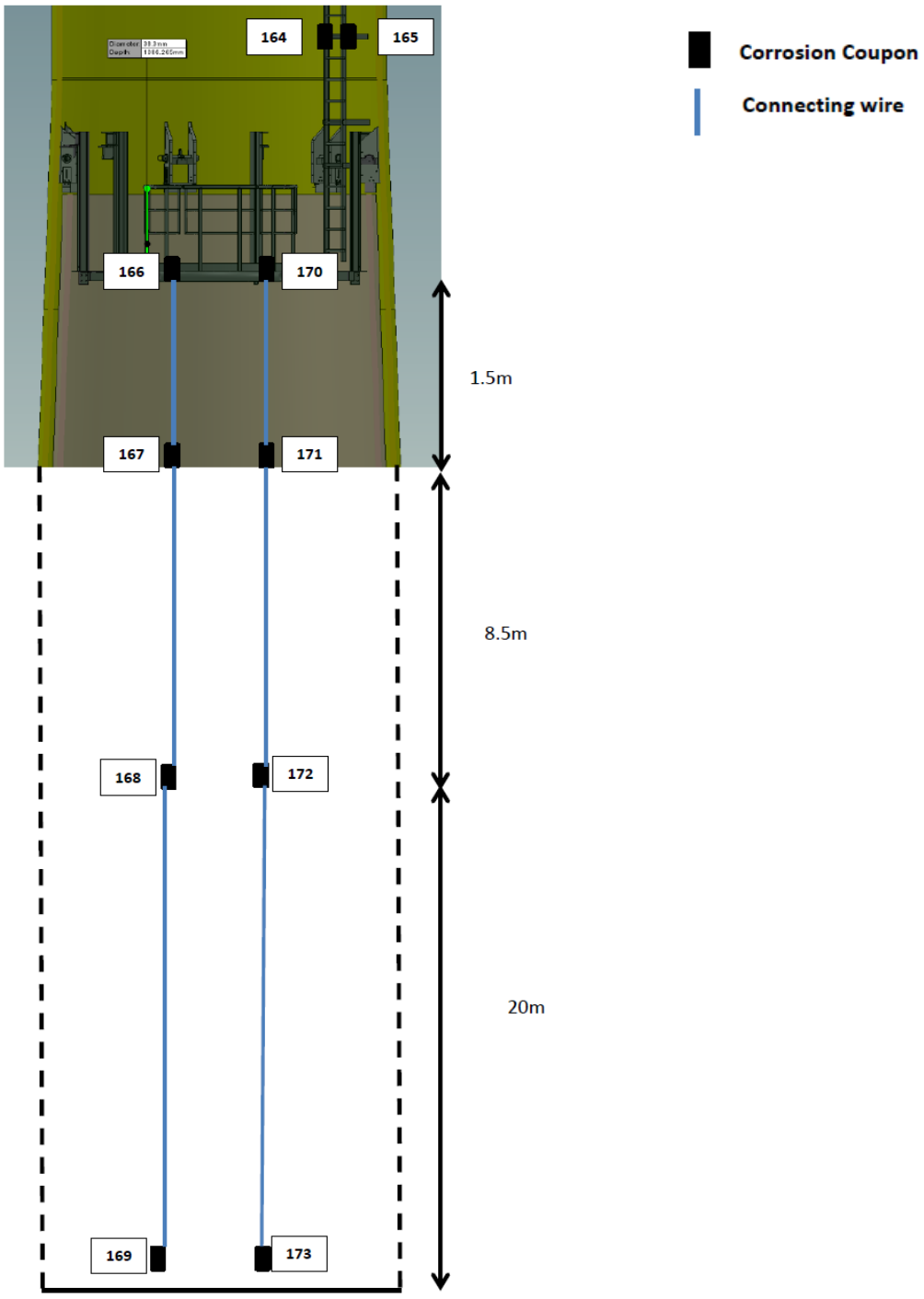

Figure 4.4 *The pre-determined locations of coupons installed within 5 foundations at Teesside. From top to bottom, the coupons are situated in the atmospheric zone, the intertidal zone (of leaking foundations), the submerged zone and the mud zone.*

4.2.4.1 **Coupon Removal**

A subset of 10 coupons were removed in September 2017 from WTG 10 and WTG 22 following a 13-month trial. Samples were taken to EDF R&D laboratories for corrosion analysis and comparison with the experimental results. In November 2017, an additional 5 coupons were removed from WTG 13 after a 15-month trial and taken for analyses. At the time of writing, the remaining 34 coupons remain in-situ within the monopile foundations at Teesside Offshore Wind Farm as part of a longer-term offshore corrosion trial.

4.3 **In-situ Coupon Results**

4.3.1 **2014 Corrosion Coupon Campaign - Results**

Upon removal from the monopile foundations, coupons were cleaned and assessed for corrosion loss. Two coupons from WTG 5A were misplaced during the retrieval process (850 and 917) and coupon 911 was left untreated for further destructive and non-destructive testing. Following the weight-loss analysis, the estimated corrosion loss and rate of corrosion for each coupon was calculated (Table 4.3).

Table 4.3: *The estimated corrosion rates of coupons retrieved from their locations within monopiles at Teesside.*

Turbine	Coupon ID	Location	Time (days)	Corrosion loss (mm)	Corrosion Rate (mm/y)
1A	915	1.2m below waterline	106	0.0097	0.0334
	916	1m above seabed	106	0.0068	0.0233
3A	908	1m below waterline	97	0.0123	0.0461
	909	Seabed	97	0.0061	0.0231
5A	849	1m below waterline	156	0.0308	0.0721
	850	Central	MISSING		
	917	0.5m above seabed	MISSING		
9A	910	1m below waterline	156	0.0088	0.0206
	911	1m above seabed	156	N/A	N/A
10B	912	Central	106	0.027	0.093
	913	Lower work platform	106	0.0321	0.1107
	914	0.1m above seabed	106	0.005	0.0173

4.3.1.1 **Scanning Electron Microscopy (SEM)**

High-resolution images of Coupon 911 surface with corrosion product were produced due to the small diameter of the primary electron beam and can be seen in Figure 4.5. The chemical composition of the corrosion product was generated by EDS.

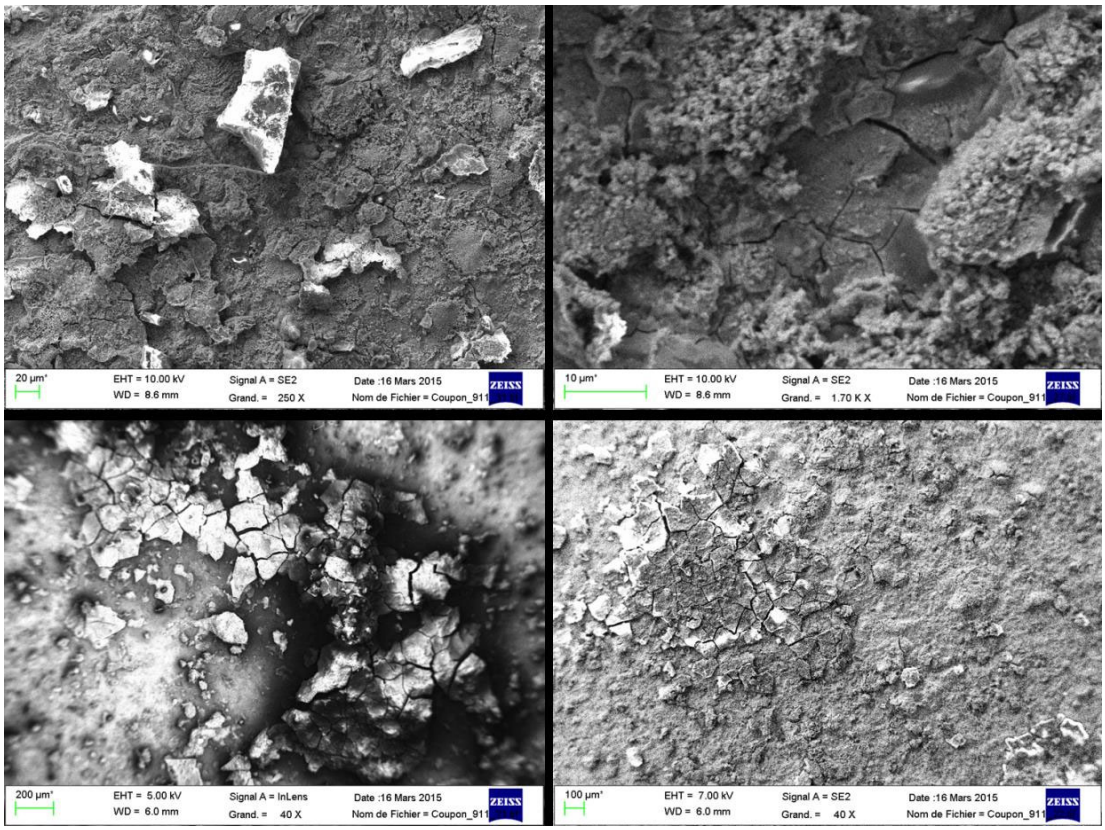

Figure 4.5: *SEM images of 4 locations (different resolutions) on the test surface of Coupon 911.*

4.3.1.2 **Energy Dispersive X-ray Spectroscopy (EDS)**

An EDS image detailing the 6 locations where X-rays were generated from the examination of coupon 911 can be seen in Figure 4.6. The EDS locations were selected on the basis that they would provide a reliable indication of the overall chemical composition of the corrosion product. Figures 4.7 to 4.10 display the spectra corresponding to the individual locations defined as “Spectre 1 to 4” in Figure 4.6. Similarly, Figure 4.11 displays another EDS scan of Coupon 911 but at a much smaller scale of 10µm. The corresponding energy spectra to the locations “Spectre 7 to 9” can be found in

Figure 4.12 to Figure 4.14. The Y-axis shows the counts (number of X-rays received and processed by the detector) and the X-axis shows the energy level of those counts. Figure 4.6 illustrates that the electron beam was not just stationary on one point but focusses on a series of spots within a scan area. The corresponding spectra generated from these spots therefore provide more localized elemental information. The chemical characterization of the specimen using EDS confirmed that iron and oxygen were the most prevalent compounds; however, sulphur and dissolved aluminium were also detected.

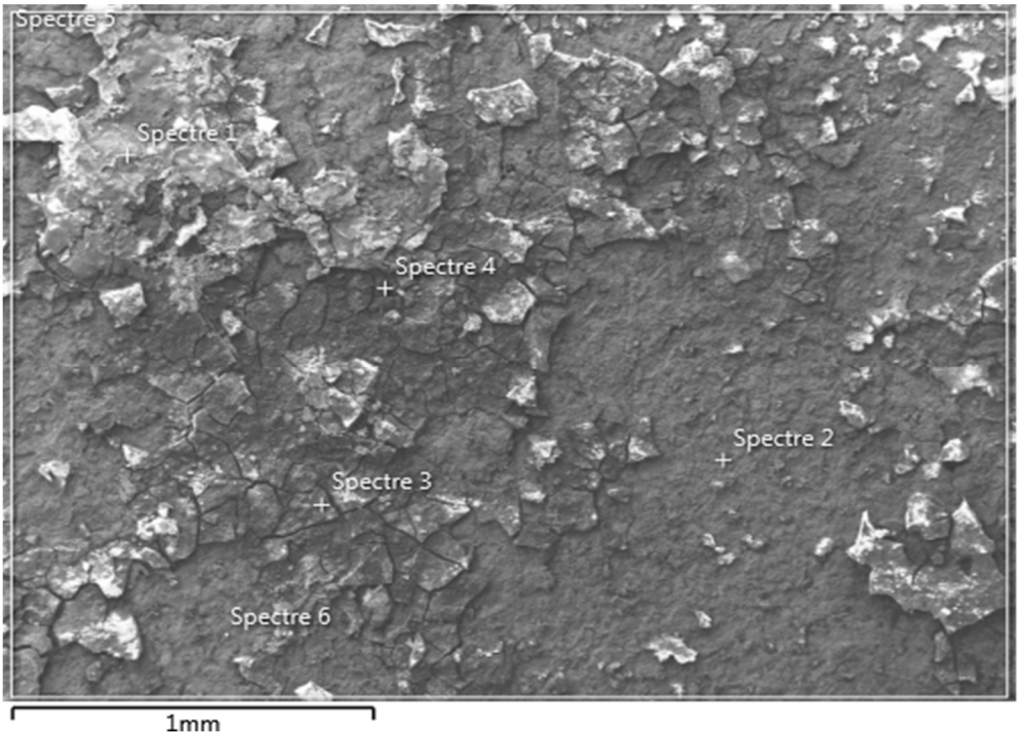

Figure 4.6: *An EDS image of Coupon 911 and the locations "Spectre 1" to "Spectre 6" where energy X-ray spectra were generated.*

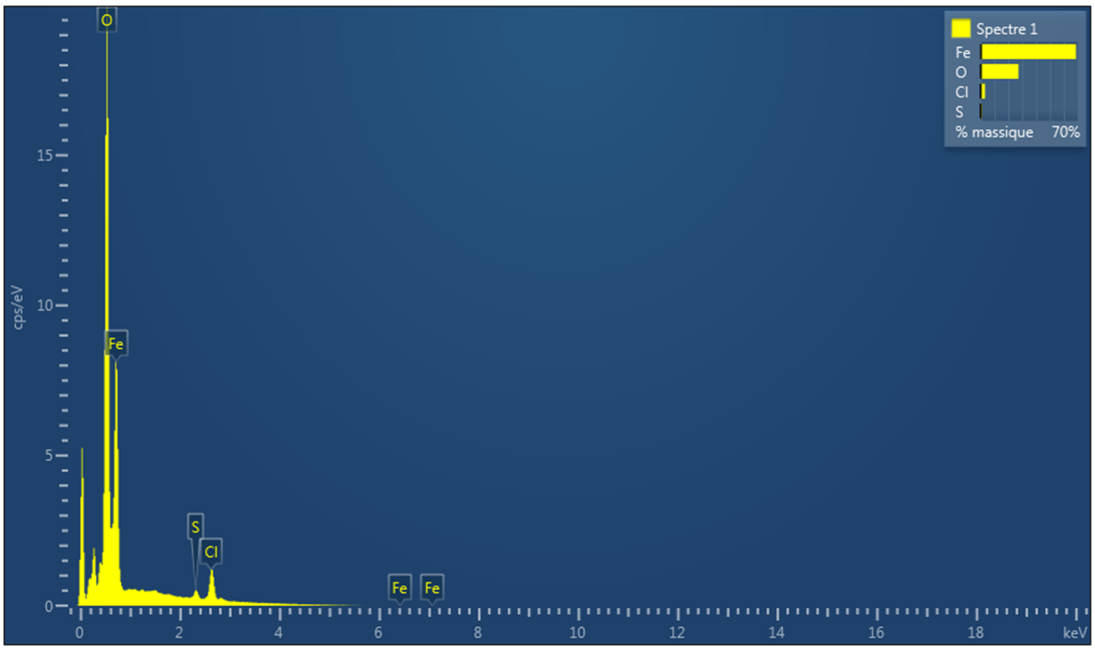

Figure 4.7: *EDS Spectra generated at the location "Spectre 1" as identified in Figure 4.6.*

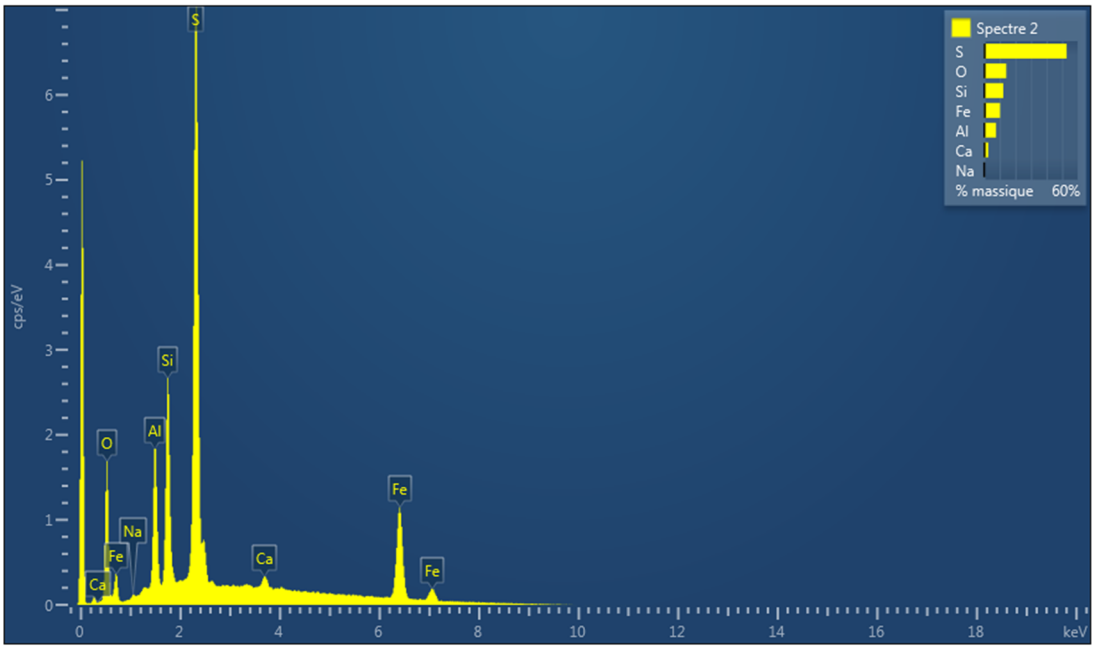

Figure 4.8: *EDS Spectra generated at the location "Spectre 2" as identified in Figure 4.6*

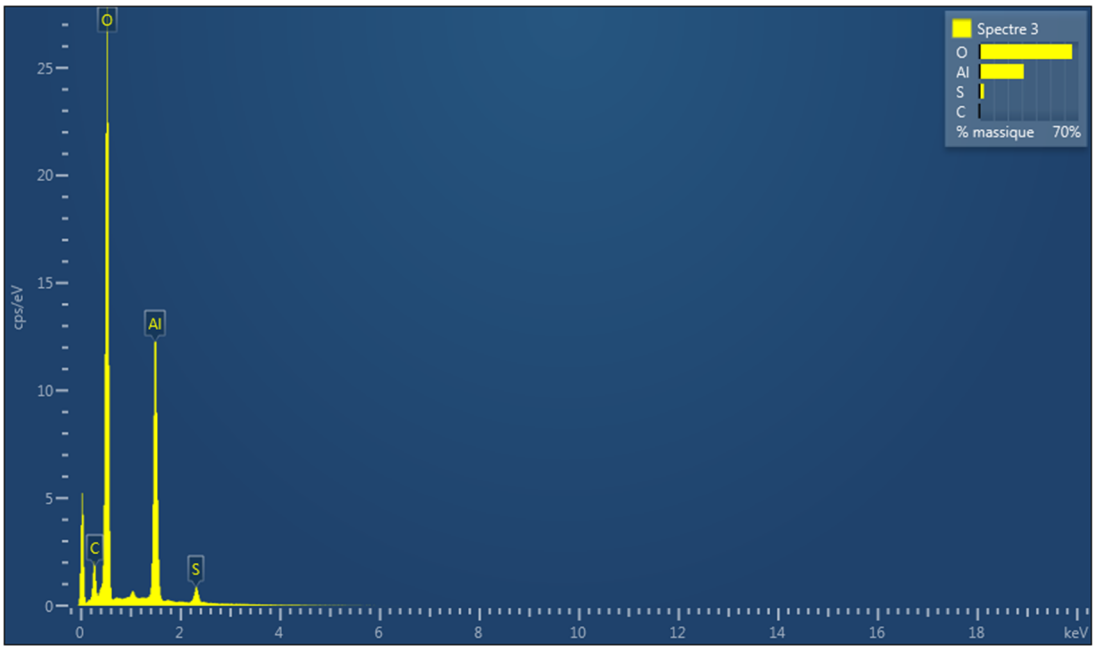

Figure 4.9: *EDS Spectra generated at the location "Spectre 3" as identified in Figure 4.6.*

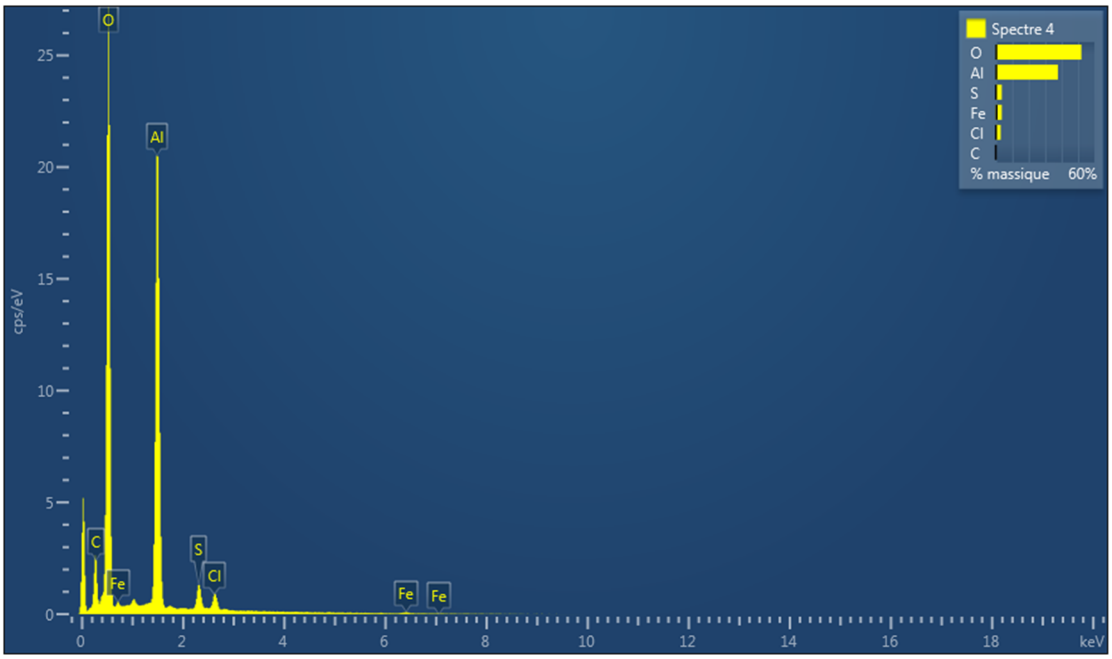

Figure 4.10: *EDS Spectra generated at the location "Spectre 4" as identified in Figure 4.6.*

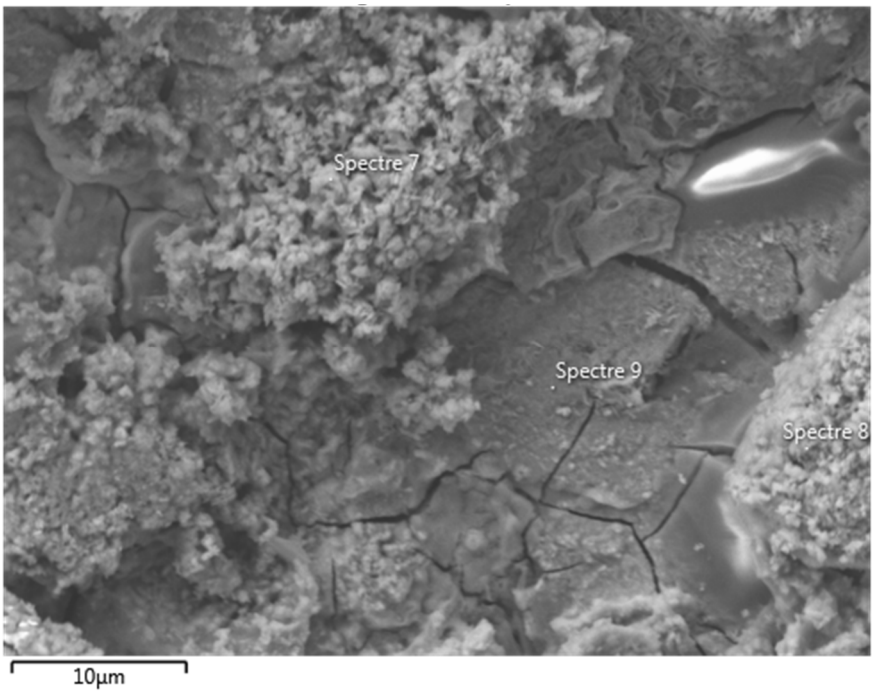

Figure 4.11: *An EDS image of Coupon 911 and the locations "Spectre 7" to "Spectre 9" where energy X-ray spectra were generated.*

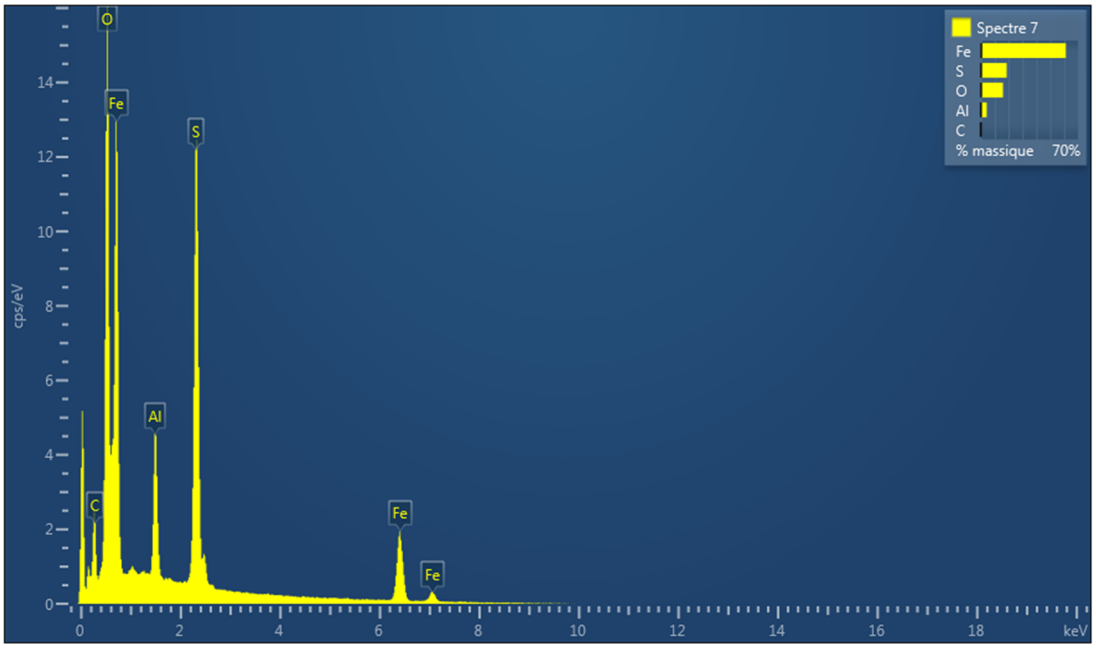

Figure 4.12: *EDS Spectra generated at the location "Spectre 7" as identified in Figure 4.11.*

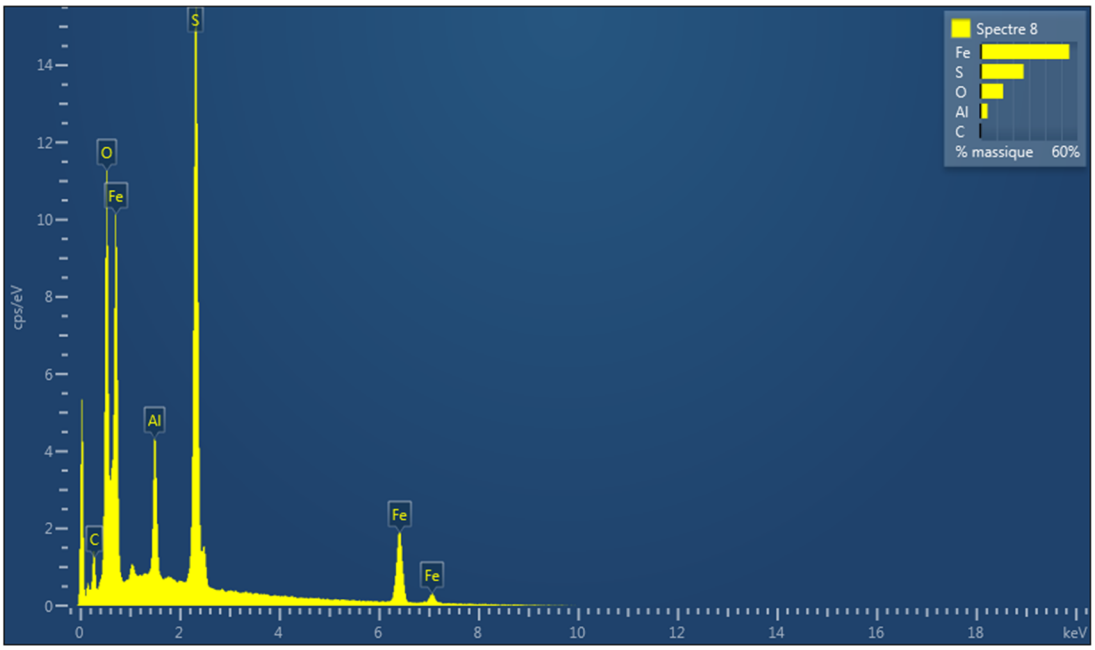

Figure 4.13: *EDS Spectra generated at the location "Spectre 8" as identified in Figure 4.11.*

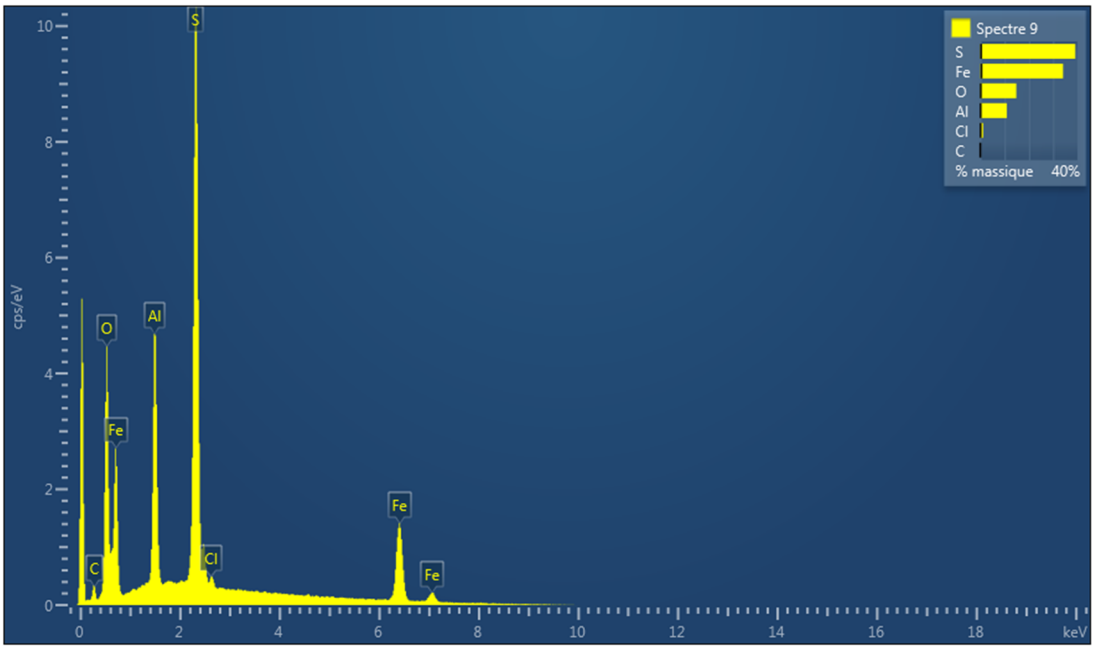

Figure 4.14: *EDS Spectra generated at the location "Spectre 9" as identified in Figure 4.11.*

4.3.1.3 **Binocular Microscopy**

Examples of the binocular images taken from coupon 911 can be seen in Figure 4.15. The yellowish/brown debris that is evident in the images suggests the presence of oxides (hematite) that have accumulated on the coupon during deployment within the monopile. Additionally, given the results of the EDS, the dark colouration corrosion product is assumed to be either magnetite or iron sulphide, or perhaps a combination of both. The mineralogical identification of the corrosion products and phases was confirmed by X-ray Diffraction.

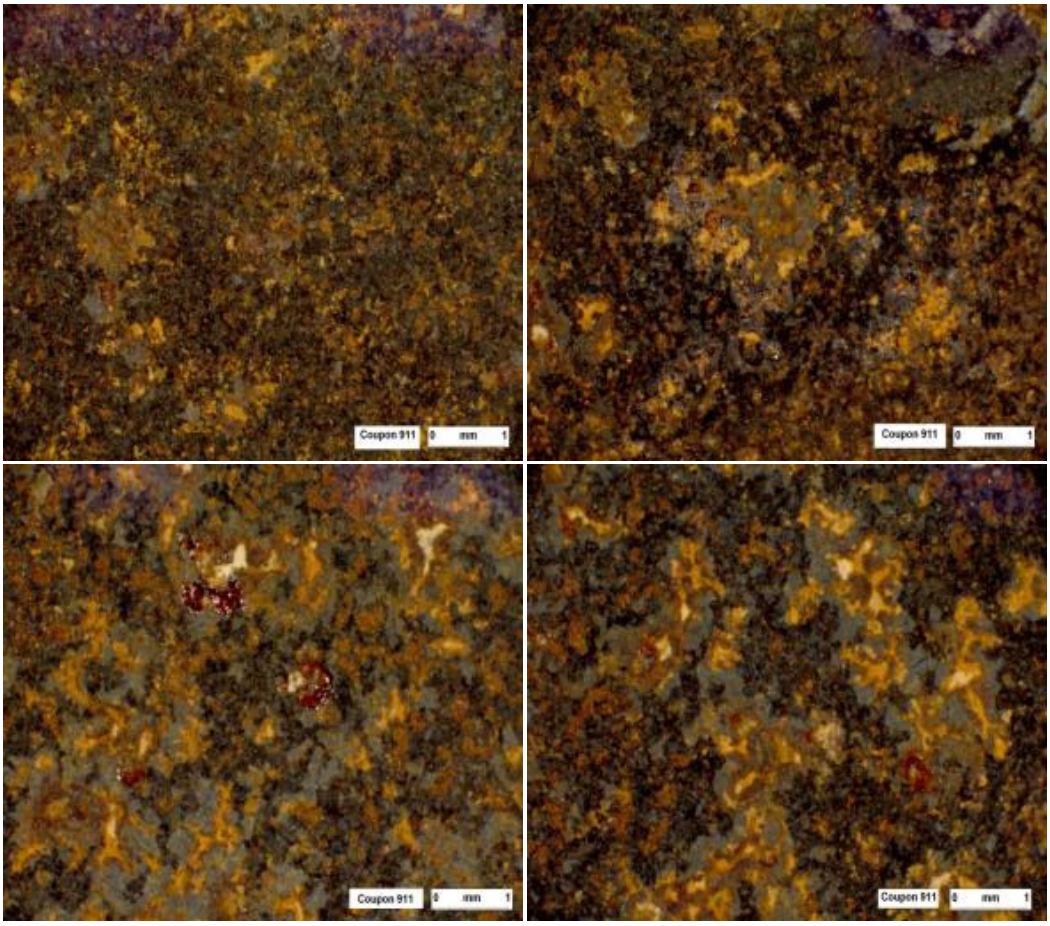

Figure 4.15: *Colour images produced by an Olympus DP 2 - Twain Binocular Microscope of the surface of Coupon 911.*

4.3.1.4 **X-ray Diffraction (XRD)**

The diffractograms displaying the detected phases are represented in Figure 4.16 to Figure 4.18. The experimental XRD data are compared to reference patterns to determine what phases are present. The reference patterns are represented by sticks and the position and intensity of the reference sticks should match the data. Figure 4.16 shows that the reference sticks accurately match the experimental data, and that 2 main phases are identified - one in red, the other in blue. The peaks at the red reference sticks corresponds to iron, and the blue reference sticks correspond to mackinawite (a form of iron sulphide).

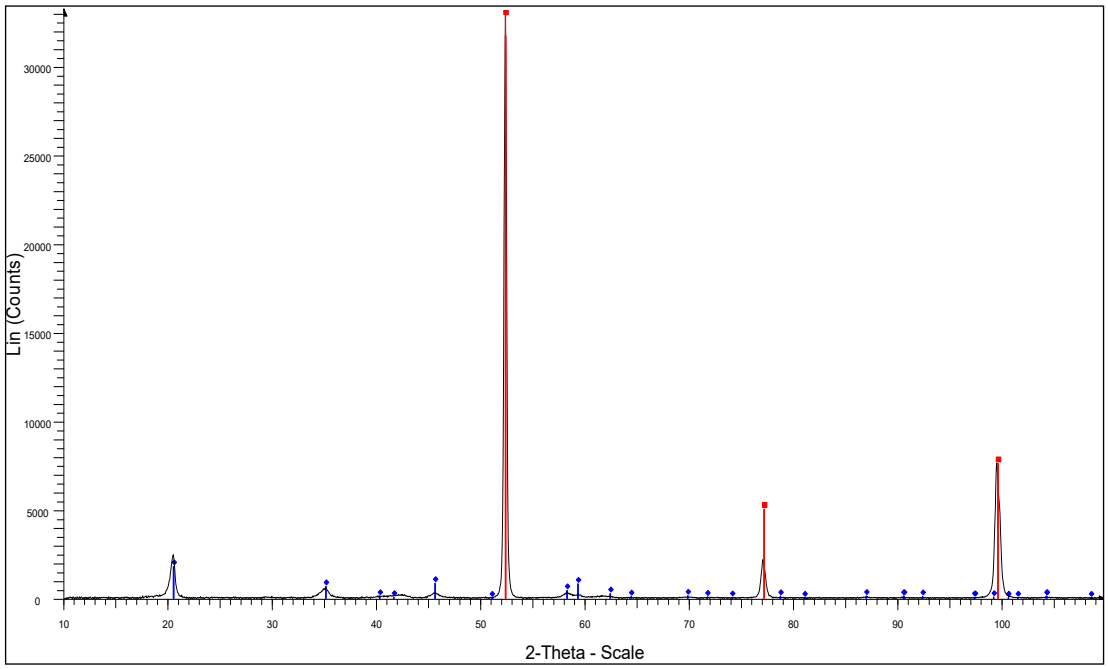

Figure 4.16: *XRD diffractogram generated from Coupon 911. Identified phases are Iron (Fe) in red and Mackinawite (FeS) in blue.*

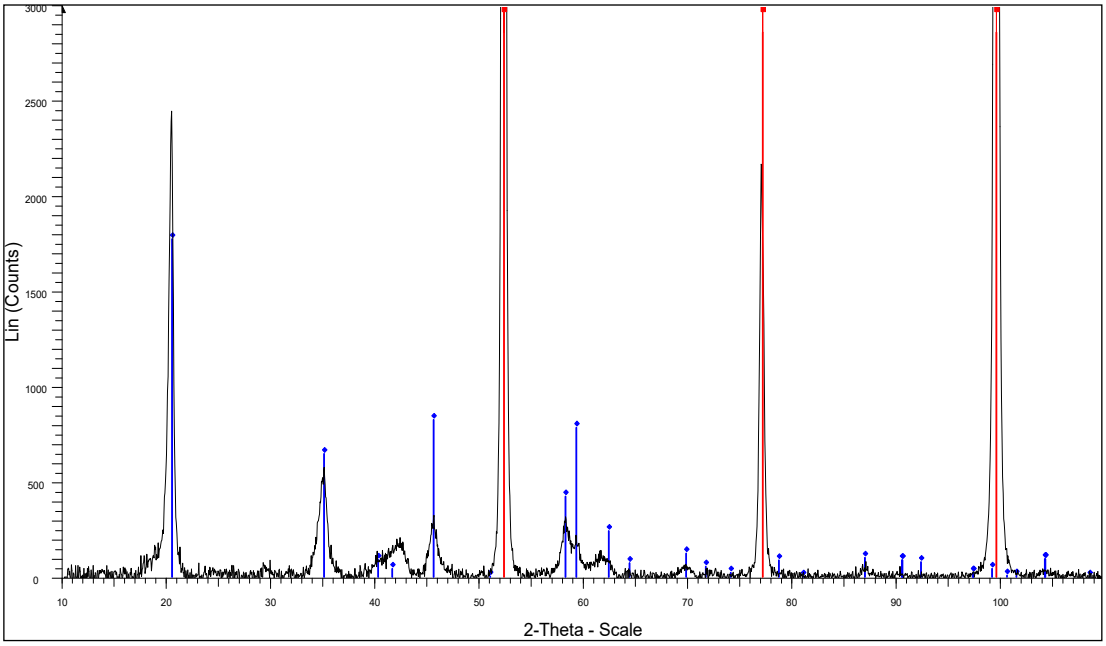

Figure 4.17: *Zoomed in Diffractogram from Figure 4.16 to better visualise the Mackinawite phase (blue).*

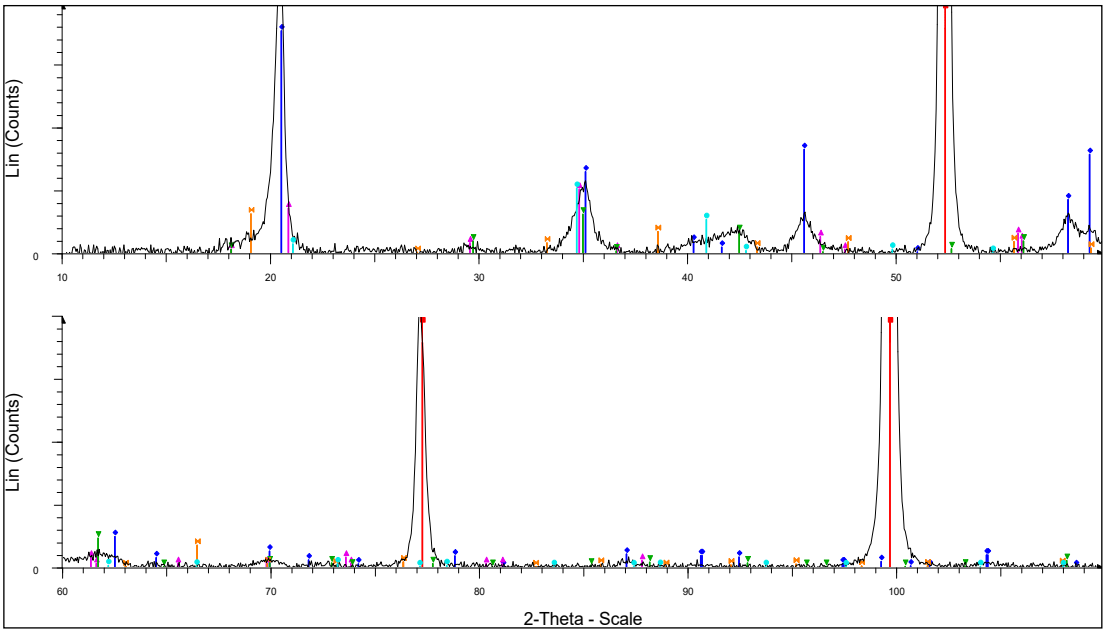

Figure 4.18: *Increased zoom to the 2θ function of the original diffractogram in Figure 4.16. More phases within the background noise are detected.*

Figure 4.17 displays a clearer representation of the main phases detected during XRD by zooming into the background noise. By zooming even further and splitting 2θ across 2 diffractograms, it can be seen that a wider range of phases are detected within the background noise, indicated by the different coloured reference patterns (Figure 4.18). However, these have much weaker signals denoted by smaller, wider peaks and therefore the presence of one or more of these extra phases on the diffraction pattern cannot be established with certainty.

4.3.1.5 **3D Optical Profilometry**

Figure 4.19 and Figure 4.20 display the 3D profiles created from the 2 coupons that had the largest pits detected; 849 and 912. Figure 4.19 illustrates the surface profile of Coupon 849 (WTG 5A) that has a maximum pit depth of -22.8μm and pit width of 110.9μm which was the widest pit detected out of all the coupons. Coupon 912 had the deepest pit of -32.64μm detected by the profiler (Figure 4.20). It can be seen from the 3D profile that despite being cleaned of any corrosion product once retrieved from the foundation, some debris on the surface of Coupon 849 exists; up to +8.48μm and is represented by red-pink colourations.

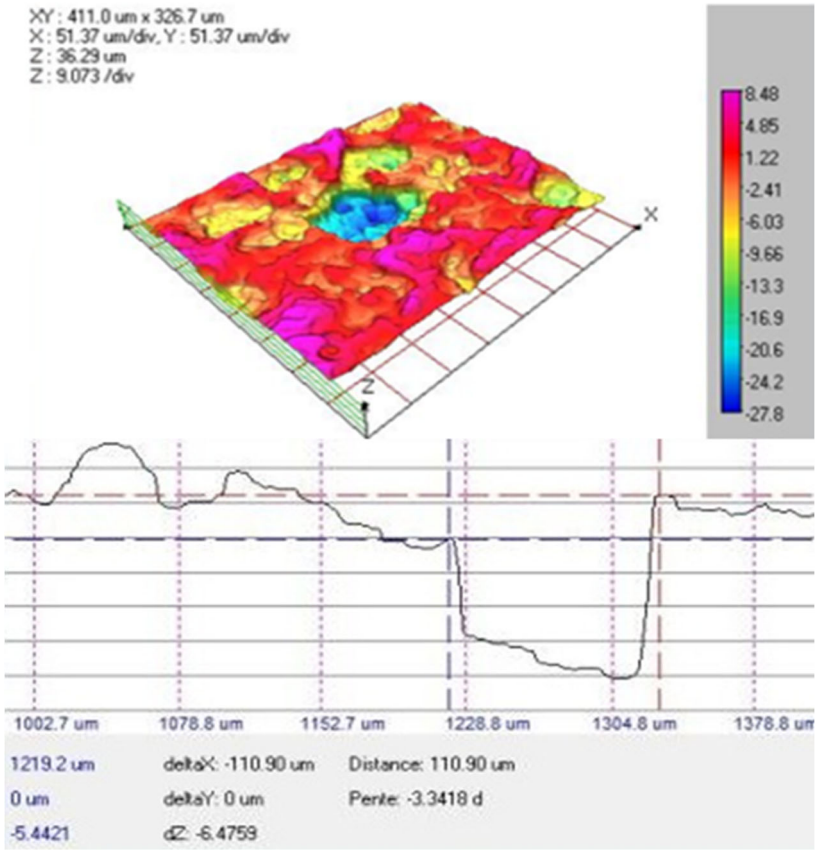

Figure 4.19: *The 3D profile of a 67.5mm² area on Coupon 849; showing pit depth (top) and maximum pit width (bottom). Coupon 849 was located 1m below sea level within WTG 5A for 156 days.*

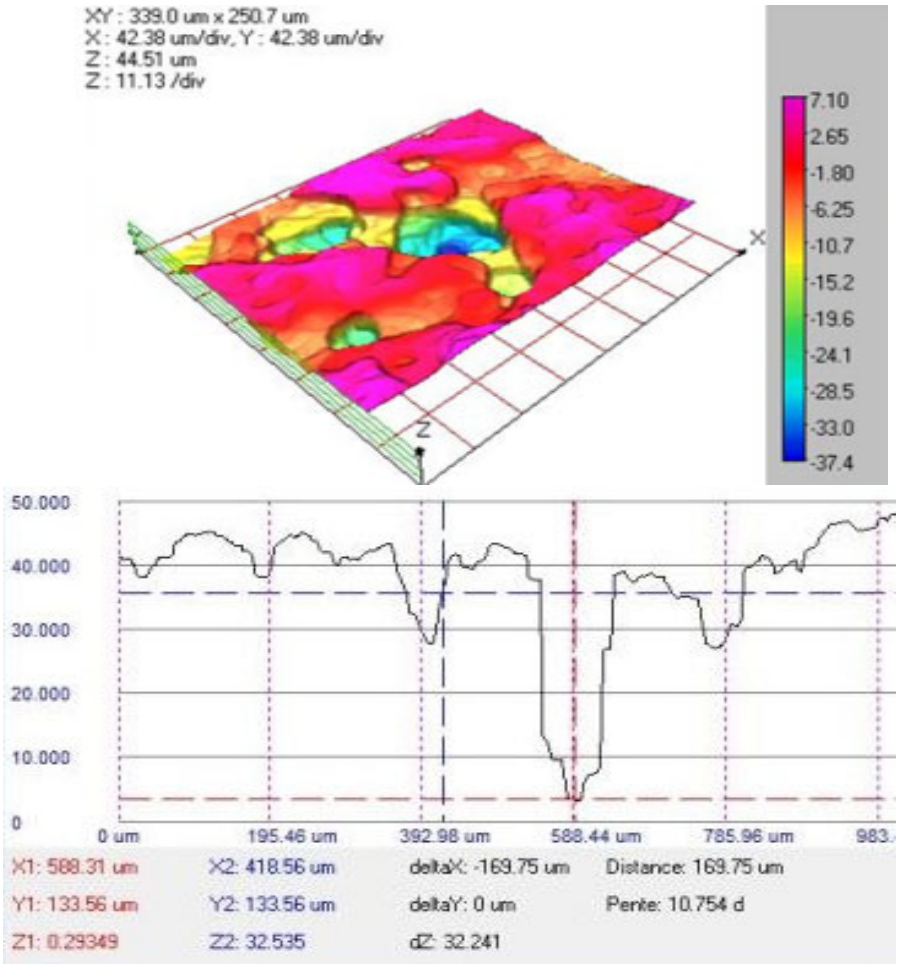

Figure 4.20: *The 3D profile of a 67.5mm² area on Coupon 912; showing pit depth (top) and maximum pit width (bottom). Coupon 912 was located centrally (approximately 20m above seabed) within WTG 10B for 106 days.*

4.3.1.6 **Nital Chemical Etching**

Figure 4.21 and Figure 4.22 display the microstructures of the sliced segments of coupon 913 (2014 Coupon Campaign); one containing the hole and the other without a hole, respectively. The most striking observation of both microstructures is that there appears to be only 1 phase present. However, the assumption was that there would be 2 phases representing the ferritic-pearlitic structure, as shown in Figure 3.1. These results suggest that the corrosion

coupons used to represent the monopile foundations at Teesside were made from a milder steel to that of the monopile that is lower in carbon. The microstructures of the coupon 913 samples appear to be entirely ferritic when compared to a microstructural image of ferrite [138] in Figure 4.23.

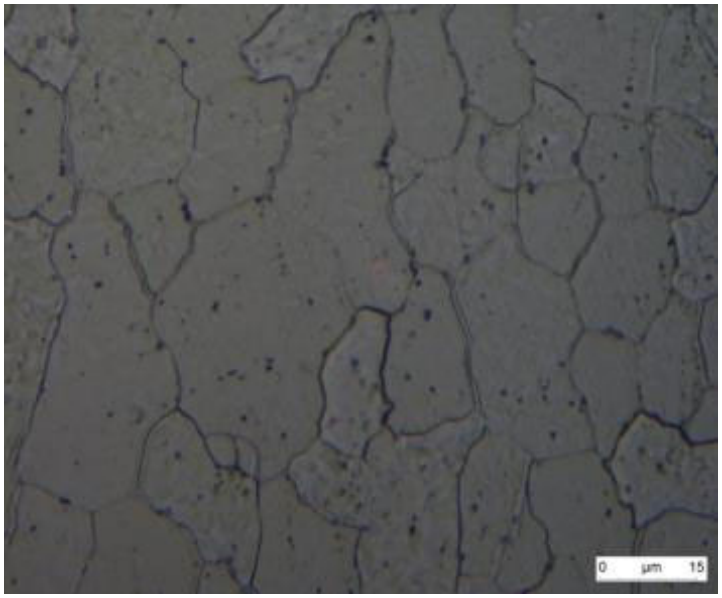

Figure 4.21: *The microstructure of sliced and polished segment of Coupon 913 (with the hole) magnified x1000.*

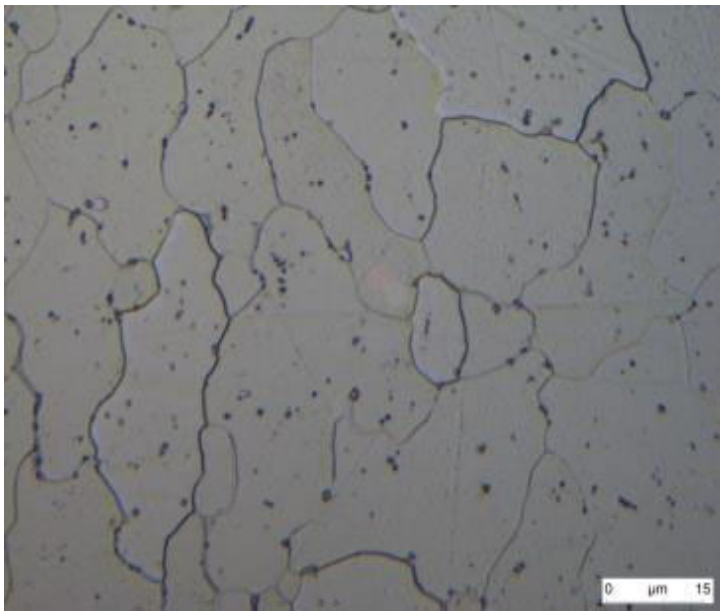

Figure 4.22: *The microstructure of sliced and polished segment of Coupon 913 (without the hole) magnified x1000*

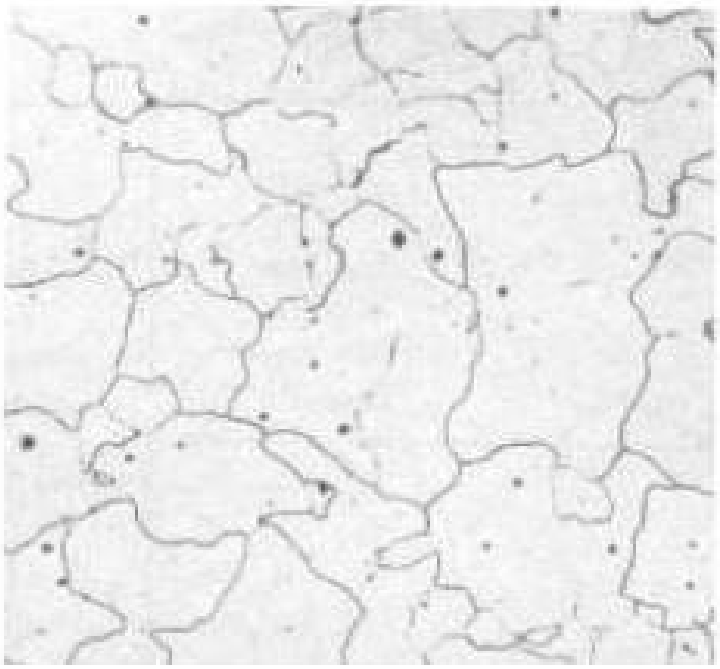

Figure 4.23: *The microstructure of ferrite taken from* [138]

4.3.2 **2016 Corrosion Coupon Campaign – Results**

The 15 coupons removed from the Teesside monopiles were taken to EDF R&D laboratory for analysis. The sample number and in-situ trial location can be seen in Figure 4.24. The appearance of the extracted coupons from WTG 10, 22 and 13 can be found in Figure 4.25, Figure 4.26 and Figure 4.27; respectively. Coupons were cleaned and de-scaled using the same process described in section 3.2.4 and in accordance with ASTM Standard Practice G1-03 [134].

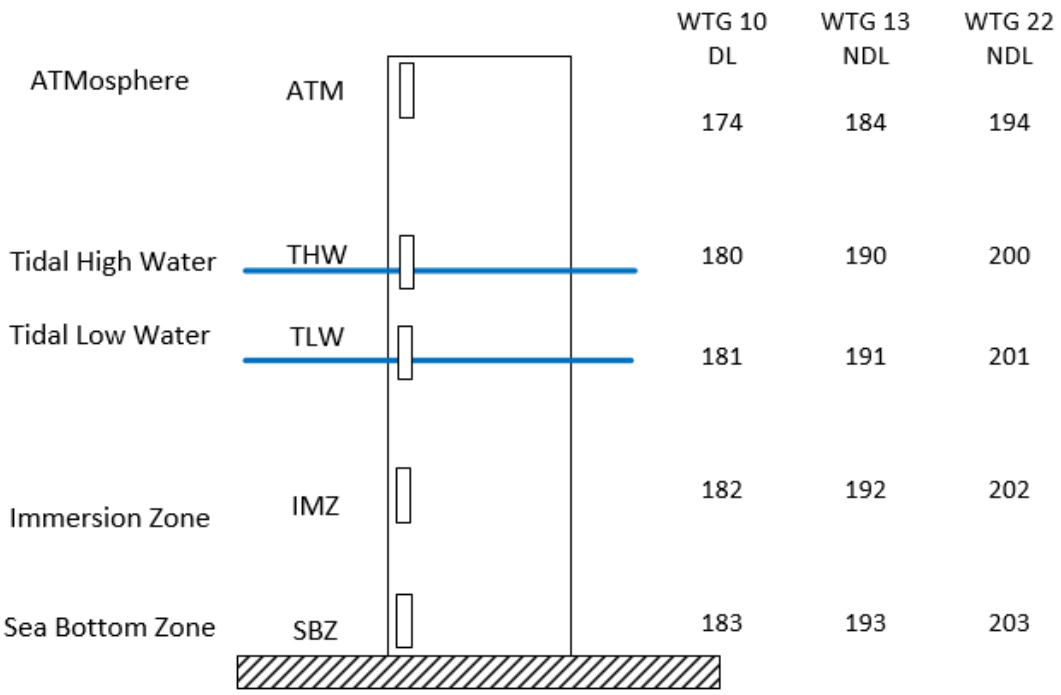

Figure 4.24: *Test locations within the monopile foundations; Atmospheric, Tidal High Water, Tidal Low Water, Immersion Zone and Sea Bottom Zone).*

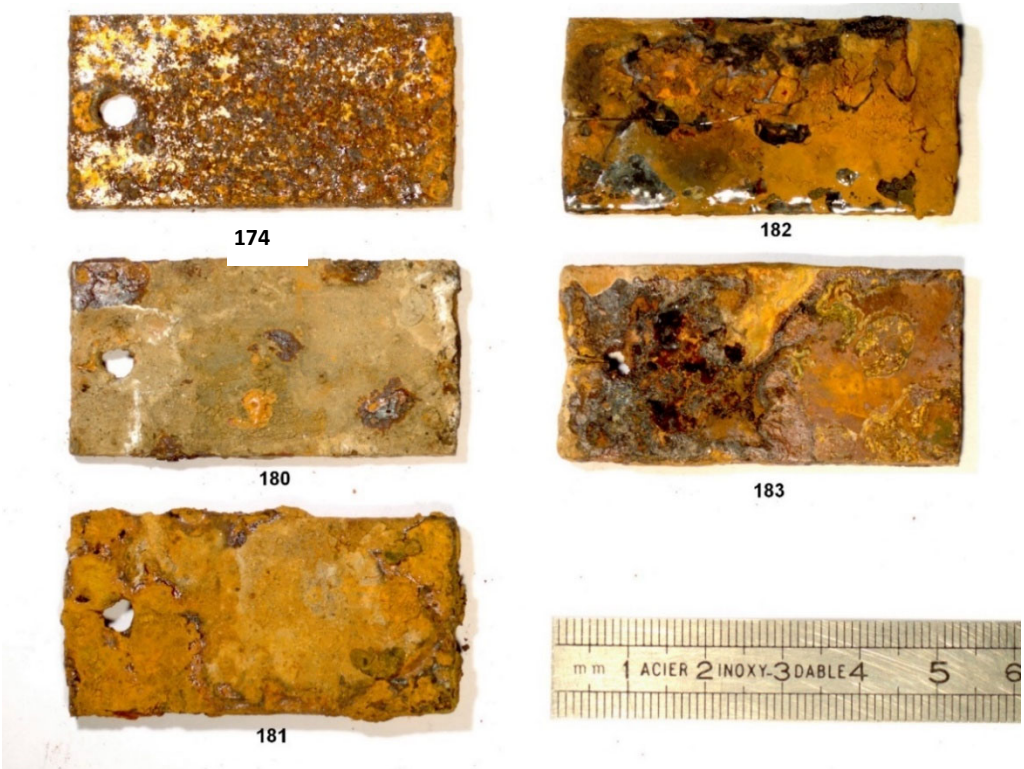

Figure 4.25: *WTG 10 Coupons following a 12-month internal monopile corrosion trial at Teesside.*

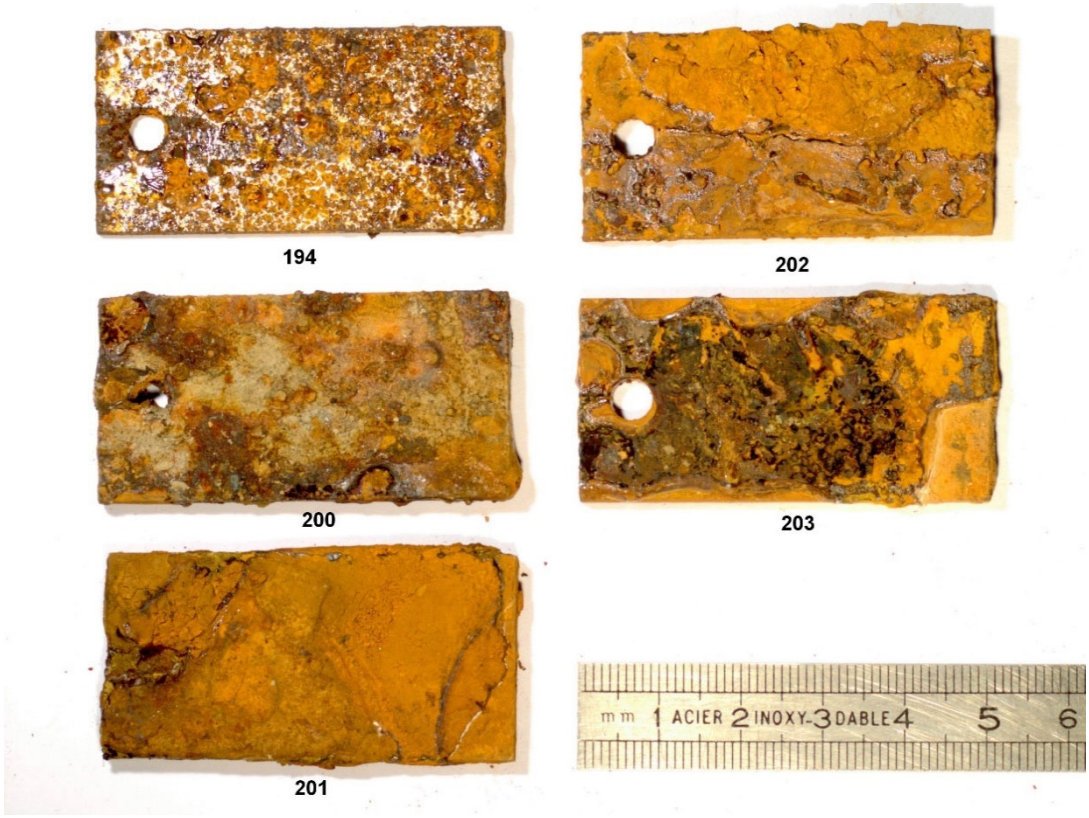

Figure 4.26: *WTG 22 Coupons following a 12-month internal monopile trial at Teesside.*

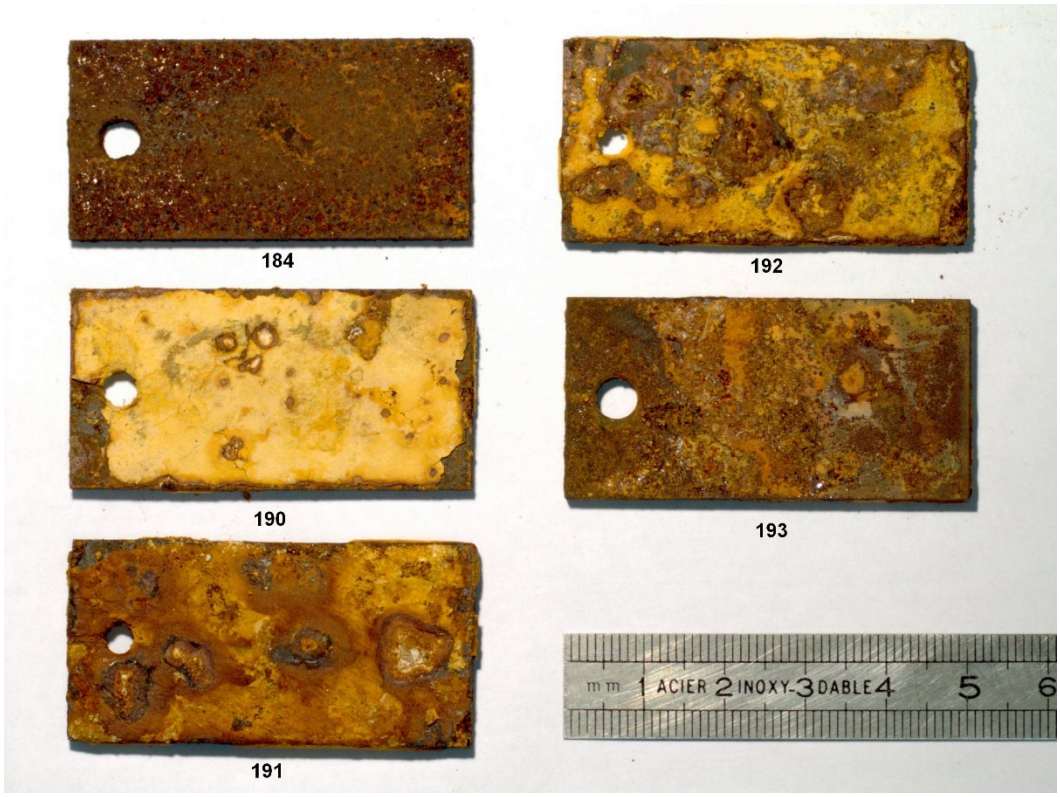

Figure 4.27: *WTG 13 Coupons following a 14-month internal monopile trial at Teesside*

Table 4.4 displays the corrosion rates obtained from the coupons extracted from the Teesside monopiles. Those that were considered to be high (0.1mm/y) are highlighted in red. For context, the corrosion rates have been inserted into the schematic of the sample locations to indicate the rate of degradation at each zone (Figure 4.28).

Following the process in section 4.2.2.3, the surface patterns of a subset of coupons were analysed using binocular microscopy. Figure 4.30 shows the microscope images of coupons 174, 182, 200, 201, 191 and 192 and the variety of surface detail across each sample.

Table 4.4: *The corrosion data obtained from the coupons extracted from WTG 10, WTG 22 and WTG 13. Locations correspond to the diagram in Figure 4.24.*

Turbine	Coupon	Location	Time (months)	Corrosion Loss (mm)	Corrosion Rate (mm/y)
10B	174	ATM	13.1	0.0282	0.0257
	180	TLW	13.1	0.0422	0.0384
	181	THW	13.1	0.1187	0.1081
	182	IMZ	13.1	0.1540	0.1402
	183	SBZ	13.1	0.1174	0.1069
22C	194	ATM	13.1	0.0376	0.0342
	200	TLW	13.1	0.1003	0.0913
	201	THW	13.1	0.0693	0.0631
	202	IMZ	13.1	0.1313	0.1195
	203	SBZ	13.1	0.0327	0.0298
13B	184	ATM	15	0.03163	0.02567
	190	TLW	15	0.07383	0.05991
	191	THW	15	0.11446	0.09288
	192	IMZ	15	0.07644	0.06204
	193	SBZ	15	0.02604	0.02113

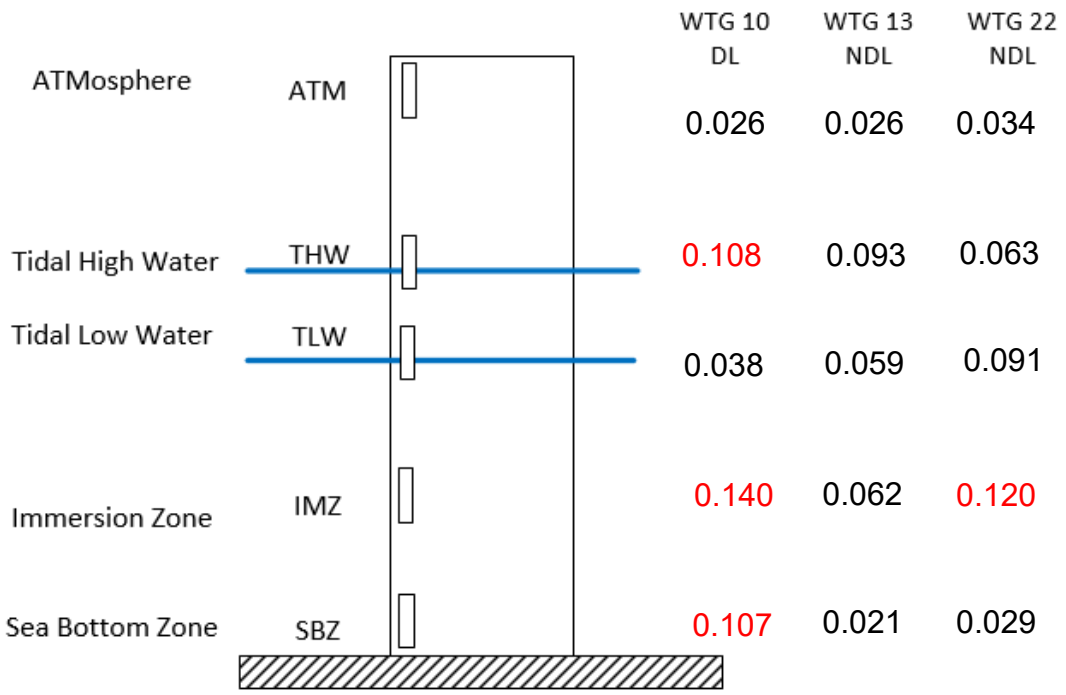

Figure 4.28: *The coupon location and corresponding corrosion rate of the sample at each zone (in mm/y).*

Following the same process described in section 4.2.2.4, XRD was performed on the oxide layers of a subset of coupons representing a range of locations from within the monopile and also those that exhibited relatively high corrosion rates:

- WTG 10 Coupon 182
- WTG 22 Coupon 202
- WTG 13 Coupons 184, 190, 192

XRD data was collected in the range 10˚ to 95˚ in 2θ with a 0.05˚ 2θ step and an integration time of 5 s per step. The phases were analysed using EVA software (BRUKER) 2002 edition and the database PDF2 version 2002 (volumes 1 to 52, 65, 70-89).

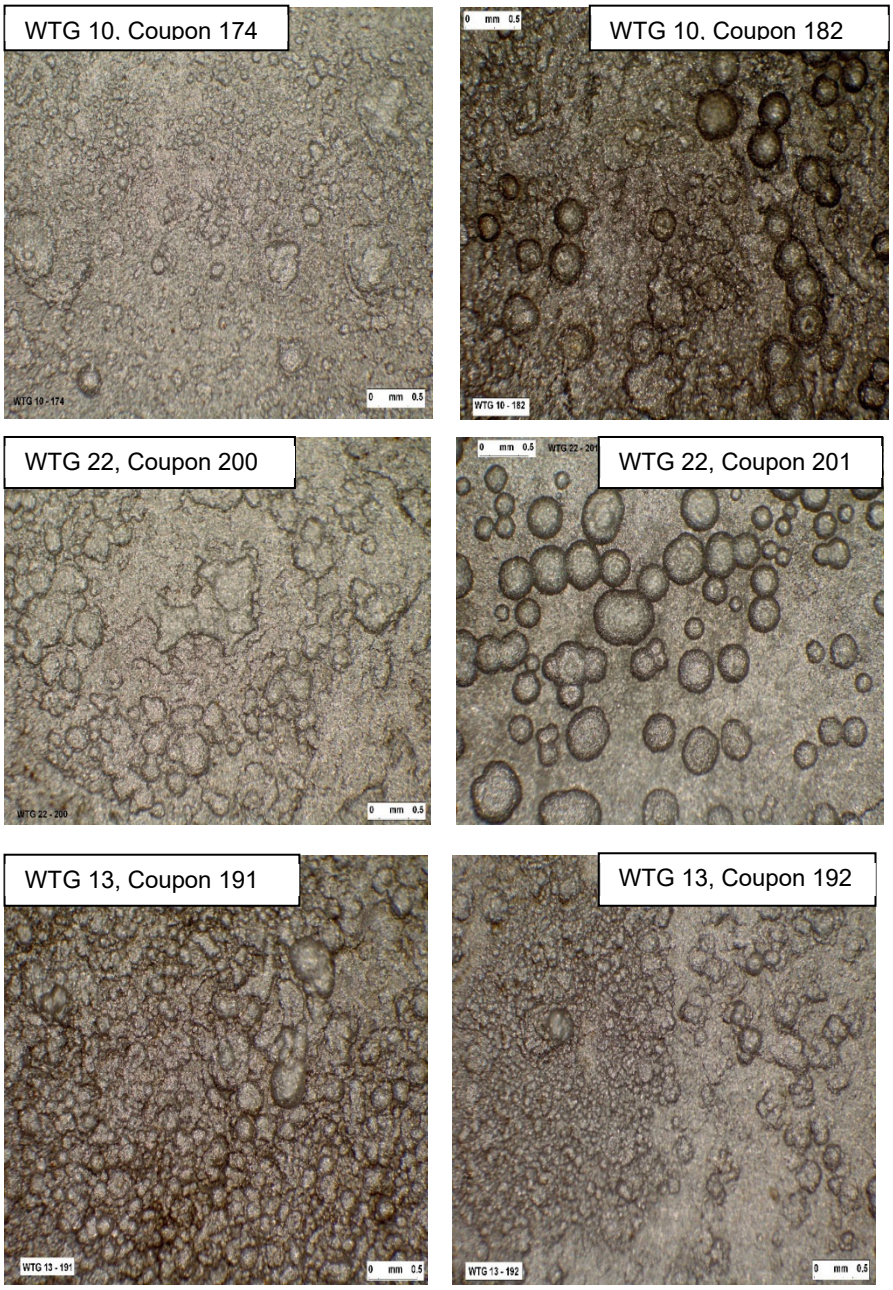

Figure 4.29: *Binocular microscopy images of 6 coupons extracted from Teesside monopiles, following cleaning and descaling (magnified x40).*

The results of the XRD demonstrated a low intensity of the diffraction peaks with respect to the background noise indicating a low crystallinity of the analysed phases. These have much weaker signals denoted by smaller, wider peaks and

therefore the presence of one or more of these extra phases on the diffraction pattern cannot be established with certainty. XRD results can be found in Figure 4.31 to Figure 4.35.

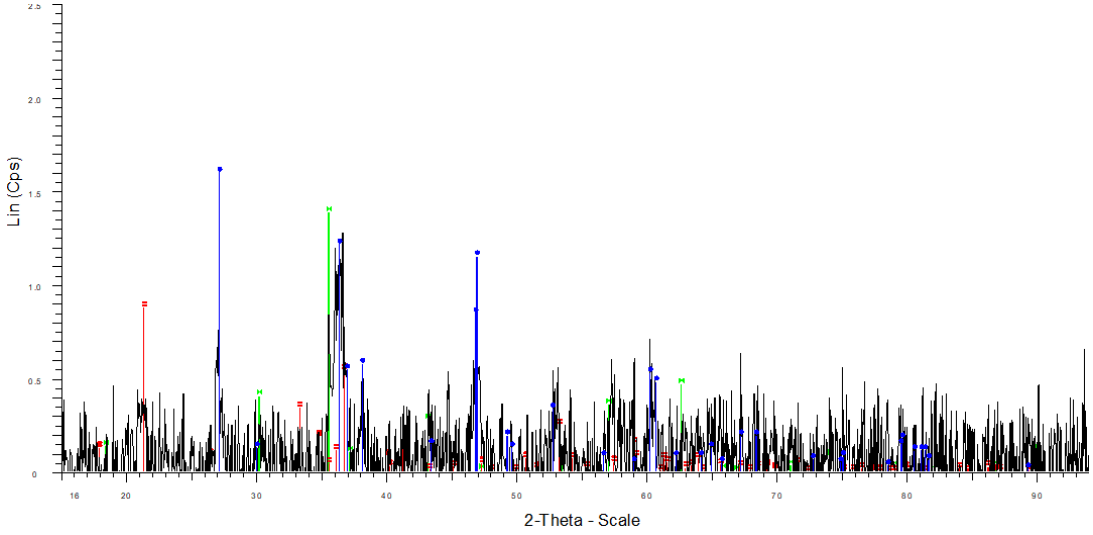

Figure 4.31: *XRD diffractogram generated from the oxide layer on Coupon 184 from WTG 13. Phases identified are lepidocrocide (blue); magnetite (green); goethite (red).*

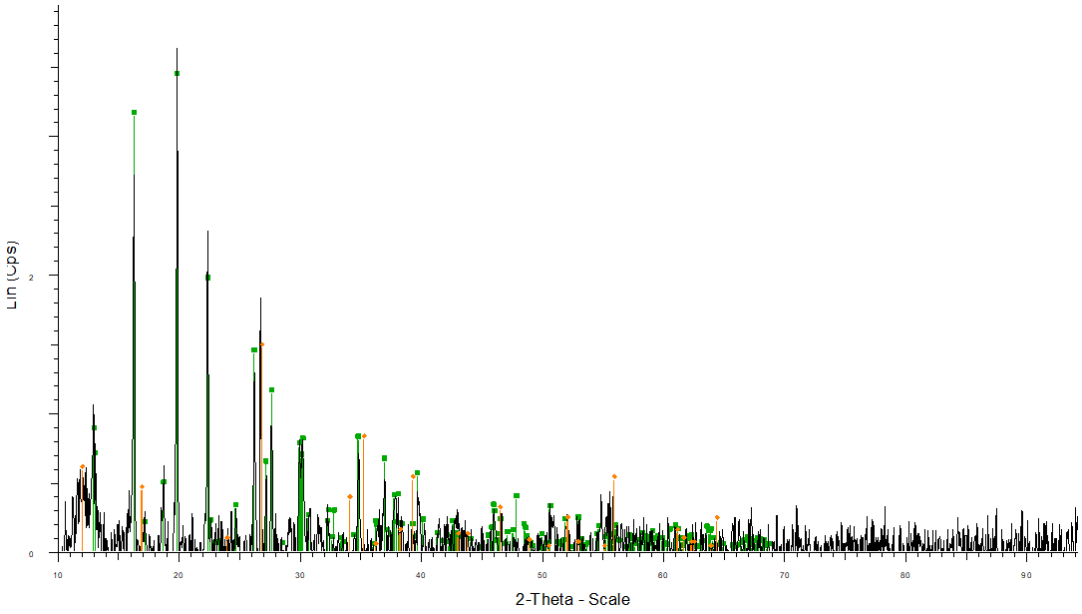

Figure 4.32: *XRD diffractogram generated from the oxide layer on Coupon 190 from WTG 13. Phases identified are rozenite (green) and akaganeite (red).*

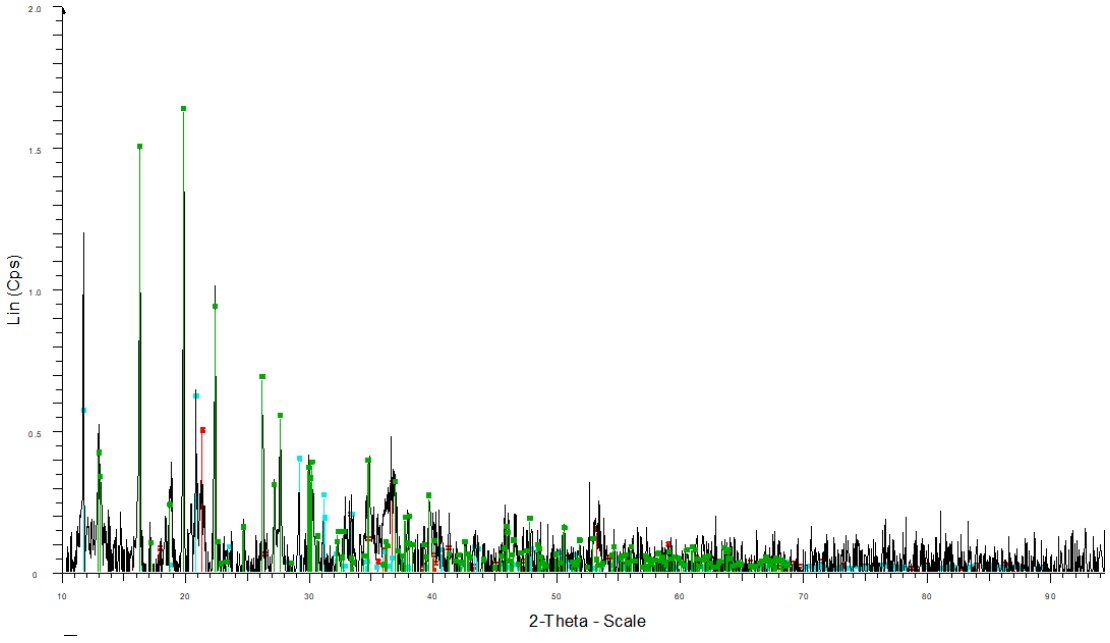

Figure 4.33: *XRD diffractogram of the oxide layer on Coupon 192 from WTG 13. Phases identified are rozenite (green); goethite (red) and gypsum (turquoise).*

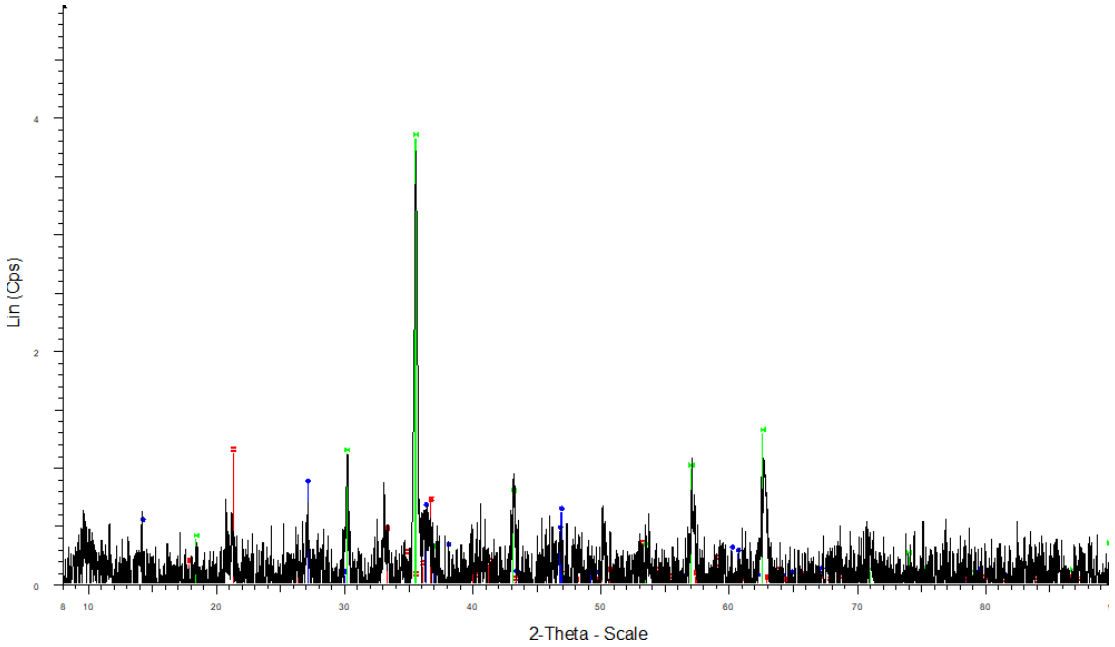

Figure 4.34: *XRD diffractogram generated from the oxide layer Coupon 182 from WTG 10. Phases identified are magnetite (green), lepidocrocite (blue) and goethite (red).*

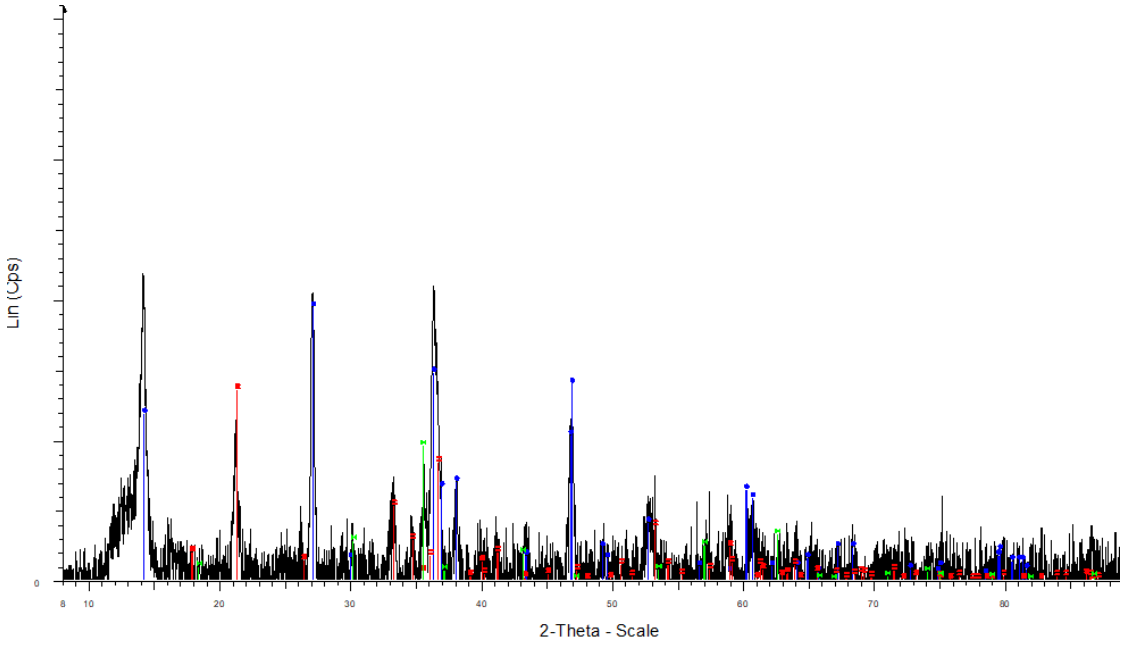

Figure 4.35 *XRD diffractogram generated from the oxide later on Coupon 202 from WTG 22. Phases identified are lepidocrocide (blue); goethite (red) and magnetite (green).*

4.4 **Discussion**

In the analysis of the 2014 corrosion coupons, chemical characterization of the surface of Coupon 911 detected iron and oxide as the primary compounds (as seen in section 4.3.1.2). This is to be expected since iron oxide is the primary corrosion product of iron and can occur in different forms, i.e. Black Fe3O4 (magnetite), and red/brown Fe2O3 (hematite). The EDS scan in Figure 4.6 displays the locations of the 4 spectra in Figure 4.7 to Figure 4.10.

It can be seen in Figure 4.6 that Spectre 1, 3 and 4 are all located on a similar type of “flakey” surface whereas Spectre 2 is located on a darker solid looking

surface. Therefore, an interesting comparison can be made between the energy spectra generated from these locations. Figure 4.7, Figure 4.9 and

show high levels of oxides are present at locations 1, 3 and 4 (most likely occurring as iron oxide), whereas at location 2 there are high levels of sulphide. Therefore, it assumed that the “flakey” surface is an iron oxide corrosion product - rust; whereas the surface with a darker colouration is most likely iron sulphide. This is supported by the energy spectra generated for the specified locations in Figure 4.11. In particular, the chemical characterization of location “Spectre 9” which is shown in Figure 4.14 detects the prevalence of sulphides. Similarly to location “Spectre 2”, “Spectre 9” is a solid surface with a much darker colouration than the other locations where oxides tend to dominate.

The presence of iron sulphides are characteristic products of bacterial induced corrosion, in particular that of Sulphate Reducing Bacteria (SRB). SRB are facultative anaerobes that utilize sulphate as a terminal electron acceptor during energy generation, producing sulphide as a by-product in the following cathodic reaction [139]:

$$SO_4{}^{2-} + 9H^+ + 8e^- \longrightarrow HS^- + 4H_2O$$

The Hydrosulphide ion HS^- produced by the reduction of sulphate ions interacts with ferrous iron produced in the typical anodic reaction:

$$Fe + 2H_2O \longrightarrow Fe(OH)_2 + 2e^- + 2H^+$$

As a result of this interaction FeS is produced rather than $Fe(OH)_2$, which is generally visible by a black encrustation around the steel .

The corrosiveness of SRB is often attributed to their formation of Hydrogen Sulphide gas (H_2S) which is a powerful anodic and cathodic reactant. It is known to react rapidly with metallic iron in the following reaction:

$$H_2S + Fe \rightarrow FeS + H_2$$

Thereby forming the characteristic corrosion product iron sulphide [54]. Therefore, the detection of sulphides on the coupon strongly suggests microbiological activity within the monopiles at Teesside; certainly, within monopile 9A near the seabed.

Another interesting result from the EDS was the detection of aluminium in Spectre 2, 3 and 4 (Figure 4.8; Figure 4.9 and

, respectively). It was not initially anticipated that aluminium would be detected within the corrosion product. However, the presence of aluminium is likely due to the aluminium alloy anodes present within the MPs that may be dissolving into the internal seawater as they cathodically protect the internal steel. The dissolution of aluminium may serve as an indication that the sacrificial anodes are working effectively to protect the surrounding steel. Nevertheless, the condition of the anodes should be checked to ensure that they are not over-working.

XRD of Coupon 911 detected the presence of mackinawite as one of the primary phases. Mackinawite is an iron nickel sulphide mineral known to occur in reducing environments such as marine sediments as a result of the metabolism of iron and SRB. In fact, studies have shown that the mackinawite is the initial sulphide film that forms on iron in the presence of SRB [140], even following only 1 month of exposure[141]. In longer periods of exposure (up to a year), mackinawite has been found to convert to pyrrhotite which is much more rich in sulphur and indicates a higher reduced state of iron [141]. However, the transformation between sulphide species depends on pH, temperature, redox potential and the relative concentrations of reactants. It has been observed that the presence of iron sulphides in an adherent thin film can be protective. Nevertheless, the inherent instability of iron sulphides can give rise to corrosion cells between the iron sulphide in direct electrical contact with the underlying steel (cathode) and the exposed steel surface (anode) [141].

Studies have found that corrosion kinetics are enhanced on carbon steel coupons due to the formation of a porous, conductive mackinawite film in the presence of SRB [142]. Enhanced corrosion is also believed to occur as a result of the direct consumption of electrons from the steel surface by SRB via their electron transport pathways. However, it is evident from Figure 4.16 and Figure 4.17 that the counts of the mackinawite phase are an order of magnitude lower than that of iron and therefore it is presumed that the iron sulphide film is very thin and still within the initial stages of formation. If the coupon had been exposed to the same conditions for a further 6-months, it is possible that this film would become more

saturated with sulphides and occur and transform into pyrrhotite or similar. This is reflected in a recent study by [143] in which mackinawite was the initial corrosion product on steel coupons contained in an environment containing SRB. As more sulphide was produced by SRB, the mackinawite was transformed to sulphur-rich corrosion products pyrrhotite and pyrite. Nevertheless this study concluded that this microbiological induced corrosion (MIC) causing a gradual accumulation of iron sulphide on the steel surface provided a form of passivity which decreases corrosion rate [143].

In the initial corrosion monitoring report prepared by an external subcontractor, it was noted that there was no pitting corrosion visible on all but one of the corrosion coupons. Contrary to this opinion, 3D optical profiling conducted at Les Renardières detected a large number of pits on all the coupons, with the lowest number being 2304 pits to the largest being 5976 pits.

Optical profiling detected debris on the surface of the Coupon 849, despite being cleaned of corrosion product prior to analyses. A possible cause of this uneven surface could be re-oxidation of the specimen following the initial cleaning process, leading to the formation of a thin oxide film. Further analyses using EDS and/or XRD would be required to confirm the presence of oxides on this coupon.

The results of pit depth measurements determined that the deepest pit of -32.64µm was located on Coupon 912. Currently this may not be considered a significant depth, however if this value is used to calculate the annual rate of pitting it corresponds to 0.112 mm/y. Therefore, after 25 years the potential maximum pit depth is calculated to be approximately 2.8mm. In the Corrosion

and Cathodic Protection design criteria [36] the extreme corrosion allowance for internal submerged zones is 2.0mm, which is stated as being “conservative” since the internal foundations will be protected using sacrificial anodes. Even though pitting corrosion may be highly localised, a pit that exceeds the corrosion allowance within the operational lifetime of the foundation could be a structural risk for the entire turbine. Using the maximum pit depth value, it is estimated that it will take 17.85 years to reach the maximum corrosion allowance of 2.0mm, although as previously mentioned this is a localised form of corrosion and is not assumed for the entire steel monopile. Nevertheless, this result highlights the importance of monitoring this internal area at approximately 20m above the seabed perhaps by deploying further corrosion coupons or via ultrasonic thickness measurements to ensure the localized corrosion rate does not accelerate over time.

Thickness loss measurements for this coupon by MCPS determined a general corrosion rate of 0.093mm/y which corresponds to a 2.33mm steel thickness loss after 25 years. Similar to the pitting corrosion rate, this value slightly exceeds the extreme corrosion allowance of 2.0mm stipulated in the design criteria. Nevertheless, it is estimated that the maximum corrosion allowance should not be reached until 21.5 years of operation when considering a general corrosion rate of 0.093mm/y, and therefore is not a significant concern at this stage.

Some mathematical models of marine corrosion of steel divides the corrosion process into 4 phases whereby phases 1 and 2 represent relatively high initial

corrosion rates, limited only by the rate at which oxygen can diffuse from the surrounding seawater. The corrosion process tends to be rapid in the initial phases prior to passivation. The instantaneous corrosion rate declines in phase 3 due to the development of an impermeable rust layer and then corrosion eventually declines to an almost constant rate represented by phase 4 (Figure 4.36).

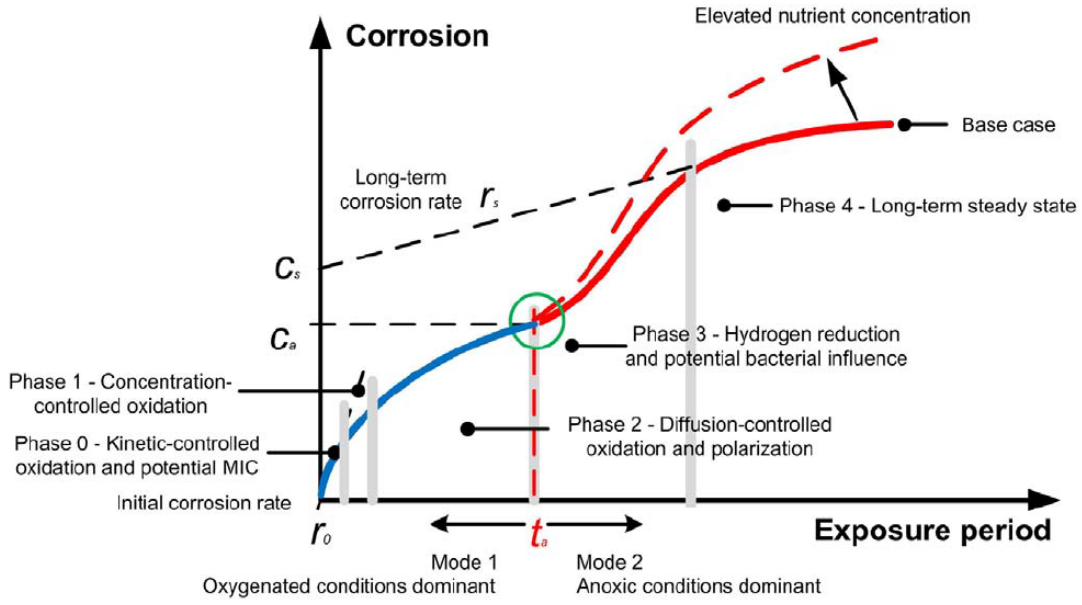

Figure 4.36: *Mathematical model for marine corrosion of steel, illustrating the sequential phases of the corrosion process* [144].

Since the coupons were only exposed to the corrosive environment for 3 to 5 months, the corrosion rates observed during this period are likely to reflect phase 1 of the corrosion model. As such, these initial corrosion rates are likely to be higher than in phase 4 which represents a more constant long-term corrosion rate. In order to make reasonable predictions about the long-term impacts of corrosion on the structure it is important to consider a long-term corrosion rate

and not just the initial corrosion rate observed within the first few months of immersion as this may not accurately reflect the long-term conditions. It is for this reason that further corrosion monitoring over a longer time period is required that will provide corrosion rate estimates for phases 3 and 4 rather than just the initial phases, as this will provide much more reliable long-term corrosion loss information and enable more reasonable lifetime predictions.

The results of the chemical etching highlighted that the corrosion coupons were not in fact made from S355NL steel which was evident from the absence of pearlite in the microstructure (Figure 4.21 and Figure 4.22). Therefore, the coupons have different material properties to the monopile steel which will influence the rate at which the specimens corrode. According to [145], the presence of pearlite improves strength and hardness of steel as the percentage volume of pearlite in the material is directly proportional to carbon content. The lack of pearlite or depletion of pearlite changes the mechanical properties of the steel and can reduce the strength against corrosion. Considering this observation, the results obtained from the various corrosion analyses on the corrosion coupons may be not accurately reflect what is occurring on the steel within the monopiles at Teesside. The mechanical properties of the steel coupons are different to those of the monopile steel and therefore the general corrosion rates and susceptibility to pitting is not necessarily representative of the monopiles. The presence of pearlite within the monopile steel may improve the corrosion resistance of the material and therefore it is possible that the general corrosion and pitting rates observed on the coupons may be over-estimated.

The 2016 corrosion coupon campaign comprised of 49 coupons being installed within 5 different foundations and placed at similar “corrosion zones”. At the time of writing, only 15 coupons have been removed over a period of 13 to 15 months for various analyses, but primarily to determine the rate of material degradation under a range of internal monopile conditions. The samples removed from WTG 10 and WTG 22 had undergone approximately 13 months of exposure to the internal monopile environment. The appearance of the samples prior to cleaning, descaling and weight loss analysis showed a thick, heterogeneous layer of oxides of different colours and consistencies (Figure 4.25 and Figure 4.26). Coupons 175 and 194 exhibit a shiny and transparent thin layer, quite different from the other samples. This is not unexpected as both samples were located in the atmospheric zone of WTG 10 and WTG 22; respectively. Therefore, the accumulation of corrosion product and material is assumed to be minimal compared to the other samples either fully immersed or partially immersed in seawater.

The coupons removed from WTG 13 following a 15-month trial have a different appearance compared to WTG 10 and WTG 22 (Figure 4.27); this has been attributed to a different storage and packaging process during removal from the turbine and during transport to the laboratory. Similar to other samples located at in the atmospheric zone; coupon 184 has minimal oxide accumulation, with a very thin layer. Coupon 190 exhibits a thin light-coloured layer of product assumed to be a calcareous deposit which can be an indirect influence of the cathodic protection (CP) system in seawater; Calcium Carbonates ($CaCO_3$) and

hydroxides (OH^-) form a shielding layer on the metal surface which reduces oxygen access and also the current requirements for CP [146].

Using the corrosion rates obtained from the 2014 and 2016 corrosion coupon campaigns, and with a general understanding of the internal monopile environments from where the samples were collected, it is possible to make general assumptions about the "phase" of corrosion by studying Melchers' bi-modal model in Figure 4.36. The coupons removed in 2014 are assumed to represent either Phase 0 or Phase 1 corrosion rates since they were removed following on 3 to 5 months of immersion. Using WTG 10 as an example since it was the only turbine to host coupons across both measurement campaigns, it is possible that the results reflect a transition between phases. Consistent corrosion rates (0.11 mm/y) were observed at the low water tidal zone/lower working platform (Figure 4.37). This suggests either a steady state corrosion at this location, or, by following Melchers' model, perhaps a transition from Mode 1 to Mode 2, since both corrosion rates are some of the highest observed throughout the offshore trials. Considering the material loss (corrosion loss) for coupons taken from the tidal zone is 4 times higher after 13 months than 3 months, yet the corrosion rate is consistent (Table 4.5), it is likely that two phases of the model are being represented. Figure 4.38 highlights suggested positions on Melchers corrosion curve.

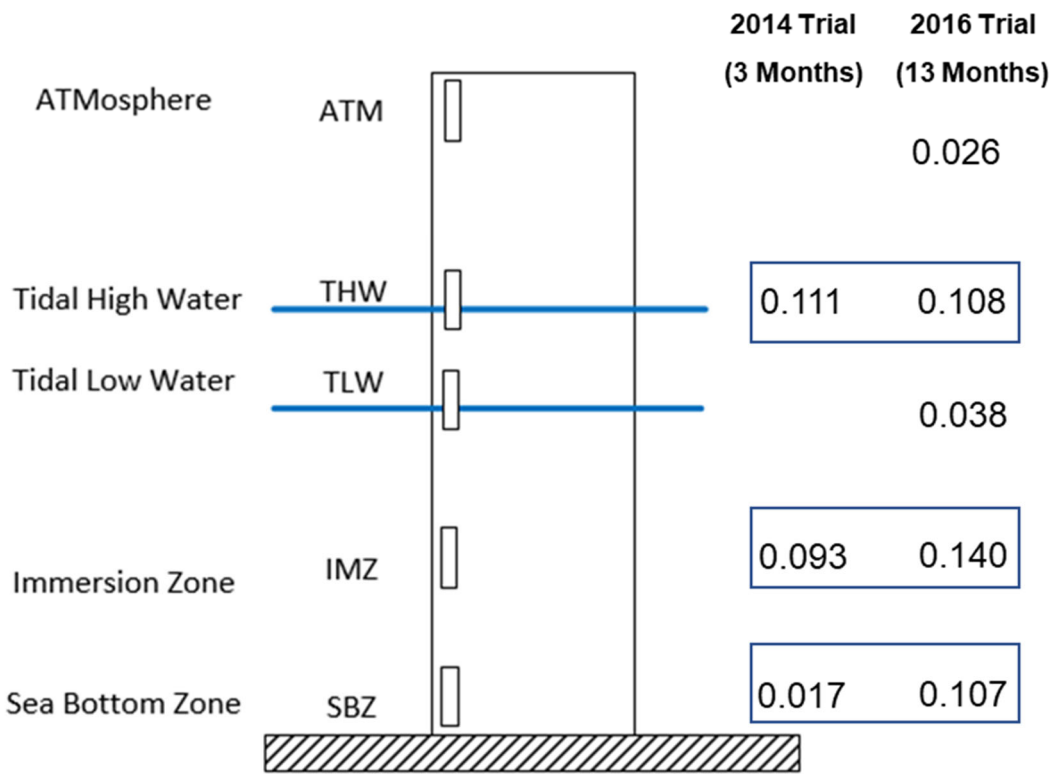

Figure 4.37: *Comparison of corrosion rates from WTG 10 following 3 months immersion and 13 months immersion at the same zones (corrosion rates in mm/y).*

Table 4.5: *Comparison of the corrosion loss data and the corrosion rates observed from WTG 10 coupons after 3-and 13-month trials.*

	Corrosion Loss (mm)		**Corrosion Rate (mm/y)**	
	3 Months	**13 Months**	**3 Months**	**13 Months**
Tidal Zone	0.032	0.12	0.111	0.108
Immersion Zone	0.027	0.15	0.093	0.14
Seabed	0.005	0.12	0.017	0.107

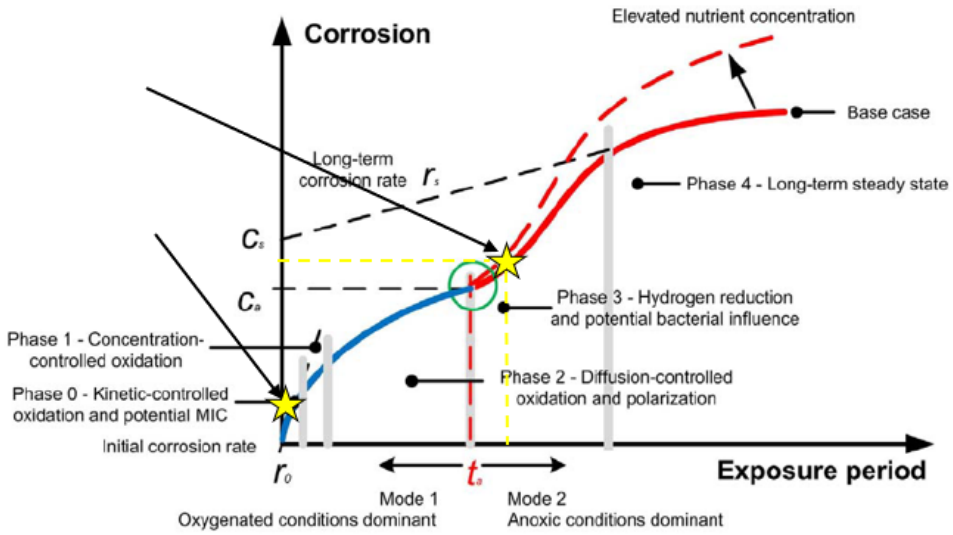

Figure 4.38: *Suggested locations on the curve for the corrosion loss data obtained from coupons following 3 and 13 months the tidal zone WTG 10.*

The proposed locations of the corrosion data imposed on the model in Figure 4.38 stems from the fact that almost identical corrosion rates were observed after both 3- and 13-month trials, yet the material degradation was 4 times greater after 13 months. This means that that slopes representing each corrosion rate must have the equivalent steepness, but different C values (C represents Corrosion Loss (mm) in this instance). At 3 months, the rate represented must be close to the initial corrosion rate or reflect the slope of the curve in Phase 0 – 1, whereby the metal begins to oxidize, the surface becomes colonized by biofilm and microbiological activity begin to develop within the film. This period is expected to last a few days [147] before moving into Phase 1 which represents a high corrosion rate, only limited by the rate at which oxygen can diffuse out of the surrounding seawater. Towards the end of Phase 2 there is a relatively sudden increase in corrosion rate, similar to that observed in Phase 1, and it is governed

by the development of anoxic regions on the corroding surface and bacterial activity. The similarities in instantaneous corrosion rate between Phase 1 and end of Phase 3 reflect the results obtained from the coupons extracted from the tidal zone in WTG 10. However, the internal tidal conditions are likely to influence the corrosion mechanisms within this zone and therefore the steel may be particularly susceptible to Accelerated Low Water Corrosion (ALWC); aggressive form of localised corrosion known to occur in tidal zones where there is differential aeriation [118] . ALWC has also been linked to microbiological activity and may be a key mechanism for the corrosion of steel at the seabed around the mud layer. Coupon 183 from WTG 10 exhibited relatively high corrosion rates following 13 months at the internal seabed zone. If the coupon had become buried during this time, the degradation of the sample is likely to be influenced by bacterial activity in this anaerobic region. However, since 183 was not analysed using XRD or SEM, it was not possible to characterise the composition of the corrosion product to identify and indications of bacterial influence. Corrosion rates as high as 0.14mm/y have measured at the internal monopile seabed zones in other UK offshore wind farms with leaking foundations [136] which is consistent with this finding at Teesside.

Interestingly, the tidal zone coupons from WTG 22 and WTG 13 did not exhibit corrosion rates as high as WTG 10 which suggests that the internal monopile conditions within WTG 10 are more corrosive to the surrounding steel. However, further monitoring and inspection of the internal environment e.g. pH, temperature, potential, dissolved oxygen etc. is required for this to be further explained. Nevertheless, this result is consistent the average corrosion rates

(0.101 mm/y) obtained from the internal tidal zone of monopiles during a corrosion monitoring campaign at another UK offshore wind farm [136]. It is also in line with the DNV guidelines value of 0.1mm/y [35].

The highest corrosion rates obtained from the offshore trials were observed at the fully immersed zones of WTG 10 (Coupon 182; 0.1402mm/y) and WTG 22 (Coupon 202; 0.1195mm/y) following 13 months. These corrosion rates are not surprising given that both foundations are leaking. If fresh, oxygenated seawater is regularly introduced within the monopile, it is likely to accelerate the corrosion process. Furthermore, these coupons represent free corrosion since they are not connected the internal cathodic protection system.

The overall results of the XRD on the coupons taken from the offshore trials were found to be consistent with marine corrosion literature. The rust layer is stratified in two parts (Figure 4.39); with an orange/brown outer-layer composed of ferric oxyhydroxides (lepidocrite (γ-FeOOH), akagenite (β- FeOOH) and goethite (α-FeOOH), whereas the inner layer is primarily constituted of sulphated green rust and iron sulphide.

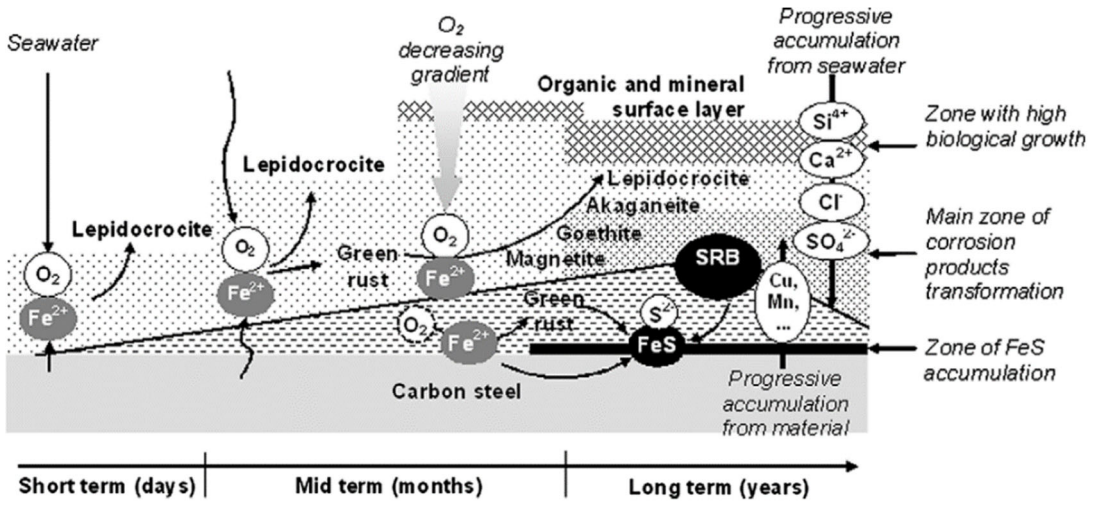

Figure 4.39: *Schematic representation of the evolution of rust layers formed on carbon steel immersed in seawater* [148].

This is consistent with the XRD results and reflects the kinetics of corrosion in the early stages of the process; controlled by the reduction of dissolved oxygen [149]. Goethite and Magnetite (Fe_3O_4) can be detected in the outer layer of the corrosion product; Goethite can often be obtained by oxidation of green rust with moderate oxygen flows [150], and Magnetite requires very low oxygen flows [151]. The presence of these compounds indicates that the transfer of oxygen to the inner layer will become more difficult as the thickness of the corrosion product layer increases. The presence of Magnetite suggests an oxygen-depleted environment, where SRB and other anaerobic micro-organisms could flourish. Magnetite was clearly detected on coupons 182 and 202; the coupons exhibiting the highest corrosion rates out of all samples. This strongly suggests that despite coming from leaking monopiles, there is very little mixing of fresh oxygenated seawater, and conditions are favourable to bacteria and potential MIC which could explain the high rates of degradation from the immersed zone.

Furthermore, the XRD samples taken from WTG13 confirmed the presence of Rozenite ($FeSO_4\ H_2O$); an Iron Sulphate. This is further indication of bacterial activity within both the tidal and immersed that could be influence the rate of degradation of the steel structures. A possible explanation for the presence of this compound in WTG 13 is that this foundation was previously a Non-Drilled, Non-Leaking structure, therefore there was little to no seawater exchange, and early pH monitoring indicated very low pH values as low as 4 (Table 3.1). Even though a leak has since developed and therefore there is now an element of seawater exchange, the relatively stagnant, acidic conditions may have facilitated the ideal conditions for anaerobic bacteria to flourish and influence the corrosion behaviour of the monopile steel.

5 Corrosion Modelling

5.1 Introduction

Chapter 3 provided a detailed description of a comprehensive laboratory study developed to simulate the internal environmental conditions observed within the monopiles at Teesside Offshore Wind Farm and to investigate the influence of key parameters on the corrosion rate of monopile steel. This work was complimented by a parallel investigation at Teesside; detailed in Chapter 4. During the offshore trials, corrosion coupons were installed within a range of leaking and non-leaking monopiles and removed after 13- and 15-month intervals to assess the corrosion rate and potential mechanisms influencing the degradation. This Chapter combines both the laboratory and Teesside corrosion data sets, along with results obtained from another UK offshore wind farm [136] and various other marine corrosion rates obtained from literature [149], [152]–[160]. This collated dataset will be used to develop an approach that could enable offshore wind operators, asset managers and turbine OEMs to make reasonable assumptions about the internal corrosion rate of their monopile foundations based on a selection of environmental parameters.

The development of a consistent and reliable approach to enable a better understanding of monopile corrosion behaviour is particularly sought after within the offshore wind industry to support decision making processes related to remaining useful life assessment, life extension and decommissioning [161], [162]. A critical set-back to the development of an industry-accepted approach

is the lack of information and data sharing throughout the sector that could highlight gaps in knowledge and on share potential solutions. ORE Catapult has engaged with various owner/operators on this topic and determined that a better understanding of internal monopile corrosion behaviour was ranked as one of the highest priority focus areas, due to concerns regarding deviations from initial design assumptions [162]. However, a series of interviews conducted with the operators concluded that the cost, health and safety implications involved in the inspection and monitoring of monopile corrosion behaviour are key barriers to an in-depth analysis of all assets within a farm. Therefore, simple, non-intrusive approaches that can utilize existing monitoring data from instrumented monopiles to provide high-level internal corrosion rate information could be an attractive solution to any operator. The tool developed herein is a Decision Tree, one of the simplest and widely used Machine Learning (ML) structures.

5.2 **Decision Tree Algorithm**

Decision tree models are used to solve classification problems. The decision tree learning algorithm generates decision trees from training (existing) data and uses it to classify new data. Tree models where the target variable can take a discrete set of values are known as classification trees.

5.2.1 **Decision Tree Classification**

Decision trees classify data through recursive partitioning of the dataset into mutually exclusive subsets which best explain the variation in the dependent

variable under observation [163] [164]. The tree classifies instances (data points) by sorting them down the tree from the root node to a leaf node which gives the classification of the instance. Each branch of the tree represents a possible scenario and its outcome [164]. Decision trees begin with a set of instances and create a new tree structure that is used to classify new instances. The tree consists of three different building blocks: tree nodes, tree branches and tree leaves. Figure 5.1 depicts a simple decision tree representation.

The aim of the algorithm is to partition the training set into subsets until each partition is either “pure” in terms of the target variable or sufficiently small. Pure refers to a subset which contains only samples of one class. Therefore, at each step of the process, the algorithm uses the feature that leads to “the purest” subsets. Each partitioning operation be described by a rule that separates the incoming data based on the values of one feature: the splitting feature.

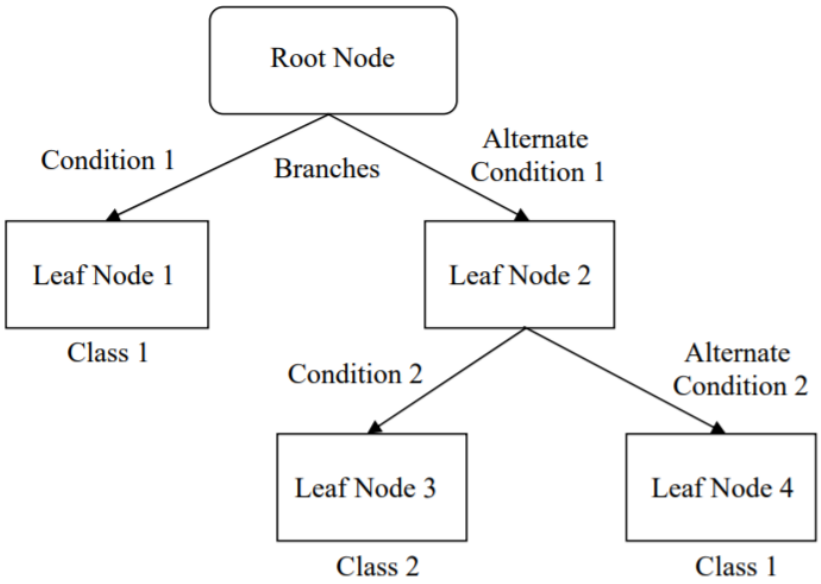

Figure 5.1: *Typical decision tree architecture.*

- **Tree Nodes** identify the splitting feature.
- **Tree Branches** identify the different values of the splitting feature.
- **Tree Leaves** at the end associate the final class to a specific decision path.

5.2.2 **Decision Tree Applications**

Decision trees have proved useful in their applications to various real-world problems i.e. diagnoses of medical conditions [165], credit card fraud detection [166], loan applications [167], semi-conductor manufacturing [168] process optimization [169], non-destructive testing [170][171]. Decision trees have also been used to predict oil pipeline corrosion behaviour [172], to categorize corroded regions along pipelines and calculate average corrosion rates in specific areas [173]. Furthermore, in a study by Chou *et al.* (2017), the performance of decision tree modelling to predict pitting corrosion risk of steel reinforced concrete and marine corrosion rate of carbon steels was assessed and compared with another advanced artificial intelligence (AI) techniques[174]. It was concluded that the decision tree performed well for predicting high class of the corrosion rate data.

Decision trees are an active research area, with an increasing interest in AI solutions and ML structures across all industries. Much of the focus is on improving methods for building, controlling and executing the decision tree algorithms [164] to achieve maximum efficiency and reliability.

5.2.3 **KNIME Analytics Platform**

KNIME (Konstanz Information Miner) is an open source, modular environment, which enables easy visual assembly and interactive execution of a data pipeline [175]. The KNIME architecture follows the following three principles:

1. Visual, interactive framework: Using drag and drop options to combine data flows.
2. Modularity: Processing units and data containers are not dependent on each other to enable independent development of different algorithms.
3. Easy expandability: New processing nodes can be added easily using simple plug-in mechanisms without complicated installation/deinstallation procedures.

5.3 **Monopile Corrosion Prediction**

The aim of this study is to train and apply a Decision Tree in KNIME Analytics Platform to predict corrosion rate classification for the internal region of offshore wind monopile foundations. The model will train a decision tree on existing corrosion data and use it classify new data. Figure 5.2 Illustrates the proposed prediction model as described in [175]

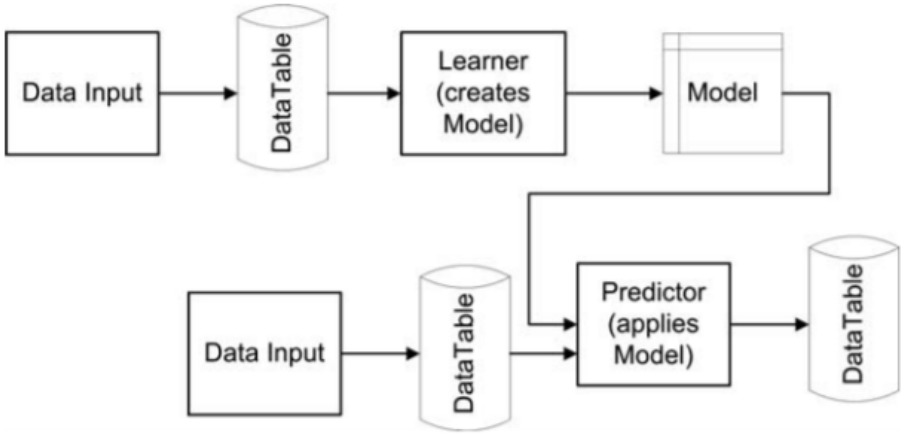

Figure 5.2: *Flowchart of the proposed decision tree algorithm.*

5.3.1 **Summary of Data Collection**

The datasets used to develop the decision tree are a combination of the experimental and field corrosion rates obtained throughout this research project, in combination with rates obtained from an additional offshore wind farm and marine corrosion literature. The database contains a total of 536 datasets, representing a combination of various treatments that influence corrosion rate which will be used to train and test the model. The full database can be found in Appendix B. Table 5.1 details the variables used for decision tree learning.

Table 5.1: Data variables of the KNIME corrosion database

Variables	Description	Category/Range
Location	Internal monopile zone where corrosion rate measurement was taken/simulated in the laboratory	Atmospheric, Tidal, Immersed, Seabed
Exposure Time	Years of exposure within a Location	0.07 - 8
pH	pH level during Exposure Time	4 - 9.26

Oxygen	Presence/absence of oxygen in the Location	Yes/No
Seawater	Type of seawater/solution depending on Location	None, Real, NaCl, Artificial with Marine Bacteria
Corrosion Rate	Material weight loss over time (mm/y)	0.0001 - 1.235

5.3.2 **Building the model**

The development of the decision tree has the following key work-steps:

5.3.2.1 **Pre-processing**

For each column, several intervals (bins) can be defined to enable categorisation of numeric values. In this instance, numeric bins have been assigned to “Corrosion Rate” to categorise rates into “High”, “Medium” and “Low” bins. Corrosion Rate bins were defined as follows:

Low: <0.03 mm/y

Medium: 0.03 mm/y to 0.1 mm/y

High: >0.1 mm/y

Corrosion rate categories were defined to support the classification of monopile corrosion behaviour in response to specific environmental conditions. Instead of predicting a specific rate of corrosion, the model classifies for the operator whether the internal conditions are a low, medium or high corrosion priority. In practice, the operator can choose to discount low outputs and focus attention on those perceived to be high corrosion scenarios.

A numeric binner was also applied to pH level to determine whether an environment is considered to be acidic/non-acidic and the potential influence this

may have on the corrosion behaviour of the steel. pH level bins were defined as follows:

Acidic: =/<6

Non-acidic: >6

In practice, any pH measurement taken from within a monopile below pH 6 could potentially raise concern among operators given that typical seawater pH is 8.2 (North Sea). pH 6 or below is a potential indication of acidification which is known to accelerate the corrosion rate of carbon steel.

With the creation of “Corrosion Rate_Binned” and “pH_Binned” columns the “Corrosion Rate” and “pH” numerical data columns can be filtered from the input table. For the Location, corrosion data sets obtained from the “Lab Tidal” and Lab Immersed” locations were considered separately from the Immersed and Tidal data collected from offshore monopiles. The reason for not combining the data sets was that despite all efforts to simulate the internal monopile conditions in the laboratory, the experimental conditions were not wholly representative of the offshore environment and therefore corrosion rates obtained may skew the model if incorporated with those obtained from the monopile trials. Nevertheless, it is still possible to compare both datasets during the model evaluation.

5.3.2.2 **Statistics**

The KNIME statistical node calculates key statistical moments within the datasets (Figure 5.3 and Figure 5.4).

Column	Min	Mean	Median	Max	Std. Dev.	Skewness	Kurtosis	No. Missing	No. +∞	No. -∞	Histogram
Exposure Time(Years)	0.0767	0.7493	?	8	0.7219	6.2538	52.8664	0	0	0	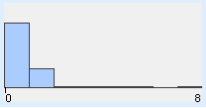
Temperature (°C)	8.75	15.5645	?	30	5.3686	0.7766	-1.0792	14	0	0	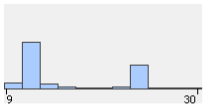
pH	4	6.7786	?	9.26	1.7957	-0.7943	-1.193	308	0	0	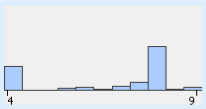
Corrosion Rate (mm/y)	0.0001	0.0632	?	1.2353	0.138	5.1552	31.1519	0	0	0	

Figure 5.3: *KNIME numerical statistical analysis*

Location	Exposure Time(Years)	Temperature (°C)	pH	Oxygen	Seawater
No. missings: 0	**No. missings:** 0	**No. missings:** 14	**No. missings:** 308	**No. missings:** 0	**No. missings:** 0
Top 20: Immersed : 139 Lab Immersed : 135 Atmospheric : 119 Tidal : 69 Seabed : 59 Lab Tidal : 15	**Top 20:** 1.03 : 58 1.2896189 : 32 0.28 : 27 0.558533667 : 19 0.605078139 : 19 0.577699038 : 18 0.51 : 15 0.8 : 15 0.238198181 : 13 0.585912768 : 12 0.287480564 : 12 0.574961127 : 10 1.0983345 : 10 0.651622611 : 9 0.301170114 : 8 0.254625642 : 8 0.265577283 : 7 0.588650678 : 7 0.303908024 : 7 0.607816049 : 7	**Top 20:** 12.0 : 286 23.0 : 144 10.0 : 20 ? : 14 22.0 : 6 21.0 : 4 27.6 : 4 14.2 : 4 30.0 : 4 25.0 : 3 13.53 : 3 14.3 : 2 13.42 : 2 14.7 : 2 13.08 : 2 14.0 : 2 8.9 : 2 13.72 : 2 17.0 : 1 18.7 : 1	**Top 20:** ? : 308 8.0 : 91 4.0 : 63 8.1 : 7 7.8 : 7 8.2 : 6 7.0 : 5 6.0 : 5 8.91 : 3 8.07 : 3 7.59 : 2 6.97 : 2 7.62 : 2 7.78 : 2 7.81 : 2 7.99 : 2 7.21 : 2 8.04 : 2 8.11 : 1 8.22 : 1	**Top 20:** No : 421 Yes : 115	**Top 20:** Real : 270 None : 116 NaCl : 83 Artificial with marine bacteria : 67
Bottom 20:	**Bottom 20:** 0.153425 : 3 1.6 : 3 4.0 : 3 3.0 : 3 0.63793306 : 3 0.933627354 : 3 0.6 : 3 1.472679114 : 3 0.273971 : 2 8.0 : 2 1.0 : 2 0.952792725 : 2 7.2 : 1 5.0 : 1 0.857534 : 1 0.164384 : 1 0.0767123 : 1 1.8 : 1 2.5 : 1 0.3 : 1	**Bottom 20:** 15.0 : 1 13.68 : 1 8.77 : 1 13.63 : 1 8.93 : 1 8.82 : 1 9.02 : 1 13.03 : 1 13.77 : 1 9.01 : 1 14.1 : 1 8.84 : 1 14.8 : 1 8.75 : 1 14.6 : 1 13.55 : 1 14.5 : 1 8.8 : 1 8.89 : 1 13.02 : 1	**Bottom 20:** 9.08 : 1 7.7 : 1 6.57 : 1 7.88 : 1 5.5 : 1 7.9 : 1 8.03 : 1 7.84 : 1 5.85 : 1 9.26 : 1 8.25 : 1 6.38 : 1 7.85 : 1 5.44 : 1 7.82 : 1 5.88 : 1 7.96 : 1 7.6 : 1 8.8 : 1 9.15 : 1	**Bottom 20:**	**Bottom 20:**

Figure 5.4: *Top/Bottom 20 statistics for the entire corrosion database*

5.3.2.3 **Model Training**

The input table is partitioned into two sets to train and test the data. For the training data, 80% of the "Corrosion Rate_Binned" data is randomly selected, the remaining 20% will be used for model testing. The algorithm provides two quality measures for split calculation to evaluate the goodness of the split; the gini index and the gain ratio. The Gini index relies on the idea of minimizing misclassification. For a dataset S containing examples from n classes, $gini\ (S)$ is defined as

$$\boldsymbol{gini}\ (\boldsymbol{S}) = \mathbf{1} - \sum \boldsymbol{p_j^2} \qquad \textit{(Eq. 5.1)}$$

Where p_j is the relative frequency of class j in S. If a split divides S into two subsets S_1 and S_2, the index of the divided data $gini_{split}(S)$ is given by

$$\boldsymbol{gini_{split}(S)} = \frac{\boldsymbol{n_1}}{\boldsymbol{n}}\boldsymbol{gini(S_1)} + \frac{\boldsymbol{n_2}}{\boldsymbol{n}}\boldsymbol{gini(S_2)} \qquad \textit{(Eq. 5.2)}$$

The advantage of this index is that its calculation requires only the distribution and class values in each of the partitions [176]. To find the most suitable split point for a node, the algorithm scans each of the node's attribute lists and evaluates splits based on that attribute. The attribute containing the split point with the lowest value for the gini index is then used to split the node [176].

Gain ratio measures how well a given attribute separates training examples into its target classes by calculating the reduction in entropy that would result from splitting the data into subsets. The Gain ratio essentially relies on the idea of

choosing the most informative feature. The information gain of example dataset S on attribute A is defined as

$$\boldsymbol{Gain(S,A) = Entropy\,(S) - \sum \frac{|S_v|}{|S|} Entropy\,(S_v)} \qquad \textbf{(Eq. 5.3)}$$

Where S is the number of instances and $|S_v|$ is a subset of instances of S where A takes the value v.

Entropy is a measure of the amount of information in an attribute, so the higher entropy, the more information is required to completely describe the data [164]. As such, when building the decision tree, the objective is to decrease the entropy of the dataset until a subset that is pure (a leaf), has zero entropy and represents instances that begin to one class [164]. Entropy is defined by

$$\boldsymbol{Entropy(s) = \sum - p(I)\, log_2\, p(I)} \qquad \textbf{(Eq. 5.4)}$$

Where $p(I)$ is the proportion of S belonging to Class I.

The values of impurity measures for binary classification problems can be found in. p refers to the fraction of records that belong to one of the two classes. All measures reach maximum value when the class distribution is uniform ($p=0.5$) and the minimum values are attained when all records belong to the same class.

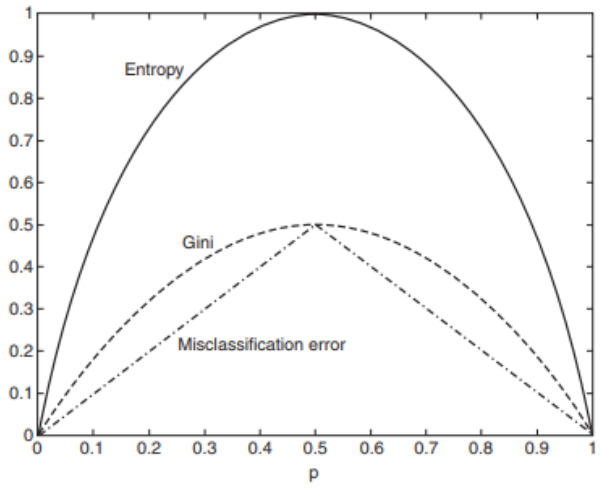

Figure 5.5 *Comparison of impurity measures in decision tree learning* [177]

Both measures for selecting the best split were tested in KNIME using the corrosion dataset and either could be applied. However, the decision tree that was generated using the Gini index demonstrated a higher accuracy in the prediction of corrosion rate (86.1% compared to 81.3%) and was selected as the preferred measure for building the decision tree in this instance.

Decision Trees, like many other ML algorithms are subject to potentially overfitting the training data. For example, trees that are too deep can result in models that are too details and cannot generalize on new data. Conversely, trees that are too shallow might lead to models that are too simple and do not fit the data. To develop a tree that generalizes better, the tree growing phase is often followed by a pruning phase reduce to avoid overfitting. During this phase, branches are cut that have become over-specialized on the training data. KNIME provides two pruning techniques; reduced error pruning and Minimum Description Length (MDL). Reduced error pruning was the preferred option for

the corrosion dataset in this instance, whereby if pruning a branch doesn't decrease the accuracy for the training set, the subtree is pruned. The tree generated using the MDL method was deemed too shallow.

5.3.2.4 **Model Evaluation**

In KNIME, the Scorer node was applied to the decision tree matrix to compare the predicted values with the actual dataset and to analyse the accuracy of the decision tree model. A confusion matrix and accuracy statistics were generated to enable visualization of the decision tree performance (Table 5.2). A confusion matric is a primary tool in visualizing the performance of a classifier, although it does not consider that some misclassifications are worse than others. To overcome this, Cohen's kappa (k) statistic is used to consider that correct values in a confusion matrix are due to chance.

Table 5.2: *Confusion matrix and accuracy statistics of corrosion prediction model*

Corrosion Rate_binned \ Prediction...	Low	Medium	High
Low	43	9	0
Medium	0	44	0
High	1	5	6

Correct classified: 93	Wrong classified: 15
Accuracy: 86.111 %	Error: 13.889 %
Cohen's kappa (κ) 0.76	

As shown in Table 5.2, the accuracy of the model is 86.1% (n = 108). The kappa statistic of 0.76 implies that the classification process avoided 76% of errors that a random classification would generate. The model wrongly predicted 9 corrosion

rates as “medium” when they were in fact “low” and also wrongly predicted 6 high corrosion rates (5 as “medium” and 1 as “low”). The spread of corrosion behaviour across different locations over time can be seen in Figure 5.2. The misclassifications of corrosion rate are highlighted in orange.

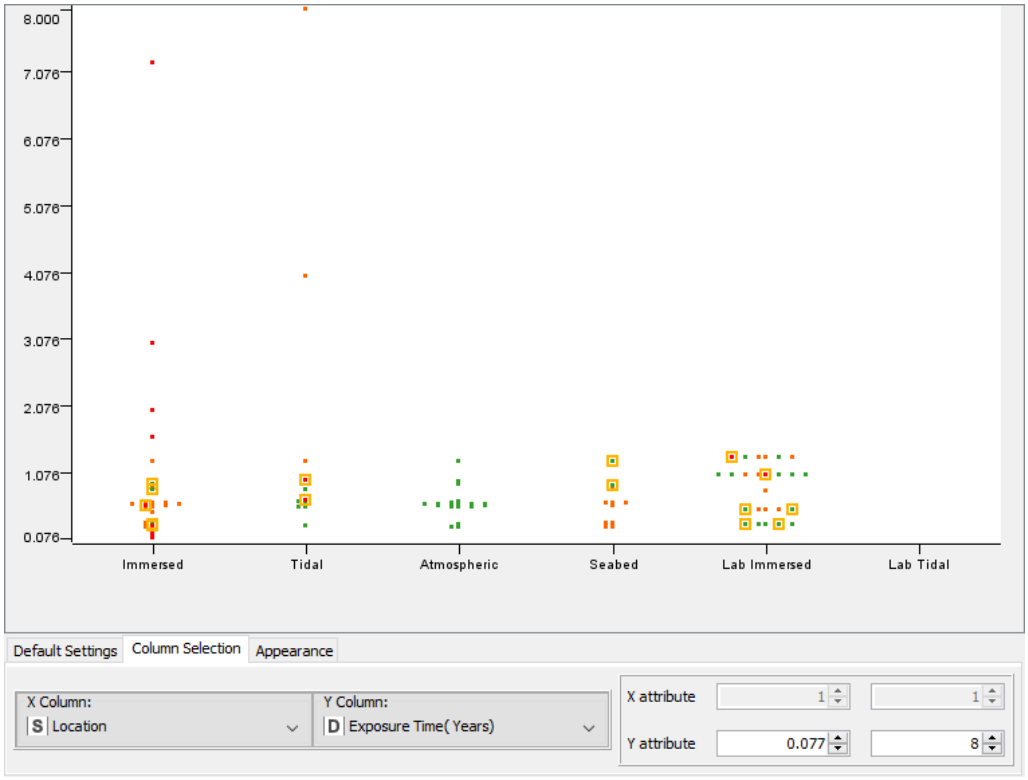

Figure 5.6: *Predicted corrosion rates at each Location using decision tree model.*

The majority of misclassifications were in the immersed zone for both field and laboratory corrosion values. There were no Lab Tidal values within the 20% of data that partitioned to test the model which is why there are no corrosion classifications in Figure 5.6. The samples with the longest exposure to fully immersed and tidal conditions were correctly predicted to exhibit high corrosion rates.

The workflow process created to build and generate the decision tree model in KNIME is represented in Figure 5.7. This highlights the pre-processing (Numeric Binner, Statistics & Partitioning) model training (Decision Tree Learner), testing (Decision Tree Predictor) and evaluation (Scorer) components of the process.

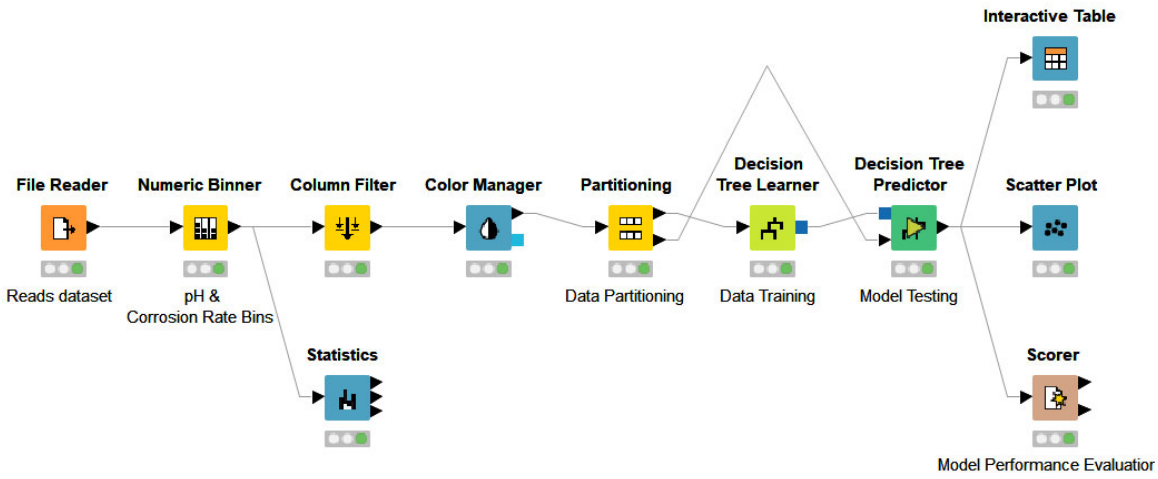

Figure 5.7 *KNIME workflow of corrosion prediction decision tree model*

5.3.2.5 **Decision Tree Interpretation**

The decision tree output is displayed across Figure 5.8,Figure 5.9Figure 5.10. The dependent variable of this decision tree Corrosion Rate_Binned which has 3 classes: low, medium and high. The root of this tree contains all 428 observations that were used to train the model (80% of the entire database). The model poses that the most influential attribute to determine whether corrosion rate should be classified as low, medium or high is Location. Due to so many missing pH values within the database (100+), the learning algorithm was unable to use this

parameter to train the model and therefore pH is not included as a node within the decision tree. All corrosion rates obtained from the Atmospheric zone were classes as low. 93.3% of corrosion rates obtained from samples exposed to the laboratory tidal simulation were high.

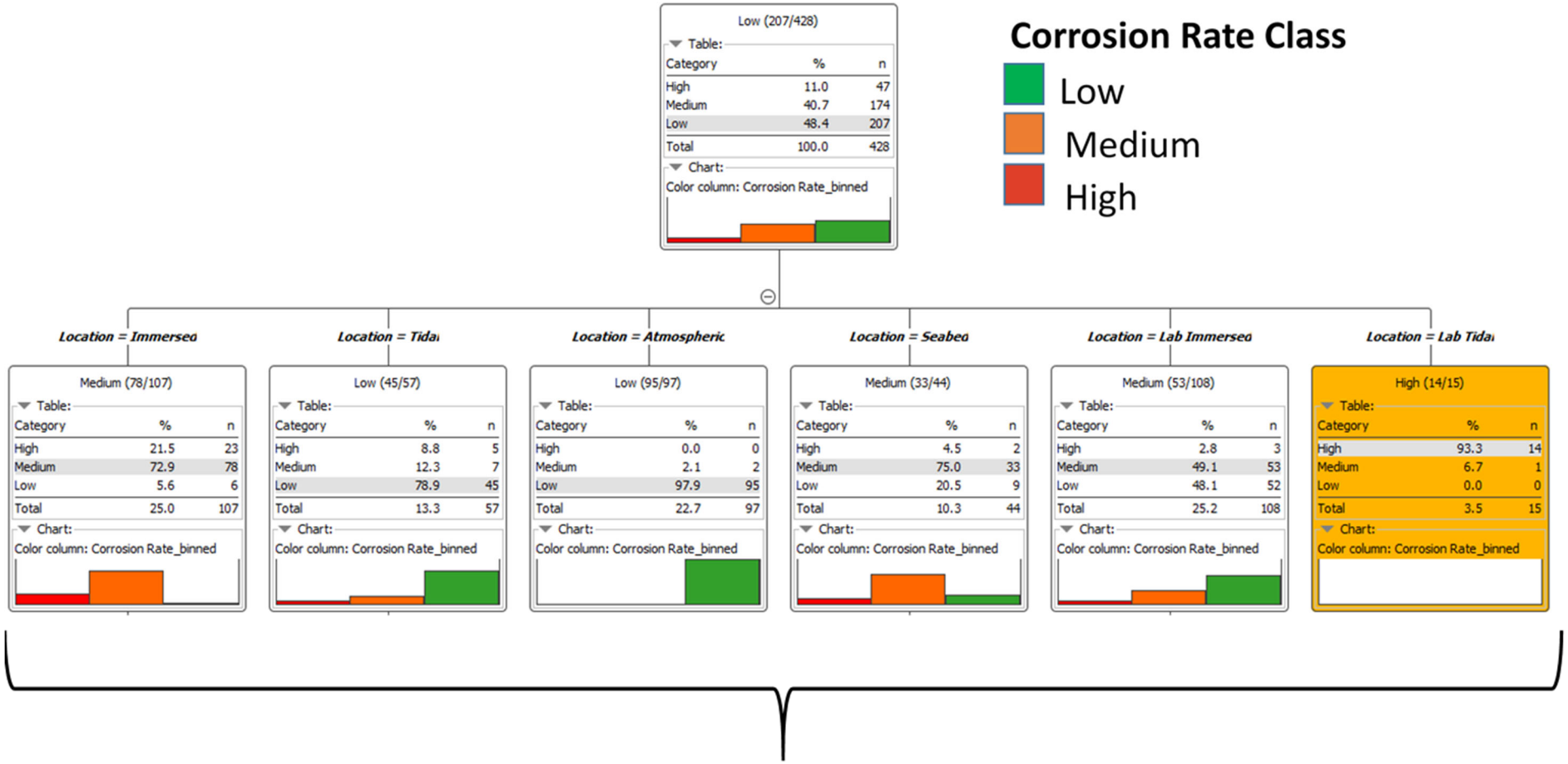

Figure 5.8: *Decision Tree (model testing) of corrosion rate classification (Root & first branch)*

Figure 5.9: Decision Tree (2nd branch + leaf nodes for Immersed, Tidal and Seabed Locations)

Figure 5.10: *Decision Tree (3rd & 4th branches and leaf nodes descending from Lab Immersed location).*

Location: Immersed

The majority of corrosion rates from a fully immersed location within a monopile were classed as medium (72.9%), with 20% classed as high and only 5.6% classed as low. In the presence of oxygen, 94.1% of corrosion rates of fully immersed steel are classed as high. Without the presence of oxygen, 85% of corrosion rates are deemed to be medium. These results are consistent with literature and operational experience. The presence of oxygen facilitates the process of corrosion through oxidation. It is expected that without access to oxygen, the corrosion process will slow and eventually cease.

Location: Tidal

78.9% of corrosion rates obtained from the Tidal region were classed as low, 12.3% were medium and only 8.8% were high. Tidal action is known to accelerate the corrosion rate of carbon steel as discussed in Chapters 3 and 4, so this result is surprising. However, when considering the time of exposure to tidal conditions, corrosion rates are extremely likely to be low (97.8%) if exposure is 0.9 years (11 months) or less, but likely to be medium (63.6%) or high (36.4%) if exposure exceeds 11 months. Therefore, monopiles and other offshore structures that experience cyclical wet/dry conditions are likely to exhibit significant corrosion loss during the first year of exposure, however longer-term exposure to these conditions without suitable corrosion protection could potentially lead to high levels of degradation and potential failure. These results suggest that operators of wind farms with leaking foundations and no internal coating/cathodic protection should ensure that foundations have suitable

corrosion monitoring equipment around the tidal zone and closely monitor any changes in behaviour after 1 year of operation at the very latest.

Location: Seabed

The majority of corrosion rates obtained from seabed samples were deemed to be medium (75%). Only 4.5% were high and 20.5% were low. Relatively short-term exposure (0.8556 years = ~10 months) to seabed conditions is 81.4% likely to lead to medium corrosion rates. 12.8% of samples had low corrosion rates and only 2.6% were deemed to be high. 80% of samples that experienced longer term exposure to the seabed (>10months) exhibited low corrosion rates. More information about the environmental conditions at the seabed is needed to better understand the corrosion behaviour of monopile steel at this location. Some monopiles contain an internal soil plug whereas others had this removed during the installation process. It is likely that steel buried in soil is exposed to anaerobic conditions and potentially microbiological activity that flourishes in that environment. Long term exposure to those conditions could lead accelerated corrosion in that zone, and potentially localized pitting. The presence of oxygen and the potential influence this may have on corrosion rates at the seabed has been discounted from the Decision Tree Learner. Therefore, more information is required before reasonable classification predictions can be made about the corrosion rate at the internal seabed zone.

Location: Lab Immersed

The presence of oxygen, exposure time and type of seawater were found to influence the corrosion rate classification of fully immersed samples in the laboratory. In an oxygenated environment, short term exposure (~5 months) led to almost a 50:50 split of low and medium corrosion rates, 80% of those samples exposed to NaCl solution were classed as low and 66.7% of those exposed to nutrient enriched seawater with live marine bacteria were classed as medium. As previously mentioned, replicating the internal monopile conditions at Teesside within a controlled laboratory environment was extremely challenging, and the lack of real seawater, in particular, led to the generation of corrosion rates that are unlikely to be representative of real offshore conditions.

5.4 **Summary**

The decision tree method is a powerful statistical tool for classification, prediction, interpretation and data manipulation that many applications across all industries. In this instance, the decision tree method was selected as the preferred corrosion prediction tool for the following reasons;

a) Simple to understand by the end user (an offshore wind farm operator).
b) Simplifies complex relationships between input variables and target variables by dividing into significant subgroups (very helpful when dealing with a range of environmental parameters).
c) Can handle a variety of input data (Nominal, Numeric, Textual).
d) Able to process erroneous datasets or missing values (e.g. pH).

e) Can handle skewed data without needing to resort to data transformation.

f) Robust to outliers.

The corrosion prediction decision tree tool that has been developed and described throughout this chapter was able to predict corrosion rate classification (low/medium/high) with an accuracy of 86.1% under pre-defined environmental conditions. This approach is a good starting point in understanding the influence of various environmental parameters on corrosion rate of internal monopile steel. Each individual parameter is known to influence corrosion rate differently but combined in various scenarios within a monopile environment, it is very challenging to predict the corrosion behaviour of the steel at different internal locations. This tool attempts to isolate specific parameters (oxygen, pH, tidal action) to better understand how each one could affect corrosion rate. The outputs from this model will support and provide input into a detailed structural analysis of the foundations at Teesside to assess the impact of such site-conditions on the structural lifetime of the assets.

One of the main limitations of using the decision tree method is the possibility of overfitting/underfitting when using a small dataset, particularly when there are missing values such as in this case. This has the potential to limit the robustness of the model. Another disadvantage is that strong correlation between input variables may result in the selection of variables that improve the model but are not causally related to the corrosion rate. Therefore, caution is needed when interpreting the decision tree model and when using the results to

hypothesis causal relationships between parameters and their influence on corrosion rate.

6 Biofouling Assessment

6.1 Introduction

The submerged steel surfaces of monopiles represent a clean hard substrate for rapid and extensive colonisation by sessile biofouling species. The accumulation of biofouling on monopiles is considered a structural burden, since the associated increase in mass of the foundation can affect the natural frequency of the structure. Additionally, increases in its diameter and surface roughness may contribute to the monopile experiencing increased hydrodynamic loads [35], [178]. Not only is the loading increased, but some fouling species have been known to facilitate corrosion (by providing a suitable environment and source of nutrients for corrosion inducing bacteria [95]), impair the cathodic protection system [179] and interfere with structural inspection [113].

Removal of biofouling from the inter-tidal zone by jet-washing is a required maintenance regime to control and manage the growth. Controlling the accumulation of marine growth around this zone is particularly important in terms of health and safety, to ensure that technicians are able to transfer safely from the vessel to the boat landing area on the transition piece. Biofouling has been identified as a slip hazard on the ladders and also can impede the hoisting of the access rope. [180]. In addition to health and safety, it is important to manage the growth of hard fouling organisms such as barnacles that can take advantage of indentations or imperfections on a coated surface. If a barnacle grows and expands within a confined area such as a pit on a coating surface, the subsequent

pressure on the coating can cause delamination from the underlying coated layer or even the steel substrate below (Figure 6.1A)[181]. This can lead to severe general corrosion on the surface if there are many barnacles attached (Figure 6.1B)[182]. Additionally, on uncoated stainless 316 grade marine steel, barnacles have led to such extensive localized pitting corrosion that has penetrated through a 5mm thick sheet after 2 years of exposure (Figure 6.2) [182]. A potential reason for the rapid pitting corrosion is the entrapment of seawater immediately on the steel surface underneath the barnacle. Microbiological activity in this zone could result in localized oxygen depletion and facilitate Microbiologically Influenced Corrosion (MIC).

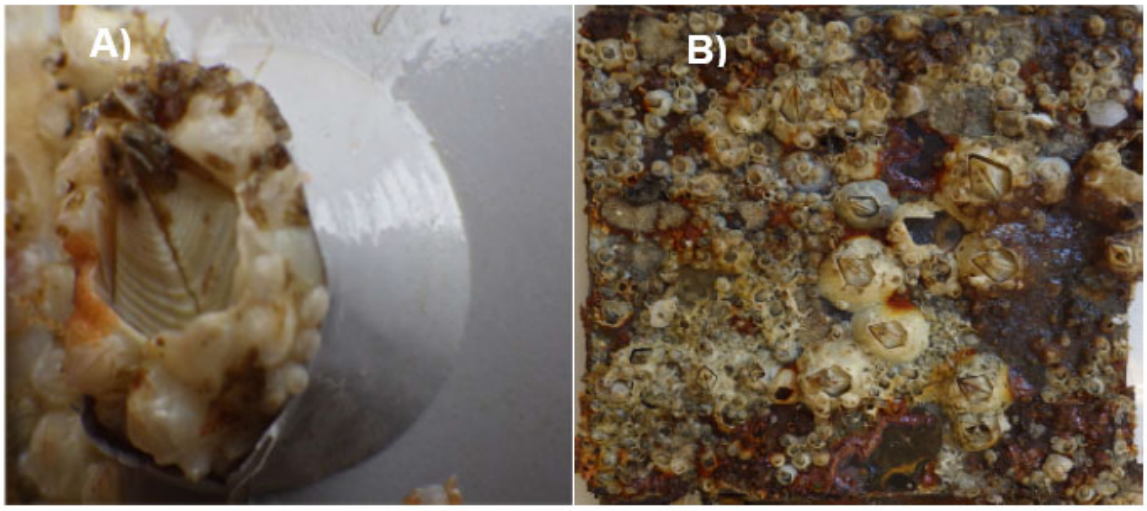

Figure 6.1: *A) Coating damage caused by growth of a barnacle* [181]*, B) Severe surface corrosion on coated panels at tidal test site* [182].

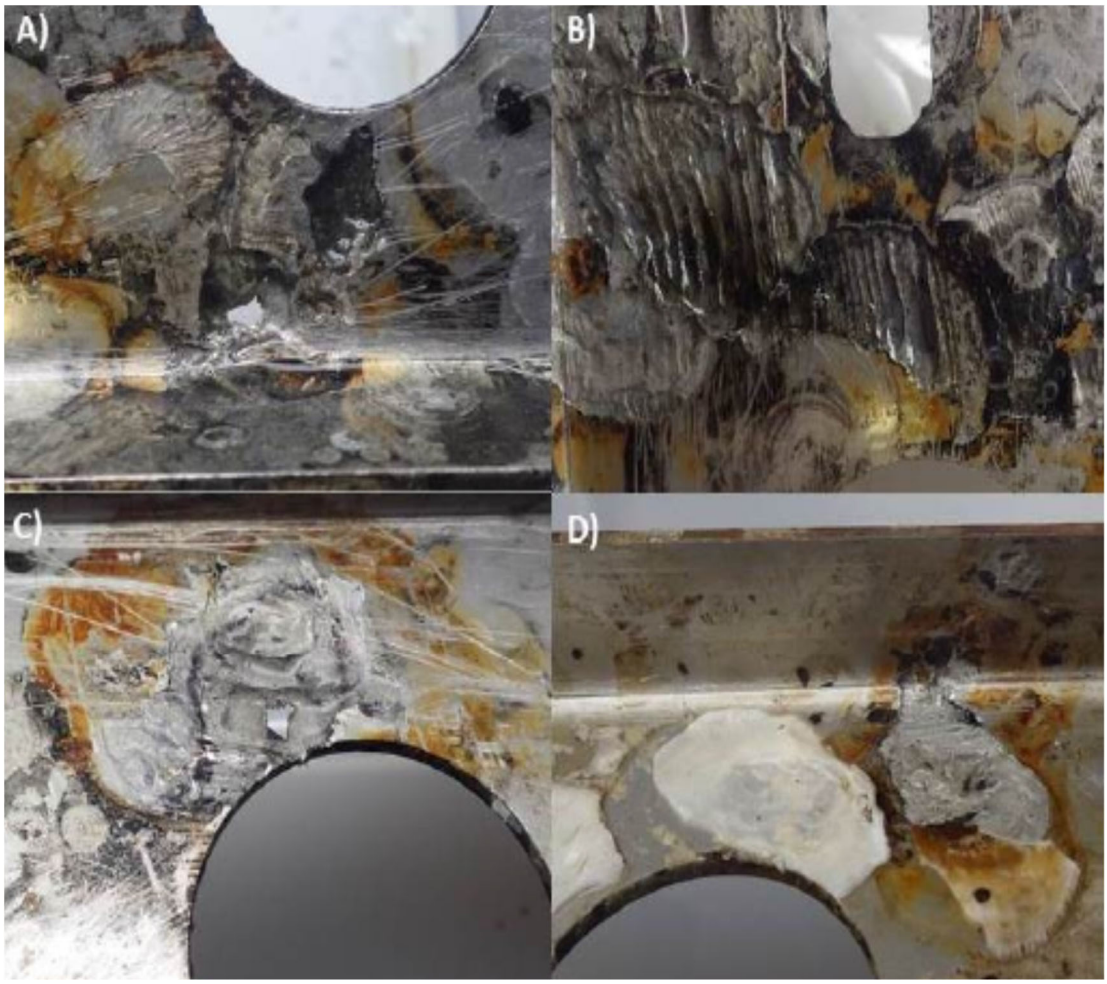

Figure 6.2: *Pitting corrosion on 5mm thick uncoated stainless 316 grade marine steel after 24 months exposure in a tidal stream* [182].

At Teesside Offshore Wind farm, accumulation of marine growth at the intertidal zone represents a key issue in terms of operation and maintenance. The intertidal and submerged zones of typical turbine at Teesside are classified in Figure 6.3. Technicians have reported that hard fouling organisms such as mussels and barnacles are the most difficult to remove from the transition piece (TP) and then rapidly recolonize within a few weeks. Biofouling accumulation around this zone is problematic, especially around the ladders and ropes, as

these are critical components used by technicians to transfer on to the structure. Figure 6.4 illustrates how biofouling can accumulate around the splash zone of the transition piece in pre and post-cleaning images. Closer inspection of Figure 6.4a shows that the access rope to which technicians must attach themselves for safe transfer onto the turbine is coated with green marine growth and also a cluster of barnacles around the pulley wheel (Figure 6.5). It has been reported that biofouling on the access rope can impede the technician transfer process by reducing the efficiency of the hoist. Additionally, the accumulation of seaweed on the ladder rungs creates a slippery surface that is a health and safety concern for technician transfer. Therefore, turbines that require access, need to be cleaned on a regular basis (every 2 weeks in some cases) which is costly in terms of time and effort. Generally, the intertidal zones at Teesside are cleaned in the summer months (June to October) when the sea temperature is warmest (averaging 12.6°C to 15.6°C). The growth tends to subside in the winter months as the sea temperature decreases. This seasonal variation reflects that of other wind farms in the North Sea such as C-Power in Thornton Bank. Samples taken at 15m depth showed low species richness over the winter months of the 2009 monitoring period (~ 10 species). Species richness then doubled from March to July and remained fairly stable (~20 species). The overall species abundances followed a similar pattern, with low densities observed in February-March 2009 and higher abundances thereafter, primarily due to the high densities of the amphipod *Jassa herdmani* [183]. At present there are no industry-accepted approaches for the collection, analysis and management of biofouling on offshore wind turbines.

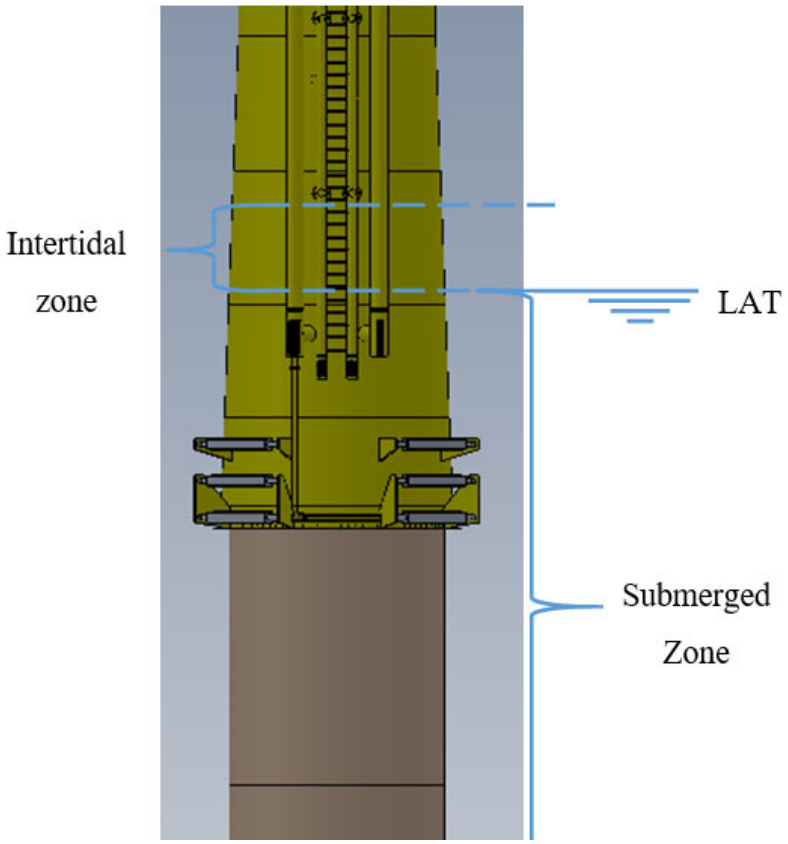

Figure 6.3: *Schematic of the splash and submerged zones where biofouling assessment took place at Teesside Offshore Wind Farm with respect to Lowest Astronomical Tide (LAT).*

(a)

(b)

Figure 6.4: *Biofouling on the ladders and access rope of TP 12 (a) Pre-cleaning and (b) Post-cleaning by jet-wash.*

Figure 6.5: *Close up image of the fouled access rope from Figure 6(a).*

The aims of this study were to

1. Characterise the key biofouling species present in the intertidal and subtidal zones on the surface of the wind turbines at Teesside;
2. Assess the efficacy of two sampling techniques and;
3. Provide management strategies for the maintenance of biofouling on offshore monopile structures.

6.2 **Material and Methods**

To understand the typical biofouling characteristics found on the exterior surfaces of the foundations, an assessment of marine growth was performed at Teesside Offshore Wind Farm. The assessment consisted of two separate investigations;

the first evaluated the biofouling growth at the intertidal zone of the transition piece on 15 turbines by taking scrape samples and estimating the weight and abundance of the predominant species. The second investigation utilized an underwater remotely operated vehicle (ROV) to capture video footage of the submerged zone of 5 turbines, which enabled a depth profile of marine growth from sea-level to seabed. The communities observed at the intertidal/splash zone are assumed to be <6 months old, as this region is often jet-washed to remove the biofouling. In the subtidal zones, the communities are assumed to be approximately 3 years old as the foundations and transition pieces were installed in 2012.

Image processing techniques used to reconstruct the submerged surface of the monopile from ROV video footage enabled estimates of biofouling surface characteristics, such as mean roughness, thickness and added mass. In addition, identification of the biofouling species observed on the structure, particularly on the boat landing area, enabled technicians to adapt and optimize their removal of marine growth according to their seasonal behaviour.

6.2.1 **Sampling Strategy**

The biofouling community on monopile-transition piece structures installed 2km offshore in Tees Bay (North Sea) was evaluated (Figure 6.6). Samples were collected from the intertidal zones of 15 turbines in June 2015, and from the

subtidal zone of five turbines in October 2015. Cost limitations prevented sampling across all 27 turbines.

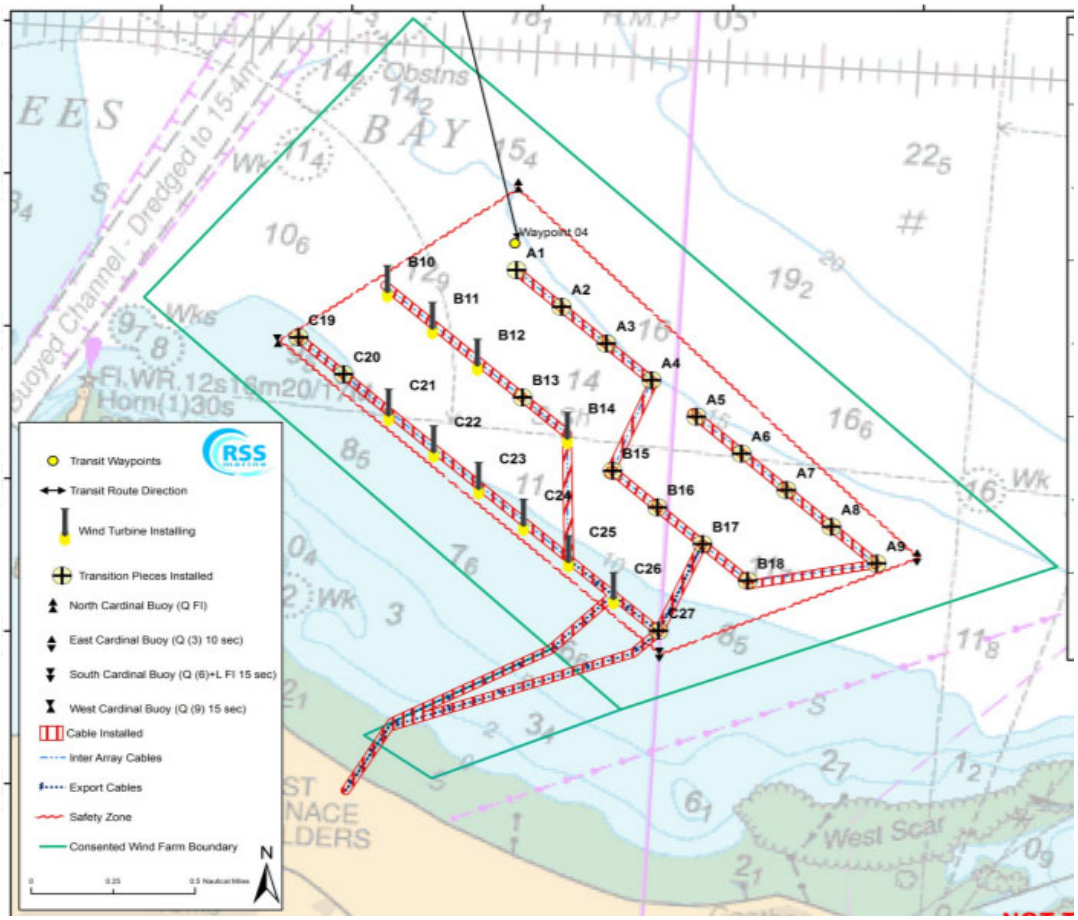

Figure 6.6: *Location of Teesside offshore wind farm*[184]

6.2.1.1 **Intertidal assessment**

Fifteen turbines were selected at random to have scrape samples of marine growth removed from the intertidal and splash zones during low tide (Figure 6.7).

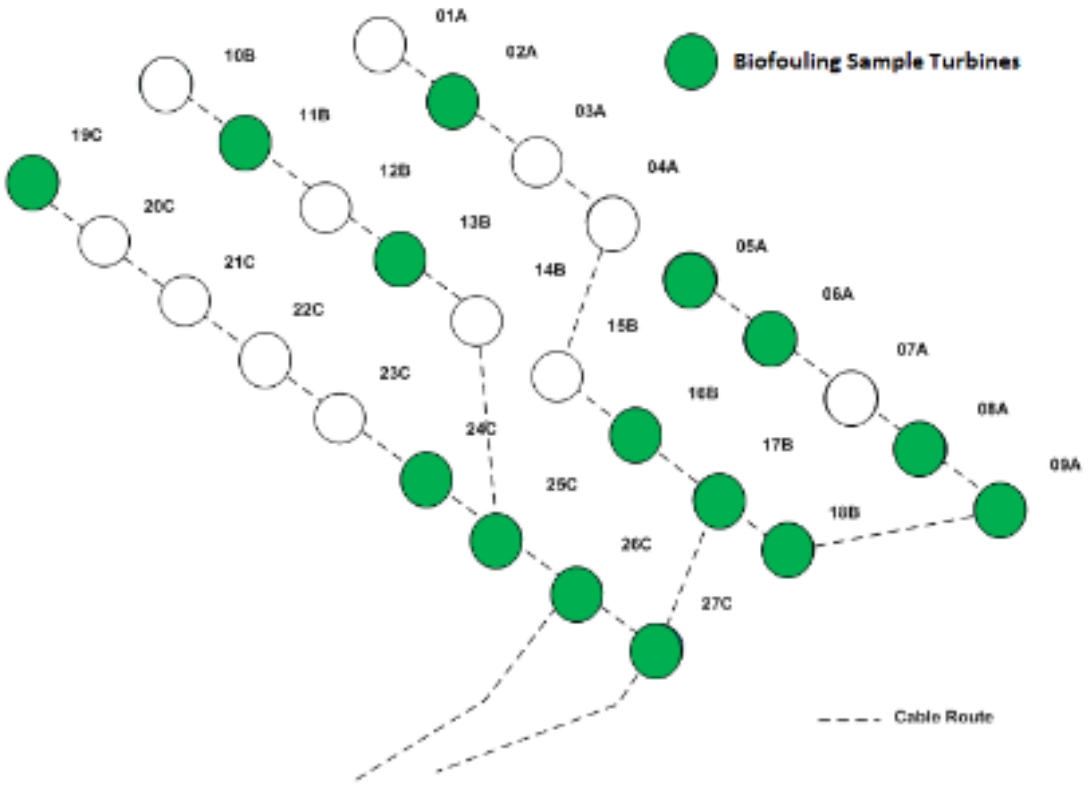

Figure 6.7: *Turbines selected for biofouling sampling of the splash zone.*

Biofouling scrapes of 0.0225m^2 were collected from the transition piece surface using a 15cm heavy-duty paint scraper, transferred into individual grip-seal bags and double-bagged. Samples were stored in an on-board miniature fridge until the vessel returned to port, then transferred into a chest freezer (-18°C). Scrape samples from four circumferential locations on each of the selected turbines were taken, to give a reliable indication of the intertidal biofouling growth around the entire structure. Once the sample was collected and placed into the grip-seal bag, a waterproof label containing the date, time, turbine number and the location of the sample (relative to the ladder) was included within the bag. Typically, the 4 locations where single scrapes were taken corresponded with the positions 45˚,

135˚, 225˚ and 315˚ relative to the turbine ladder as a point of reference (Figure 6.8). Frozen samples were shipped overnight to the Scottish Association for Marine Science (SAMS) laboratory where they were sorted and analysed.

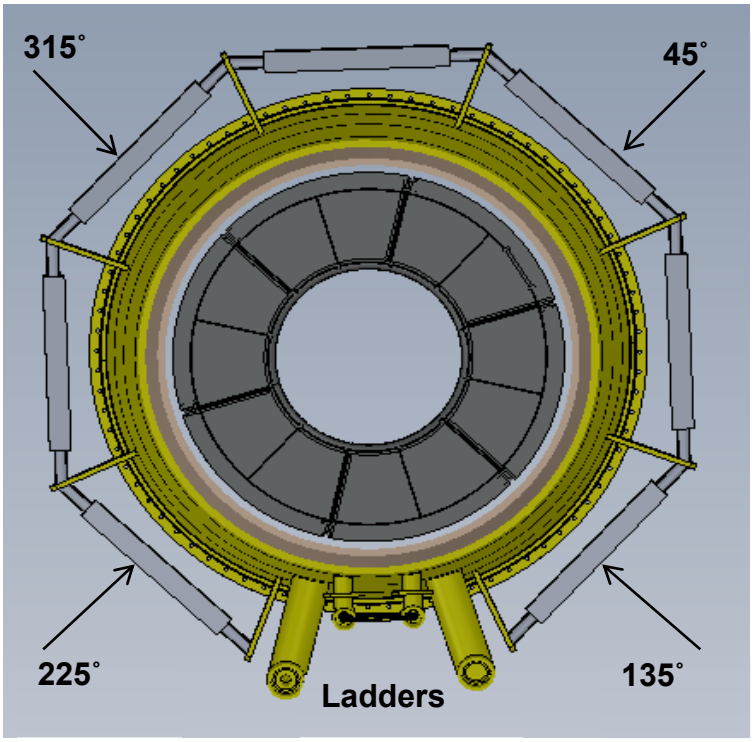

Figure 6.8: *Schematic showing the 4 circumferential locations where scrape samples were taken from (relative to the ladders) on each of the 15 turbines.*

Once defrosted, samples were rinsed thoroughly over a sieve with a mesh size of 1mm, sorted and preserved in ethanol. Samples were sorted by separating out the different types of biofouling and estimating the relative abundance of organisms. Specimens were identified to species level wherever possible or to the nearest higher taxonomic level. The relative abundance of organisms in each sample was estimated. Depending on the growth form; encrusting/solitary, and size or percentage coverage, the species were categorised according to the levels defined in the SACFOR scale (Superabundant, Abundant, Common,

Frequent, Occasional, Rare) as developed by the Joint Nature Conservancy Council (JNCC) [185] (Table 6.1). The wet weight (0.01g) of the dominant fouling organisms was measured using an electronic scale (Sartorius Universal U6100S). These measurements were only recorded if the material was ≥25g. This material was added to a large water-filled plastic pipe and the displacement of water was used to measure the volume (0.01ml) of biofouling. The relative abundance of each identified species in each scrape sample was calculated and discussed.

Table 6.1: *SACFOR scale in relation to coverage and density* [185]***.***

Growth form				Size of individuals/colonies				
% cover	Crust/Meadow	Massive/Turf	<1cm	1-3 cm	3-15 cm	>15 cm	Density	
>80%	S		S				>1/0.001 m^2 (1x1 cm)	>10,000 / m^{-2}
40-79%	A	S	A	S			1-9/0.001 m^2	1000-9999 / m^{-2}
20-39%	C	A	C	A	S		1-9 / 0.01 m^2 (10 x 10 cm)	100-999 / m^{-2}
10-19%	F	C	F	C	A	S	1-9 / 0.1 m^2	10-99 / m^{-2}
5-9%	O	F	O	F	C	A	1-9 / m^2	
1-5% or density	R	O	R	O	F	C	1-9 / 10m^2 (3.16 x 3.16 m)	
<1% or density		R		R	O	F	1-9 / 100 m^2 (10 x 10 m)	
					R	O	1-9 / 1000 m^2 (31.6 x 31.6 m)	
						R	<1/1000 m^2	

S, superabundant; A, abundant; C, common; F, frequent; O, occasional; R, rare

6.2.1.2 **Submerged assessment**

In the submerged/subtidal zones, the vertical distribution of the biofouling community was investigated in August 2015. An underwater survey was conducted using an Ocean Module V8 remotely operated vehicle (ROV) with an

onboard camera. In total, inspection footage from 5 foundations (Figure 6.9) was captured. The ROV inspections took place from a crew transfer vessel (CTV) equipped with a surface positioning system, receiver and monitor for visualisation. The ROV was deployed using the CTV crane (Figure 6.10). Upon deployment from the vessel, the ROV was navigated to the turbine along the surface of the water and then began its descent once the turbine was in view. A continuous recording of video images by means of the camera mounted on the ROV enabled a clear view of the marine growth from sea surface to seabed. The camera also recorded the time, depth, heading and inclination. Footage was viewed using VLC media player version 2.2.6 and species abundance was estimated from footage while playing, as stills were often blurry given the low video resolution and jerky movements of the camera.

3D mapping of the biofouling surface of the Teesside monopiles has been conducted at EDF R&D in the UK and in France to estimate the roughness and thickness of marine growth at each depth. Surface roughness evaluation of a 3D model was conducted using CloudCompare and an estimation of biofouling thickness around the monopile is being conducted through a pile radius evaluation.

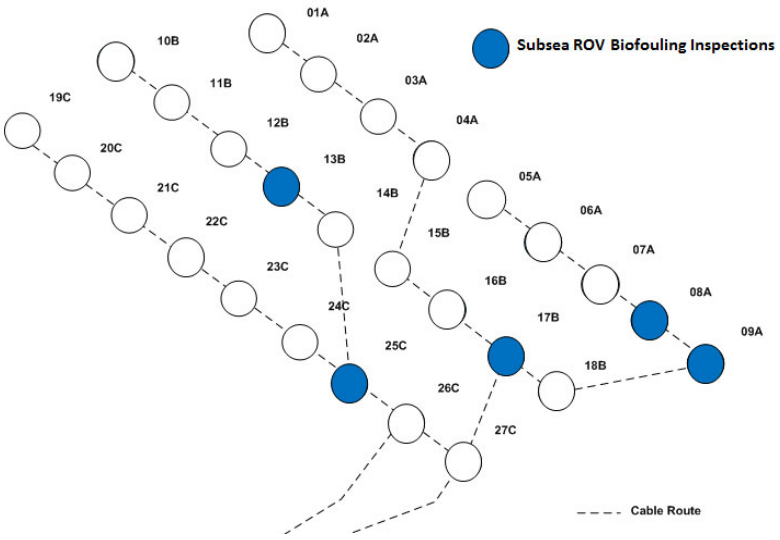

Figure 6.9: *Turbines selected for subsea ROV inspections***.**

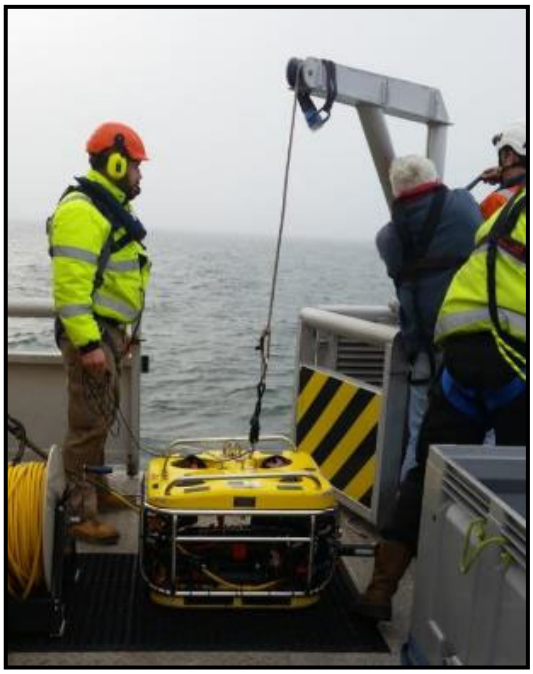

Figure 6.10: *Deployment of Ocean Module V8 ROV from the CTV at Teesside Offshore Wind Farm.*

6.3 **Results**

6.3.1 **Intertidal zone**

During the study period of Summer 2015, nine species were identified in the intertidal scrape samples; five of which were considered as the dominant species observed across almost all 60 samples. The dominant organisms consist of Purple laver (*Porphyra umbilicalis*), two species of barnacles; Acorn (*Balanus crenatus*) and Darwin (*Austrominius modestus*); Marine Splash Midge larvae (*Telmatogeton japonicus*) and green filamentous algae (*Ulothrix* spp.). *A. modestus* and *T. japonicus* are non-indigenous species. The relative abundance of taxa was estimated using the SACFOR scale according to [185] and shown in Table 6.2. The wet-weight and volume of biofouling material from each scrape sample was calculated and presented in Table 6.3. The totals are summarised in Table 6.4.

Table 6.2: *Overview of recorded intertidal species at Teesside Offshore Windfarm with indication of their abundance according to the SACFOR scale as developed by the Joint Nature Conservancy Council (JNCC)* [185].

Turbine Row A	A02				A05				A06				A08				A09			
	45	135	225	315	45	135	225	315	45	135	225	315	45	135	225	315	45	135	225	315
Rhodophyta																				
Porphyra umbilicalis (Kützing, 1843) •	O	S	R	S	R	F	A	S	R	R	O	R	R	R	A	R	O	O	A	O
Audouinella spp. (Bory de Saint-Vincent, 1823)	-	O	-	-	R	-	-	F	-	-	R	-	-	-	O	R	-	-	-	-
Chlorophyta																				
Ultothrix spp. (Kützing, 1843) •	C	R	O	-	R				A	C	A	C	C	S	R	A	O	A	F	F
Ulva lactuca (Linnaeus, 1753)	-	-	-	-	-	-	-	-	R	-	-	R	-	-	-	R	-	-	-	-
Cirripedia																				
Balanus crenatus (Bruguière, 1789) •	A	-	C	R	-	-	-	-	C	-	F	F	C	F	O	A	C	-	-	C
Austrominius modestus (Darwin, 1854)* •	S	-	F	R	R	A	-	-	-	-	-	F	F	-	-	A	F	-	-	C
Insecta																				
Telmatogeton japonicus (Tokunaga, 1933)* •	A	-	A	C	C	A	-	-	A	C	A	A	A	A	A	A	A	A	A	A
Gastropoda																				
Patella vulgata (Linnaeus, 1753)	-	-	-	-	S	-	-	-	-	-	-	-	-	-	-	-	-	-	-	-
Turbine Row B	B11				B13				B16				B17				B18			
	45	135	225	315	45	135	225	315	45	135	225	315	45	135	225	315	45	135	225	315
Rhodophyta																				
Porphyra umbilicalis (Kützing, 1843)	S	O	S	A	F	C	S	S	F	R	A	O	S	R	A	C	R	R	O	O
Audouinella spp. (Bory de Saint-Vincent, 1823)	O	O	-	-	-	-	-	R	-	-	-	-	F	-	-	R	O	-	F	O
Chlorophyta																				
Ultothrix spp. (Kützing, 1843)	-	R	-	A	R	R	-	-	R	C	R	F	R	-	R	O	-	A	S	A
Ulva lactuca (Linnaeus, 1753)	-	-	-	-	-	-	-	-	-	-	-	-	-	-	-	-	-	-	R	R
Cirripedia																				
Balanus crenatus (Bruguière, 1789)	R	F	R	-	A	A	-	-	F	-	O	F	R	F	F	F	A	S	S	C
Austrominius modestus (Darwin, 1854)	-	F	R	-	A	-	-	-	-	-	-	-	-	-	O	O	A	A	A	F
Insecta																				
Telmatogeton japonicus (Tokunaga, 1933)	-	C	C	A	A	A	-	C	C	A	A	A	A	A	A	A	S	S	A	A
Gastropoda																				
Patella vulgata (Linnaeus, 1753)*	-	S	-	-	-	-	-	-	C	-	-	-	-	-	-	-	-	-	-	-
Turbine Row C	C19				C24				C25				C26				C27			
	45	135	225	315	45	135	225	315	45	135	225	315	45	135	225	315	45	135	225	315
Rhodophyta																				
Porphyra umbilicalis (Kützing, 1843)	O	F	R	C	F	R	S	O	O	R	S	C	A	R	C	S	-	-	R	0
Audouinella spp. (Bory de Saint-Vincent, 1823)	-	-	-	R	-	-	-	-	O	-	-	-	R	-	-	-	-	-	-	-
Chlorophyta																				
Ultothrix spp. (Kützing, 1843)	-	-	F	O	R	F	F	-	C	C	O	O	-	-	R	R	-	-	R	-
Ulva lactuca (Linnaeus, 1753)	-	-	-	-	-	-	-	-	-	-	-	-	-	-	-	-	-	-	-	-
Cirripedia																				
Balanus crenatus (Bruguière, 1789)	-	S	S	O	F	R	F	F	F	F	R	F	F	R	A	F	R	R	O	O
Austrominius modestus (Darwin, 1854)	S	-	S	R	F	R	-	O	-	O	-	F	F	R	C	F	-	R	O	R
Insecta																				
Telmatogeton japonicus (Tokunaga, 1933)	S	S	A	C	A	C	A	A	A	C	A	A	A	C	A	A	-	-	-	C
Idotea Balthica (Pallas, 1772)	-	-	-	-	-	-	-	-	-	-	-	-	-	R	-	-	-	-	-	-
Gastropoda																				
Patella vulgata (Linnaeus, 1753)*	-	-	-	S	-	-	-	-	-	-	-	-	-	-	A	-	-	C	C	-
Bivalvia																				
Mytilus edulis (Linnaeus, 1758)	-	-	-	-	-	-	-	-	-	-	-	-	-	S	-	-	-	-	-	-
Nemertea																				
Emplectonema spp. (Stimpson 1857)	-	-	-	-	-	-	-	-	-	-	-	-	-	A	-	-	-	-	-	-

*** Non-indigenous species**

• Dominant species

Table 6.3: The wet-weight and volume of biofouling material collected from the intertidal zone of foundations at Teesside. "n/a" refers to samples that were less than 25g in weight and removed from analysis. Blank cells mean that no species were present.

Turbine Row A	A02		A05		A06		A08		A09	
	Weight (g)	Volume (cm^3)	Weight (g)	Volume (cm^3)	Weight (g)	Volume (cm^3)	Weight (g)	Volume (cm^3)	Weight (g)	Volume (cm^3)
Porphyra umbilicalis	278	206	102.8	127.5	n/a	n/a	27.9	23.7	89.5	99.5
Ultothrix spp.									149	n/a
B. crenatus & A. modestus	137.1	130							186.1	179
Patella vulgata			84.4	88						
Turbine Row B	B11		B13		B16		B17		B18	
	Weight (g)	Volume (cm^3)	Weight (g)	Volume (cm^3)	Weight (g)	Volume (cm^3)	Weight (g)	Volume (cm^3)	Weight (g)	Volume (cm^3)
Porphyra umbilicalis	255	160	427.4	235	77.07	79.4	100.8	103		
Ultothrix spp.	76.9	72.6								
B. crenatus & A. modestus			171.1	186.6					127	113.3
Patella vulgata	107.3	100								
Turbine Row C	C19		C24		C25		C26		C27	
	Weight (g)	Volume (cm^3)	Weight (g)	Volume (cm^3)	Weight (g)	Volume (cm^3)	Weight (g)	Volume (cm^3)	Weight (g)	Volume (cm^3)
Porphyra umbilicalis			107	102.2	106.8	116	61.5	42.9	n/a	n/a
B. crenatus & A. modestus	246.3	235.1					38.5	6.8		
Patella vulgata	97.6	84.5					25	15		
Mytilus edulis							726.5	550		

Table 6.4: *The total weight and volume of biofouling material sampled across each turbine.*

Turbine Row A	**A02**	**A05**	**A08**	**A08**	**A09**
Total Weight (g)	415.1	336	27.9	n/a	424.6
Total Volume cm^3	336	187.2	23.7		278.5
Turbine Row B	**B11**	**B13**	**B16**	**B17**	**B18**
Total Weight (g)	439.2	598.5	77.1	100.8	127
Total Volume cm^3	332.6	421.6	79.4	103	113.3
Turbine Row C	**C19**	**C24**	**C25**	**C26**	**C27**
Total Weight (g)	343.9	107	106.8	851.5	n/a
Total Volume cm^3	319.6	102.2	116	614.7	

Each biofouling organism was allocated a percentage of the total wet-weight distribution at each of the sample location (Figure 6.11). At the 45˚ location shown in Figure 6.11a), barnacles represent the greatest proportion of the total wet-weight. At the 135˚ location in 86b), the mussel sample represents over 50% of the total wet-weight measured at this sample site, even though this reflects only 1 sample. At the 225˚ and 315˚ locations, purple laver represents the greatest wet-weight out of all the sampled organisms.

The relative abundance of biofouling species across all scrape samples is indicated in Figure 6.12. The y-axis shows the frequency of occurrence of each percentile range for each species out of the 60 samples that were analysed. The <1% band refers to the absence of a particular species, i.e. Blue Mussels were only found in 1 sample for which they were Superabundant (>80%) and were absent from the remaining 59 samples. Purple Laver and Marine Splash Midge larvae have the lowest occurrence in the <1% band because they were occurred in almost all samples, particularly Purple Laver which was only absent from 3 out of 60 samples.

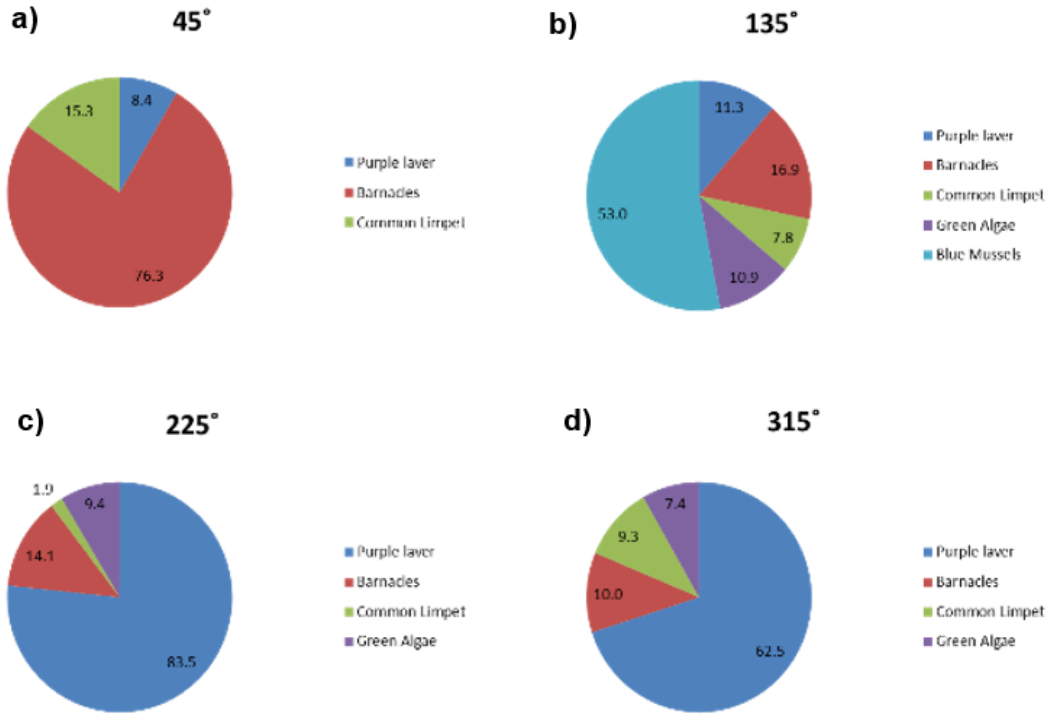

Figure 6.11: *The percentage allocation of the total wet-weight of each biofouling organism measured at each circumferential location.*

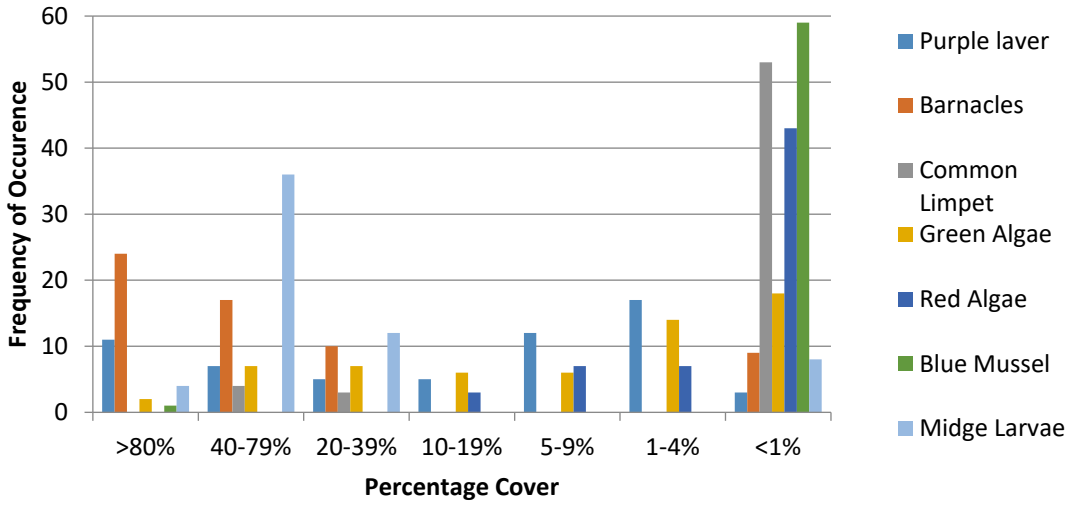

Figure 6.12: *The relative abundance of each biofouling organism across the 60 scrape samples.*

6.3.2 **Subtidal Zone**

The video footage obtained from the ROV inspection of 5 foundations at Teesside OWF was visually analysed in slow motion and in individual frames to identify biofouling species and record patterns of biofouling zonation with depth. Biofouling species could be easily identified when the camera was recording in colour; however, the majority of footage was recorded in monochrome to improve visual inspection of the cable protection system. Across all foundations, the most commonly observed species were Blue mussel (*M. edulis*), Kelp (*Laminaria spp.*) and Plumose anemone (*M. senile*). The full list of identified species in the submerged zone can be found in Table 6.5.

Table 6.5: *The biofouling organisms identified during the subsea ROV inspection of 5 turbine foundations at Teesside OWF.*

Subtidal Biofouling Assessment	
Mytilus edulis	Blue mussel
Laminaria spp.	Kelp
Metridium senile	Plumose anemone
Asterias rubens	Common starfish
Ophiothrix fraglis	Brittle star
Echinus spp.	Sea urchin
Hydroides spp.	Serpulid worm
Cancer pagurus	Edible crab
Necora puber	Velvet swimming crab
Homarus gammarus	Common lobster

A clear zonation pattern of biofouling organisms was observed across the foundations that is consistent with literature. Clusters of Kelp (*Laminaria* spp.) dominated the upper 2-metres on the boat fenders (Figure 6.13). Immediately

below the kelp, dense clusters of mussels (*M. edulis*) form around the boat fenders and on the secondary steel, down to a depth of approximately 5-6m where the galvanic anode cage begins. Clusters of mussels were also observed around the anodes (Figure 6.14). From the anodes down to the cable exit and seabed (9 to 13m) there was a mixed community primarily dominated by plumose anemone (*Metridium senile*) and starfish (*Asterias rubens*). However, dense patches of brittle stars (*Ophiothrix fraglis*) were commonly observed when colour footage was available. Crabs (*Necora puber* and *Cancer pagarus*) were commonly observed within crevices created by the transition piece/monopile grout connection and below the Teklink© cable protection system. The presence of lobsters (*Homarus gammarus*) was noted where the exit cable met the seabed, and in crevices between the cable and scour protection. Additionally, towards the seabed numerous pelagic fish were recorded aggregating around the bottom of the pile and the cable.

Figure 6.13: *Kelp/Blue mussel transition zone at 1.9m depth on WTG B17.*

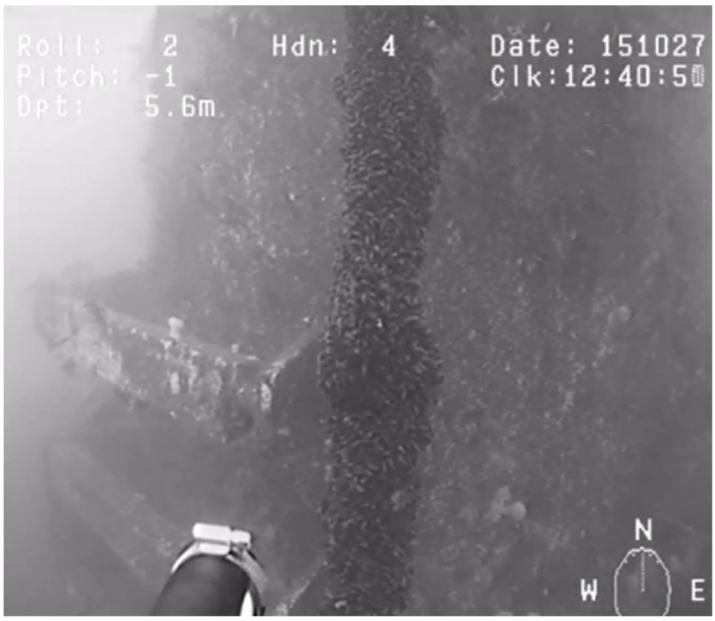

Figure 6.14: *Clusters of Blue mussels by the anode cage at 5.6m depth on WTG A08.*

6.4 **Discussion**

6.4.1 **Biofouling Observations**

A biofouling assessment was conducted at Teesside Offshore Wind Farm to ascertain the type and extent of marine growth on both the intertidal and submerged zones of the turbines. An assessment of the marine growth was not only an opportunity to improve the understanding of the species diversity and community morphology, but also enabled the development and testing of two sampling methodologies for the intertidal and subsea zones of offshore wind turbines; scrape sampling and underwater ROV surveying, respectively.

Some samples had so little biofouling material that anything below 25g was considered insignificant in terms of additional mass. Additionally, for soft fouling and green algae in particular, the change in volume was so minute for samples <25 to 30g and very difficult to measure using the displacement technique. Even in samples where green algae was superabundant, the wet-weight and volume of the material was relatively low, i.e. 14.4g and 11.6cm^3 respectively at 225˚ on WTG18B. The total weight and volume of biofouling material on each foundation is displayed in Table 6.3.

Only 1 out of the 60 scrape samples contained mussels despite the fact that they have been visually observed on all foundations at Teesside. This sample was collected from WTG 26C at the 135˚ location and was almost entirely comprised of blue mussels of approximately 4cm length. The mussels had the greatest wet-weight and volume of all the sampled material; 726.5g and 550cm^3 respectively. When considering that this sample was collected from only a small area of 0.023m^2, this is a significant added mass on the structure. If we scale up the 0.023m^2 area to consider the possibility that this mussel layer is occurring around the entire circumference of the structure this would be an approximate area of 2.2 m^2, i.e. 0.1524m x 14.4m (MP circumference length). In this area, approximately 69,491g (~70kg) of mussels could potentially be attached which is a substantial additional weight.

The biofouling assessment from the splash and submerged zones suggests three clear zones of marine growth communities with depth. The splash zone is dominated by the Marine Splash Midge, Purple Laver and Barnacles, as

these organisms were observed in almost all samples; particularly the Midge larvae. The submerged zone can be split into the infralittoral zone; which comprises the first 6m from LAT to the anode cage, then the subtidal zone which covers from the anode cage down to the seabed. The infralittoral zone is dominated by Kelp and Mussels; this is particularly notable on the boat fenders and secondary steel, whereas the subtidal zone is dominated by Cnidiarians (anemones) and Echinoderms (starfish, brittle star and sea urchin). A schematic of the biofouling zonation can be seen in Figure 6.15.

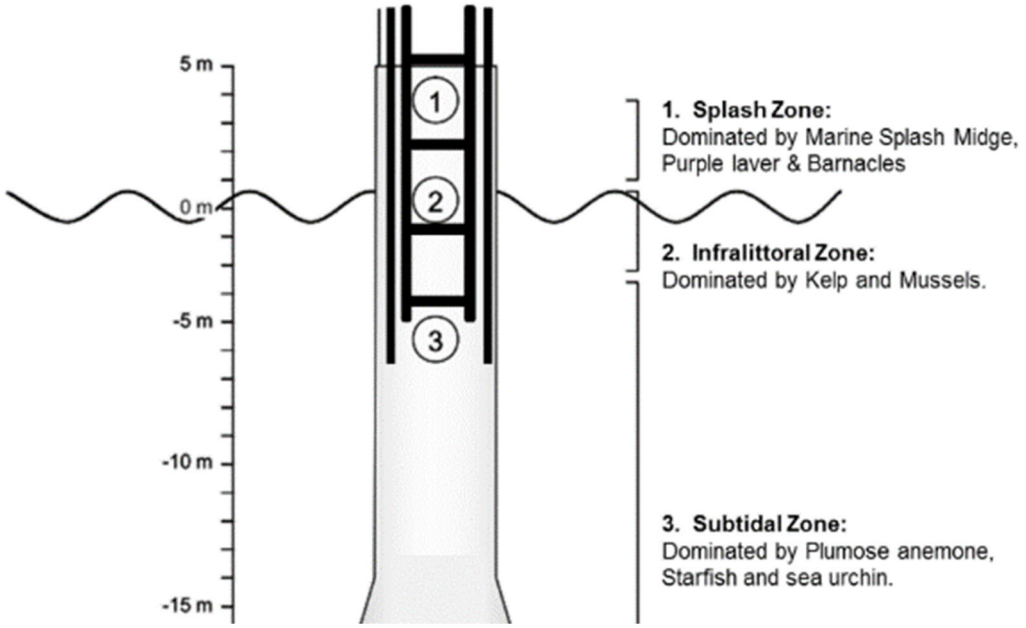

Figure 6.15: The observed zonation pattern of biofouling organisms on the turbines at Teesside OWF.

Similarly to observations at Thornton Bank offshore wind farm (around 30km off of the Belgian coast), the intertidal-splash zone on Teesside monopiles was dominated by the presence of *Telmatogeton japonicus* larvae. These larvae was found in almost all samples, and up to 800 individuals were counted in a

single sample (WTG 19C at 45˚). It was difficult to identify the larvae as although this species has been observed on offshore structures in Europe, it has not been documented at any other offshore wind farm in the UK North Sea. Samples of the collected material were sent to Yngve Brodin; an expert in the field of Diptera research who compared the larvae with his own material from the Baltic Sea [106] and confirmed that it was in fact most likely to be *T. japonicus.* The presence of the midge larvae at Teesside is of particular interest as it confirms that this non-native species is expanding its geographical range from its known European locations (Germany, Denmark and Sweden). Currently, there is no published occurrence of this species at any other UK offshore wind farm.

Examination of the biofouling material identified the presence of 2 key species that were present among almost all samples; Purple laver (*Porphyra umbilicalis*) and Marine Splash Midge larvae (*Telmatogeton japonicus*). Blue Mussels (*M. edulis*) were only present within one scrape sample, however represented almost 100% of the abundance within that sample. Visual observations and photographic evidence of the splash zones collected by the technicians at Teesside confirm that mussels are common in the intertidal zone and therefore their occurrence in 1 sample out of 60 is not a true representation of their presence at this zone throughout the windfarm. However, it is likely that access to mussels would only be possible during low tide when they are most exposed and therefore perhaps only a single sample was possible during the sampling period. Additionally, the size of the mussels (up to 4cm) suggests that they were probably at least 1-2 years old when sampled. In optimal

conditions, *M. edulis* can grow to 6cm-8cm in length within 2 years, but in the high intertidal zone growth can be significantly lower and it may take 15-20 years to reach 20-30mm in length [186]. Therefore, this patch of mussels had been able to grow for a significant period without removal by jet-wash cleaning. Whereas other turbines that are visited more frequently are likely to be cleaned more regularly and therefore have less mussel-dominated communities at the splash zone. Cleaning can effectively reset the community succession, keeping it in a continuous young stage and affecting the species composition [187]. This may explain the sole presence of some small barnacles within some samples (1-2mm) and very little else. Nevertheless, the subsea inspection found that dense clusters of mussels were present below the surface to the anode cages in all sampled turbines. The lack of mussel presence beyond this depth is likely to be controlled by predation pressure from starfish (*Asterias rubens*) [188][189] and sea urchins (*Echinus spp*) that could be seen from approximately 6m depth down to the seabed. Crabs are also known predators of mussels and would control the extent of their growth below the sublittoral zone. In this instance, crabs were primarily found toward the seabed within the crevices created by the Tekmar system, however in some occasions they were observed on the external anodes close to the mussel-dominated zone. Similar zonation patterns with the mussel/barnacle belt in the first 5 to 6m have been reported on other artificial hard substrata in the intertidal zone, and on other wind farms in the North Sea [97], [183]. In order to optimise the cleaning regime and removal of hard marine growth from

the transition piece, it is important to understand their life cycle and seasonal patterns.

6.4.2 **The Intertidal Zone**

6.4.2.1 **Lifecycle and seasonal patterns of hard biofouling at Teesside**

Balanus crenatus barnacles are one of the dominant species observed at the intertidal zone. The larvae are released between February and September, with peaks in April and late summer when phytoplankton levels are highest. However, the release is not synchronised with the spring algal bloom like other species, *Semibalanus balanoides* for example [190]. Peak settlement of larvae occurs in April and declines until October. This species grow rapidly except in the winter months. April-settled individuals may release larvae the same July and reach full size before their first winter, whereas individuals that settled later reach maximum size by the end of Spring the following year [191]. *B. crenatus* has a life span of 18 months [192] and their growth rate varies greatly with the degree of current flow and the presence of silt.

Austrominius modestus was the other barnacle species commonly observed at the intertidal zone. This species occurs naturally in Australasia and was first reported in Britain in 1964, by which time it was widespread in the South East of England. This non-native species not only competes with native British species, particularly *Balanus balanoides,* but has colonised some sheltered and estuarine habitats not previously inhabited by them. *A. modestus* prefers sheltered shores, but it grows very fast and tolerates lower salinity and higher

temperatures than most native barnacles, except other introduced species [193]. *A. modestus* has a relatively long life span compared to *B. crenatus* which is estimated to be around 5 years [194]. It reaches sexual maturity around 8 weeks after settling and breeding normally begins when the temperature exceeds 6˚C. This species is known to have a very high fecundity and release successive broods throughout the year, with each brood being released after 2 weeks. However, in the winter months development could take 60 to 80 days [193]. *A. modestus* competes with other shallow water barnacles for space. At its northern limit reproduction begins later than in the native species, and other species have already settled by the time *A. modestus* is ready to settle. Also, it is able to settle at higher levels of the shore than *S. balanoides* as well as deeper into subtidal levels. Since it may reproduce throughout the year it has a high reproductive potential, and in some places could therefore be dominating barnacle species. In some places it may have completely replaced the native barnacles [195]. In the majority of Teesside samples containing barnacles, both *A. modestus* and *B. crenatus* individuals were observed. There were only 3 instances where *A. modestus* was the only barnacle species: Turbine A05 at 45° and 135°, and Turbine C19 at 45°.

Blue mussels (*M. edulis*) are a gregarious species, and at high densities form dense beds of up to 6 layers, with individuals bound together by byssus threads. Young mussels colonize spaces within the bed increasing the spatial complexity, and the bed provides numerous niches for other organisms. For example, within the Teesside samples, different species of worms were identified within the mussel bed. Overcrowding results in mortality as

underlying mussels are starved or suffocated by the accumulation of silt and faeces especially in rapidly growing populations [196]. Although sometimes abundant in the subtidal, *Mytilus edulis* is primarily an intertidal species that can withstand extreme wave exposure, maintaining byssal attachment in high energy environments. The upper limit of Mytilus edulis populations on rocky shores is determined by its tolerance of temperature and desiccation, which may be synergistic, i.e. sudden mass mortalities at the upper limit of intertidal mussel beds are often associated with prolonged periods of unusually high temperatures and desiccation stress [186] The lower limit of distribution is strongly influenced by predation, primarily from starfish but also dog whelks and crabs. For example, on the east coast of England, the starfish *Asterias rubens* and the dog whelk *Nucella lapillus* eliminate mussels from the lower intertidal [197]. In Ireland, however, the lower limit is probably controlled by the crabs *Carcinus sp*. and *Liocarcinus sp*., the dog whelk *Nucella lapillus* and the starfish *Marthasterias glacialis*. In terms of spawning, in the North East of England, there is a partial spawning in spring followed by a less intensive secondary spawning in summer to late August or September [197]. Mantle tissues store nutrient reserves between August and October, ready for gametogenesis in winter when food is scarce [186]. Larvae spawned in spring can take advantage of the phytoplankton bloom. The secondary spawning is opportunistic, depending on favourable environmental conditions and food availability.

The common limpet (*Patella vulgata*) spawning process takes place once a year, usually from October to December, although the timing varies around

the British Isles. It has been stated in the literature that spawning actually starts in September in Scotland and North-East England [198]. Fertilisation occurs externally and the larvae spend their first few days of life in the water column, after which time they settle. The life span varies but is between 10 and 20 years.

The variation in sample size and species abundance can perhaps be attributed to the last time turbines were cleaned of marine growth. At Teesside, fouling removal takes place during the summer months when growth is high. With peak settlement occurring in April for some barnacle species that will then go on to spawn 2 to 3 months later, removal in the summer will not only clear recently settled individuals but could also prevent these individuals from spawning the same season. This could account for the lack of barnacles, or presence of particularly tiny barnacles in some scrape samples that had only recently settled and metamorphosed. Figure 6.12 illustrates that barnacles were Superabundant, Abundant, Common or not present, therefore it is unlikely that only a few barnacles would be found in a single sample and their presence/absence is likely to be determined by cleaning.

As a result of this biofouling research, a better understanding of intertidal biofouling species and their lifecycles has improved and optimized the marine growth removal from the boat landing area of the Teesside TPs. Cleaning schedules now coincide with the peak larval settlement period of barnacles and mussels to reduce and even prevent the settlement of the larvae, and

consequently limit the further release of larvae during the summer months. This reduces the number of jet washing maintenance trips throughout the year.

6.4.2.2 **Non-Native Species**

The presence of the non-native Marine Splash Midge larvae (*Telmatogeton japonicus*) and its domination of the splash zone was not initially anticipated, however, the same observations have been reported at other offshore wind farms [22], [183]. Similarly to Teesside, *T. japonicus* formed a distinct belt within the splash zone at Thornton Bank and a monoculture at Horns Rev. With very little published literature on this species and its potential influence on native biofouling species, it is difficult to speculate what the local ecological impacts might be, Brodin and Andersson (2009) reported that larvae, pupae and adults are active throughout the year, and flying adults can also be seen under winter conditions with an air temperature below freezing [106]. This suggests that the species can tolerate low temperatures and produce larvae even during the winter. Rapid colonisation of this species on offshore wind farms and artificial substrata has been reported, which strongly suggests that it can quite easily become a dominant species and out-compete other species, less tolerant to low temperatures. The possible detrimental ecological impacts of this non-native species have not yet been evaluated. Therefore, further research is required to determine if this could be a potential problem at Teesside since the species possesses several features appropriate for a marine invasive; namely its high ability to survive harsh, highly variable, and unpredictable conditions.

6.4.3 **The Submerged Zone**

In terms of the subsea inspection, the biofouling characteristics observed on the monopiles were not representative of current design codes and guidelines. As discussed in Chapter 2, The design codes advise that an offshore wind turbine in the North Sea should be designed to withstand approximately 100mm thickness of marine growth at each subsea zone [35]. Footage from the ROV survey strongly suggests that the values provided in these guidelines are overly conservative and therefore structures likely to be over-engineered to account for marine growth that is, in reality, a fraction of the advised thickness guidelines. There was significant soft fouling in the subtidal zone that was primarily dominated by Plumose anemone (*Metridium senile*) and the aforementioned predators that control the spread of the mussel community. From an engineering perspective, soft fouling is not a concern when considering the potential increase in hydrodynamic loads due to biofouling [199]. This layer is thin and has a very low roughness; therefore, the subtidal zone can be discounted from future analysis of biofouling thickness and roughness measurements and their influence on loading behaviour. More research is needed at the intertidal zone, where large kelp communities and dense mussel aggregations form on the boat-landing platform. These communities could significantly increase the mass and drag of the structure which in turn will influence loading. A survey of biofouling at Egmond aan Zee Offshore Wind Farm determined that the increase in drag coefficient of the hard fouling communities on the upper part of the monopile is a factor of 2.4,

between smooth and rough [199]. It is necessary to quantify these characteristics in the sub-littoral zone of fixed offshore wind turbines to ensure that the thickness and roughness measurements are in line with the current standards.

6.4.3.1 **Biofouling Mapping**

3D mapping of the biofouling surface of the Teesside monopiles has began at EDF R&D in the UK and in France to estimate the roughness and thickness of marine growth at each depth [200]. A 3D map has been created for one foundation (Figure 6.16) which can then be used as a representative for the entire farm, from which roughness (Figure 6.17) and thickness (Figure 6.18) can be evaluated. From this it is possible to determine how the real values differ from those provided in the guidelines.

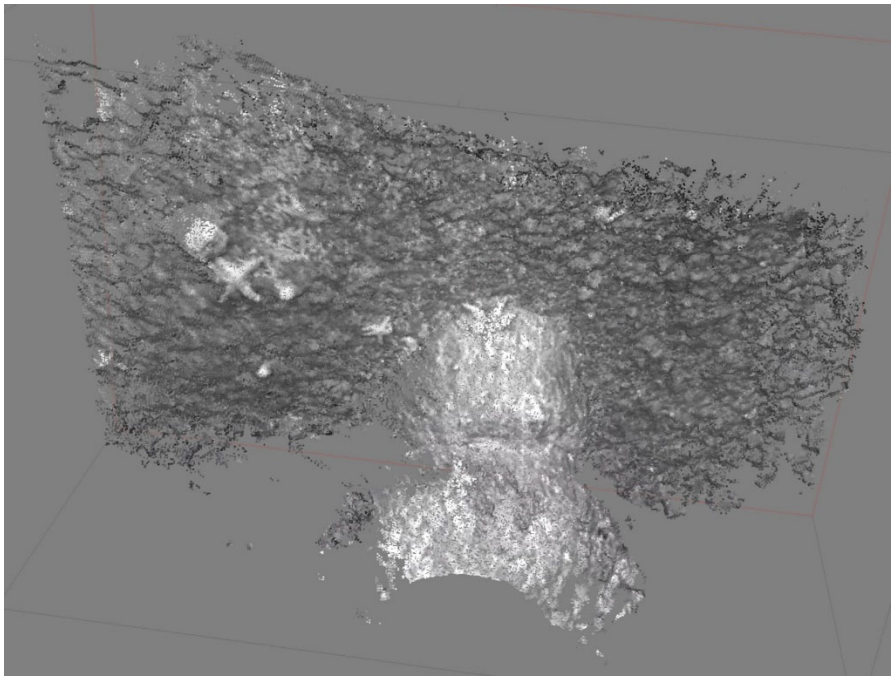

Figure 6.16: Surface reconstruction of a monopile foundation at Teesside [200]

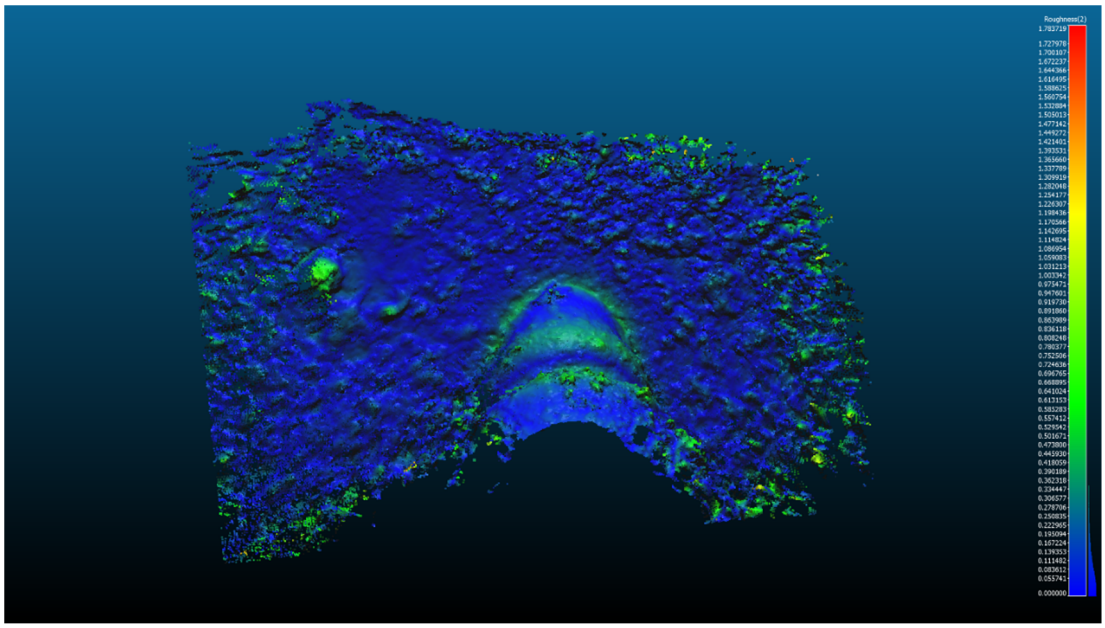

Figure 6.17: Surface roughness evaluation [200]

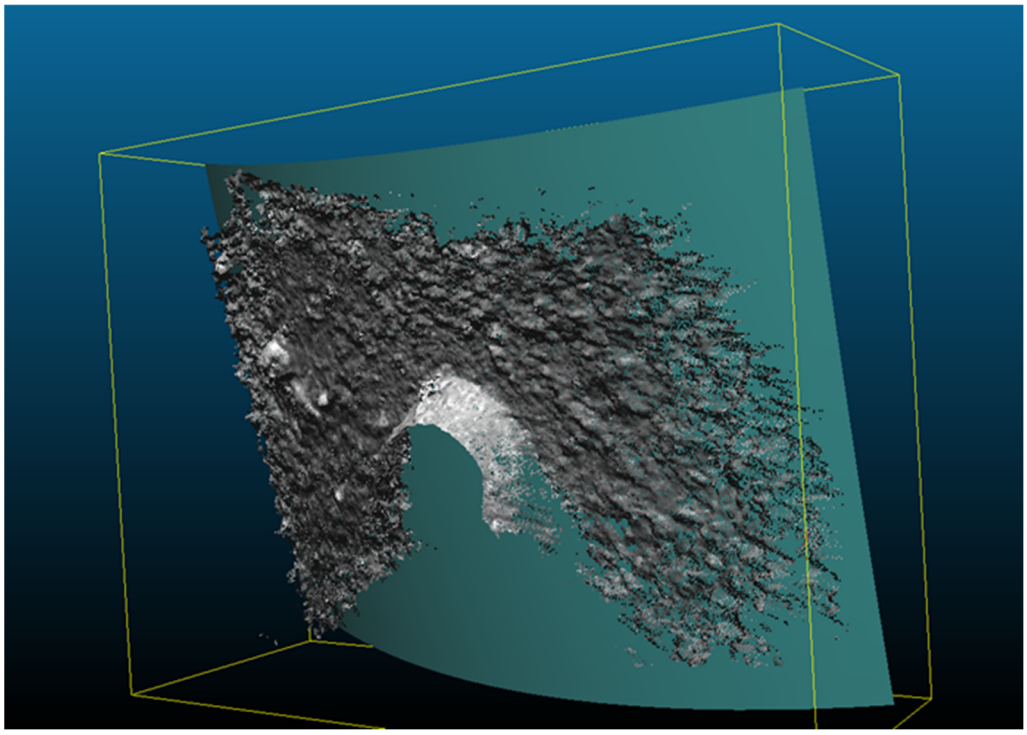

Figure 6.18: Monopile radius evaluation

Results from this study can be used to improve the design of future monopiles to ensure they are not over-engineered for 100mm of biofouling thickness from sea surface to seabed. Additionally, improved guidelines with more realistic biofouling thickness and roughness values are required for offshore wind farms in the North Sea are required.

7 Concluding Remarks

7.1 Approach to The Problem

This thesis presents an approach to better understand the influence of internal monopile corrosion and external biofouling on the operation of offshore wind farms. The challenges associated with corrosion and biofouling assessment of offshore structures are discussed in a comprehensive literature review that outlines key knowledge gaps and opportunities to develop a better understanding on how to manage these issues in the offshore wind industry. In recent years, offshore wind operators have expressed a growing concern that turbine foundations may be operating outside their design criteria, due to unexpected issues such as internal leaks, tidal conditions and acidification. In combination with external biofouling accumulation, this poses not only a structural concern but also a health & safety risk to technicians during turbine transfer. The principal aims of this thesis were to assess the internal monopile corrosion behaviour and biofouling characteristics at Teesside Offshore Wind Farm and to develop a predictive model to classify the internal corrosion rate of monopiles influenced by a range of environmental factors. The methodologies and tools developed through this work can then be adopted by offshore wind operators and replicated across a range of sites to support monopile fatigue life assessment and O&M decision making.

The principal environmental parameters influencing the internal corrosion behaviour of monopiles at Teesside were identified and investigated in a comprehensive laboratory study across 15 months. Individual parameters were isolated during trials (pH, oxygen, tidal conditions) to evaluate their individual effect on the corrosion rate of monopile steel specimens.

Complementary trials were conducted at Teesside Offshore Wind Farm, whereby specimens were mounted to various locations within a selection of foundations to assess the corrosion behaviour of monopile steel at different internal regions (atmospheric, tidal, immersed and seabed). Corrosion analysis was conducted at EDF R&D MMC Laboratory in France in parallel with the laboratory trials.

The corrosion rate data generated from both the experimental and offshore trials, was combined with that of another UK offshore wind farm to develop a predictive decision tree tool for corrosion rate classification under specific environmental conditions. The model can support detailed structural integrity analysis and fatigue life calculations for foundations.

In addition to the ongoing corrosion work, a comprehensive biofouling assessment was conducted at Teesside Offshore Wind Farm. Two different sampling methodologies were designed and trialled for two different biofouling zones; the intertidal zone on the transition piece and the submerged zone (using an underwater ROV). The data collected from each sampling strategy was analysed and a detailed account of species morphology and biofouling characteristics at Teesside was given. This work has already led to

improvements in maintenance strategies and will support a structural integrity analysis.

7.2 Findings and Contribution to Knowledge

The overarching conclusion from this research is that internal monopile corrosion is a critical issue for offshore wind operators and is an active area of research within the industry. The accumulation of biofouling is also a challenge, particularly in terms of health and safety and in the spread of invasive or non-native species.

An in-depth assessment of the post-construction issues at Teesside Offshore Wind Farm identified key operational and lifetime considerations that were the driving force of this industrial research project. This investigation confirmed initial assumptions that the leaking cable seals and utilisation of cathodic protection in confined space are key mechanisms in influencing the corrosion behaviour of the internal monopile steel. The results from both experimental and offshore trials suggest that internal tidal conditions created by the leak, which also facilitates fresh oxygenated seawater ingress are primary drivers for high corrosion rates. This was reflected in the predictive decision tree tool that also highlighted the importance of exposure time. Longer-term exposure to aerobic tidal conditions is expected to accelerate corrosion rate.

The results from this study will hopefully provide an evidence base and support an update in DNV standards and guidance documentation for assessing and monitoring internal corrosion of monopile foundations.

Detailed analyses of the corrosion samples taken from Teesside monopiles strongly suggested the presence of sulphate-reducing bacteria (SRB) in the mud-zone which and microbiologically influence corrosion at this zone. This was also reinforced by evidence of localised pitting corrosion on samples. Although not the focus of this study, this result presents an interesting opportunity for investigation, to better understand the bacterial composition within the monopile mud-zone and its influence on corrosion.

Due to constraints associated with timing, resource and offshore access to the turbines, the corrosion trials were limited to a 15-month duration. Longer term trials over several years would provide a much better indication of the corrosion behaviour of the structures over the long term and an opportunity to monitor changes in corrosion rate over a greater exposure time. The long-term corrosion rate of the structures reflected in Phase 4 of Figure 4.36 is of greater value to the operator of an offshore wind farm as it enables a more realistic calculation of fatigue life assessment. Future corrosion loss measurements of the remaining coupons within the monopiles at Teesside will support this detailed assessment.

The decision tree method for predictive corrosion analytics performed well using the database collated throughout this research (86.1% accuracy). To resolve some of the limitations with this tool, a much larger dataset is required. This decision tree model has the potential to be a powerful

tool in classifying the corrosion behaviour of internal monopile regions if wind farm operators could openly share their corrosion inspection and monitoring data and create a much wider, more detailed database.

The biofouling assessment at Teesside tested two methodologies to survey the marine growth from both the splash zone and the submerged zone. The scrape sampling technique was successful in the removal of the marine growth and the shipment for laboratory analysis. Additionally, the sorting and identification process, although laborious was reliable and ensured that each organism was identified accurately. The variation in samples, i.e. some superabundant with a range of species and others almost empty with very little to analyse, could be a result of the sporadic cleaning process of turbines. This could also explain the lack of samples containing mussels despite visual observations that confirm they are present on all splash zones.

The ROV survey method was another successful assessment of biofouling, despite that the primary scope for the ROV works was to inspect the Tekmar cable protection system. The video footage obtained was predominately monochrome, however short bursts of colour footage enabled easier species identification. Any further biofouling assessment work involving an underwater camera should maintain colour footage as much as possible.

The species identified in both zones and the observed zonation of species with depth are consistent with the findings from other wind farms and offshore platforms. The significant presence of the non-native midge larvae at the

intertidal zone also reflects that of other wind farms. However, further study is required to evaluate the potential ecological implications of a marine invasive species at Teesside.

An improved understanding of the growth cycle of the barnacle and mussel species identified at the splash zone has already enabled the biofouling removal process to be optimized and reduced, considering the peak settlement and spawning times for these organisms:

1. By beginning the removal process earlier in the year (late April), this will take advantage of the peak settlement period of Acorn barnacles. Removal of the April-settled individuals prevents those releasing larvae the same July. This may also prevent the settlement of Blue mussel larvae following the spring spawning.
2. A second removal in late summer/early autumn should eliminate the remaining barnacles that have settled during the summer and the potential secondary spawning of blue mussels.

As a result of this improvement, the number of trips offshore to clean turbines at Teesside can now be reduced throughout the year, which saves on vessel cost, fuel and also allows technicians more time to conduct more pressing O&M tasks.

The thickness of marine growth at all subsea locations does not reflect the 100mm guidelines advised by DNV, and in fact is much less. The majority of

marine growth on the monopile and transition piece is soft fouling, primarily anemones that are assumed to have a negligible influence on hydrodynamic loading. The kelp and mussel dominated sublittoral zone on the other hand could increase the drag and inertia and therefore influence the loads. Additional dynamic loading analysis may be necessary at this particular zone.

7.3 **Conclusions**

- At Teesside, the cathodic protection system is insufficient to achieve the minimum requirement of -800mV at all submerged levels within the monopile foundations. This is particularly evident in the drilled foundations that have a much greater surface area of steel to protect.

- In some central locations within the monopile foundations, the internal cathodic protection system is over-protecting the steel by exceeding -1050mV. This level of potential suggests that the anodes are over-working. This could not only cause a reduction in anode lifetime, but also increases the risk of hydrogen induced cracking at welds and other highly stressed locations.

- The current anode distribution for drilled monopile foundations is not optimized to provide a uniform protection potential of -800mV along the internal surface length exposed to seawater. This means some areas will

be under/over-protected. However, The CP system was never designed to protect such a large volume of steel submerged under water.

- The reactions taking place at the aluminium anodes are contributing to water acidification, which has a negative knock-on effect on the performance of the anodes in a low pH environment.

- Cathodic protection in a confined space leads to hydrogen gas production, which can have dangerous implications for the monopile structural integrity and safety of personnel if not properly ventilated from the moonpool area.

- Oxygen ingress, low pH and tidal action are the key environmental parameters influencing the corrosion rate of monopile steel at Teesside.

- Controlled laboratory conditions are useful for isolating the individual parameters influencing corrosion but are not wholly representative the of offshore environment.

- Decision Tree analytics can be a useful tool for predicting corrosion rate classification but in this instance limited by sample size and missing pH values.

- The biofouling community composition and zonation patterns at Teesside are consistent with other UK offshore wind farms. Biofouling mapping of

these communities can provide useful structural characteristics such as roughness, thickness and drag.

- A clearer understanding of biofouling settlement patterns and lifecycles can help to optimize the biofouling removal (jet-washing) regime across a windfarm which. This facilitates O&M cost reduction and reduces the time spent offshore.

7.4 Recommendations for Further Work

- Implementation of a long-term corrosion monitoring campaign by installing internal and external corrosion coupons on selected foundations. This will provide steady-state corrosion rate data and enable the validation of predictive corrosion models for offshore wind monopile foundations.

- Improve experimental conditions for laboratory trials by using real seawater, mud samples from inside the monopile and mock monopile foundations as experimental chambers.

- Compare the merits and disadvantages of various modelling techniques for corrosion rate prediction and benchmarking of the decision tree tool. A reliable tool for predicting long-term corrosion rates is extremely sought after across the industry.

- A dedicated investigation on the specific effect of low pH on internal monopile steel is needed. It is assumed that low pH accelerates the corrosion rate by preventing the accumulation of calcareous deposits on the steel surface.

- Assessing the long-term impact of fresh oxygenated seawater leaking into the internal monopile environment – this could become a mitigation over time if the leak rate can be controlled and it serves to keep the pH level from becoming acidic. Ideally this would be conducted in a real offshore environment.

- Special consideration when considering aluminium galvanic anode cathodic protection for the internal monopile environment. This type of CP has been proven to cause acidic conditions in a confined space and facilitate hydrogen gas production - both of which are dangerous. Zinc or magnesium would be safer alternatives although the volumes of anodes needed would be more expensive than aluminium. A detailed cost-benefit analysis should be conducted when considering any CP.

- Review of innovative inspection and monitoring solutions for assessing internal monopile corrosion and external biofouling behaviour and the influence on structural integrity. Low cost solutions that prevent the need for technicians to transfer to a turbine are extremely sought after within the industry.

- The development of an industry-wide methodology or approach to fatigue life assessment of monopiles. Operators and asset managers need to share operational data to facilitate the development of consistent and reliable approach.

- Additional assessment of the mussel and kelp dominated community at Teesside is needed, i.e. quantification of thickness, roughness and added mass. By feeding this data into a structural model, combined with real operational data, condition monitoring data and corrosion rate information, this would generate a unique and robust insight into the overall structural performance of operating assets.

- Monitoring of *Telmatogeton japonicus* to determine the influence (if any) on the local ecosystem.

- Engagement with Standards Organisation for improvement to current guidelines (DNV GL), i.e. More realistic recommendations for marine growth thickness at different depths, and updated design codes that reflect the complex internal monopile environment and how it might influence the corrosion behaviour of monopile steel. In addition, a standardised approach for measuring and monitoring internal corrosion rate would be incredibly useful and could enable operators to make reliable predictions about fatigue life.

- Additional ROV surveys with all colour footage and scrape sample for more in-depth analysis and species identification. Regular surveys will show how the community changes over time and help to predict the growth at future sites.

References

[1] J. G. . Olivier, G. Janssens-Maenhout, M. Muntean, and J. A. H. . Peters, “Trends in Global CO2 Emissions: 2013 Report,” 2013.

[2] N. L. Panwar, S. C. Kaushik, and S. Kothari, “Role of renewable energy sources in environmental protection: A review,” *Renew. Sustain. Energy Rev.*, vol. 15, no. 3, pp. 1513–1524, Apr. 2011.

[3] M. da Graça Carvalho, “EU energy and climate change strategy,” *Energy*, vol. 40, no. 1, pp. 19–22, Apr. 2012.

[4] M. D. Esteban, J. J. Diez, J. S. López, and V. Negro, “Why offshore wind energy?,” *Renewable Energy*, vol. 36. pp. 444–450, 2011.

[5] A. R. Henderson, C. Morgan, B. Smith, H. C. Sorensen, R. J. Barthelmie, and B. Boesmans, “Offshore Wind Energy in Europe? A Review of the State-of-the-Art,” *Wind Energy*, vol. 6, no. 1, pp. 35–52, Jan. 2003.

[6] Wind Europe, “Offshore wind in Europe,” *Refocus*, pp. 1–37, 2018.

[7] ORE Catapult, “Offshore Wind Industry Prospectus,” no. October, 2018.

[8] Wind Europe, “The European offshore wind industry: Key trends and statistics 2016,” 2017.

[9] M. Bilgili, A. Yasar, and E. Simsek, “Offshore wind power development in Europe and its comparison with onshore counterpart,” *Renew. Sustain. Energy Rev.*, vol. 15, no. 2, pp. 905–915, Feb. 2011.

[10] X. Sun, D. Huang, and G. Wu, “The current state of offshore wind energy technology development,” *Energy*, vol. 41, no. 1, pp. 298–312, May 2012.

[11] A. Czyzewski, “Wind energy gets serial,” *www.theengineer.co.uk*, 2012. [Online]. Available: http://www.theengineer.co.uk/in-depth/the-big-story/wind-energy-gets-serial/1012449.article?sm=1012449. [Accessed: 09-Dec-2014].

[12] DNV GL AS, “Support structures for wind turbines,” *Dnvgl-St-0126*, no. July, 2016.

[13] 4C Offshore, “Monopile Support Structures,” 2013. .

[14] L. R. Hilbert, A. R. Black, F. Andersen, T. Mathiesen, and F. Technology, “Inspection and monitoring of corrosion inside monopile foundations for offshore wind turbines,” no. 4730, pp. 1–14, 2011.

[15] A. Mehmanparast, O. Adedipe, F. Brennan, and A. Chahardehi, “Welding sequence effects on residual stress distribution in offshore wind monopile structures,” *Frat. ed Integrita Strutt.*, vol. 10, no. 35, pp. 125–131, Jan. 2016.

[16] A. Kolios, L. Wang, A. Mehmanparast, and F. Brennan, “Determination of stress concentration factors in offshore wind welded structures through a hybrid experimental and numerical approach,” *Ocean Eng.*, vol. 178, pp. 38–47, Apr. 2019.

[17] W. Weijtjens, “MONITORING THE CONSUMED FATIGUE LIFE OF WIND TURBINES ON MONOPILE FOUNDATIONS.”

[18] A. Iliopoulos, W. Weijtjens, D. Van Hemelrijck, and C. Devriendt, “Fatigue assessment of offshore wind turbines on monopile foundations using multi-band modal expansion,” *Wind Energy*, vol. 20, no. 8, pp. 1463–1479, Aug. 2017.

[19] A. Right, “Offshore Wind Turbines Substructures,” *Renewable Green Energy Power*, 2012. [Online]. Available: http://www.renewablegreenenergypower.com/offshore-wind-turbines-substructures/. [Accessed: 11-Dec-2014].

[20] A. W. Momber, P. Plagemann, and V. Stenzel, “Performance and integrity of protective coating systems for offshore wind power structures after three years under offshore site conditions,” *Renew. Energy*, vol. 74, no. 0, pp. 606–617, Feb. 2015.

[21] A. Momber, P. Plagemann, and M. Schneider, “Investigating Corrosion Protection of Offshore Wind Towers,” no. April, 2008.

[22] N. Sea, F. Kerckhof, A. Norro, T. Jacques, and S. Degraer, “Chapter 4 . Early colonisation of a concrete offshore windmill foundation by marine biofouling on the Thornton.”

[23] A. Momber, “Corrosion and corrosion protection of support structures for offshore wind energy devices (OWEA),” *Mater. Corros.*, vol. 62, no. 5, pp. 391–404, May 2011.

[24] K. Mühlberg, “Corrosion protection of offshore wind turbines - A challenge for the steel builder and paint applicator,” *J. Prot. Coatings Linings*, vol. 27, no. 3, pp. 20–32, 2010.

[25] R. E. Melchers, “The effect of corrosion on the structural reliability of steel offshore structures,” *Corros. Sci.*, vol. 47, no. 10, pp. 2391–2410, Oct. 2005.

[26] K. E. Diamond, “Extreme Weather Impacts on Offshore Wind Turbines: Lessons Learned,” *Nat. Resour. Environ.*, vol. 27, no. 2, pp. 1–5, 2012.

[27] O. Adedipe, F. Brennan, and A. Kolios, “Review of corrosion fatigue in offshore structures: Present status and challenges in the offshore wind sector,” *Renewable and Sustainable Energy Reviews*. 2016.

[28] P. M. Scott, T. W. Thorpe, and D. R. V. Silvester, “Rate-determining processes for corrosion fatigue crack growth in ferritic steels in seawater,” *Corros. Sci.*, vol. 23, no. 6, pp. 559–575, 1983.

[29] T. W. Thorpe, P. M. Scott, A. Rance, and D. Silvester, “Corrosion

fatigue of BS 4360:50D structural steel in seawater," *Int. J. Fatigue*, vol. 5, no. 3, pp. 123–133, 1983.

[30] L. Q. Yu *et al.*, "Long-term dynamic behavior of monopile supported offshore wind turbines in sand," *Theoretical and Applied Mechanics Letters*. 2015.

[31] V. Igwemezie, A. Mehmanparast, and A. Kolios, "Materials selection for XL wind turbine support structures: A corrosion-fatigue perspective," *Mar. Struct.*, vol. 61, pp. 381–397, Sep. 2018.

[32] Ramboll, "TEESSIDE OFFSHORE WINDFARM- DESIGN REPORT-," vol. 0001, no. 0, pp. 0–20, 2011.

[33] S. McLean, "Personal Communication," *EDF Energy Renewables*, 2015.

[34] "Tekmar," *2015*. .

[35] DNV, "DNV-OS-J101: Design of Offshore Wind Turbine Structures," 2014.

[36] Ramboll, "Teesside Offshore Windfarm Corrosion and Cathodic Protection," 2012.

[37] DNV, "DNV-RP-B401 Cathodic Protection Design," 2011.

[38] P. Pedeferri, "Cathodic protection and cathodic prevention.pdf," *Construction and Building Materials*, vol. 10, no. 5. pp. 391–402, 1996.

[39] V. Dr. Cicek, "Cathodic Protection," *Cathodic Prot. Ind. Solut. Prot. Against Corros.*, vol. 1, pp. 131–156, 2013.

[40] V. Ashworth, "Principles of cathodic protection," *Shreir's Corros.*, vol. 2, pp. 2747–2762, 2010.

[41] DNV GL, "Cathodic Protection Design DNVGL-RP-B401," 2017.

[42] L. Kolarik, M. Kolarikova, P. Vondrous, and R. Hrabina, “THE CHOICE OF PARAMETERS FOR WELDING OF STEEL S355NL,” *Ann. DAAAM 2012 Proc. 23rd Int. DAAAM Symp.*, vol. 23, no. 1, pp. 1027–1030, 2012.

[43] L. Lichtenstein, “DNV GL Standard Harmonization Recommended Practice on Corrosion Protection of Offshore Wind Farms,” pp. 659–663, 2015.

[44] DNV GL, “Corrosion protection for wind turbines DNVGL-RP-0416,” no. March, 2016.

[45] T. Mathiesen, A. Black, and F. Grønvold, “Monitoring and Inspection Options for Evaluating Corrosion in Offshore Wind Foundations,” *NACE Corros. 2016*, no. March, 2016.

[46] S. . Briskeby, L. Borvik, and S. . Hesjevik, “Cathodic Protection in Closed Compartments - pH Effect and Performance of Anode Materials,” in *CORROSION*, 2015, no. 5657, pp. 1–11.

[47] P. R. Roberge, “Corrosion Basics,” *Corrosion Engineering*. McGraw Hill Professional, Access Engineering, 2008.

[48] D. Brondel, R. Edwards, A. Hayman, D. Hill, and T. Semerad, “Corrosion in the Oil Industry,” *Oilfield Review*, pp. 4–69, 1994.

[49] R. W. Revie, *Corrosion and corrosion control*. John Wiley & Sons, 2008.

[50] J. R. Davis, *Corrosion: Understanding the basics*. ASM International, 2000.

[51] R. Singh, *Corrosion Control for Offshore Structures: Cathodic Protection and High-Efficiency Coating*. Elsevier Science, 2014.

[52] NPTEL Web Course, “Lecture 1 Corrosion : Introduction – Definitions

and Types.” pp. 1–9.

[53] NACE International, “Corrosion Fatigue.” [Online]. Available: https://www.nace.org/Corrosion-Central/Corrosion-101/Corrosion-Fatigue/. [Accessed: 08-Oct-2017].

[54] D. Enning and J. Garrelfs, “Corrosion of iron by sulfate-reducing bacteria: new views of an old problem.,” *Appl. Environ. Microbiol.*, vol. 80, no. 4, pp. 1226–36, Feb. 2014.

[55] T. R. Lenhart *et al.*, “Identification and characterization of microbial biofilm communities associated with corroded oil pipeline surfaces.,” *Biofouling*, vol. 30, no. 7, pp. 823–35, Jan. 2014.

[56] H. A. Videla and L. K. Herrera, “Microbiologically influenced corrosion: looking to the future,” *Int. Microbiol.*, vol. 8, no. 3, p. 169, 2005.

[57] H. A. Videla and L. K. Herrera, “Biocorrosion,” *Stud. Surf. Sci. Catal.*, vol. 151, pp. 193–218, 2004.

[58] J. D. Zardus, B. T. Nedved, Y. Huang, C. Tran, and M. G. Hadfield, “Microbial Biofilms Facilitate Adhesion in Biofouling Invertebrates,” *Biol. Bull.* , vol. 214, no. 1, pp. 91–98, Feb. 2008.

[59] D. A. Shifler, “Understanding material interactions in marine environments to promote extended structural life,” *Corros. Sci.*, vol. 47, no. 10, pp. 2335–2352, Oct. 2005.

[60] D. T. Ruppel, S. C. Dexter, and G. W. Luther III, “Role of manganese dioxide in corrosion in the presence of natural biofilms,” *Corrosion*, vol. 57, no. 10, pp. 863–873, 2001.

[61] P. Linhardt, “Failure of chromium-nickel steel in a hydroelectric power plant by manganese-oxidizing bacteria,” *Microbially Influ. Corros. Mater. eds. E. Heitz, H.-C. Flemming, W. Sand (New York, NY Springer Berlin Heidelberg, 1996)*, pp. 221–230, 1996.

[62] B. H. Olesen, R. Avci, and Z. Lewandowski, “Manganese dioxide as a potential cathodic reactant in corrosion of stainless steels,” *Corros. Sci.*, vol. 42, no. 2, pp. 211–227, 2000.

[63] NACE International, *Cooling Water Treatment Manual, TPC 1*. N A C E International, 1990.

[64] R. Javaherdashti, “Reviewed paper A review of some characteristics of MIC caused by sulfate- reducing bacteria : past , present and future,” no. January, pp. 173–180, 1999.

[65] H. Venzlaff *et al.*, “Accelerated cathodic reaction in microbial corrosion of iron due to direct electron uptake by sulfate-reducing bacteria,” *Corros. Sci.*, vol. 66, pp. 88–96, Jan. 2013.

[66] C. A. H. von Wolzogen Kuehr and L. S. Van der Vlugt, “Graphitization of cast iron as an electrobiochemical process in anaerobic soils,” *Water*, vol. 18, no. 16, pp. 147–165, 1934.

[67] S. Kakooei, M. C. Ismail, and B. Ariwahjoedi, “Mechanisms of microbiologically influenced corrosion: a review,” *World Appl. Sci. J*, vol. 17, no. 4, pp. 524–531, 2012.

[68] P. Marcus, *Corrosion mechanisms in theory and practice*. CRC Press, 2011.

[69] K. Mori, H. Tsurumaru, and S. Harayama, “Iron corrosion activity of anaerobic hydrogen-consuming microorganisms isolated from oil facilities.,” *J. Biosci. Bioeng.*, vol. 110, no. 4, pp. 426–30, Oct. 2010.

[70] W. A. Hamilton, “Microbially influenced corrosion as a model system for the study of metal microbe interactions: a unifying electron transfer hypothesis,” *Biofouling*, vol. 19, no. 1, pp. 65–76, 2003.

[71] NACE International, “NACE International.” [Online]. Available: http://www.nace.org/. [Accessed: 29-Dec-2014].

[72] L. S. Moroz and T. E. Mingin, “Hydrogen embrittlement of steel,” *Met. Sci. Heat Treat.*, vol. 4, no. 3, pp. 135–137, 1962.

[73] G. M. Pressouyre, “Current solutions to hydrogen problems in steel,” 1982.

[74] R. . Tresseder and R. W. Staehle, “Stress Corrosion Cracking and Hydrogen Embrittlement of Iron Base Alloys,” in *NACE*, 1977, p. 147.

[75] R. A. Carneiro, R. C. Ratnapuli, and V. de Freitas Cunha Lins, “The influence of chemical composition and microstructure of API linepipe steels on hydrogen induced cracking and sulfide stress corrosion cracking,” *Mater. Sci. Eng. A*, vol. 357, no. 1, pp. 104–110, 2003.

[76] M. Biezma, “The role of hydrogen in microbiologically influenced corrosion and stress corrosion cracking,” *Int. J. Hydrogen Energy*, vol. 26, no. 5, pp. 515–520, 2001.

[77] H. A. Videla, L. K. Herrera, and G. Edyvean, “An Updated Overview of SRB Induced Corrosion and Protection of Carbon Steel.” NACE International.

[78] L. T. Popoola, A. S. Grema, G. K. Latinwo, B. Gutti, and A. S. Balogun, “Corrosion problems during oil and gas production and its mitigation,” *Int. J. Ind. Chem.*, vol. 4, no. 1, p. 35, 2013.

[79] G. V Chilingar, R. Mourhatch, and A. Al-Qahtani, *The Fundamentals of Corrosion and Scaling for Petroleum & Environmental Engineers*. Elsevier, 2013.

[80] M. Smith, C. Bowley, and L. Williams, “©NACE International. All rights reserved. Paper Number 02214 reproduced with permission from CORROSION/2002 Annual Conference and Exhibition, Denver,CO.,” no. 02214, 2002.

[81] DNV, “DNV-OS-J101 Design of Offshore Wind Turbine Structures,” no.

February, 2013.

[82] J. P. Ault, “The use of coatings for corrosion control on offshore oil structures,” *J. Prot. Coatings Linings*, vol. 23, no. 4, p. 42, 2006.

[83] B. J. Little, P. A. Wagner, and F. Mansfield, *Microbiologically Influenced Corrosion*, vol. 298, no. 0704. NACE International, 1997.

[84] L. R. Hilbert, T. Mathiesen, A. R. Black, C. Christensen, and F. Technology, “Mud zone corrosion in offshore renewable energy structures,” no. Mic, pp. 1–5, 2013.

[85] D. J. Hughes, E. J. Cook, and M. D. J. Sayer, “BIOFILTRATION AND BIOFOULING ON ARTIFICIAL STRUCTURES IN EUROPE : THE POTENTIAL FOR MITIGATING ORGANIC IMPACTS,” pp. 123–172, 2005.

[86] S. Abarzua and S. Jakubowski, “Biotechnological investigation for the prevention of biofouling. 1. Biological and biochemical principles for the prevention of biofouling,” *Mar. Ecol. Prog. Ser.*, vol. 123, no. 1–3, p. 301, 1995.

[87] R. G. J. Edyvean, “Biodeterioration problems of North Sea oil and gas production—A review,” *Int. Biodeterior.*, vol. 23, no. 4, pp. 199–231, Jan. 1987.

[88] L. Hall-Stoodley, J. W. Costerton, and P. Stoodley, “Bacterial biofilms: from the Natural environment to infectious diseases,” *Nat Rev Micro*, vol. 2, no. 2, pp. 95–108, Feb. 2004.

[89] O. E. Petrova and K. Sauer, “Sticky situations: key components that control bacterial surface attachment.,” *J. Bacteriol.*, vol. 194, no. 10, pp. 2413–25, May 2012.

[90] T. R. Lenhart *et al.*, “Identification and characterization of microbial biofilm communities associated with corroded oil pipeline surfaces,”

Biofouling, vol. 30, no. 7, pp. 823–835, Aug. 2014.

[91] J. Kilbane II, B. Bogan, and B. Lamb, “Quantifying the Contribution of Various Bacterial Groups to Microbiologically Influenced Corrosion.” NACE International.

[92] G. Relini, F. Tixi, M. Relini, and G. Torchia, “The macrofouling on offshore platforms at Ravenna,” *Int. Biodeterior. Biodegradation*, vol. 41, no. 1, pp. 41–55, Jan. 1998.

[93] A. K. A. Macleod, “The role of Marine Renewable Energy structures and biofouling communities in promoting self-sustaining populations of Non-Native Species at the University of Aberdeen,” 2013.

[94] N. J. Heaf, “THE EFFECT OF MARINE GROWTH ON THE PERFORMANCE OF FIXED OFFSHORE PLATFORMS IN THE NORTH SEA,” in *Offshore Technology Conference*, 1979.

[95] M. J. Picken and C. Grier, “Fouling and corrosion off the outer Hebrides,” *Corros. Mar. Growth Offshore Struct.*, pp. 45–52, 1982.

[96] R. Kingsbury, “Marine fouling of North Sea installations,” *Mar. FOULING OFFSHORE Struct. VOL. 1 2, 1981, vp*, 1981.

[97] P. Whomersley and G. B. Picken, “Long-term dynamics of fouling communities found on offshore installations in the North Sea,” *J. Mar. Biol. Assoc. UK*, vol. 83, no. 05, pp. 897–901, 2003.

[98] J. H. Connell and R. O. Slatyer, “Mechanisms of Succession in Natural Communities and Their Role in Community Stability and Organization,” *The American Naturalist*, vol. 111. p. 1119, 1977.

[99] A. Schröder, C. Orejas, and T. Joschko, “Benthos in the Vicinity of Piles: FINO 1 (North Sea),” in *Offshore Wind Energy SE - 12*, J. Köller, J. Köppel, and W. Peters, Eds. Springer Berlin Heidelberg, 2006, pp. 185–200.

[100] D. Wilhelmsson and T. Malm, “Fouling assemblages on offshore wind power plants and adjacent substrata,” *Estuar. Coast. Shelf Sci.*, vol. 79, no. 3, pp. 459–466, Sep. 2008.

[101] F. Kerckhof, B. Rumes, T. Jacques, S. Degraer, and a Norro, “Early development of the subtidal marine biofouling on a concrete offshore windmill foundation on the Thornton Bank (southern North Sea): first monitoring results,” *Underw. Technol.*, vol. 29, no. 3, pp. 137–149, Nov. 2010.

[102] N. Davis, G. R. Vanblaricom, and P. K. Dayton, “Man-Made Structures on Marine Sediments : Effects on Adjacent Benthic Communities,” vol. 303, no. January 1977, pp. 295–303, 1982.

[103] I. De Mesel, F. Kerckhof, A. Norro, B. Rumes, and S. Degraer, “Succession and seasonal dynamics of the epifauna community on offshore wind farm foundations and their role as stepping stones for non-indigenous species,” *Hydrobiologia*, vol. 756, no. 1, pp. 37–50, 2015.

[104] O. Langhamer, “Artificial Reef Effect in relation to Offshore Renewable Energy Conversion: State of the Art,” *Sci. World J.*, vol. 2012, p. e386713, 2012.

[105] T. M. Glasby, S. D. Connell, M. G. Holloway, and C. L. Hewitt, “Nonindigenous biota on artificial structures: could habitat creation facilitate biological invasions?,” *Mar. Biol.*, vol. 151, no. 3, pp. 887–895, 2006.

[106] Y. Brodin and M. H. Andersson, “The marine splash midge Telmatogon japonicus (Diptera; Chironomidae)—extreme and alien?,” *Biol. Invasions*, vol. 11, no. 6, pp. 1311–1317, 2008.

[107] T. A. Shiganova, “Invasion of the Black Sea by the ctenophore Mnemiopsis leidyi and recent changes in pelagic community structure,”

Fish. Oceanogr., vol. 7, no. 3-4, pp. 305–310, 1998.

[108] N. Bax, A. Williamson, M. Aguero, E. Gonzalez, and W. Geeves, “Marine invasive alien species: A threat to global biodiversity,” *Mar. Policy*, vol. 27, no. 4, pp. 313–323, 2003.

[109] E. D. Grosholz, G. M. Ruiz, C. A. Dean, K. A. Shirley, J. L. Maron, and P. G. Connors, “THE IMPACTS OF A NONINDIGENOUS MARINE PREDATOR IN A CALIFORNIA BAY,” *Ecology*, vol. 81, no. 5, pp. 1206–1224, 2000.

[110] A. Pour and E. D. F. Client, “Nf en iso 19902,” 2016.

[111] NORSOK, “NORSOK: N-003 Actions and action effects,” *Nor. Oil Ind. Assoc. Fed. Nor. Manuf. Ind.*, no. September, 2007.

[112] D. N. Veritas, “DNV-OS-J101 Design of Offshore Wind Turbine Structures,” no. May, 2014.

[113] L. S. Fevag, “Influence of marine growth on support structure design for offshore wind turbines,” Norwegian University of Science and Technology, 2012.

[114] K. R. Larsen, “Retrofitting Wind Turbine Monopiles with Cathodic Protection,” *Materials Performance*, pp. 28–32, Aug-2017.

[115] I. Tavares, P. Ernst, G. John, R. Jacob, and B. Wyatt, “Internal Cathodic Protection of Offshore Wind Turbine Monopile Foundations,” *Corros. Manag.*, no. 123, pp. 14–17, 2015.

[116] G. Hinds, “NPL REPORT MAT (RES) 263 Guidelines for in situ measurement of internal cathodic protection system performance in wind turbine monopiles G HINDS DRAFT PROTECT - COMMERCIAL Guidelines for in situ measurement of internal cathodic protection system perform,” no. January, 2015.

[117] S. Elbeik, A. C. . Tseung, and A. . Mackay, “The formation of calcareous deposits during the corrosion of mild steel in sea water,” *Corros. Sci.*, vol. 26, no. 9, pp. 669–680, 1986.

[118] R. E. Melchers and R. Jeffrey, “Corrosion of long vertical steel strips in the marine tidal zone and implications for ALWC,” vol. 65, pp. 26–36, 2012.

[119] Working Group 44 of the Maritime Navigation Commission, “Accelerated Low Water Corrosion,” 2005.

[120] J. E. Breakell *et al.*, *Management of accelerated low water corrosion in steel maritime structures*. London: CIRIA, 2005.

[121] R. E. Melchers, “Modelling long term corrosion of steel infrastructure in natural marine environments,” in *Understanding Biocorrosion: Fundamentals and Principles*, 2014, p. 231.

[122] A. Bjørgum and O. Ø. Knudsen, “Corrosion protection of offshore wind turbines,” in *NACE*, 2015.

[123] C. Soraghan and R. T. Engineer, “Management of Hydrogen Sulphide (H 2 S) Gas in Wind Turbine Sub-Structures : identifying and managing H 2 S,” no. April, 2016.

[124] European Corrosion Supplies Limited, “Certificate of Compliance DIN 50049 3.1B.” Worcs, UK, 2016.

[125] “S355 European Standard Steel,” *S355 EN 10025: 2004 Standard Structural Steel Plate*, 2004. [Online]. Available: http://xvator.com/documents/S355 European Standard Steel.pdf. [Accessed: 27-Sep-2016].

[126] S. I. Al-rubaiey, E. a Anoon, and M. M. Hanoon, “The Influence of Microstructure on the Corrosion Rate of Carbon Steels,” vol. 31, no. 10, p. 12, 2013.

[127] International Organization for Standards, “ISO 4287:1997 Geometrical Product Specifications (GPS) Surface texture: Profile method -- Terms, definitions and surface texture parameters,” 1997.

[128] F. De Dardel, “Approximate sea water analysis,” 2011. [Online]. Available: http://dardel.info/IX/other_info/sea_water.html. [Accessed: 11-Sep-2017].

[129] B. A. Morris and E. A. Goulbourne, “Method for preservation of marine microorganisms,” US 6376229 B2, 2002.

[130] ASTM International, “Standard Practice for Operating Salt Spray (FOG) Apparatus. - B117 - 16,” *Water*, vol. 03, no. February, pp. 1–15, 2003.

[131] R. E. Melchers, “Development of new applied models for steel corrosion in marine applications including shipping,” *Ships Offshore Struct.*, vol. 3, no. 2, pp. 135–144, 2008.

[132] M. Menzinger and R. Wolfgang, *The Meaning and Use of the Arrhenius Activation Energy*, vol. 8, no. 6. Wiley Online Library, 1969.

[133] ASTM International, “Standard Test Methods for Corrosivity of Water in the Absence of Heat Transfer,” 2015.

[134] ASTM International, “Standard Practice for Preparing , Cleaning , and Evaluating Corrosion Test,” 1999.

[135] E. Brillas and P.-L. Cabot, *Trends in Electrochemistry and Corrosion at The Beginning of The 21st Century*. 2004.

[136] Confidential, “Corrosion Monitoring Report (reference available upon request pending approval),” 2013.

[137] “Purdue University: Radiological and Enviromental Management.” [Online]. Available: https://www.purdue.edu/ehps/rem/rs/sem.htm. [Accessed: 27-Jul-2015].

[138] K. P. Shah, “The Hand Book on Mechanical Maintenance.” [Online]. Available: http://practicalmaintenance.net/?p=1315. [Accessed: 14-Aug-2015].

[139] B. W. A. Sherar, I. M. Power, P. G. Keech, S. Mitlin, G. Southam, and D. W. Shoesmith, “Characterizing the effect of carbon steel exposure in sulfide containing solutions to microbially induced corrosion,” *Corros. Sci.*, vol. 53, no. 3, pp. 955–960, Mar. 2011.

[140] R. . King and D. S. Wakerly, “Corrosion of mild steel by ferrous sulfide,” *Br. Corros. J.*, vol. 8, pp. 41–45, 1973.

[141] J. S. Lee, R. I. Ray, E. J. Lemieux, A. U. Falster, and B. J. Little, “An evaluation of carbon steel corrosion under stagnant seawater conditions.,” *Biofouling*, vol. 20, no. April 2015, pp. 237–247.

[142] X. Api-l *et al.*, “International Biodeterioration & Biodegradation Influence of sulfate reducing bacterial biofilm on corrosion behavior,” vol. 78, pp. 34–42, 2013.

[143] Y. El Mendili, a Abdelouas, H. El Hajj, and J.-F. Bardeau, “Phase transitions of iron sulphides formed by steel microbial corrosion,” *RSC Adv.*, vol. 3, no. 48, p. 26343, 2013.

[144] R. E. Melchers, “Microbiological and abiotic processes in modelling longer-term marine corrosion of steel,” *Bioelectrochemistry*, vol. 97, pp. 89–96, 2014.

[145] A. O.O. and M. a.F., “Microstructural Analysis of Selected Corroded Materials from Nigeria Oil and Gas Industr,” *Am. J. Mater. Sci.*, vol. 1, no. 2, pp. 108–112, 2012.

[146] J. Stutzmann, “Cathodic Corrosion Protection in the Context of Lifetime Extension of Monopile-based Offshore Wind Turbines,” 2017.

[147] R. E. Melchers, “Using models to interpret data for monitoring and life

prediction of deteriorating infrastructure systems," *Struct. Infrastruct. Eng.*, vol. 11, no. March, pp. 63–72, 2014.

[148] S. Pineau *et al.*, *Formation of the Fe(II–III) hydroxysulphate green rust during marine corrosion of steel associated to molecular detection of dissimilatory sulphite-reductase*, vol. 50. 2008.

[149] R. E. Melchers and R. Jeffrey, "Early corrosion of mild steel in seawater," *Corros. Sci.*, vol. 47, pp. 1678–1693, 2005.

[150] F. Gilbert, P. Refait, F. Lévêque, C. Remazeilles, and E. Conforto, "Synthesis of goethite from Fe(OH)2 precipitates: Influence of Fe(II) concentration and stirring speed," *J. Phys. Chem. Solids*, vol. 69, no. 8, pp. 2124–2130, Aug. 2008.

[151] C. Ruby *et al.*, "Oxidation modes and thermodynamics of FeII-III oxyhydroxycarbonate green rust : dissolution-precipitation versus in-situ deprotonation ; about the fougerite mineral To cite this version : HAL Id : hal-00522806," 2010.

[152] R. E. Melchers, "Modeling of marine immersion corrosion for mild and low-alloy steels-part 1: Phenomenological Model," *Corrosion*, vol. 59, no. 4, pp. 335–344, 2003.

[153] R. E. Melchers, "Probabilistic Models for Corrosion in Structural Reliability Assessment—Part 1: Empirical Models," *J. Offshore Mech. Arct. Eng.*, vol. 125, no. November 2003, p. 264, 2003.

[154] R. E. Melchers and R. Jeffrey, "Influence of Water Velocity on Marine Immersion Corrosion of Mild Steel," *CORROSION*, vol. 60, no. 1, pp. 84–94, Jan. 2004.

[155] R. E. Melchers, "Advances in Mathematical-Probabilistic Modelling of the Atmospheric Corrosion of Structural Steels in Ocean Environments," *3rd Int. ASRANet Colloq.*, no. July, pp. 1–12, 2006.

[156] R. Melchers and R. Jeffrey, “The critical involvement of anaerobic bacterial activity in modelling the corrosion behaviour of mild steel in marine environments,” *Electrochim. Acta*, vol. 54, no. 1, pp. 80–85, 2008.

[157] R. E. Melchers, “Long-term immersion corrosion of steels in seawaters with elevated nutrient concentration,” *Corros. Sci.*, vol. 81, pp. 110–116, 2014.

[158] R. E. Melchers, “Effect of Nutrient-Based Water Pollution on the Corrosion of Mild Steel in Marine Immersion Conditions,” *CORROSION*, vol. 61, no. 3, pp. 237–245, Mar. 2005.

[159] O. S. Ting, N. S. Potty, and M. S. Liew, “Prediction of corrosion rates in marine and offshore structures,” *2011 Natl. Postgrad. Conf. - Energy Sustain. Explor. Innov. Minds, NPC 2011*, pp. 1–6, 2011.

[160] M. R. E., “Recent Progress in the Modeling of Corrosion of Structural Steel Immersed in Seawaters,” *J. Infrastruct. Syst.*, vol. 12, no. 3, pp. 154–162, Sep. 2006.

[161] Owner/operators of UK offshore wind farms., “Offshore Wind O&M Forum,” 2018.

[162] ORE Catapult, “Offshore Wind Farm Substructure Monitoring and Inspection Operations and Maintenance,” no. June, pp. 1–31, 2017.

[163] E. Witten, “Selecting Multiway Splits in Decision Trees,” *NeuroCOLD Tech. Rep.*, no. February 1997, 1996.

[164] M. H. Rangwala, “Emprirical Investigation of Decision Tree Extraction From Neural Networks,” Ohio University, 2006.

[165] V. Podgorelec, P. Kokol, B. Stiglic, and I. Rozman, *Decision Trees: An Overview and Their Use in Medicine*, vol. 26. 2002.

[166] M. Computing, “Credit Card Fraud Detection Using Decision Tree Induction Algorithm,” vol. 4, no. 4, pp. 92–95, 2015.

[167] K. Chitra and B. Subashini, “Data Mining Techniques and its Applications in Banking Sector,” in *International Journal of Emerging Technology and …*, vol. 3, no. 8, 2015, pp. 219–226.

[168] K. B. Irani, J. Cheng, U. M. Fayyad, and Z. Qian, *Applying Machine Learning to Semiconductor Manufacturing*, vol. 8. 1993.

[169] C. Gröger, F. Niedermann, and B. Mitschang, *Data Mining-driven Manufacturing Process Optimization*, vol. 3. 2012.

[170] G. D’Angelo and S. Rampone, “Shape-based defect classification for non destructive testing,” in *2015 IEEE Metrology for Aerospace (MetroAeroSpace)*, 2015, pp. 406–410.

[171] P. Madhumitha, S. Ramkishore, K. Srikanth, and P. Palanichamy, “Application of decision trees for the identification of weld central line in austenitic stainless steel weld joints,” *2014 Int. Conf. Comput. Power, Energy, Inf. Commun. ICCPEIC 2014*, no. April 2014, pp. 400–405, 2014.

[172] H. Chern-Tong and I. B. A. Aziz, “A corrosion prediction model for oil and gas pipeline using CMARPGA,” *2016 3rd Int. Conf. Comput. Inf. Sci. ICCOINS 2016 - Proc.*, no. February 2015, pp. 403–407, 2016.

[173] B. Gu, R. Kania, S. Sharma, and M. Gao, “Approach to Assessment of Corrosion Growth in Pipelines,” no. January 2002, pp. 1837–1847, 2009.

[174] J. S. Chou, N. T. Ngo, and W. K. Chong, “The use of artificial intelligence combiners for modeling steel pitting risk and corrosion rate,” *Eng. Appl. Artif. Intell.*, vol. 65, no. January, pp. 471–483, 2017.

[175] A. Fink *et al.*, “KNIME: The Konstanz Information Miner,” in *Studies in*

Classification, Data Analysis, and Knowledge Organization, 2010, pp. 229–239.

[176] J. Shafer, R. Agrawal, and M. Mehta, *SPRINT: A scalable parallel classifier for data mining*. 2000.

[177] Unknown, “Classification: Basic concepts, decision trees, and model evaluation,” .

[178] ABS, “Offshore Wind Turbine Installations,” 2010.

[179] M. Eashwar, G. Subramanian, P. Chandrasekaran, S. T. Manickam, S. Maruthamuthu, and K. Balakrishnan, “The interrelation of cathodic protection and marine macrofouling,” *Biofouling*, vol. 8, no. 4, pp. 303–312, 1995.

[180] C. Canning, “Biofouling Assessment at Teesside Offshore Wind Farm,” 2016.

[181] T. Vance, R. Ellis, and T. Fileman, “ETI MA1001 - Reliable Data Acquisition Platform for Tidal (ReDAPT) project : ME8.5 ‘final report,’” 2014.

[182] T. Vance and R. Ellis, “ETI MA1001 - Reliable Data Acquisition Platform for Tidal (ReDAPT) project: ME8.4 ‘Biofouling Experiment Results,’” 2014.

[183] F. Kerckhof, B. Rumes, a Norro, T. G. Jacques, and S. Degraer, “Chapter 5 . Seasonal variation and vertical zonation of the marine biofouling on a concrete offshore windmill foundation on the Thornton Bank (southern North Sea),” *Degraer, S., Brabant. R. Rumes, B. Offshore Wind farms Belgian part North Sea Early Environ. impact Assess. Spat. Var. R. Belgian Inst. Nat. Sci. Manag. Unit North S*, pp. 53–68, 2010.

[184] RSS Marine, “Teesside Offshore Wind Farm — Construction

Information," no. December 2012, 2013.

[185] W. Wolff, "Book review: Marine nature conservation review: rationale and methods, K. Hiscock (Ed.), Joint Nature Conservation Committee, Peterborough, 1996. 167 pp. Price £85.00 plus postage and packing (JNCC publications are distributed solely by the Natural Histor," *Aquat. Conserv. Mar. Freshw. Ecosyst.*, vol. 7, no. 4, p. 327, Dec. 1997.

[186] R. Seed and T. K. Suchanek, "Population and community ecology of Mytilus," *Dev.Aquacult.Fish Sci*, 1992.

[187] T. van der Stap, J. W. P. Coolen, and H. J. Lindeboom, "Data from: Marine fouling assemblages on Offshore Gas Platforms in the Dutch part of the North Sea: Effects of depth and distance from shore on biodiversity.," *Dryad Digit. Repos.*, pp. 19–21, 2015.

[188] A. Agüera, "The role of starfish (Asterias rubens L.) predation in blue mussel (Mytilus edulis L.) seedbed stability," 2015.

[189] M. Wilcox and A. Jeffs, *Impacts of sea star predation on mussel bed restoration: Sea star predation on restored mussels*, vol. 27. 2018.

[190] N. White, "Balanus crenatus: An Acorn Barnacle.," Plymouth, 2004.

[191] P. S. Rainbow, "An introduction to the biology of British littoral barnacles," *Field Studies*, vol. 6. pp. 1–51, 1984.

[192] H. Barnes and H. T. Powell, "The growth of Balanus balanoides and B. crenatus Brug. under varying conditions of submersion," *J. Mar. Biol. Assoc. United Kingdom*, vol. 32, no. 1, 1953.

[193] K. R. Jensen, "NOBANIS - Marine invasive species in Nordic waters - Fact Sheet - Eliminius modestus," *Identif. key to Mar. invasive species Nord. waters*, pp. 1–3, 2010.

[194] H. Barnes, "Organic production by Elminius modestus Darwin in an

enclosed basin," *J. Exp. Mar. Bio. Ecol.*, vol. 6, no. 1, pp. 79–82, 1971.

[195] J. Lawson, J. Davenport, and A. Whitaker, "Barnacle distribution in Lough Hyne Marine Nature Reserve: a new baseline and an account of invasion by the introduced Australasian species Elminius modestus Darwin," *Estuar. Coast. Shelf Sci.*, vol. 60, no. 4, pp. 729–735, Aug. 2004.

[196] C. A. Richardson and R. Seed, "Predictions of mussel (Mytilus edulis) biomass on an offshore platform from single population samples," *Biofouling*, vol. 2, no. 4, pp. 289–297, 1990.

[197] R. Seed, "The ecology of Mytilus edulis L. (Lamellibranchiata) on exposed rocky shores," *Oecologia*, vol. 3, no. 3, pp. 277–316, 1969.

[198] P. a. Ribeiro, R. Xavier, A. M. Santos, and S. J. Hawkins, "Reproductive cycles of four species of Patella (Mollusca: Gastropoda) on the northern and central Portuguese coast," *J. Mar. Biol. Assoc. United Kingdom*, vol. 89, no. 6, pp. 1215–1221, 2009.

[199] C. M. Brujis, Maarten, "Survey of marine fouling on turbine support structures of the Offshore Windfarm Egmond aan Zee," 2010.

[200] D. Boldo, "CR-P15-2016-016 Test of 3D reconstruction from submarine video inspection of Teesside offshore wind turbine." EDF R&D, 2016.

Appendix A - Polishing and preparation of Coupon 913

Figure 7.1 *The slicing of coupon 913 into 2 small segments (right)*

Figure 7.2: *A coupon segment is held in place (left) and then set in epoxy resin with sliced area exposed (right)*

Figure 7.3: *Polishing of the 2 samples. The bottom right image shows the use of lubricant during the polishing.*

Figure 7.4: *The surfaces of both samples following preparation steps 3a) to d).*

Figure 7.5: *Specimens are agitated in an ultra-sonic cleaner to remove any excess lubricant.*

Figure 7.6: *The last step in the polishing process involves repeating step 3d) to remove any excess diamond product.*

Appendix B – Corrosion Database

Location	Exposure Time (Years)	Temperature (°C)	pH	Oxygen	Seawater	Corrosion Rate (mm/y)
Immersed	0.577699038	8.75	7.85	No	Real	0.072
Immersed	0.62971933	8.77	7.88	No	Real	0.0392
Immersed	0.607816049	8.8	8.04	No	Real	0.0406
Immersed	0.607816049	8.82	8.07	No	Real	0.0501
Immersed	0.6	8.84	7.99	No	Real	0.0359
Immersed	0.569485307	8.89	7.8	No	Real	0.1235
Immersed	0.594126498	8.9	7.62	No	Real	0.0539
Immersed	0.301170114	8.9	7.96	No	Real	0.0669
Immersed	0.591388588	8.92	7.59	No	Real	0.0495
Immersed	0.605078139	8.93	7.9	No	Real	0.0584
Immersed	0.602340229	8.96	8	No	Real	0.0648
Immersed	0.63245724	9.01		No	Real	0.0563
Immersed	0.62698142	9.02	7.84	No	Real	0.0771
Immersed	0.605078139	9.1	9.08	No	Real	0.0483
Seabed	1.232241788	10	6	No	Real	0.02114
Atmospheric	1.0983345	10	7.8	No	Real	0.02566
Atmospheric	1.232241788	10	6	No	Real	0.02568
Seabed	1.0983345	10	7	No	Real	0.02979
Lab Immersed	1.2896189	10	8	Yes	NaCl	0.03237
Lab Immersed	1.03	10	8	Yes	NaCl	0.03267
Atmospheric	1.0983345	10	7	No	Real	0.03419

Location	Exposure Time (Years)	Temperature (°C)	pH	Oxygen	Seawater	Corrosion Rate (mm/y)
Lab Immersed	1.03	10	8	Yes	NaCl	0.03442
Lab Immersed	1.2896189	10	8	Yes	NaCl	0.03482
Tidal	1.0983345	10	7.8	No	Real	0.03845
Tidal	1.232241788	10	6	No	Real	0.05992
Immersed	1.232241788	10	6	No	Real	0.06204
Tidal	1.0983345	10	7	No	Real	0.06306
Tidal	1.0983345	10	7	No	Real	0.09131
Tidal	1.232241788	10	6	No	Real	0.09289
Seabed	1.0983345	10	7.8	No	Real	0.10689
Tidal	1.0983345	10	7.8	No	Real	0.10806
Immersed	1.0983345	10	7	No	Real	0.11952
Immersed	7.2	10	8.2	Yes	Real	0.12
Immersed	1.0983345	10	7.8	No	Real	0.14024
Atmospheric	0.265577283	12		No	None	0.0001
Tidal	0.303908024	12		No	Real	0.0001
Atmospheric	0.287480564	12		No	None	0.0002
Tidal	0.287480564	12		No	Real	0.0002
Atmospheric	0.276528923	12		No	None	0.0003
Atmospheric	0.287480564	12		No	None	0.0003
Atmospheric	0.287480564	12		No	None	0.0003
Atmospheric	0.298432204	12		No	None	0.0003
Atmospheric	0.276528923	12		No	None	0.0004
Atmospheric	0.287480564	12		No	None	0.0004

Location	Exposure Time (Years)	Temperature (°C)	pH	Oxygen	Seawater	Corrosion Rate (mm/y)
Tidal	0.287480564	12		No	Real	0.0005
Atmospheric	0.303908024	12		No	None	0.0005
Atmospheric	0.303908024	12		No	None	0.0006
Tidal	0.602340229	12		No	Real	0.0006
Atmospheric	0.298432204	12		No	None	0.0008
Tidal	0.607816049	12		No	Real	0.0008
Atmospheric	0.62698142	12		No	None	0.0008
Tidal	0.8378005	12		No	Real	0.0008
Atmospheric	0.254625642	12		No	None	0.0009
Tidal	0.298432204	12		No	Real	0.0009
Atmospheric	0.353190407	12		No	None	0.0009
Tidal	0.605078139	12		No	Real	0.0009
Atmospheric	0.353190407	12		No	None	0.001
Tidal	0.257363552	12		No	Real	0.0011
Tidal	0.265577283	12		No	Real	0.0011
Atmospheric	0.292956384	12		No	None	0.0011
Atmospheric	0.265577283	12		No	None	0.0012
Tidal	0.566747397	12		No	Real	0.0014
Atmospheric	0.254625642	12		No	None	0.0016
Tidal	0.588650678	12		No	Real	0.0016
Tidal	0.63245724	12		No	Real	0.0016

Location	Exposure Time (Years)	Temperature (°C)	pH	Oxygen	Seawater	Corrosion Rate (mm/y)
Atmospheric	0.257363552	12		No	None	0.0017
Tidal	0.476396363	12		No	Real	0.0017
Tidal	0.62971933	12		No	Real	0.0017
Tidal	0.254625642	12		No	Real	0.0019
Tidal	0.558533667	12		No	Real	0.0019
Tidal	0.873393332	12		No	Real	0.0019
Tidal	0.62698142	12		No	Real	0.002
Atmospheric	0.292956384	12		No	None	0.0021
Atmospheric	0.605078139	12		No	None	0.0021
Atmospheric	0.257363552	12		No	None	0.0022
Atmospheric	0.591388588	12		No	None	0.0022
Atmospheric	0.625612465	12		No	None	0.0023
Tidal	0.238198181	12		No	Real	0.0024
Atmospheric	0.933627354	12		No	None	0.0024
Atmospheric	0.265577283	12		No	None	0.0025
Tidal	0.625612465	12		No	Real	0.0025
Atmospheric	0.238198181	12		No	None	0.0026
Tidal	0.585912768	12		No	Real	0.0026
Tidal	0.235460271	12		No	Real	0.0027
Tidal	0.569485307	12		No	Real	0.0027

Location	Exposure Time (Years)	Temperature (°C)	pH	Oxygen	Seawater	Corrosion Rate (mm/y)
Tidal	0.574961127	12		No	Real	0.0027
Tidal	0.276528923	12		No	Real	0.0029
Tidal	0.42163816	12		No	Real	0.0029
Atmospheric	0.238198181	12		No	None	0.003
Atmospheric	0.577699038	12		No	None	0.003
Tidal	0.577699038	12		No	Real	0.003
Atmospheric	0.818635129	12		No	None	0.003
Atmospheric	0.580436948	12		No	None	0.0031
Atmospheric	0.605078139	12		No	None	0.0031
Tidal	0.651622611	12		No	Real	0.0031
Atmospheric	0.42163816	12		No	None	0.0033
Atmospheric	0.818635129	12		No	None	0.0034
Atmospheric	0.569485307	12		No	None	0.0035
Atmospheric	0.238198181	12		No	None	0.0036
Atmospheric	0.62698142	12		No	None	0.0036
Atmospheric	0.238198181	12		No	None	0.0037
Atmospheric	0.583174858	12		No	None	0.0037
Tidal	0.605078139	12		No	Real	0.0038
Tidal	0.238198181	12		No	Real	0.0039
Atmospheric	0.605078139	12		No	None	0.0039
Atmospheric	0.63793306	12		No	None	0.0039

Location	Exposure Time (Years)	Temperature (°C)	pH	Oxygen	Seawater	Corrosion Rate (mm/y)
Atmospheric	0.818635129	12		No	None	0.004
Tidal	0.769352747	12		No	Real	0.0041
Atmospheric	0.651622611	12		No	None	0.0044
Atmospheric	0.235460271	12		No	None	0.0045
Tidal	0.574961127	12		No	Real	0.0046
Tidal	0.585912768	12		No	Real	0.0046
Atmospheric	0.8378005	12		No	None	0.0046
Atmospheric	0.238198181	12		No	None	0.0047
Atmospheric	0.292956384	12		No	None	0.0047
Atmospheric	0.63245724	12		No	None	0.0047
Atmospheric	0.577699038	12		No	None	0.0048
Atmospheric	0.8378005	12		No	None	0.0048
Tidal	0.580436948	12		No	Real	0.0049
Atmospheric	0.769352747	12		No	None	0.0049
Tidal	0.818635129	12		No	Real	0.0049
Atmospheric	0.303908024	12		No	None	0.005
Atmospheric	0.62971933	12		No	None	0.005
Atmospheric	0.873393332	12		No	None	0.005
Atmospheric	0.235460271	12		No	None	0.0052
Atmospheric	0.892558703	12		No	None	0.0053
Atmospheric	0.605078139	12		No	None	0.0055

Location	Exposure Time (Years)	Temperature (°C)	pH	Oxygen	Seawater	Corrosion Rate (mm/y)
Tidal	0.63793306	12		No	Real	0.0055
Atmospheric	0.892558703	12		No	None	0.0056
Atmospheric	0.574961127	12		No	None	0.0057
Atmospheric	0.544844116	12		No	None	0.0059
Atmospheric	0.8378005	12		No	None	0.006
Atmospheric	0.933627354	12		No	None	0.006
Atmospheric	0.63245724	12		No	None	0.0062
Atmospheric	0.769352747	12		No	None	0.0064
Tidal	0.292956384	12		No	Real	0.0065
Atmospheric	0.577699038	12		No	None	0.0065
Atmospheric	0.577699038	12		No	None	0.0065
Tidal	0.577699038	12		No	Real	0.0067
Atmospheric	0.558533667	12		No	None	0.0069
Tidal	0.558533667	12		No	Real	0.0069
Atmospheric	0.607816049	12		No	None	0.0069
Atmospheric	0.580436948	12		No	None	0.007
Atmospheric	0.873393332	12		No	None	0.007
Atmospheric	0.564009487	12		No	None	0.0071
Atmospheric	0.63245724	12		No	None	0.0073
Atmospheric	0.585912768	12		No	None	0.0076
Atmospheric	0.602340229	12		No	None	0.0076

Location	Exposure Time (Years)	Temperature (°C)	pH	Oxygen	Seawater	Corrosion Rate (mm/y)
Tidal	0.564009487	12		No	Real	0.0077
Atmospheric	0.605078139	12		No	None	0.0077
Tidal	0.547582026	12		No	Real	0.0079
Atmospheric	0.577699038	12		No	None	0.0079
Atmospheric	0.588650678	12		No	None	0.0079
Atmospheric	0.605078139	12		No	None	0.0079
Tidal	0.577699038	12		No	Real	0.0081
Atmospheric	0.605078139	12		No	None	0.0081
Tidal	0.558533667	12		No	Real	0.0084
Atmospheric	0.558533667	12		No	None	0.0087
Atmospheric	0.585912768	12		No	None	0.0087
Tidal	0.544844116	12		No	Real	0.0088
Atmospheric	0.564009487	12		No	None	0.0088
Atmospheric	0.616029779	12		No	None	0.0088
Atmospheric	0.873393332	12		No	None	0.0088
Atmospheric	0.558533667	12		No	None	0.009
Atmospheric	0.588650678	12		No	None	0.0091
Atmospheric	0.651622611	12		No	None	0.0092
Atmospheric	0.574961127	12		No	None	0.0093

Location	Exposure Time (Years)	Temperature (°C)	pH	Oxygen	Seawater	Corrosion Rate (mm/y)
Atmospheric	0.607816049	12		No	None	0.0093
Tidal	0.353190407	12		No	Real	0.0097
Atmospheric	0.651622611	12		No	None	0.0098
Atmospheric	0.257363552	12		No	None	0.01
Tidal	0.594126498	12		No	Real	0.0101
Atmospheric	0.952792725	12		No	None	0.0101
Atmospheric	0.651622611	12		No	None	0.0102
Atmospheric	0.63793306	12		No	None	0.0104
Atmospheric	0.62698142	12		No	None	0.0105
Atmospheric	0.585912768	12		No	None	0.0106
Atmospheric	0.476396363	12		No	None	0.0109
Atmospheric	0.561271577	12		No	None	0.0109
Atmospheric	0.558533667	12		No	None	0.0112
Atmospheric	0.577699038	12		No	None	0.0112
Tidal	0.583174858	12		No	Real	0.0116
Atmospheric	0.62971933	12		No	None	0.0121
Atmospheric	0.547582026	12		No	None	0.0122
Atmospheric	0.301170114	12		No	None	0.0123
Atmospheric	0.561271577	12		No	None	0.0123
Atmospheric	0.594126498	12		No	None	0.0123
Tidal	0.525678745	12		No	Real	0.0124

Location	Exposure Time (Years)	Temperature (°C)	pH	Oxygen	Seawater	Corrosion Rate (mm/y)
Atmospheric	0.607816049	12		No	None	0.0134
Atmospheric	0.566747397	12		No	None	0.0137
Tidal	0.591388588	12		No	Real	0.0148
Tidal	0.933627354	12		No	Real	0.015
Seabed	0.585912768	12		No	Real	0.016
Atmospheric	0.591388588	12		No	None	0.0168
Atmospheric	0.235460271	12		No	None	0.0171
Atmospheric	0.525678745	12		No	None	0.0183
Tidal	0.616029779	12		No	Real	0.0187
Immersed	0.892558703	12		No	Real	0.0187
Seabed	0.235460271	12		No	Real	0.0191
Atmospheric	0.558533667	12		No	None	0.0193
Immersed	0.588650678	12		No	Real	0.0195
Atmospheric	0.585912768	12		No	None	0.0201
Atmospheric	0.301170114	12		No	None	0.0203
Seabed	0.892558703	12		No	Real	0.0226
Seabed	0.588650678	12		No	Real	0.0228
Seabed	0.265577283	12		No	Real	0.023
Atmospheric	0.588650678	12		No	None	0.0234

Location	Exposure Time (Years)	Temperature (°C)	pH	Oxygen	Seawater	Corrosion Rate (mm/y)
Immersed	0.287480564	12		No	Real	0.0238
Immersed	0.769352747	12		No	Real	0.0245
Seabed	0.303908024	12		No	Real	0.0253
Seabed	0.287480564	12		No	Real	0.0266
Seabed	0.873393332	12		No	Real	0.0281
Immersed	0.287480564	12		No	Real	0.0283
Immersed	0.818635129	12	8.8	No	Real	0.0287
Seabed	0.476396363	12		No	Real	0.0287
Atmospheric	0.625612465	12		No	None	0.0287
Tidal	0.561271577	12		No	Real	0.0289
Tidal	0.558533667	12		No	Real	0.0296
Seabed	0.583174858	12		No	Real	0.0299
Seabed	0.769352747	12		No	Real	0.0302
Immersed	0.235460271	12		No	Real	0.0327
Seabed	0.605078139	12		No	Real	0.0327
Seabed	0.564009487	12		No	Real	0.033
Immersed	0.62971933	12	7.8	No	Real	0.0332
Seabed	0.591388588	12		No	Real	0.0333
Atmospheric	0.583174858	12		No	None	0.0337
Seabed	0.544844116	12		No	Real	0.0344

Location	Exposure Time (Years)	Temperature (°C)	pH	Oxygen	Seawater	Corrosion Rate (mm/y)
Immersed	0.892558703	12		No	Real	0.0347
Immersed	0.544844116	12		No	Real	0.035
Immersed	0.605078139	12		No	Real	0.0356
Seabed	0.577699038	12		No	Real	0.0368
Immersed	0.605078139	12		No	Real	0.0369
Seabed	0.63245724	12		No	Real	0.037
Seabed	0.62971933	12		No	Real	0.0375
Tidal	0.892558703	12		No	Real	0.0375
Immersed	0.238198181	12		No	Real	0.0399
Seabed	0.238198181	12		No	Real	0.0404
Seabed	0.558533667	12		No	Real	0.0407
Immersed	0.42163816	12		No	Real	0.0408
Immersed	0.873393332	12		No	Real	0.0409
Immersed	0.63245724	12		No	Real	0.0413
Immersed	0.818635129	12		No	Real	0.0414
Seabed	0.547582026	12		No	Real	0.0415
Seabed	0.8378005	12		No	Real	0.0419
Immersed	0.238198181	12		No	Real	0.042
Immersed	0.583174858	12		No	Real	0.0424
Seabed	0.607816049	12		No	Real	0.0425
Immersed	0.585912768	12		No	Real	0.0434

Location	Exposure Time (Years)	Temperature (°C)	pH	Oxygen	Seawater	Corrosion Rate (mm/y)
Seabed	0.574961127	12		No	Real	0.0435
Immersed	0.544844116	12		No	Real	0.0443
Immersed	0.585912768	12		No	Real	0.0444
Immersed	0.769352747	12		No	Real	0.0459
Seabed	0.818635129	12		No	Real	0.046
Immersed	0.583174858	12		No	Real	0.0471
Immersed	0.62698142	12		No	Real	0.0473
Immersed	0.476396363	12		No	Real	0.0475
Seabed	0.585912768	12		No	Real	0.0485
Seabed	0.525678745	12		No	Real	0.0489
Immersed	0.8378005	12		No	Real	0.0497
Seabed	0.616029779	12		No	Real	0.05
Immersed	0.235460271	12		No	Real	0.0501
Immersed	0.564009487	12		No	Real	0.0503
Seabed	0.577699038	12		No	Real	0.0512
Seabed	0.238198181	12		No	Real	0.0514
Immersed	0.574961127	12		No	Real	0.0516
Seabed	0.42163816	12		No	Real	0.0517
Seabed	0.62698142	12		No	Real	0.0517
Immersed	0.238198181	12	7.6	No	Real	0.0518
Seabed	0.257363552	12		No	Real	0.0521

Location	Exposure Time (Years)	Temperature (°C)	pH	Oxygen	Seawater	Corrosion Rate (mm/y)
Seabed	0.651622611	12		No	Real	0.0524
Immersed	0.525678745	12		No	Real	0.054
Seabed	0.353190407	12		No	Real	0.0558
Immersed	0.42163816	12		No	Real	0.0562
Immersed	0.287480564	12		No	Real	0.0563
Seabed	0.276528923	12		No	Real	0.0574
Immersed	0.547582026	12		No	Real	0.0575
Seabed	0.301170114	12		No	Real	0.0577
Immersed	0.558533667	12		No	Real	0.0579
Tidal	0.605078139	12		No	Real	0.0593
Seabed	0.566747397	12		No	Real	0.0594
Immersed	0.585912768	12		No	Real	0.0601
Seabed	0.301170114	12		No	Real	0.0624
Immersed	0.558533667	12		No	Real	0.0629
Seabed	0.287480564	12		No	Real	0.0632
Immersed	0.476396363	12		No	Real	0.0644
Seabed	0.254625642	12		No	Real	0.0646
Seabed	0.254625642	12		No	Real	0.065
Immersed	0.577699038	12		No	Real	0.065
Immersed	0.8378005	12		No	Real	0.0658

Location	Exposure Time (Years)	Temperature (°C)	pH	Oxygen	Seawater	Corrosion Rate (mm/y)
Immersed	0.574961127	12		No	Real	0.0668
Seabed	0.594126498	12		No	Real	0.0673
Seabed	0.605078139	12		No	Real	0.0692
Immersed	0.651622611	12		No	Real	0.0694
Seabed	0.558533667	12		No	Real	0.0721
Seabed	0.558533667	12		No	Real	0.0724
Immersed	0.238198181	12		No	Real	0.0728
Immersed	0.625612465	12		No	Real	0.0743
Seabed	0.602340229	12		No	Real	0.0746
Seabed	0.558533667	12		No	Real	0.0748
Immersed	0.254625642	12		No	Real	0.0766
Immersed	0.254625642	12		No	Real	0.0772
Seabed	0.605078139	12		No	Real	0.0804
Seabed	0.577699038	12		No	Real	0.0838
Seabed	0.574961127	12		No	Real	0.0842
Seabed	0.298432204	12		No	Real	0.0885
Immersed	0.353190407	12		No	Real	0.089
Immersed	0.616029779	12		No	Real	0.0894
Immersed	0.257363552	12		No	Real	0.0898

Location	Exposure Time (Years)	Temperature (°C)	pH	Oxygen	Seawater	Corrosion Rate (mm/y)
Seabed	0.569485307	12		No	Real	0.0909
Immersed	0.580436948	12		No	Real	0.0961
Immersed	0.616029779	12		No	Real	0.0966
Immersed	0.580436948	12		No	Real	0.0995
Seabed	0.625612465	12		No	Real	0.1006
Immersed	0.287480564	12		No	Real	0.115
Seabed	0.561271577	12		No	Real	0.1216
Immersed	0.569485307	12		No	Real	0.1268
Immersed	0.577699038	12		No	Real	0.1289
Tidal	0.952792725	12		No	Real	0.132
Seabed	0.580436948	12		No	Real	0.1409
Tidal	0.651622611	12		No	Real	0.1473
Immersed	0.547582026	13.02	7.81	No	Real	0.0449
Immersed	0.577699038	13.03	7.81	No	Real	0.0716
Immersed	0.873393332	13.08	9.15	No	Real	0.03
Immersed	0.585912768	13.08	9.26	No	Real	0.0524
Immersed	0.6	13.42	8.25	No	Real	0.0589
Immersed	0.651622611	13.42	7.7	No	Real	0.0913
Immersed	0.558533667	13.53	7.21	No	Real	0.0399
Immersed	0.558533667	13.53	6.97	No	Real	0.0556

Location	Exposure Time (Years)	Temperature (°C)	pH	Oxygen	Seawater	Corrosion Rate (mm/y)
Immersed	0.605078139	13.53	7.21	No	Real	0.0652
Immersed	0.594126498	13.54	6.97	No	Real	0.0907
Immersed	0.566747397	13.55	5.44	No	Real	0.0599
Immersed	0.577699038	13.63	5.5	No	Real	0.0832
Immersed	0.577699038	13.68	6.57	No	Real	0.0791
Immersed	0.276528923	13.72	6.38	No	Real	0.0354
Immersed	0.254625642	13.72	5.88	No	Real	0.0584
Immersed	0.301170114	13.77	5.85	No	Real	0.0889
Immersed	0.265577283	14	8.91	No	Real	0.0061
Immersed	0.591388588	14	8.91	No	Real	0.035
Immersed	0.6	14.1	8.1	No	Real	0.046
Immersed	0.257363552	14.2	7.82	No	Real	0.0493
Immersed	0.561271577	14.2	7.99	No	Real	0.0792
Immersed	0.561271577	14.2		No	Real	0.0829
Immersed	0.625612465	14.2	7.78	No	Real	0.1102
Immersed	0.564009487	14.3	8.91	No	Real	0.058
Immersed	0.558533667	14.3	8.22	No	Real	0.0647
Immersed	0.558533667	14.4	8.11	No	Real	0.0579
Immersed	0.298432204	14.5	8.07	No	Real	0.0586
Immersed	0.303908024	14.6	7.59	No	Real	0.0486

Location	Exposure Time (Years)	Temperature (°C)	pH	Oxygen	Seawater	Corrosion Rate (mm/y)
Immersed	0.525678745	14.7	8.03	No	Real	0.0594
Immersed	0.566747397	14.7	7.62	No	Real	0.0667
Immersed	0.574961127	14.8	8.04	No	Real	0.0547
Immersed	0.574961127	15	8.07	No	Real	0.0716
Immersed	2.5	15.5	8	Yes	Real	0.208
Immersed	5	17		Yes	Real	0.12
Immersed	0.153425	18	8.1	Yes	Real	0.20857
Immersed	0.153425	18.7	8.2	Yes	Real	0.6
Immersed	2	20	8.1	Yes	Real	0.75
Immersed	1.6	21	8.2	Yes	Real	0.17
Immersed	1.6	21	8.2	Yes	Real	0.175
Immersed	0.857534	21	8.2	Yes	Real	0.2
Immersed	0.164384	21	8.2	Yes	Real	0.43799
Immersed	0.273971	22	8.1	Yes	Real	0.1241
Immersed	1.8	22	8	Yes	Real	0.1666
Immersed	1.6	22	8	Yes	Real	0.225
Immersed	0.153425	22	8.1	Yes	Real	0.36499
Immersed	0.273971	22	8.1	Yes	Real	0.45
Immersed	0.0767123	22	8.1	Yes	Real	0.4562
Lab Immersed	1.2896189	23	8	No	NaCl	0.0011
Lab Immersed	1.2896189	23	8	No	NaCl	0.00129
Lab Immersed	1.2896189	23	8	No	NaCl	0.00133
Lab Immersed	1.03	23	8	No	NaCl	0.00152
Lab Immersed	1.03	23	8	No	NaCl	0.00155
Lab Immersed	1.03	23	8	No	NaCl	0.00158

Location	Exposure Time (Years)	Temperature (°C)	pH	Oxygen	Seawater	Corrosion Rate (mm/y)
Lab Immersed	1.03	23	8	No	NaCl	0.00159
Lab Immersed	1.03	23	8	No	NaCl	0.00161
Lab Immersed	1.03	23	8	No	NaCl	0.00162
Lab Immersed	1.03	23	8	No	NaCl	0.00164
Lab Immersed	1.2896189	23	8	No	Artificial with marine bacteria	0.00177
Lab Immersed	1.03	23	8	No	NaCl	0.0018
Lab Immersed	1.03	23	8	No	NaCl	0.00197
Lab Immersed	1.2896189	23	4	No	NaCl	0.00223
Lab Immersed	1.2896189	23	4	No	NaCl	0.0023
Lab Immersed	1.2896189	23	4	No	NaCl	0.0024
Lab Immersed	1.03	23	4	No	NaCl	0.00295
Lab Immersed	1.03	23	4	No	NaCl	0.00299
Lab Immersed	1.03	23	4	No	NaCl	0.00304
Lab Immersed	1.03	23	8	No	Artificial with marine bacteria	0.00344
Lab Immersed	1.03	23	8	No	Artificial with marine bacteria	0.00347
Lab Immersed	1.03	23	8	No	Artificial with marine bacteria	0.00347

Location	Exposure Time (Years)	Temperature (°C)	pH	Oxygen	Seawater	Corrosion Rate (mm/y)
Lab Immersed	1.03	23	8	No	Artificial with marine bacteria	0.00372
Lab Immersed	1.03	23	8	No	Artificial with marine bacteria	0.00394
Lab Immersed	1.03	23	4	No	NaCl	0.00434
Lab Immersed	1.03	23	4	No	NaCl	0.00436
Lab Immersed	1.03	23	8	No	Artificial with marine bacteria	0.00444
Lab Immersed	1.03	23	8	No	Artificial with marine bacteria	0.00444
Lab Immersed	1.03	23	4	No	NaCl	0.00451
Lab Immersed	1.03	23	4	No	NaCl	0.00496
Lab Immersed	1.2896189	23	4	No	Artificial with marine bacteria	0.00534
Lab Immersed	0.28	23	8	No	NaCl	0.00603
Lab Immersed	1.03	23	4	No	Artificial with marine bacteria	0.00612
Lab Immersed	1.03	23	4	No	Artificial with marine bacteria	0.00626
Lab Immersed	1.03	23	4	No	Artificial with marine bacteria	0.00629

Location	Exposure Time (Years)	Temperature (°C)	pH	Oxygen	Seawater	Corrosion Rate (mm/y)
Lab Immersed	0.28	23	8	No	Artificial with marine bacteria	0.00633
Lab Immersed	0.28	23	8	No	NaCl	0.00644
Lab Immersed	0.28	23	8	No	NaCl	0.00645
Lab Immersed	1.03	23	4	No	NaCl	0.00652
Lab Immersed	1.03	23	4	No	NaCl	0.00674
Lab Immersed	0.28	23	8	No	Artificial with marine bacteria	0.00693
Lab Immersed	0.28	23	8	No	Artificial with marine bacteria	0.00707
Lab Immersed	1.03	23	4	No	Artificial with marine bacteria	0.00728
Lab Immersed	1.03	23	4	No	Artificial with marine bacteria	0.00738
Lab Immersed	1.03	23	4	No	Artificial with marine bacteria	0.00792
Lab Immersed	0.28	23	4	No	NaCl	0.0124
Lab Immersed	0.28	23	4	No	NaCl	0.01417
Lab Immersed	0.28	23	4	No	NaCl	0.01428
Lab Immersed	1.2896189	23	8	No	Artificial with marine bacteria	0.01553

Location	Exposure Time (Years)	Temperature (°C)	pH	Oxygen	Seawater	Corrosion Rate (mm/y)
Lab Immersed	0.28	23	4	No	Artificial with marine bacteria	0.01723
Lab Immersed	0.28	23	4	No	Artificial with marine bacteria	0.01763
Lab Immersed	0.28	23	4	No	Artificial with marine bacteria	0.01771
Lab Immersed	1.2896189	23	4	No	Artificial with marine bacteria	0.01961
Lab Immersed	0.28	23	4	Yes	Artificial with marine bacteria	0.02006
Lab Immersed	0.28	23	4	Yes	Artificial with marine bacteria	0.02206
Lab Immersed	1.2896189	23	8	No	Artificial with marine bacteria	0.02241
Lab Immersed	1.2896189	23	8	No	Artificial with marine bacteria	0.02445
Lab Immersed	1.03	23	8	No	Artificial with marine bacteria	0.02466
Lab Immersed	1.2896189	23	4	No	Artificial with marine bacteria	0.02477
Lab Immersed	0.51	23	4	Yes	Artificial with marine bacteria	0.02498

Location	Exposure Time (Years)	Temperature (°C)	pH	Oxygen	Seawater	Corrosion Rate (mm/y)
Lab Immersed	1.03	23	8	No	Artificial with marine bacteria	0.02518
Lab Immersed	0.51	23	4	Yes	Artificial with marine bacteria	0.02528
Lab Immersed	1.03	23	4	No	Artificial with marine bacteria	0.0253
Lab Immersed	0.28	23	8	Yes	NaCl	0.02531
Lab Immersed	0.51	23	4	Yes	Artificial with marine bacteria	0.02672
Lab Immersed	0.28	23	8	Yes	NaCl	0.02692
Lab Immersed	1.2896189	23	4	No	Artificial with marine bacteria	0.0273
Lab Immersed	0.28	23	8	Yes	NaCl	0.02891
Lab Immersed	0.28	23	4	Yes	NaCl	0.02905
Lab Immersed	1.03	23	4	No	Artificial with marine bacteria	0.03074
Lab Immersed	1.03	23	4	No	Artificial with marine bacteria	0.03158
Lab Immersed	0.28	23	4	Yes	NaCl	0.03178
Lab Immersed	0.51	23	4	Yes	NaCl	0.03226
Lab Immersed	0.28	23	4	Yes	NaCl	0.03275

Location	Exposure Time (Years)	Temperature (°C)	pH	Oxygen	Seawater	Corrosion Rate (mm/y)
Lab Immersed	0.28	23	4	Yes	Artificial with marine bacteria	0.03287
Lab Immersed	0.51	23	4	Yes	NaCl	0.03292
Lab Immersed	0.51	23	8	Yes	NaCl	0.03304
Lab Immersed	1.03	23	8	Yes	NaCl	0.03347
Lab Immersed	0.28	23	8	Yes	Artificial with marine bacteria	0.03405
Lab Immersed	0.51	23	8	Yes	NaCl	0.03405
Lab Immersed	1.03	23	8	Yes	NaCl	0.03435
Lab Immersed	0.28	23	8	Yes	Artificial with marine bacteria	0.03497
Lab Immersed	0.51	23	8	Yes	NaCl	0.03511
Lab Immersed	0.28	23	8	Yes	Artificial with marine bacteria	0.03562
Lab Immersed	1.03	23	8	No	Artificial with marine bacteria	0.03564
Lab Immersed	1.2896189	23	8	Yes	NaCl	0.03586
Lab Immersed	1.2896189	23	8	Yes	NaCl	0.03667
Lab Immersed	1.03	23	8	Yes	NaCl	0.03746
Lab Immersed	0.8	23	4	Yes	Artificial with marine bacteria	0.03753

Location	Exposure Time (Years)	Temperature (°C)	pH	Oxygen	Seawater	Corrosion Rate (mm/y)
Lab Immersed	1.2896189	23	8	Yes	NaCl	0.0376
Lab Immersed	0.51	23	8	Yes	Artificial with marine bacteria	0.03815
Lab Immersed	0.51	23	8	Yes	Artificial with marine bacteria	0.03923
Lab Immersed	0.8	23	8	Yes	NaCl	0.03928
Lab Immersed	0.8	23	4	Yes	Artificial with marine bacteria	0.03938
Lab Tidal	0.8	23	8	Yes	NaCl	0.03966
Lab Immersed	0.51	23	8	Yes	Artificial with marine bacteria	0.03972
Lab Immersed	0.8	23	8	Yes	NaCl	0.04153
Lab Immersed	0.8	23	8	Yes	Artificial with marine bacteria	0.04242
Lab Immersed	0.8	23	8	Yes	Artificial with marine bacteria	0.04246
Lab Immersed	0.8	23	8	Yes	Artificial with marine bacteria	0.04332
Lab Immersed	1.03	23	4	Yes	Artificial with marine bacteria	0.04446
Lab Immersed	1.03	23	4	Yes	Artificial with marine bacteria	0.04587

Location	Exposure Time (Years)	Temperature (°C)	pH	Oxygen	Seawater	Corrosion Rate (mm/y)
Lab Immersed	1.2896189	23	8	Yes	Artificial with marine bacteria	0.04605
Lab Immersed	1.2896189	23	8	Yes	Artificial with marine bacteria	0.04636
Lab Immersed	1.2896189	23	4	Yes	Artificial with marine bacteria	0.0466
Lab Immersed	1.2896189	23	8	Yes	Artificial with marine bacteria	0.04861
Lab Immersed	1.2896189	23	4	Yes	NaCl	0.04988
Lab Immersed	1.03	23	4	Yes	NaCl	0.04998
Lab Immersed	1.2896189	23	4	Yes	NaCl	0.05012
Lab Immersed	1.2896189	23	4	Yes	NaCl	0.05043
Lab Immersed	1.03	23	4	Yes	NaCl	0.05111
Lab Immersed	1.03	23	4	Yes	Artificial with marine bacteria	0.05196
Lab Immersed	1.2896189	23	4	Yes	Artificial with marine bacteria	0.0547
Lab Immersed	1.03	23	8	Yes	Artificial with marine bacteria	0.05532
Lab Immersed	1.03	23	8	Yes	Artificial with marine bacteria	0.0579

Location	Exposure Time (Years)	Temperature (°C)	pH	Oxygen	Seawater	Corrosion Rate (mm/y)
Lab Immersed	1.2896189	23	8	Yes	Artificial with marine bacteria	0.05864
Lab Immersed	1.03	23	8	Yes	Artificial with marine bacteria	0.06065
Lab Immersed	1.03	23	8	Yes	Artificial with marine bacteria	0.06187
Lab Immersed	0.8	23	4	Yes	NaCl	0.06339
Lab Immersed	0.8	23	4	Yes	NaCl	0.06483
Lab Immersed	0.8	23	4	Yes	NaCl	0.06547
Lab Immersed	0.51	23	4	Yes	NaCl	0.06976
Lab Immersed	1.2896189	23	4	Yes	Artificial with marine bacteria	0.07199
Immersed	1	23		Yes	Real	0.1
Lab Immersed	1.03	23	4	Yes	NaCl	0.11772
Lab Tidal	1.472679114	23	8	Yes	NaCl	0.12958
Lab Immersed	0.8	23	4	Yes	Artificial with marine bacteria	0.1431
Lab Immersed	1.03	23	4	Yes	Artificial with marine bacteria	0.15413
Lab Immersed	1.2896189	23	4	Yes	Artificial with marine bacteria	0.17572
Immersed	1	23		Yes	Real	0.23

Location	Exposure Time (Years)	Temperature (°C)	pH	Oxygen	Seawater	Corrosion Rate (mm/y)
Lab Tidal	1.472679114	23	8	Yes	NaCl	0.4592
Lab Tidal	1.03	23	8	Yes	NaCl	0.53669
Lab Tidal	1.03	23	8	Yes	NaCl	0.53929
Lab Tidal	1.472679114	23	8	Yes	NaCl	0.58588
Lab Tidal	1.03	23	8	Yes	NaCl	0.59475
Lab Tidal	0.8	23	8	Yes	NaCl	0.60854
Lab Tidal	0.8	23	8	Yes	NaCl	0.64926
Lab Tidal	0.8	23	8	Yes	NaCl	0.66057
Lab Immersed	0.51	23	8	Yes	NaCl	0.76856
Lab Tidal	0.51	23	8	Yes	NaCl	0.81829
Lab Tidal	0.51	23	8	Yes	NaCl	0.83079
Lab Tidal	0.28	23	8	Yes	NaCl	1.03359
Lab Tidal	0.28	23	8	Yes	NaCl	1.22681
Lab Tidal	0.28	23	8	Yes	NaCl	1.23527
Immersed	2	25		No	Real	0.1
Tidal	2	25		Yes	Real	0.21
Immersed	2	25		Yes	Real	0.42
Tidal	8	27.6		Yes	Real	0.07375
Tidal	4	27.6		Yes	Real	0.08
Immersed	8	27.6		Yes	Real	0.08125
Immersed	4	27.6		Yes	Real	0.1
Lab Immersed	1.03	30	8	Yes	NaCl	0.04019
Lab Immersed	1.03	30	8	Yes	NaCl	0.04108
Lab Immersed	1.2896189	30	8	Yes	NaCl	0.05282
Lab Immersed	1.2896189	30	8	Yes	NaCl	0.05376
Immersed	0.353190407	13..38	7.78	No	Real	0.0459
Immersed	0.588650678			No	Real	0.0337

Location	Exposure Time (Years)	Temperature (°C)	pH	Oxygen	Seawater	Corrosion Rate (mm/y)
Immersed	0.301170114			No	Real	0.0502
Immersed	0.265577283			No	Real	0.0549
Immersed	0.3			No	Real	0.0605
Immersed	0.303908024			No	Real	0.065
Immersed	0.298432204			No	Real	0.0678
Immersed	4			Yes	Real	0.075
Immersed	0.301170114			No	Real	0.0764
Immersed	0.605078139			No	Real	0.0985
Immersed	0.276528923			No	Real	0.1197
Immersed	3			Yes	Real	0.2333
Tidal	3			Yes	Real	0.26
Tidal	3			Yes	Real	0.31666